Master's thesis

Herman Sletmoen

Quark and Hybrid Stars with the Quark-Meson Model

Including Preliminaries to Compact Stars

Master's thesis in Physics and Mathematics
Supervisor: Jens Oluf Andersen
June 2022

NTNU
Norwegian University of Science and Technology
Faculty of Natural Sciences
Department of Physics

The Crab Pulsar at the heart of the Crab Nabula. Credit: NASA/CXC/SAO (X-ray), NASA/STScI (optical), NASA-JPL-Caltech (infrared).

NTNU
Norwegian University of
Science and Technology

Herman Sletmoen

Quark and Hybrid Stars with the Quark-Meson Model

Including Preliminaries to Compact Stars

Master's thesis in Physics and Mathematics
Supervisor: Jens Oluf Andersen
June 2022

Norwegian University of Science and Technology
Faculty of Natural Sciences
Department of Physics

NTNU
Norwegian University of
Science and Technology

Acknowledgements

This thesis marks the end of five great years of studying physics at NTNU in Trondheim.

My supervisor, Professor Jens Oluf Andersen, has regularly given me thoughtful and invaluable feedback on my work. When I first met you, I remember that I was a little lost as you sketched the plan for this thesis. Over the coming two semesters, you guided me through the steps of your plan at an understanding and adaptive pace. Looking back, I see very clearly how well-thought-out your plan was, and how you challenged me to take daunting steps into unknown territory along the way while always having realistic expectations of my work. Your friendliness makes you a breeze to cooperate with, and your flexibility has encouraged me to work under freedom and steer relevant pieces of the work towards my own interests and skills. I am sincerely grateful for the time and effort you have devoted to me!

I also wish to thank my loving mother, father and grandparents, in particular for supporting me in whatever I do without ever pressuring me to do what you would do. I love you!

Last, but not least, I am very grateful to the large group of fellow students that I have spent much of my time in Trondheim with. You have made life here very enjoyable and entertaining!

Disclaimer (to the examiner)

This document joins the work of a project and master thesis and is split in three parts:

1. Part I comprises the project thesis.
2. Part II comprises the master thesis and builds upon the work of part I.
3. Part III comprises appendices for both part I and part II.

During evaluation, part II and appendices D, E and G should be considered part of the master thesis. This structure was chosen to avoid self-plagiarism by clearly separating the work of the project thesis from the master thesis, while maintaining continuity from part I to part II. I believe both are valuable works and would find it a shame to omit the project thesis from being published with the master thesis.

Part II frequently refers back to part I for readers who seek background information, but such references are accompanied by short summaries for those who rather wish to read the master thesis independently of the project thesis.

Abstract

Part I (project thesis): Preliminaries to Compact Stars

General relativity and quantum field theory are necessary tools for studying compact stars that are composed of subatomic particles with high density. In this project, we solve the Tolman-Oppenheimer-Volkoff equation for a degenerate Fermi gas composed of free neutrons, producing a mass-radius curve for ideal neutron stars parametrized by central pressure, then finally analyze their stability. First, we derive the Tolman-Oppenheimer-Volkoff equation from the Einstein field equations in a radially symmetric metric for a perfect fluid in equilibrium. Second, we present thermal field theory and use it to express the partition function of a free Fermi gas as a path integral. Next, we combine these two results by numerically integrating the Tolman-Oppenheimer-Volkoff equation with the equation of state that follows from the partition function, yielding the mass-radius curve. Finally, we apply perturbation theory to the initial equilibrium analysis of general relativity to find a Sturm-Liouville problem that determines normal vibration modes for small radial oscillations of stars, then solve it with the shooting method to analyze the stability of the stars. Our mass-radius curve reproduces the upper mass limit of 0.71 solar masses for neutron stars originally calculated by Oppenheimer and Volkoff in 1939. Likewise, our quantitative stability analysis reproduces a set of qualitative rules based on curvature and extrema in the mass-radius diagram. Many observations have been made of neutron stars around 2 solar masses, so the model is too simple for describing them. Nevertheless, this project establishes a broad base platform from which one can continue to study more advanced models for compact stars.

Part II (master thesis): Quark and Hybrid Stars with the Quark-Meson Model

According to quantum chromodynamics, hadron-confined quarks break free into a state of deconfined quark matter at high density. Recent observations of the massive $2M_\odot$-pulsars PSR J1614−2230, PSR J0348+0432 and PSR J0740+6620 suggest that the density in neutron stars could reach sufficiently high levels for formation of small cores of deconfined quark matter in what is then referred to as hybrid stars. If the strange matter hypothesis is true and strange quark matter is stable, even pure strange quark stars consisting only of deconfined strange quark matter could exist. After reviewing the MIT bag model, we model quark stars with the effective quark-meson model of quantum chromodynamics, calculating its grand potential to one fermion loop in the mean-field approximation for bosons, which is consistent in the large-N_c limit. We find maximum masses $M \leq 2.0\,M_\odot$ and $M \leq 1.8\,M_\odot$ with two and three flavors, respectively, but fail to model strange quark stars consistently. In particular, we struggle to fit measured masses of the σ meson to the grand potential at tree-level, but resolve this using recent work of Adhikari and others who consistently fit parameters in the one-loop large-N_c limit. Finally, we assemble hybrid stars by joining the quark-meson model with the hadronic Akmal-Pandharipande-Ravenhall equation of state. This generates short branches of stable hybrid stars with plausible maximum masses $1.9M_\odot \leq M \leq 2.1M_\odot$ and small two-flavor and three-flavor quark cores up to $0.12M_\odot$ and $0.02M_\odot$, respectively. A discontinuous phase transition destabilizes stars with heavier quark cores. The results agree with other work that uses variations of the quark-meson model and the Nambu-Jona-Lasinio model.

Sammendrag

Del I (prosjektoppgave): Grunnelementer innen kompakte stjerner

Generell relativitetsteori og kvantefeltteori er nødvendige verktøy for å studere kompakte stjerner som består av subatomære partikler med høy tetthet. I dette prosjektet løser vi Tolman-Oppenheimer-Volkoff-ligningen for en degenerert Fermigass som består av frie nøytroner, noe som produserer en masse-radius kurve for ideelle nøytronstjerner parametrisert med sentraltrykk, og til slutt analyserer vi stabiliteten deres. Først utleder vi Tolman-Oppenheimer-Volkoff-ligningen fra Einsteins feltlikninger i en kulesymmetrisk metrikk for en perfekt væske i likevekt. Deretter presenterer vi termisk feltteori og bruker det til å uttrykke partisjonsfunksjonen for en fri Fermigass som et veiintegral. Så kombinerer vi disse to resultatene ved å numerisk integrere Tolman-Oppenheimer-Volkoff-ligningen med tilstandsligningen som følger fra partisjonsfunksjonen, og genererer slik masse-radius-kurven. Til slutt bruker vi perturbasjonsteori på den innledende likevektsanalysen av generell relativitetsteori for å finne et Sturm-Liouville-problem som bestemmer normale vibrasjonsmoder for små radielle oscillasjoner av stjerner, og løser det med skytemetoden for å analysere stabilitet deres. Vår masse-radius-kurve reproduserer den øvre massegrensen på 0.71 solmasser for nøytronstjerner opprinnelig beregnet av Oppenheimer og Volkoff i 1939. På samme måte reproduserer vår kvantitative stabilitetsanalyse et sett med kvalitative regler basert på krumning og ekstremalpunkter i masse-radius-diagrammet. Mange nøytronstjerner rundt 2 solmasser har blitt observert, så modellen er for enkel for å beskrive dem. Uansett etablerer dette prosjektet en bred grunnplattform som man kan studere mer avanserte modeller for kompakte stjerner fra.

Del II (masteroppgave): Kvark- og hybridstjerner med kvark-meson-modellen

Ifølge kvantekromodynamikk bryter innesperrede kvarker fri fra hadroner til en tilstand av uavgrenset kvarkmaterie ved høy tetthet. Nylige observasjoner av de massive $2M_\odot$-pulsarene PSR J1614−2230, PSR J0348+0432 og PSR J0740+6620 antyder at tettheten i nøytronstjerner kan bli høy nok til at små kjerner med uavgrenset kvarkmaterie dannes i det som da kalles en hybridstjerne. Hvis hypotesen om at sær-kvarkmaterie er stabilt stemmer, kan til og med rene sær-kvarkstjerner bestående kun av uavgrenset sær-kvarkmaterie eksistere. Etter en gjennomgang av MIT-pose-modellen, modellerer vi kvarkstjerner med den effektive kvark-meson-modellen for kvantekromodynamikk, der vi beregner den frie energien med én fermionløkke i middelfelt-tilnærmingen for bosoner, noe som er konsistent i grensen der N_c er stor. Vi finner maksimumsmasser $M \leq 2.0\,M_\odot$ og $M \leq 1.8\,M_\odot$ med to og tre kvarktyper, henholdsvis, men klarer ikke modellere sær-kvarkstjerner på en konsistent måte. Spesielt sliter vi med å tilpasse målte masser av σ-mesonet til den frie energien på trenivå, men løser opp i dette med nylig arbeid av Adhikari og andre som konsistent tilpasser parameterene med én løkke i grensen der N_c er stor. Til slutt setter vi sammen hybridstjerner ved å koble kvark-meson-modellen sammen med den hadronske tilstandsligningen fra Akmal, Pandharipande og Ravenhall. Dette genererer korte grener av stabile hybridstjerner med rimelige maksimumsmasser $1.9M_\odot \leq M \leq 2.1M_\odot$ og små kjerner med to og tre kvarktyper opptil $0.12M_\odot$ og $0.02M_\odot$, henholdsvis. En diskontinuerlig faseovergang destabiliserer stjerner med tyngre kvarkkjerner. Resultatene samsvarer godt med annet arbeid som bruker variasjoner av kvark-meson-modellen og Nambu-Jona-Lasinio-modellen.

Contents

Notation and Conventions

Units

In part I we use arbitrary units with explicit factors $\hbar$, c, G and k_B everywhere.

In part II we use natural units in which $\hbar/[\hbar] = 1$ and $c/[c] = 1$ when discussing particle physics, but restore SI units when we carry the results over to gravitational physics and discuss stars.

Metric signature

We use the $(+,-,-,-)$ metric signature.

Summation convention

We use the Einstein summation convention, in which an index that appears once as a superscript and again as a subscript in the same term is to be summed over. If the index is Latin, the sum runs from 1 to 3, and if it is Greek, it also runs over 0. For example,

$$T^{\mu}{}_{\mu} = \sum_{\mu=0}^{3} T^{\mu}{}_{\mu} \qquad \text{and} \qquad T^{i}{}_{i} = \sum_{i=1}^{3} T^{i}{}_{i}\,.$$

Part I

Preliminaries to Compact Stars

(project thesis)

Chapter 1

Introduction

Ever since the dawn of mankind, humans have gazed upon the night sky with great curiosity of what lies beyond our immediate reach. Not until the Copernican Revolution in the 16th century did we begin to draw a correct picture of how it really looks and where we fit into it. Nicolaus Copernicus correctly claimed that the Earth revolves around the Sun at the center of a solar system, leading to a number of important discoveries by Tycho Brahe, Johannes Kepler, Galileo Galilei, and culminated in the 17th century as Isaac Newton's described his theory of gravity and motion. With Newton's theory, humans gained a first scientific understanding of the motion and structure of planets and stars. During the following scientific revolution, technological advancements in optics and observational techniques made possible not only observation of a number of new stars and planets, but also measurements of their temperature and distance from Earth. In the 20th century, physicists developed two theories whose application gives unprecedented new insight into stars. First, Albert Einstein's theory of general relativity accurately describes macroscopic aspects of stars where Newton's theory breaks down. Second, quantum theory developed by physicists like Niels Bohr, Erwin Schrödinger, Werner Heisenberg, Paul Dirac, Enrico Fermi and many others gives us a new understanding of the microscopic properties of stars and their structure. In this thesis, we will review the fundamental gravitational and quantum theory for studying neutron stars, the smallest and most massive type of star we know of that has not collapsed to a black hole.

This chapter is inspired by references [Gle00], [Pot10], [Lov+21] and [Wiki21c].

1.1 Life, death and structure of stars

The mother of any star is an enormous accumulation of light elements called a **giant molecular cloud**. Such clouds consist predominantly of hydrogen and some helium produced in the nucleosynthesis that followed the Big Bang. In addition, there are trace amounts of heavier elements from the ashes of dying stars at the end of the life cycle we have just begun to describe. They can contain millions of solar masses distributed over a huge region measuring hundreds of lightyears across with a relatively low average density. Internally, the dynamics of a molecular cloud is chiefly governed by a balance between the attractive force of gravity between particles and the repulsive thermal pressure from their motion and collisions.

Due to the force of gravity, parts of the cloud can clump together in regions of greater density. As more mass accumulates, the force of gravity attracting the surrounding material only increases, causing a snowball effect that amplifies the growth of the clump. Initially, the clump is not so dense, and thermal radiation can escape to the outside, resulting in low temperatures and pressure and allowing the clump to contract with little resistance. However, once the density reaches a sufficiently high level, the clump becomes opaque and traps the thermal radiation inside. When this happens, the temperature rises, in turn causing the outward pressure to

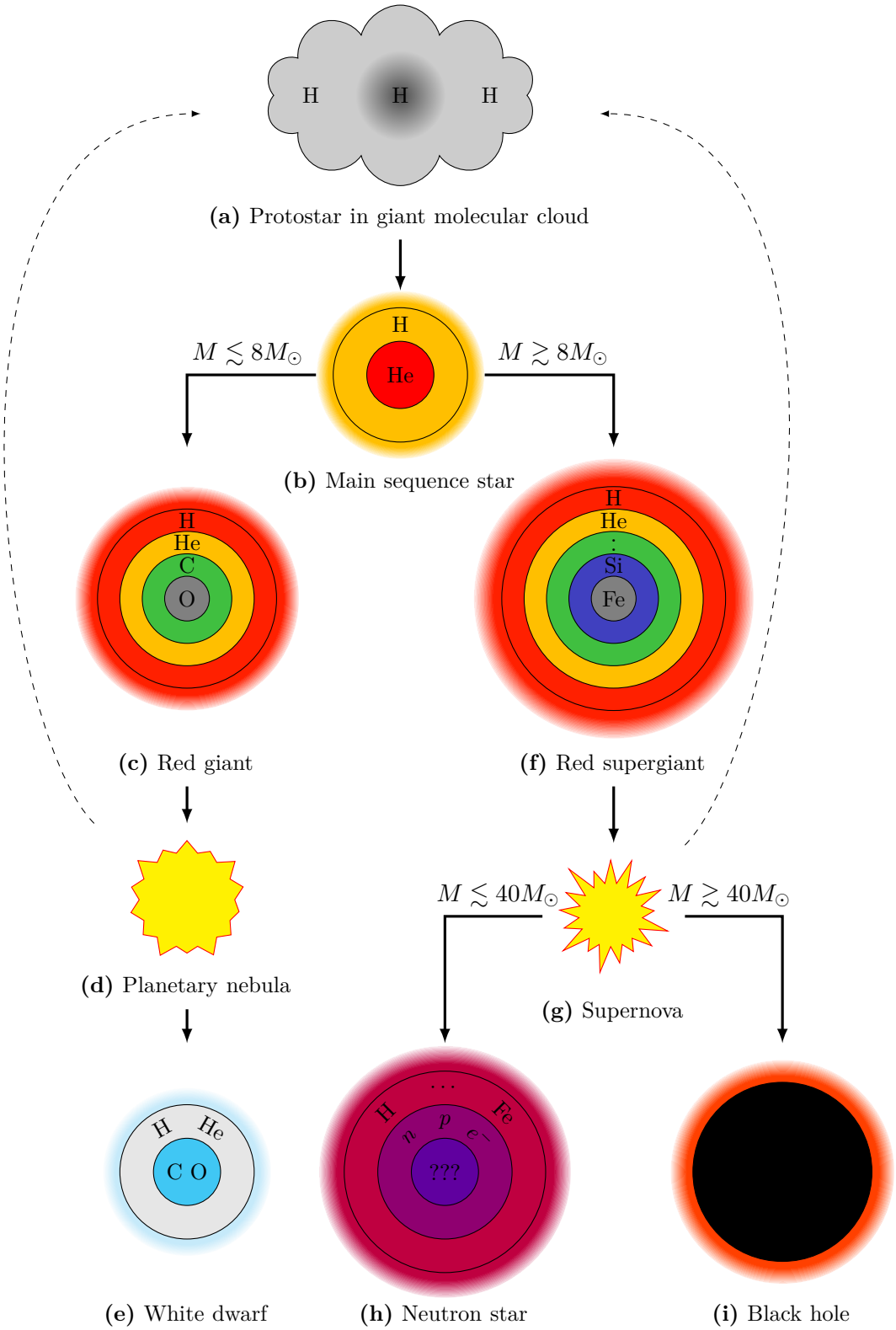

Figure 1.1: Simplified life cycle of stars and their main structure at every stage (not to scale).

increase, ultimately counteracting and slowing down the inwards gravitational collapse. During this stage, as the child "clump" grows by sucking up material from its parent cloud, it receives the honorable name **protostar** (figure 1.1a).

Sooner or later, the protostar has depleted the cloud of its available mass and is promoted to a **pre-main-sequence star**. Whatever total mass M has been gathered by now will determine the fate of the star for the rest of its life. The contraction continues until the temperature and pressure have increased sufficiently for the star to reach a state of equilibrium. Provided that the protostar has accumulated at least $M \gtrsim 0.08 M_\odot$, the temperature will reach $T \gtrsim 10^7\,\mathrm{K}$ – sufficient for the fusion of hydrogen into helium to take place. The ignition of hydrogen marks the transition into a **main sequence star** (figure 1.1b). For billions of years, the star supports itself in this state by burning hydrogen into helium. As time goes on, the hydrogen in the central region is depleted, leaving behind a helium *core* surrounded by a hydrogen *envelope*. Stars smaller than $M \lesssim 0.08 M_\odot$ never reach high enough temperatures for fusing hydrogen and are classified as **brown dwarfs** (not depicted in figure 1.1). Brown dwarfs slowly cool and fade away over hundreds of millions of years without undergoing any further major transitions.

What happens once there is no more hydrogen that can burn depends heavily on the mass of the star. Stars up to $M \lesssim 8 M_\odot$ evolve into **red giants** (figure 1.1c). As the hydrogen is exhausted, the pressure falls and fails to support the star, so the core begins to contract again, in turn causing another increase in temperature. For heavier red giants, the temperature can increase to $T \gtrsim 10^8\,\mathrm{K}$, activating both fusion of helium to carbon and carbon to oxygen, but not of heavier elements. As these processes take place and the burning of each element successively finishes, the core develops shells with elements of increasing mass towards the center as shown in the figure, from hydrogen to helium, carbon or oxygen, depending on the exact mass of the star. Due to the sudden increase in temperature, much energy is transported into the envelope, where it reignites leftover hydrogen and inflates the envelope up to 200 solar radii, motivating the term *giant*.

Eventually, explosions in the envelope of a red giant trigger unstable pulsations of the hydrogen envelope. This causes a **planetary nebula** (figure 1.1d) – an ejection of the outer shells of the red giant into new clouds from which new stars are born. The remaining inert core that is left intact from the nebula forms a **white dwarf** (figure 1.1e). Since no further reactions occur in the core, it is supported against collapse solely by the degeneracy pressure of a sea of electrons that have been ripped away from their parent atoms due to the high density, forced to occupy different states by the Pauli exclusion principle. White dwarfs can be as hot as $T \approx 10^7\,\mathrm{K}$ upon formation, but gradually cool down as they radiate away their energy. Importantly, Chandrasekhar showed that white dwarfs can only support masses up to $M \lesssim 1.47 M_\odot$. [Cha35] He modeled the interior as a relativistic Fermi gas of protons, neutrons and electrons and found that virtually all the pressure that prevents collapse comes from the degeneracy of the electrons, while the protons and neutrons contribute most of the energy density due to their much greater mass. In his honor, the true upper mass limit of white dwarfs is named the Chandrasekhar limit and is currently believed to be closer to $M \lesssim 1.44 M_\odot$. [Gle00]

If the mass of a main sequence star exceeds $M \gtrsim 8 M_\odot$, it first becomes a larger and more intense red giant – a **red supergiant** (figure 1.1f). The increased mass sends the temperature soaring well above $T \gtrsim 10^8\,\mathrm{K}$, activating not only fusion from hydrogen to helium, carbon and oxygen, but even to heavier elements such as neon and iron. When the reactions reach iron, something dramatic happens. As shown in figure 1.2, fusion from elements lighter than iron *release* energy, while fusion from heavier elements *require* energy, causing the burning to stop at iron. At this point, due to the heavy elements, the core of a red supergiant is so massive that it exceeds the Chandrasekhar limit. Inevitably, the core collapses and produces an extremely powerful explosion called a **supernova** (figure 1.1g).

For supergiants lighter than $M \lesssim 40 M_\odot$, the supernova leaves behind an inert core called a **neutron star** (figure 1.1h). The core is then so massive that it is compressed *past* the

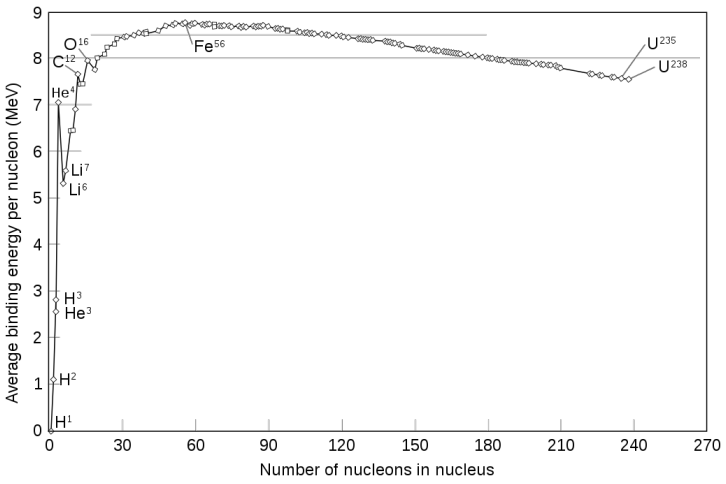

Figure 1.2: The binding energy per nucleon displays a peak near iron. **Credit:** "Fastfission" (https://commons.wikimedia.org/wiki/File:Binding_energy_curve_-_common_isotopes.svg).

Chandrasekhar limit for white dwarfs. The resulting extreme density and Fermi energy makes it energetically favorable for electrons and protons to combine into neutrons in inverse beta decay. In general, the outer core of a neutron star can consist of a neutron (n) superfluid mixed with superconducting protons (p), electrons (e^-) and muons (μ^-). The precise composition of the inner core is an open question, but it is believed that it may contain λ and Σ^- baryons, π and K mesons and deconfined quark matter. [Pot10] Thus, compact stars are not only important for astrophysics as an isolated field, but also serve as a test bed for nuclear and particle physics. Outside the core, there is an envelope consisting of more "ordinary" matter with isolated atomic nuclei, such as iron. Despite their differences, all the particles group up for a last stand against gravity, reaching a new equilibrium configuration that is known as a neutron star. As with white dwarfs, there is a limit for the gravitational force that their degeneracy pressure can withstand. Assuming a neutron star consists of an ideal Fermi gas of pure neutrons, Oppenheimer and Volkoff computed the mass bound $M \lesssim 0.7 M_\odot$ in 1939, building upon earlier work by Tolman. [Opp+39; Tol34] More advanced theories and observations place the so named *Tolman-Oppenheimer-Volkoff limit* for the maximum mass of real neutron stars somewhere between $2M_\odot$ and $3M_\odot$. Like white dwarfs, neutron stars only cool down by radiating their stored energy, from initial core temperatures $T \approx 10^{10}\,\mathrm{K}$ to $T \approx 10^8\,\mathrm{K}$ in a month, then to $T \approx 10^6\,\mathrm{K}$ in less than a million years. [Gle00]

Finally, for supergiants more massive than $M \gtrsim 40 M_\odot$, the Tolman-Oppenheimer-Volkoff limit is exceeded, and not even the degeneracy pressure of neutrons can resist gravity. Beyond this limit, no known star has escaped the collapse to a **black hole** (figure 1.1i). However, it is an open question whether there can be other types of stars that fall between the Tolman-Oppenheimer-Volkoff limit and the lightest observed black holes. No such star has been observed yet, and they are therefore referred to as **exotic stars**, of which **quark stars** is one example.

This marks the last possible path of evolution in the somewhat simplified diagram in figure 1.1.

1.2 Proposition and observation of neutron stars

Only two years after James Chadwick discovered the neutron in 1932, [Cha32] Walter Baade and Fritz Zwicky proposed the existence of stars composed of them. At the time, physicists had only recently begun to study supernovas and the origin of cosmic rays. In developing an explanation of the detailed mechanisms involved in a supernova, they suggested – with great accuracy – that [Baa+34, page 263]

> (...) a super-nova represents the transition of an ordinary star into a *neutron star*, consisting mainly of neutrons. Such a star may possess a very small radius and an extremely high density. As neutrons can be packed much more closely than ordinary nuclei and electrons, the "gravitational packing" energy in a cold neutron star may become very large, and, under certain circumstances, may far exceed the ordinary nuclear packing fractions. A neutron star would therefore represent the most stable configuration of matter as such.

Up until the late 1960s, the existence of neutron stars was only considered a theoretical possibility. How *on Earth* would one ever detect such an object, given their assumed small size, rarity and faint thermal radiation? It was first in 1968 that Jocelyn Bell, a PhD student of Antony Hewish, recorded an unusual **pulsa**ting **r**adio signal from an extraterrestrial source, now referred to as a **pulsar**. [Hew+68] The signal consisted of short, Gaussian pulses lasting about 0.3 s each, repeating themselves with extreme accuracy with a period of 1.337 s. At first, it was speculated that the source could be a white dwarf oscillating radially at the corresponding frequency. Thomas Gold provided an alternative explanation, suggesting the signal arose from a *rotating* neutron star with a strong magnetic field. [Gol68] He imagined the star's magnetic field to be reminiscent of a dipole and that a directional signal was emitted from localized spots on the star corresponding to the magnetic poles. This picture naturally explained the Gaussian shape of the short pulses, as one would detect a similar pattern by measuring the intensity of a directed, rotating lighthouse beam from a fixed position. In contrast, radial pulsations did not explain the shape nor the extreme regularity of the signal. Not long after, Richard Lovelace and others measured a similar signal from the pulsar NP 0532 in the Crab Nebula – also referred to as the Crab Pulsar – with a period of only 33 ms, which was even more challenging to explain by radial oscillations. [Com+69] Moreover, David Richards discovered that the period slightly increased with time in the way that it should for a rotating object that radiates away its energy. This evidence convinced physicists that the signals were indeed from real, rotating and pulsating **neutron stars**. Controversially, Bell's supervisor and first author Hewish later got the Nobel Prize for the discovery of the neutron star, although it was Jocelyn who made the actual measurements and in hindsight is credited first.

1.3 Outline of this thesis

In this thesis, we first develop the fundamental theoretical tools that are necessary to study neutron stars, then apply them to calculate their masses and radii and study their stability.

In **chapter 1**, you already know that we have presented the life cycle of stars and the history of the proposition and discovery of neutron stars.

In **chapter 2**, we derive the **Tolman-Oppenheimer-Volkoff equation**

$$\frac{\mathrm{d}P}{\mathrm{d}r} = -\frac{Gm\epsilon}{r^2c^2}\left(1+\frac{P}{\epsilon}\right)\left(1+\frac{4\pi r^3 P}{mc^2}\right)\left(1-\frac{2Gm}{rc^2}\right)^{-1},$$
$$\frac{\mathrm{d}m}{\mathrm{d}r} = \frac{4\pi r^2\epsilon}{c^2},$$

from the Einstein field equations of general relativity. It is a system of two differential equations for the unknown pressure $P(r)$, mass $m(r)$ and energy density $\epsilon(r)$ at radius r from the center of a star composed of a *perfect fluid* in *equilibrium*. An additional equation of state $\epsilon = \epsilon(P)$ that allows computation of the energy density corresponding to a given pressure is needed to solve the system. This is outside the scope of general relativity and belongs to the field of quantum theory and statistical mechanics. Given the equation of state, however, one may impose the boundary condition $m(0) = 0$ and any central pressure $P(0) = P_c$ and solve the system for the pressure profile $P(r)$ and mass profile $m(r)$ in the star. By defining the surface $r = R$ of the star where the pressure $P(R) = 0$ vanishes, one can obtain the radius R and mass

$M = m(R)$ of the star. In particular, we will solve the system analytically for a star of constant energy density $\epsilon(P) = \epsilon_0$ to derive the Buchdal limit $M/R < 4c^2/9G$ on the mass-radius ratio of *any* star.

In **chapter 3**, we will study **thermal field theory** – the formalism needed to find the effects of quantum fields at nonzero temperature. We will show how to write the quantum partition function

$$Z = \mathrm{tr}\left[e^{-\beta(\hat{H}-\mu_i\hat{N}_i)}\right]$$

as a path integral. First, we use the path integral to find the partition function of a gas of free bosons. Next, we introduce Grassmann numbers and fermionic coherent states to derive a path integral that is valid for fermions, and calculate it for a free Fermi gas. From this partition function, we can calculate the energy density and pressure and hence the equation of state.

In **chapter 4**, we put together the pieces of chapter 2 and chapter 3 and study **ideal neutron stars** made of a **cold free Fermi gas**. From the partition function Z of chapter 3, we find the equation of state

$$\epsilon = \epsilon(P)$$

for the Fermi gas at zero temperature. We then solve the Tolman-Oppenheimer-Volkoff equation numerically for this equation of state to find a mass-radius curve $[R(P_c),\ M(P_c)]$ for such stars parametrized by their central pressure. Finally, we study whether stars on the curve are in stable or unstable equilibrium. We begin by establishing a set of necessary criteria from simple physical considerations. Then we derive a necessary *and* sufficient criterion for stability by using perturbation theory on the treatment in chapter 2, studying the behavior of the perfect fluid as it is disturbed from equilibrium. This results in a Sturm-Liouville problem for radial vibration modes $U_n(r)$ of fluid elements with corresponding squared eigenfrequencies ω_n^2 that will determine whether the star is in a stable or unstable state of equilibrium.

In **chapter 5**, we **conclude** by **discussing** our results in light of observations and presenting an **outlook** on more advanced theories of neutron stars.

In **appendix A**, we give a comprehensive **review of the theory of general relativity**. Here, we derive the Einstein field equations from the principle of least action and cover all aspects of general relativity that we require for chapter 2 and chapter 4, including a detailed discussion of the Newtonian limit.

In **appendix B**, we briefly summarize **relativistic fluid mechanics** for a perfect fluid. Here, we derive relativistic generalizations of results from ordinary fluid mechanics, such as the Euler equation and the equation of energy conservation. These results are needed to understand the behavior of fluids out of equilibrium in the stability analysis in chapter 4.

In **appendix C**, we describe the technique of **Matsubara frequency summation**. This is an elegant mathematical tool that allows us to compute a general class of infinite sums we encounter in chapter 3. Despite their purely mathematical foundation, the results of this appendix naturally give rise to the Bose-Einstein and Fermi-Dirac distributions, and are therefore of great physical interest, too.

In **appendix F**, we give concise derivations of all **integrals** used throughout this thesis. Whenever we encounter difficult integrals in the main text, we will always write the result directly and refer back to this appendix for readers who wish to investigate them in more detail.

In **appendix G**, we describe implementations of **numerical methods and algorithms**. Here, we present dimensionless forms of the Tolman-Oppenheimer-Volkoff equation from chapter 2 and the equations of stellar instability in chapter 4, and solve them with Runge-Kutta methods and the shooting method, respectively.

Chapter 2

The Tolman-Oppenheimer-Volkoff Equation

In 1687, Sir Isaac Newton sparked a revolution in the field of physics when he described motion of bodies with the concept of forces and modeled gravity as an attractive force [New87]

$$\boldsymbol{F} = -G\frac{m_1 m_2}{r^2}\hat{\boldsymbol{r}}.$$

For a long time, his three laws of motion and law of gravity seemed to accurately explain all observable macroscopic motion. In particular, his laws provided an explanation for the three laws of planetary motion that Johannes Kepler found by empirical observation many years earlier in 1609 and 1619. [Kep09; Kep19]

However, in 1859, Urbain Le Verrier observed that Mercury's orbit deviates from the one predicted by Kepler's and Newton's laws. [Le 59] The resolution came half a century later, when Albert Einstein proposed his theory of special relativity in 1905 and ten years later incorporated gravity into this framework with the theory of general relativity. [Ein05; Ein16] While Newton thought gravity *disturbs a body* from moving straight through spacetime, Einstein explained gravity as *curvature of spacetime* that instead reshapes the straight paths along which a body moves. Such a "curved straight path" is called a *geodesic*. Spacetime is curved according to the Einstein field equations

$$G_{\mu\nu} = R_{\mu\nu} - \frac{1}{2}Rg_{\mu\nu} = \frac{8\pi G}{c^4}T_{\mu\nu},$$

expressing how energy and momentum on the rightmost side – such as mass and light – determine the geometry of spacetime on the left side.

The most important result of this chapter will be the Tolman-Oppenheimer-Volkoff equation

$$\frac{\mathrm{d}P(r)}{\mathrm{d}r} = -\frac{Gm(r)\epsilon(r)}{r^2c^2}\left[1+\frac{P(r)}{\epsilon(r)}\right]\left[1+\frac{4\pi r^3 P(r)}{m(r)c^2}\right]\left[1-\frac{2Gm(r)}{rc^2}\right]^{-1},$$

which we will derive from the Einstein field equations. With this equation, we can find the pressure profile and radius of a star once we have an equation of state that relates the pressure and energy of the material inside. This will be an essential tool for our following analysis of different equations of state. The equation was originally derived in 1939 by Robert Oppenheimer and George Volkoff, building on earlier work of Richard Tolman. [Opp+39; Tol34]

We will also examine the general consequences of this equation applied to the extreme case of an incompressible star. To make sense of our results, we also investigate the Newtonian limit of the Tolman-Oppenheimer-Volkoff equation.

We make heavy use of the results from our review of general relativity in appendix A.

This chapter is inspired by references [Car19], [MTW73] and [Kac20].

2.1 Derivation from the Einstein field equations

To analyze astrophysical objects like stars, it is of considerable interest to relate the pressure $P(x)$ and energy density $\epsilon(x)$ or mass density $\rho(x)$ at every position x inside the object. We will derive the relativistic relation between these quantities from the **Einstein field equations**

$$G_{\mu\nu} = R_{\mu\nu} - \frac{1}{2}Rg_{\mu\nu} = \frac{8\pi G}{c^4}T_{\mu\nu}. \tag{2.1}$$

It describes how the geometry of spacetime, expressed by the Ricci tensor $R_{\mu\nu}$ and Ricci scalar R and encapsulated in the Einstein tensor $G_{\mu\nu}$, responds to the presence of energy-momentum in the energy-momentum tensor $T_{\mu\nu}$. In appendix A.1, we review how one begins with the metric (A.10) to successively construct the Christoffel symbols (A.24), Riemann tensor (A.30), Ricci tensor (A.32) and Ricci scalar (A.33). Since these quantities ultimately depend on only the metric and nothing else, *the metric alone encodes all information about the geometry of spacetime*. In appendix A.2, we show how the Einstein field equations arises from the least-action principle of a classical field theory involving a Lagrangian density built from the Ricci scalar. Here, G is the gravitational constant and c is the speed of light.

As we will later compare our findings to those of Newtonian gravity, it will be useful to connect the energy density ϵ to the mass density ρ by the **mass-energy equivalence relation**

$$\epsilon = \rho c^2. \tag{2.2}$$

Unless rotating very fast, stars are well approximated by spheres. For our purposes, we therefore use the coordinates

$$x^\mu = (ct, r, \theta, \phi) \quad \text{with} \quad -\infty < t < \infty, \quad 0 \le r < \infty, \quad 0 \le \theta \le \pi, \quad 0 \le \phi < 2\pi, \tag{2.3}$$

and consider the most general form of a spherically symmetric metric, [Car19, equation 5.11]

$$\mathrm{d}s^2 = e^{2\alpha(r)}c^2\,\mathrm{d}t^2 - e^{2\beta(r)}\,\mathrm{d}r^2 - r^2\left(\mathrm{d}\theta^2 + \sin^2\theta\,\mathrm{d}\phi^2\right). \tag{2.4}$$

We model the interior of the star as a perfect fluid in equilibrium. In appendix B, we show that a perfect fluid with four-velocity field u^μ has the energy-momentum tensor

$$T_{\mu\nu} = \frac{u_\mu u_\nu}{c^2}(\epsilon + P) - g_{\mu\nu}P. \tag{2.5}$$

Due to the combination of equilibrium and spherical symmetry, we assume that $\epsilon = \epsilon(r)$ and $P = P(r)$ only depend on the radial coordinate r, and not on time nor angles. In the rest frame of the fluid, the four-velocity is $u_\mu = (u_0, \mathbf{0})$, and the normalization condition $u_\mu u^\mu = c^2$ requires $u_0 = \pm e^\alpha c$. As we are interested in the evolution of the star, we choose the positive sign so the four-velocity lies in the future light cone. The energy-momentum tensor then takes the diagonal form

$$T_{\mu\nu} = \begin{bmatrix} \epsilon e^{2\alpha} & 0 & 0 & 0 \\ 0 & Pe^{2\beta} & 0 & 0 \\ 0 & 0 & Pr^2 & 0 \\ 0 & 0 & 0 & Pr^2\sin^2\theta \end{bmatrix} \quad \text{or} \quad T^\mu{}_\nu = \begin{bmatrix} \epsilon & 0 & 0 & 0 \\ 0 & -P & 0 & 0 \\ 0 & 0 & -P & 0 \\ 0 & 0 & 0 & -P \end{bmatrix}. \tag{2.6}$$

Starting with the metric (2.4), it is now straightforward, although tedious, to compute the left side of the Einstein field equations (2.1) from the Christoffel symbols (A.24), Riemann tensor (A.30), Ricci tensor (A.32) and Ricci scalar (A.33). For the details, inspect the algebra script in

appendix A.4 or refer to [Car19, equation 5.11-5.15]. After also inserting the energy-momentum tensor on the right and simplifying, we find the three independent equations

$$\frac{1}{r^2}e^{-2\beta}\left(2r\beta' - 1 + e^{2\beta}\right) = \frac{8\pi G}{c^4}\epsilon \qquad \left(G_{00} = \frac{8\pi G}{c^4}T_{00}\right), \tag{2.7a}$$

$$\frac{1}{r^2}e^{-2\beta}\left(2r\alpha' + 1 - e^{2\beta}\right) = \frac{8\pi G}{c^4}P \qquad \left(G_{11} = \frac{8\pi G}{c^4}T_{11}\right), \tag{2.7b}$$

$$e^{-2\beta}\left(\alpha'' + (\alpha')^2 - \alpha'\beta' + \frac{1}{r}(\alpha' - \beta')\right) = \frac{8\pi G}{c^4}P \qquad \left(G_{22} = \frac{8\pi G}{c^4}T_{22}\right). \tag{2.7c}$$

The fourth equation $G_{33} = (8\pi G/c^4)T_{33}$ turns out proportional to the third.

Exterior solution

First, let us quickly review the Schwarzschild solution outside the star, where there is no pressure nor energy density and all right sides vanish. Adding equation (2.7a) and (2.7b) then yields $(\alpha + \beta)' = 0$, so $\alpha + \beta = C$ for some constant C. The constant can be found by noting that far away from the star, as $r \to \infty$, the metric should reduce to the spherical Minkowski metric with $e^{2\alpha} = e^{2\beta} = 1$, so we must have $\alpha + \beta = 0$. Inserting $\beta' = -\alpha'$ into equation (2.7c) then gives a differential equation for α whose solution is $\alpha = \log(1 - D/r)/2$ for some constant D. To determine it, we use that in the Newtonian limit (A.68), the temporal metric element should reduce to $e^{2\alpha} = 1 + 2V/c^2$ where $V = -GM/r$ is the Newtonian gravitational potential of the star and M is the *Newtonian mass* of the star. Thus, $D = 2GM/c^2$ so the metric outside the star is the well-known **Schwarzschild metric**

$$\mathrm{d}s^2 = \left(1 - \frac{2GM}{rc^2}\right)c^2\,\mathrm{d}t^2 - \left(1 - \frac{2GM}{rc^2}\right)^{-1}\mathrm{d}r^2 - r^2\left(\mathrm{d}\theta^2 + \sin^2\theta\,\mathrm{d}\phi^2\right). \tag{2.8}$$

In particular, this metric is singular at the **Schwarzschild radius**

$$R_S = 2GM/c^2. \tag{2.9}$$

This is an **event horizon**. No event occurring inside $r < R_S$ can ever affect an event occurring outside $r > R_S$. [Car19, section 5.6] In other words, nothing that crosses into the horizon can ever come back out – not even light! If a star is so small and massive that its Schwarzschild radius $R_S > R$ lies *outside* the surface, it is invisible from the outside, and we say the star has collapsed to a **black hole**.

Interior solution

We now return to the analysis inside the star. To imitate the Schwarzschild metric element g_{11}, let us define the function $m(r)$ by

$$e^{2\beta(r)} = \left[1 - \frac{2Gm(r)}{rc^2}\right]^{-1}. \tag{2.10}$$

Using this definition to eliminate $\beta(r)$ in favor of $m(r)$ in equation (2.7a), it becomes

$$\frac{\mathrm{d}m(r)}{\mathrm{d}r} = \frac{1}{c^2}4\pi r^2\epsilon(r), \tag{2.11}$$

directly relating $m(r)$ and $\epsilon(r)$. If we set $m(0) = 0$, we can integrate to get

$$m(r) = \frac{1}{c^2}\int_0^r \mathrm{d}r'\,4\pi r'^2\epsilon(r'). \tag{2.12}$$

In [MTW73, page 602] it is shown that setting $m(0) \neq 0$ creates a singularity at the origin, which is not physically acceptable. Meanwhile, definition (2.10) turns equation (2.7b) into

$$\frac{\mathrm{d}\alpha(r)}{\mathrm{d}r} = \frac{G}{r^2c^4}\frac{m(r)c^2 + 4\pi r^3P(r)}{1 - 2Gm(r)/rc^2}. \tag{2.13}$$

To finally eliminate α, we can replace all occurrences of α' and β in the remaining equation (2.7c) with the expressions (2.13) and (2.10). Doing so is straightforward, but cumbersome and most easily done by a computer algebra system – this is the approach we take in appendix A.4. A more elegant, but less straightforward argument is to use local energy-momentum conservation $\nabla_\mu T^{\mu\nu} = 0$, which is both physically reasonable and in fact possible to prove directly from the Einstein field equations (2.1). For two different proofs, see [Wiki21b] and [Kac20, section 8.3.2]. Calculating the necessary Christoffel symbols and taking the covariant derivative (A.18), the component $\nu = 1$ gives

$$\begin{aligned} 0 &= \nabla_\mu T^\mu{}_1 \\ &= \partial_1 T^1{}_1 + \Gamma^\sigma_{1\sigma} T^1{}_1 - \Gamma^\sigma_{1\mu} T^\mu{}_\sigma \\ &= \partial_1 T^1{}_1 + \Gamma^0_{10} T^1{}_1 + \sum_{i=1}^{3} \Gamma^i_{1i} T^1{}_1 - \Gamma^0_{10} T^0{}_0 - \sum_{i=1}^{3} \Gamma^i_{1i} T^i{}_i \,. \end{aligned} \tag{2.14}$$

Using $T^0{}_0 = \epsilon$ and $T^1{}_1 = T^2{}_2 = T^3{}_3 = -P$ from equation (2.6), the explicit sums cancel. With $\Gamma^0_{10} = \frac{1}{2} g^{00} \partial_1 g_{00} = \mathrm{d}\alpha/\mathrm{d}r$, we are left with only

$$\frac{\mathrm{d}\alpha}{\mathrm{d}r} = \frac{-1}{\epsilon + P} \frac{\mathrm{d}P}{\mathrm{d}r}. \tag{2.15}$$

Now α is easily eliminated by equating (2.13) and (2.15). Whichever approach we follow, we end up with the **Tolman-Oppenheimer-Volkoff equation (TOV equation)**

$$\frac{\mathrm{d}P(r)}{\mathrm{d}r} = -\frac{Gm(r)\epsilon(r)}{r^2 c^2} \left[1 + \frac{P(r)}{\epsilon(r)}\right] \left[1 + \frac{4\pi r^3 P(r)}{m(r)c^2}\right] \left[1 - \frac{2Gm(r)}{rc^2}\right]^{-1}. \tag{2.16}$$

It expresses the pressure gradient $\mathrm{d}P/\mathrm{d}r$ at radius r from the center of a spherical star composed of a perfect fluid in equilibrium. Equations (2.11) and (2.16) constitute two equations for the three unknowns $P(r)$, $\epsilon(r)$ and $m(r)$. To determine them, an additional **equation of state**

$$\epsilon = \epsilon(P) \tag{2.17}$$

that relates the thermodynamic variables is required, typically obtained from statistical physics.

Note that the Tolman-Oppenheimer-Volkoff equation states that $\mathrm{d}P/\mathrm{d}r < 0$, provided that the last factor is positive. Indeed, we should have $1 - 2Gm(r)/c^2 r > 0$ for all r, for otherwise the region inside r would be a black hole. Near the center $r \to 0$, we can explicitly see that this holds by using the boundary condition $m(0) = 0$ and the mass gradient (2.11) to Taylor expand $1 - 2Gm(r)/rc^2 \simeq 1 - 2Gm'(r)c^2 = 1 - 8\pi G\epsilon(0)r^2/c^4 \to 1$. Moreover, in section 4.3.1 we will see that an equation of state $\epsilon = \epsilon(P)$ must satisfy $\mathrm{d}P/\mathrm{d}\epsilon > 0$ to be stable and exhibit a non-imaginary speed of sound. Since $\epsilon = \epsilon(P) = \epsilon(P(r))$, this implies that $(\mathrm{d}P/\mathrm{d}r) \,/\, (\mathrm{d}\epsilon/\mathrm{d}r) > 0$ too, so we must also have $\mathrm{d}\epsilon/\mathrm{d}r < 0$. In summary, we have shown that *both the pressure and energy density strictly decreases away from the center of a star.*

Given all three equations (2.11), (2.16) and (2.17), the initial mass $m(0) = 0$ and some central pressure $P(0) = P_c$ or energy density $\epsilon(0) = \epsilon_c$, we can integrate them to find the pressure $P(r)$, mass $m(r)$ and energy density $\epsilon(r)$ everywhere inside the star. We define the surface of the star to be the radius $r = R$ at which the pressure $P(r) = 0$ vanishes, and the star's mass as the corresponding value $m(R) = M$. After obtaining these functions, we can even calculate the full metric functions $\alpha(r)$ and $\beta(r)$ from definition (2.10) and by integrating equation (2.15) subject to matching the Schwarzschild metric (2.8) at $r = R$. Beyond the surface $r > R$, the Schwarzschild metric (2.8) takes over. Solving these equations is therefore our ultimate goal.

Interpretation of mass

One matter that deserves comment is our definition of the star's mass $M = m(R)$. We should be a little careful about this, since it is not obvious how to think of "mass" in relativistic terms.

At the surface $r = R$ of the star, the radial metric element (2.10) matches the Schwarzschild metric (2.8) with the mass

$$M = m(R) = \frac{1}{c^2}\int_0^R \mathrm{d}r\, 4\pi r^2 \epsilon(r) = \int_0^R \mathrm{d}r\, 4\pi r^2 \rho(r). \tag{2.18}$$

We *defined* this mass in the Schwarzschild metric to be the *Newtonian mass* of the star.

However, the mass-energy equivalence (2.2) suggests that we should think of mass proportional to the volume integral of the energy density. The proper volume integral contains the factor $\sqrt{-|g_{ij}|} = e^{\beta(r)}4\pi r^2$ from the full spatial metric, with an extra factor $e^{\beta(r)}$ compared to the Newtonian mass (2.18). With this interpretation, the "mass" is instead

$$\bar{M} = \frac{1}{c^2}\int_0^R \mathrm{d}r\, 4\pi r^2 e^{\beta(r)} \epsilon(r) = \int_0^R \mathrm{d}r\, 4\pi r^2 e^{\beta(r)} \rho(r). \tag{2.19}$$

What is the difference between the two masses (2.18) and (2.19)? In fact, we can show that

$$\bar{M}c^2 - Mc^2 = \int_0^R \mathrm{d}r\, 4\pi r^2 \epsilon(r) \left[\left(1 - \frac{2Gm(r)}{rc^2}\right)^{-1/2} - 1\right] > 0 \tag{2.20}$$

is the *binding energy* that arises due to the gravitational attraction between the individual fluid elements in the star. To see this, let us take the Newtonian limit (A.62). From definition (2.10), we then have

$$g^{11} = -1 + \frac{2Gm(r)}{rc^2} \qquad \text{with} \qquad \frac{Gm(r)}{rc^2} \ll 1. \tag{2.21}$$

Using the Taylor expansion $(1-x)^{-1/2} = 1 + x/2$, we get

$$\bar{M}c^2 - Mc^2 \simeq \int_0^R \mathrm{d}r\, 4\pi r^2 \frac{\epsilon(r)}{c^2}\frac{Gm(r)}{r} = \int_0^R \mathrm{d}r\, 4\pi r^2 \rho(r)\frac{Gm(r)}{r}. \tag{2.22}$$

As shown in [MTW73, exercise 23.7], this is precisely the energy required to construct the star by sequentially placing thin shells of mass $\mathrm{d}m = \rho(r)4\pi r^2\,\mathrm{d}r$ on top of each other, each subject to the gravitational attraction of the shells already placed below it. This is indeed the binding energy that would be required to disperse all the matter in the star to infinity.

The moral of this story is that the mass $M = m(R)$ in the Tolman-Oppenheimer-Volkoff equation should be interpreted as the *Newtonian* mass of the star. But Mc^2 is *not* the total energy of the star, as we saw above that it differs by the binding energy. Experimentally, this implies that we can measure masses of distant stars using *Newtonian* results like Kepler's third law that rely only on simple observations. Moreover, it makes it meaningful to compare masses obtained from general relativity to those found using Newtonian gravity.

2.2 Solution for an incompressible star

Although meaningful equations of state must generally come from quantum theory, statistical physics, thermodynamics and the likes, we can imagine a semi-realistic one that is very simple and special from our gravitational mindset. Namely, suppose that the energy density

$$\epsilon(P) = \epsilon_0 = \text{constant} \tag{2.23}$$

is *independent* of pressure, and thus constant throughout an *incompressible star*. For example, this means the speed of sound (B.36) takes the completely unrealistic value $v = c\sqrt{\mathrm{d}P/\mathrm{d}\epsilon} =$

$c\sqrt{1/(\mathrm{d}\epsilon/\mathrm{d}P)} = c\sqrt{1/0} = \infty$. Anyway, let us press on and see what we get. Integrating the masses (2.12) and (2.18) yield

$$m(r)c^2 = \frac{4}{3}\pi r^3 \epsilon_0 \quad \text{and} \quad Mc^2 = \frac{4}{3}\pi R^3 \epsilon_0. \tag{2.24}$$

Inserting the energy density (2.23) and mass (2.24) into the Tolman-Oppenheimer-Volkoff equation (2.16), P and r separate to

$$\int \frac{\mathrm{d}P}{(\epsilon_0 + P)(\epsilon_0 + 3P)} = -\int \frac{4\pi G r \,\mathrm{d}r}{3c^4 - 8\pi G r^2 \epsilon_0}. \tag{2.25}$$

The left side can now be split by the partial fraction decomposition

$$\frac{1}{(\epsilon_0 + P)(\epsilon_0 + 3P)} = \frac{1}{2P}\left(\frac{1}{\epsilon_0 + P} - \frac{1}{\epsilon_0 + 3P}\right). \tag{2.26}$$

Applying integral (F.1) and (F.2) and imposing the boundary condition $P(R) = 0$, we eventually find the pressure

$$P(r) = \epsilon_0 \frac{\sqrt{1 - \frac{2GMr^2}{R^3c^2}} - \sqrt{1 - \frac{2GM}{Rc^2}}}{3\sqrt{1 - \frac{2GM}{Rc^2}} - \sqrt{1 - \frac{2GMr^2}{R^3c^2}}}. \tag{2.27}$$

In particular, the central pressure is

$$P(0) = \epsilon_0 \frac{1 - \sqrt{1 - \frac{2GM}{Rc^2}}}{3\sqrt{1 - \frac{2GM}{Rc^2}} - 1}. \tag{2.28}$$

It is interesting to note that the pressure is positive for $GM/Rc^2 < 4/9$, but explodes at $GM/Rc^2 = 4/9$ and becomes negative for $GM/Rc^2 > 4/9$. The pressure profile for stars approaching this limit is shown in figure 2.1b. Physically, this means that a star compressed to this limit could only be supported by an infinite central pressure. Nothing can provide such a pressure, so the star would have no other choice than to collapse. In fact, **Buchdal's theorem** states that for an *arbitrary* energy density profile $\epsilon(r)$ that decreases outwards, *any* static spherical star composed of a perfect fluid must satisfy [Buc59]

$$\frac{M}{R} < \frac{4c^2}{9G}. \tag{2.29}$$

We have already shown that the energy density must decrease away from the center for stable stars. His original proof requires careful work, but we can still understand the result intuitively. If there is a maximum density that is supported by nature, then the most massive object we can make should necessarily have that density everywhere. Thus, the bound we have found in our computation with constant energy density should be the most extreme bound. In figure 2.1a, we compare the mass-radius relation (2.24) for incompressible stars to this maximum supported mass.

Another way of looking at the Buchdal's theorem is that the radius of a star must satisfy

$$R > \frac{9}{4}\frac{GM}{c^2} = \frac{9}{8}R_S, \tag{2.30}$$

where R_S is the Schwarzschild radius (2.9). Since $R > 9R_S/8 > R_S$, we see that a stable star that satisfies the Buchdal bound $R > 9GM/4c^2$ is guaranteed to not be a black hole. If we somehow *do* manage to compress a star to the radius $R = 9R_S/8$, we expect it would become unstable, implode and collapse further until its surface is inside the Schwarzschild radius, hence becoming a black hole.

We will shortly see that Buchdal's theorem is a relativistic result and that no such bound arises from Newtonian gravity.

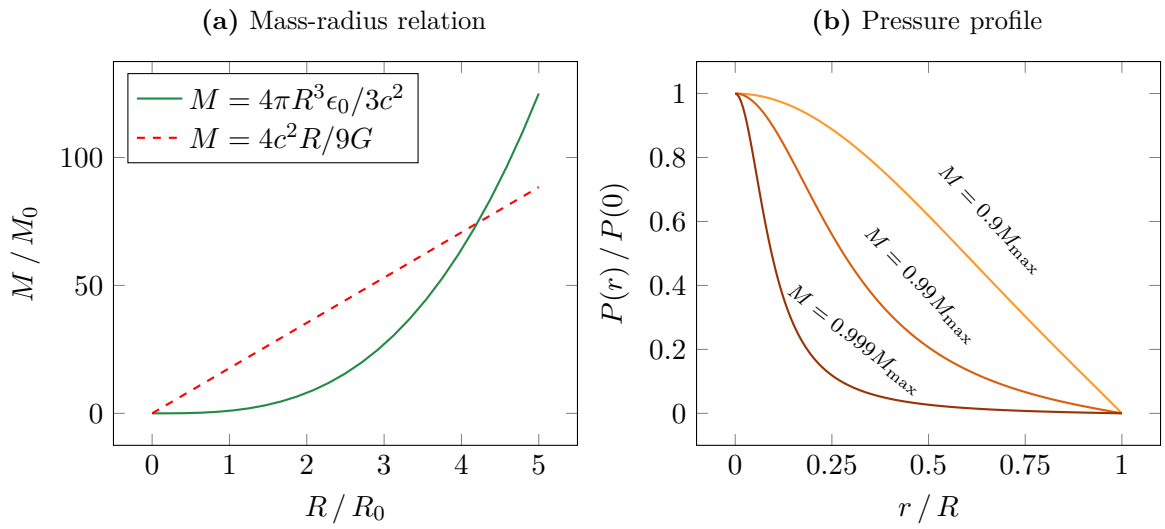

Figure 2.1: **(a)** Mass-radius relation $M = 4\pi R^3\epsilon_0/3c^2$ for stars of constant energy density ϵ_0 compared to the Buchdal bound $M < 4c^2R/9G = M_{\max}$. **(b)** Pressure profile $P(r)$ for stars of radius $R = R_0$ and masses M approaching the Buchdal bound. The constants $R_0 = \sqrt{c^4/G\epsilon_0}$ and $M_0 = 4\pi R_0^3\epsilon_0/3c^2$ are two scales of mass and radius.

2.3 Newtonian limit

In appendix A.3, we thoroughly discuss the conditions under which one should expect general relativity to reduce to Newtonian gravity. Let us derive the pressure gradient in a star using Newtonian gravity and show that the Tolman-Oppenheimer-Volkoff equation (2.16) reduces to it in the Newtonian limit.

Following figure 2.2, consider the mass element $\mathrm{d}m = \rho(r)\,\mathrm{d}A\,\mathrm{d}r$ at distance r from the center of a Newtonian star. By Gauss' law it is attracted to the mass $m(r)$ inside the radius r as if it were concentrated at the center, but experiences no attraction whatsoever from the remaining mass outside r due to symmetry. By Newton's law of gravity it is therefore pulled upon by the force

$$\mathrm{d}\mathbf{F}_1 = -\frac{Gm(r)\,\mathrm{d}m}{r^2}\hat{\mathbf{r}}. \tag{2.31}$$

If the star is in hydrostatic equilibrium, this force must be exactly canceled by the force

$$\mathrm{d}\mathbf{F}_2 = -\Big[P(r+\mathrm{d}r) - P(r)\Big]\,\mathrm{d}A\,\hat{\mathbf{r}} = -\,\mathrm{d}P\,\mathrm{d}A\,\hat{\mathbf{r}} \tag{2.32}$$

that arises from the pressure difference above and below the element. Setting $\mathrm{d}\mathbf{F}_1 + \mathrm{d}\mathbf{F}_2 = 0$ then gives the **Newtonian pressure gradient**

$$\frac{\mathrm{d}P(r)}{\mathrm{d}r} = -\frac{Gm(r)\rho(r)}{r^2}. \tag{2.33}$$

For example, solving this differential equation for a star of constant mass density $\rho(r) = \rho_0$ and mass $m(r) = 4\pi r^3\rho_0/3$, like we solved the Tolman-Oppenheimer-Volkoff equation (2.16) for constant energy density $\epsilon(r) = \epsilon_0$ in section 2.2, we get the pressures

$$P(r) = \frac{\rho_0}{2}\frac{GM}{R}\left(1 + \frac{r}{R}\right)\left(1 - \frac{r}{R}\right) \quad \text{and} \quad P(0) = \frac{\rho_0}{2}\frac{GM}{R}. \tag{2.34}$$

In this case, the pressure is well-behaved for all r. This shows that Buchdal's theorem (2.29) is a purely *relativistic* result.

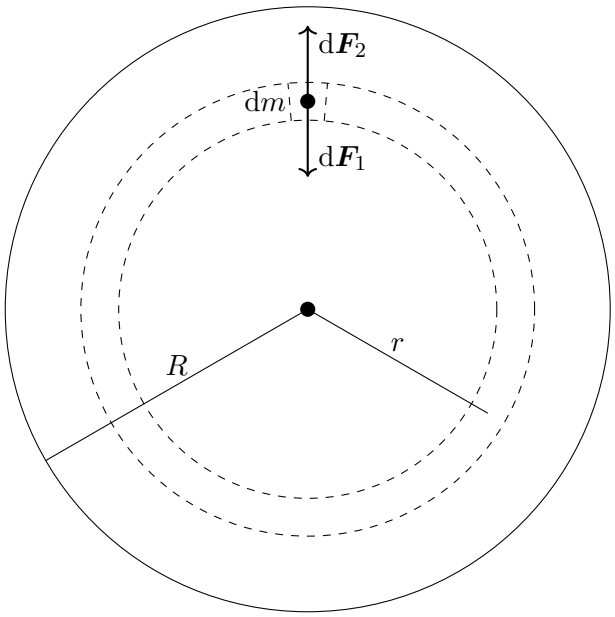

Figure 2.2: When a star of radius R is in hydrostatic equilibrium, the gravitational force $\mathrm{d}\boldsymbol{F}_1$ acting on a mass element $\mathrm{d}m$ at distance r from the center must exactly cancel the pressure gradient force $\mathrm{d}\boldsymbol{F}_2$.

We expect that the Newtonian gradient (2.33) follows from the relativistic gradient (2.16) in the Newtonian limit. Comparing the two, we see that the latter indeed reduces to the former *if* all the corrections to 1 in the three parentheses vanish. Let us verify that this is the case.

First, note that we already invoked the Newtonian limit in equation (2.21), showing that the rightmost parenthesis in the Tolman-Oppenheimer-Volkoff equation (2.16) can be neglected. Second, condition (A.60c) of the Newtonian limit ensures that we can neglect the pressure-energy density ratio

$$\frac{P}{\epsilon} \ll 1 \tag{2.35}$$

in the leftmost parenthesis. Third, we have already argued that stable stars should have non-increasing energy density $\epsilon(r)$ away from the center $r = 0$. We can then pull the minimum density $\min \epsilon(0 \leq r' \leq r) = \epsilon(r)$ outside the integral (2.12) to bound $m(r)c^2 \geq 4\pi r^3 \epsilon(r)/3$. From this and equation (2.35), it follows that

$$\frac{4\pi r^3 P(r)}{m(r)c^2} \leq \frac{4\pi r^3 P(r)}{\frac{4}{3}\pi r^3 \epsilon(r)} = \frac{3P(r)}{\epsilon(r)} \ll 1. \tag{2.36}$$

Thus, all three corrections in the Tolman-Oppenheimer-Volkoff equation (2.16) vanish, so we do indeed recover the Newtonian pressure gradient (2.33) in the Newtonian limit!

In fact, there is an alternative way to see it that requires much less work. After replacing the energy density ϵ with the mass density $\rho = \epsilon/c^2$, the Tolman-Oppenheimer-Volkoff equation takes the form

$$\frac{\mathrm{d}P(r)}{\mathrm{d}r} = -\frac{Gm(r)\rho(r)}{r^2}\left[1 + \frac{P(r)}{\rho(r)c^2}\right]\left[1 + \frac{4\pi r^3 P(r)}{m(r)c^2}\right]\left[1 - \frac{2Gm(r)}{rc^2}\right]^{-1}. \tag{2.37}$$

The Newtonian limit corresponds to sending $c \to \infty$, as this reduces the Lorentz transformations of relativity to the Galilei transformations of Newtonian physics. But sending $c \to \infty$ kills all corrections in the three parentheses of equation (2.37), which restores the Newtonian pressure gradient (2.33)!

2.4 Summary

The most important result of this chapter is the Tolman-Oppenheimer-Volkoff equation (2.16). Together with the mass gradient (2.11) and an assumed *known* equation of state $\epsilon = \epsilon(P)$, they are best viewed as the system of two differential equations

$$\frac{\mathrm{d}P}{\mathrm{d}r} = -\frac{Gm\epsilon(P)}{r^2c^2}\left(1+\frac{P}{\epsilon(P)}\right)\left(1+\frac{4\pi r^3 P}{mc^2}\right)\left(1-\frac{2Gm}{rc^2}\right)^{-1}, \tag{2.38a}$$

$$\frac{\mathrm{d}m}{\mathrm{d}r} = \frac{4\pi r^2\epsilon(P)}{c^2}, \tag{2.38b}$$

for the two unknown functions $P(r)$ and $m(r)$, to be integrated from $m(0) = 0$ and some central pressure $P(0) = P_c$ or energy density $\epsilon(0) = \epsilon_c$. We defined the surface of the star as the radius $r = R$ with zero pressure $P(r) = 0$, and the corresponding mass $m(R) = M$ as the *Newtonian* mass of the star. After solving the system, we can also calculate the full metric functions $\alpha(r)$ and $\beta(r)$ from definition (2.10) and by integrating equation (2.15) subject to matching the Schwarzschild metric (2.8) at $r = R$. Outside the star, the Schwarzschild metric takes over and can be calculated from the mass M, if desired. Thus, solving this system gives us the full spacetime geometry both inside and outside the star! In appendix G.2, we present a program that integrates the system numerically for an arbitrary equation of state.

By solving this system for an incompressible star with constant energy density ϵ_0, we derived the Buchdal limit $M < 4c^2R/9G$. Finally, we saw that the Tolman-Oppenheimer-Volkoff equation reduced to the Newtonian pressure gradient (2.33) in the Newtonian limit.

Chapter 3

Thermal Field Theory

In this chapter, we will develop the theory for studying quantum fields at finite temperature T. We will see that there is an elegant mathematical analogy between the path integral for the transition amplitude of a process and the partition function Z of statistical mechanics, allowing us to express the latter in terms of the former.

In a quantum system in the grand canonical ensemble, the partition function is [Alt+10, equation 4.23]

$$Z = \operatorname{tr}\left[e^{-\beta(\hat{H}-\mu_i\hat{N}_i)}\right] = e^{-\beta\Omega}, \tag{3.1}$$

where $\hat{H}$ is the Hamiltonian operator, $\beta = 1/k_BT$ is the inverse temperature, μ_i are chemical potentials with corresponding number operators $\hat{N}_i$, and k_B is the Boltzmann constant. The trace can be evaluated in any basis. If we find $\log Z$, then we have established the link to thermodynamics with the grand potential $\Omega = -k_BT\log Z$, and can obtain thermodynamic observables such as [And12, chapter 5]

$$\text{the average number of particles} \qquad \langle N_i\rangle = k_BT\frac{\partial\log Z}{\partial\mu_i}, \tag{3.2a}$$

$$\text{the average energy} \qquad \langle E\rangle = \mu_i\langle N_i\rangle - \frac{\partial\log Z}{\partial\beta}, \tag{3.2b}$$

$$\text{the pressure} \qquad P = \frac{k_BT}{V}\log Z. \tag{3.2c}$$

In the Tolman-Oppenheimer-Volkoff equation (2.16), it is precisely the energy density $\epsilon = \langle E\rangle / V$ expressed in terms of the pressure P that we want to insert. As all relevant information about a system can be derived from the partition function, we say that we have "solved the system completely" once we have found Z.

First, we will review how the transition amplitude for a process can be expressed as a path integral. Then we will show how the bosonic partition function Z can be expressed as a path integral by Wick rotating the transition amplitude. By introducing anti-commuting Grassmann numbers, we will see that the partition function for a fermionic field looks quite similar to the bosonic one, although their mathematical foundation is very different. Finally, we will explicitly calculate the partition function for a bosonic and fermionic gas.

This chapter is inspired by references [Kap+06], [Alt+10], [Lai16] and [Sch13].

3.1 Path integral for the bosonic partition function

In this section, we will find a path integral representation of the partition function (3.1) for bosons. First, we will review some elementary properties of the bosonic field $\phi(\boldsymbol{x})$ and the

conjugate momentum field $\pi(\boldsymbol{x})$. Then we will review how the transition amplitude between two states can be written as a path integral. Finally, we will show that we can connect the transition amplitude to the partition function and thereby obtain a path integral representation of it.

Consider a quantum field theory for some field ϕ with Lagrangian density $\mathcal{L}$. The conjugate momentum field is defined as

$$\pi = \frac{\delta \mathcal{L}}{\delta \dot{\phi}}. \tag{3.3}$$

In the Schrödinger picture, the quantized fields have field operators $\hat{\phi}(\boldsymbol{x})$ and $\hat{\pi}(\boldsymbol{x})$, and the Hamiltonian operator is

$$\hat{H} = \int \mathrm{d}^3x\, \mathcal{H}\left(\hat{\pi}(\boldsymbol{x}), \hat{\phi}(\boldsymbol{x})\right), \tag{3.4}$$

where $\mathcal{H} = \pi\dot{\phi} - \mathcal{L}$ is the Hamiltonian density obtained from a Legendre transformation of the Lagrangian density. In analogy with a set of generalized coordinates q_i and momenta p_i in classical mechanics and their corresponding operators $\hat{q}_i$ and $\hat{p}_i$ in quantum mechanics labeled by a discrete index i, we can think of $\hat{\phi}(\boldsymbol{x})$ and $\hat{\pi}(\boldsymbol{x})$ as operators in "position-space" and "momentum-space" labeled by a continuous index $\boldsymbol{x}$.

The field operators $\hat{\phi}(\boldsymbol{x})$ and $\hat{\pi}(\boldsymbol{x})$ have eigenstates $|\phi\rangle$ and $|\pi\rangle$ with corresponding eigenvalues $\phi(\boldsymbol{x})$ and $\pi(\boldsymbol{x})$ at every point $\boldsymbol{x}$, as expressed by the eigenvalue equations

$$\hat{\phi}(\boldsymbol{x})\,|\phi\rangle = \phi(\boldsymbol{x})\,|\phi\rangle \qquad \text{and} \qquad \hat{\pi}(\boldsymbol{x})\,|\pi\rangle = \pi(\boldsymbol{x})\,|\pi\rangle\,. \tag{3.5}$$

By assumption, the field and the momentum satisfy the bosonic commutation relations

$$[\hat{\phi}(\boldsymbol{x}), \hat{\pi}(\boldsymbol{y})] = i\hbar\delta(\boldsymbol{x}-\boldsymbol{y}) \qquad \text{and} \qquad [\hat{\phi}(\boldsymbol{x}), \hat{\phi}(\boldsymbol{y})] = [\hat{\pi}(\boldsymbol{x}), \hat{\pi}(\boldsymbol{y})] = 0. \tag{3.6}$$

We take the position-space eigenstates to be orthogonal and complete in the sense

$$\langle\phi|\phi'\rangle = \prod_{\boldsymbol{x}} \delta\left(\phi(\boldsymbol{x}) - \phi'(\boldsymbol{x})\right) \qquad \text{and} \qquad \int \mathrm{d}\phi\,|\phi\rangle\,\langle\phi| = \mathbb{1}. \tag{3.7}$$

If we find the inner product $\langle\phi|\pi\rangle$, we can use it together with the completeness relation (3.7) to express position-space states and momentum-space states in terms of each other through

$$|\pi\rangle = \int \mathrm{d}\phi\,|\phi\rangle\,\langle\phi|\pi\rangle \qquad \text{and} \qquad |\phi\rangle = \int \mathrm{d}\pi\,|\pi\rangle\,\langle\pi|\phi\rangle\,. \tag{3.8}$$

To do so, let us use the position-space representation $\hat{\pi} = (\hbar/i)\,\delta/\delta\phi$ (like $\hat{p} = (\hbar/i)\,\partial/\partial x$) of the momentum operator. This gives us a first-order differential equation

$$\langle\phi|\hat{\pi}|\pi\rangle = \pi(\boldsymbol{x})\,\langle\phi|\pi\rangle = \frac{\hbar}{i}\frac{\delta}{\delta\phi}\,\langle\phi|\pi\rangle \tag{3.9}$$

for the inner product $\langle\phi|\pi\rangle$. Choosing the solution with prefactor 1, we obtain

$$\langle\phi|\pi\rangle = \exp\left[\frac{i}{\hbar}\int \mathrm{d}^3x\,\pi(\boldsymbol{x})\phi(\boldsymbol{x})\right]. \tag{3.10}$$

The momentum states are also orthogonal and complete, but with slightly different factors. Using the Fourier transformation convention

$$f(x) = \int \frac{\mathrm{d}k}{2\pi}\,e^{-ikx}\,\hat{f}(k) = \int \mathrm{d}x' \underbrace{\int \frac{\mathrm{d}k}{2\pi}\,e^{ik(x'-x)}}_{\delta(x'-x)} f(x'), \tag{3.11}$$

we have the Delta function $\delta(x'-x) = \int (\mathrm{d}k/2\pi)\, e^{ik(x'-x)}$, so orthogonality takes the form

$$\begin{aligned}\langle \pi|\pi'\rangle &= \int \mathrm{d}\phi\, \langle \pi|\phi\rangle\, \langle \phi|\pi'\rangle \\ &= \int \mathrm{d}\phi \exp\left\{\frac{i}{\hbar}\int \mathrm{d}^3x\, \left[\pi'(\boldsymbol{x}) - \pi(\boldsymbol{x})\right]\phi(\boldsymbol{x})\right\} \\ &= 2\pi\hbar\, \delta\big(\pi(\boldsymbol{x}) - \pi'(\boldsymbol{x})\big).\end{aligned} \tag{3.12}$$

To find the completeness relation for $\hat{\pi}(\boldsymbol{x})$, we postulate it up to a constant B. Consider

$$\begin{aligned}1 &= \int \frac{\mathrm{d}\pi(\boldsymbol{x})}{B}\, |\pi\rangle\, \langle \pi| \\ &= \int \frac{\mathrm{d}\pi(\boldsymbol{x})}{B}\, |\pi\rangle \int \frac{\mathrm{d}\pi'(\boldsymbol{x})}{B} \int \mathrm{d}\phi(\boldsymbol{x})\, \langle \pi|\phi\rangle\, \langle \phi|\pi'\rangle\, \langle \pi'| \\ &= \int \frac{\mathrm{d}\pi(\boldsymbol{x})}{B}\, |\pi\rangle \int \frac{\mathrm{d}\pi'(\boldsymbol{x})}{B} \underbrace{\int \mathrm{d}\phi(\boldsymbol{x}) \exp\left\{\frac{i}{\hbar}\int \mathrm{d}^3x\, \left[\pi'(\boldsymbol{x}) - \pi(\boldsymbol{x})\right]\phi(\boldsymbol{x})\right\}}_{2\pi\hbar\, \delta(\pi'(\boldsymbol{x}) - \pi(\boldsymbol{x}))} \langle \pi'| \\ &= \frac{2\pi\hbar}{B} \underbrace{\int \frac{\mathrm{d}\pi(\boldsymbol{x})}{B}\, |\pi\rangle\, \langle \pi|}_{1}.\end{aligned} \tag{3.13}$$

This would be inconsistent unless $B = 2\pi\hbar$, so completeness in momentum-space is

$$\int \frac{\mathrm{d}\pi(\boldsymbol{x})}{2\pi\hbar}\, |\pi\rangle\, \langle \pi| = 1. \tag{3.14}$$

Let us use these properties to demonstrate how a transition amplitude between two states can be written as a path integral. When the Hamiltonian $\hat{H}$ is independent of time, a quantum system evolves from an initial state $|\phi_A\rangle$ to the state $e^{-i\hat{H}T/\hbar}\, |\phi_A\rangle$ during the time T. [Sak+21, equation 2.28] Later we will study statistical mechanics for a star in thermal equilibrium – then the Hamiltonian is always independent of time, otherwise the system would not be in equilibrium. The transition amplitude for going from the state $|\phi_A\rangle$ to a different state $|\phi_B\rangle$ in the time T is therefore

$$\left\langle \phi_B \middle| e^{-i\hat{H}T/\hbar} \middle| \phi_A \right\rangle \qquad (A \to B). \tag{3.15}$$

Now split the time interval T into N intervals $\Delta t = T/N$, and decompose the evolution operator $e^{-i\hat{H}T/\hbar}$ into equally many products of $e^{-i\hat{H}\Delta t/\hbar}$ to write

$$\left\langle \phi_B \middle| e^{-i\hat{H}T/\hbar} \middle| \phi_A \right\rangle = \left\langle \phi_B \middle| e^{-i\hat{H}\Delta t/\hbar} \cdots e^{-i\hat{H}\Delta t/\hbar} \cdots e^{-i\hat{H}\Delta t/\hbar} \middle| \phi_A \right\rangle. \tag{3.16}$$

We will take the limit $N \to \infty$ in the end, so we assume that each interval Δt is small. Now comes the most important trick – take a deep breath and do the following:

- Insert N complete sets of *momentum* states $1 = \int \mathrm{d}\pi_n/(2\pi\hbar)\, |\pi_n\rangle\, \langle \pi_n|$ to the *left* of every exponential, including the rightmost one, with n increasing from right to left.
- Insert $N-1$ complete sets of *position* states $1 = \int \mathrm{d}\phi_n\, |\phi_n\rangle\, \langle \phi_n|$ to the *right* of every exponential, excluding the rightmost one, with n increasing from right to left.

Now exhale. With this trick, the transition amplitude can be written as the product

$$\left\langle \phi_B \middle| e^{-i\hat{H}T/\hbar} \middle| \phi_A \right\rangle = \prod_{n=0}^{N} \int \mathrm{d}\phi_n \int \frac{\mathrm{d}\pi_n}{2\pi\hbar} \left\langle \phi_{n+1} \middle| \pi_n \right\rangle \left\langle \pi_n \middle| e^{-i\hat{H}\Delta t/\hbar} \middle| \phi_n \right\rangle, \tag{3.17}$$

where we have defined the first and last states

$$|\phi_0\rangle = |\phi_A\rangle \qquad \text{and} \qquad |\phi_{N+1}\rangle = |\phi_B\rangle. \tag{3.18}$$

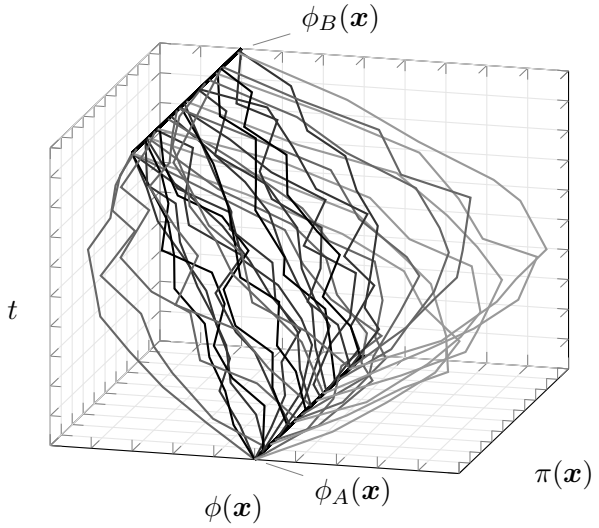

Figure 3.1: A quantum system that evolves from the initial field $\phi_A(\boldsymbol{x})$ to the final field $\phi_B(\boldsymbol{x})$ can take all possible paths through phase space, but some are more likely than others. The conjugate momentum field $\pi(\boldsymbol{x})$ does not need to be the same at the start and the end.

The inner products $\langle\phi_{n+1}|\pi_n\rangle$ can simply be replaced by the exponential (3.10), so let us turn our attention to the matrix elements $\langle\pi_n|e^{-i\hat{H}\Delta t/\hbar}|\phi_n\rangle$. Since the time step Δt is assumed to be small, we can expand the exponential $e^{-i\hat{H}\Delta t/\hbar} \simeq 1 - i\hat{H}\Delta t/\hbar$ to first order in time. Under the assumption that the Hamiltonian $\hat{H}$ is a sum of terms with all *position*-space operators $\hat{\phi}$ on the *right* and all *momentum*-space operators $\hat{\pi}$ on the *left*, we can pull it out of the product at the additional benefit of replacing its operators by their eigenvalues. We then obtain

$$\begin{aligned}\left\langle \pi_n \middle| e^{-i\hat{H}\Delta t/\hbar} \middle| \phi_n \right\rangle &\simeq \left\langle \pi_n \middle| \left(1 - i\hat{H}\Delta t/\hbar\right) \middle| \phi_n \right\rangle \\ &= \left\langle \pi_n \middle| \phi_n \right\rangle \left(1 - iH_n\Delta t/\hbar\right) \\ &\simeq \left\langle \pi_n \middle| \phi_n \right\rangle e^{-iH_n\Delta t/\hbar},\end{aligned} \tag{3.19}$$

where we have no more *operators*, but only the Hamiltonian *eigenvalue* at the n-th timestep,

$$H_n = \int \mathrm{d}^3x\, \mathcal{H}\left(\pi_n(\boldsymbol{x}), \phi_n(\boldsymbol{x})\right). \tag{3.20}$$

Since $\hat{H} = \hat{H}^\dagger$ is Hermitian, this should still be valid if $\hat{\pi}$ and $\hat{\phi}$ are ordered right-to-left instead of left-to-right. The left-right ordering was only assumed for pedagogical reasons to match the left $\langle\pi_n|$ and right $|\phi_n\rangle$ in equation (3.19). We will only study Hamiltonians that is fully left-right or right-left ordered, for which these steps are valid. Note the importance of expanding the exponential to first order in time only. If the Hamiltonian contained *any* mixed sequence of operators such as $H \propto \hat{\pi}\hat{\phi}$, then higher powers like $\hat{H}^2 \propto \hat{\pi}\hat{\phi}\hat{\pi}\hat{\phi}$ in the power series expansion of the time evolution operator would not be in the assumed left-right or right-left order.

Substituting equations (3.10), (3.19) and (3.20), the transition amplitude (3.17) becomes

$$\begin{aligned}\left\langle \phi_B \middle| e^{-i\hat{H}T/\hbar} \middle| \phi_A \right\rangle = &\left(\prod_{n=1}^{N} \int \mathrm{d}\phi_n \int \frac{\mathrm{d}\pi_n}{2\pi\hbar}\right) \\ &\times \exp\left\{\frac{i\Delta t}{\hbar} \sum_{n=1}^{N} \int \mathrm{d}^3x \left[\pi_n(\boldsymbol{x}) \frac{\phi_{n+1}(\boldsymbol{x}) - \phi_n(\boldsymbol{x})}{\Delta t} - \mathcal{H}\left(\pi_n(\boldsymbol{x}), \phi_n(\boldsymbol{x})\right)\right]\right\}.\end{aligned} \tag{3.21}$$

Finally, we take the continuum limit by sending $N \to \infty$. It is then natural to define $\phi(\boldsymbol{x}, t_n) = \phi_n(\boldsymbol{x}, t_n)$ and $\pi(\boldsymbol{x}, t_n) = \pi_n(\boldsymbol{x}, t_n)$ to be the spatial fields at each timestep t_n. Both

become continuous functions of time in the continuum limit. We also use the finite difference definition of the derivative to turn the fraction in the exponential into a partial derivative $\dot{\phi}(\boldsymbol{x},t) = \partial\phi(\boldsymbol{x},t)/\partial t$. Similarly, we use the Riemann sum definition of the integral to turn the sum $\Delta t \sum$ into an integral $\int \mathrm{d}t$. We also define the **functional integrals**

$$\int \mathcal{D}\phi = \lim_{N\to\infty} \prod_{n=1}^{N} \int \mathrm{d}\phi_n \qquad \text{and} \qquad \int \mathcal{D}\pi = \lim_{N\to\infty} \prod_{n=1}^{N} \int \frac{\mathrm{d}\pi_n}{2\pi\hbar}. \tag{3.22}$$

With all of these steps, the transition amplitude takes the form of the **path integral**

$$\begin{aligned} \left\langle \phi_B \left| e^{-i\hat{H}T/\hbar} \right| \phi_A \right\rangle = \int \mathcal{D}\pi \int_{\phi(\boldsymbol{x},0)=\phi_A(\boldsymbol{x})}^{\phi(\boldsymbol{x},T)=\phi_B(\boldsymbol{x})} \mathcal{D}\phi \\ \times \exp\left\{ \frac{i}{\hbar} \int_0^T \mathrm{d}t \int \mathrm{d}^3x \left[\pi(\boldsymbol{x},t)\dot{\phi}(\boldsymbol{x},t) - \mathcal{H}\left(\pi(\boldsymbol{x},t), \phi(\boldsymbol{x},t)\right) \right] \right\}. \end{aligned} \tag{3.23}$$

It is tempting to recognize $\pi\dot{\phi} - \mathcal{H}$ as the Legendre transformation that converts to the Lagrangian density and write $\mathcal{L}$ in its place. But we should be careful – the Legendre transformation converts the independent variable $\dot{\phi}$ in $\mathcal{L}(\phi, \dot{\phi}, \nabla\phi)$ to π in $\mathcal{H}(\phi, \pi, \nabla\phi)$. We are integrating over π and should therefore not lose track of it by writing $\mathcal{L} = \mathcal{L}(\phi, \dot{\phi}, \nabla\phi)$. Thus, we do not modify the integral further.

The path integral expresses the transition amplitude for the process $A \to B$ as a sum over all possible paths through phase space, each weighted by the value on the unit circle with phase corresponding to the action of the path. This interpretation is illustrated in figure 3.1. Note that the position-space integral $\int \mathcal{D}\phi$ is constrained to start and end in the initial and final states due to the leftmost and rightmost products with the edge states $\langle\phi_B|$ and $|\phi_A\rangle$ in the transition amplitude, but the momentum integral $\int \mathcal{D}\pi$ has no such constraint.

Why have we spent so much time on this transition amplitude, when we really are only interested in the partition function (3.1)? If we evaluate the trace in the basis of fields $|\phi_0\rangle$, we obtain

$$Z = \int \mathrm{d}\phi_0 \left\langle \phi_0 \left| e^{-\beta(\hat{H} - \mu_i \hat{N}_i)} \right| \phi_0 \right\rangle. \tag{3.24}$$

This is precisely an integral over transition amplitudes (3.23), but now with

- equal start and end states $|\phi_A\rangle = |\phi_B\rangle = |\phi_0\rangle$,
- the Hamiltonian $\hat{H} - \mu_i \hat{N}_i$ and
- a purely imaginary time variable $t = -i\tau$ with τ running from 0 to $\beta\hbar$.

Thus, we can express the partition function (3.24) as path integrals (3.23) with these simple substitutions! We redefine the field $\phi(\boldsymbol{x},t) \to \phi(\boldsymbol{x},\tau)$ to be functions of the new "inverse temperature time" τ. Therefore, we substitute $i\int \mathrm{d}t \to \int \mathrm{d}\tau$ and $\dot{\phi}(x,t) = \partial\phi(\boldsymbol{x},t)/\partial t \to \partial\phi(\boldsymbol{x},\tau)/\partial(-i\tau) = i\dot{\phi}(\boldsymbol{x},\tau)$. Omitting the arguments of the fields from now, we obtain the **bosonic partition function**

$$Z = \int \mathcal{D}\pi \oint_{+} \mathcal{D}\phi \exp\left[\frac{1}{\hbar} \int_0^{\beta\hbar} \mathrm{d}\tau \int \mathrm{d}^3x \left(i\pi\dot{\phi} - \mathcal{H} + \mu\mathcal{N} \right) \right] \tag{3.25}$$

where we have absorbed $\int \mathrm{d}\phi_0$ into the path integral $\int \mathcal{D}\phi$ and write $\oint_+$ to indicate that we integrate over all fields $\phi(x,\tau) = \phi(x,\tau+\beta\hbar)$ that are *periodic* in τ, due to the equal start and end states $\phi_A(\boldsymbol{x}) = \phi_B(\boldsymbol{x})$ in equation (3.24). Thus, thermal field theory – statistical mechanics for quantum fields at finite temperature – is essentially equivalent to ordinary quantum field theory with temperature-dependent time and periodic fields, and the partition function is obtained by integrating along closed paths in phase space!

The only ingredients in the path integral we have not yet discussed are the chemical potential μ and the number density $\mathcal{N}$. In statistical mechanics, we can associate a chemical potential μ with any conserved quantity N of the system in the "shifted Hamiltonian" $H' = H - \mu N$. How can we connect this to the field theory under study? Suppose that the field theory admits a conserved current

$$j^\nu(x) \text{ with } \partial_\nu j^\nu(x) = 0 \text{ and conserved charge } Q = \int \mathrm{d}^3x\, j^0(x) \text{ with } \frac{\mathrm{d}Q}{\mathrm{d}t} = 0. \tag{3.26}$$

In the corresponding quantized quantum field theory, this is equivalent to the commutation $[\hat{H}, \hat{Q}] = 0$ between the Hamiltonian operator and charge operator, for then $\mathrm{d}\langle Q\rangle/\mathrm{d}t = \langle[\hat{H}, \hat{Q}]\rangle = 0$ by the Ehrenfest theorem. The conserved current $j^\nu(x)$ can be coupled to a gauge field $A_\nu(x)$ by adding the term $A_\nu(x)j^\nu(x)$ to the Lagrangian density $\mathcal{L}$, or $-A_\nu(x)j^\nu(x)$ to the Hamiltonian density $\mathcal{H}$. Under a standard, Abelian gauge transformation

$$A_\nu(x) \quad \to \quad A'_\nu(x) = A_\nu(x) + \partial_\nu\lambda(x), \tag{3.27}$$

we can apply the product rule backwards to show that the Lagrangian density changes as

$$\mathcal{L} = \mathcal{L}_0 + A_\nu j^\nu \quad \to \quad \mathcal{L}' = \mathcal{L}_0 + A'_\nu j^\nu = \mathcal{L} + (\partial_\nu\lambda)j^\nu = \mathcal{L} + \partial_\nu(\lambda j^\nu) - \lambda\partial_\nu j^\nu. \tag{3.28}$$

Thus, the Lagrangian is invariant up to the surface term $\partial_\nu(\lambda j^\nu)$, provided that the current is conserved according to $\partial_\nu j^\nu = 0$, so the equations of motion are unchanged. To make contact between the field theory and the grand canonical ensemble where $\mathcal{H}' = \mathcal{H} - \mu\mathcal{N}$, we see that the chemical potential μ is equivalent to the temporal component of a constant gauge field

$$A_\nu(x) = \mu\delta^0{}_\nu \quad \text{coupled to the conserved current} \quad \mathcal{N}(x) = j^0(x)! \tag{3.29}$$

In conclusion, the so far unspecified density $\mathcal{N}$ in the partition function is identified with the charge density j^0 corresponding to a conserved charge $Q = \int \mathrm{d}^3x\, j^0(x)$.

To what extent is this coupling physical? In other words, is it possible to remove the gauge field A_ν with a gauge transformation (3.27) such that $A'_\nu = 0$? To achieve this, we would have to choose $\lambda(x) = -ct\mu$ up to a constant, because then $A'_\nu = \delta^0{}_\nu\mu + \delta^0{}_\nu\partial_0\lambda = \mu - \mu = 0$. But the gauge function $\lambda(t, \boldsymbol{x}) \neq \lambda(t + \beta\hbar, \boldsymbol{x})$ is not single-valued on the *periodic* manifold of fields we are considering. We therefore conclude that the gauge transformation is ill-defined, and that the coupling between the chemical potential and conserved current is truly physical.

Later, we will see examples of theories both with and without conserved charges. When studying Dirac fermions, we will see that the conserved charge corresponds to the difference between the number of particles and antiparticles. The associated chemical potential essentially functions as a knob with which we can regulate the balance between particles and antiparticles in the system.

3.2 Path integral for the fermionic partition function

We will now develop a path integral for a fermionic field described by a four-spinor $\psi = [\psi_0, \psi_1, \psi_2, \psi_3]$, For example, the Dirac Lagrangian is $\mathcal{L} = \bar{\psi}(i\hbar c\,\partial\!\!\!/ - mc^2)\psi$ with conjugate momentum $\pi = \delta\mathcal{L}\big/\delta\dot{\psi} = i\hbar\psi^\dagger$, so we are instructed to treat the field and its conjugate *independently* in the path integral. This is not a peculiarity of fermionic fields only – for a complex scalar field ϕ, for example, we would also be instructed to treat ϕ and ϕ^* separately.

Why do we need to derive the path integral for fermions separately – can we not just use the bosonic path integral (3.25) with the appropriate conjugate momentum? By assumption, the fermion field operators obey the fermionic **anti-commutation relations**

$$\{\hat{\psi}_\alpha(\boldsymbol{x}), \hat{\psi}_\beta(\boldsymbol{y})\} = \{\hat{\psi}^\dagger_\alpha(\boldsymbol{x}), \hat{\psi}^\dagger_\beta(\boldsymbol{y})\} = 0, \tag{3.30a}$$

$$\{\hat{\psi}_\alpha(\boldsymbol{x}), \hat{\psi}^\dagger_\beta(\boldsymbol{y})\} = \{\hat{\psi}^\dagger_\alpha(\boldsymbol{x}), \hat{\psi}_\beta(\boldsymbol{y})\} = \delta_{\alpha\beta}\delta(\boldsymbol{x} - \boldsymbol{y}), \tag{3.30b}$$

in contrast to the bosonic commutators (3.6). In the derivation of the bosonic path integral (3.25), we treated the eigenvalues ϕ and π of the operators $\hat{\phi}$ and $\hat{\pi}$ as ordinary numbers. However, the anti-commutators (3.30) of the fermionic field operators in fact requires their eigenvalues to anti-commute! For example,

$$\begin{aligned} &\text{if} \quad \hat{\psi}\,|\psi\rangle = \psi\,|\psi\rangle \quad \text{and} \quad \langle\psi|\,\hat{\psi}^\dagger = \langle\psi|\,\psi^*, \\ &\text{then} \quad \langle\psi|\hat{\psi}^\dagger\hat{\psi}|\psi\rangle = \langle\psi|\psi^*\psi|\psi\rangle = -\langle\psi|\psi\psi^*|\psi\rangle = -\langle\psi|\hat{\psi}\hat{\psi}^\dagger|\psi\rangle \quad \text{by (3.30)}, \\ &\text{so} \quad \{\psi,\psi^*\} = 0. \end{aligned} \tag{3.31}$$

By replacing only one operator with its eigenvalue in the second line, we can also deduce the requirements $\{\psi,\hat{\psi}^\dagger\} = \{\psi,\hat{\psi}\} = 0$ between operators and eigenvalues. The bosonic path integral (3.25) and its derivation is therefore not valid for fermions.

Grassmann numbers

To develop the fermionic path integral, we therefore replace the algebra of ordinary commuting numbers in the bosonic case with anti-commuting **Grassmann numbers**. We will need only a few basic properties of Grassmann numbers, so let us quickly review them here.

The algebra of a set of N Grassmann numbers ψ_i and their conjugates ψ_i^* is defined by the anti-commutators

$$\{\psi_i,\psi_j\} = \{\psi_i,\psi_j^*\} = \{\psi_i^*,\psi_j^*\} = 0. \tag{3.32}$$

In particular, this implies that $\psi_i^2 = 0$, so $\psi_i^n = 0$ for any $n \geq 2$. Functions of Grassmann numbers are defined by their Taylor expansion, but the property $\psi_i^2 = 0$ will always terminate the Taylor series after a finite number of terms. Thus, the most general function of N Grassmann numbers and their conjugates can be written

$$\begin{aligned} f(\psi) = A + \sum_i A_i\psi_i + \sum_i B_i\psi_i^* + \sum_{i,j} A_{ij}\psi_i\psi_j + \sum_{i,j} B_{ij}\psi_i\psi_j^* + \sum_{i,j} C_{ij}\psi_i^*\psi_j^* \\ + \ldots + Z_{1\cdots N}\psi_1\psi_1^*\cdots\psi_N\psi_N^*. \end{aligned} \tag{3.33}$$

For example, for the exponential function of one Grassmann number ψ, only the first two terms survive the Taylor series

$$\exp(\psi) = \sum_{n=0}^{\infty}\frac{\psi^n}{n!} = 1 + \psi. \tag{3.34}$$

Integration over Grassmann numbers is defined by

$$\int \mathrm{d}\psi_i\, 1 = 0, \tag{3.35a}$$

$$\int \mathrm{d}\psi_i\, \psi_j = \delta_{ij}. \tag{3.35b}$$

These are the Grassmann number properties that we will need.

Fermionic coherent states

In the derivation of the bosonic path integral (3.25), we relied heavily on using eigenstates of the system to take the trace in (3.1), insert completeness relations and take inner products between eigenstates. To find analogous ways of doing this with fermionic fields, we will introduce **fermionic coherent states**.

Let us get to work. Suppose we have a finite number N of Grassmann numbers ψ_i with conjugates ψ_i^* and as many **creation** and **annihilation** operators $\hat{\psi}_i^\dagger$ and $\hat{\psi}_i$. Right after

equation (3.31), we argued that Grassmann numbers anti-commute not only with each other, but also with the operators. By assumption, we therefore start with all the anti-commutators

$$\{\hat{\psi}_i, \hat{\psi}_j\} = \{\hat{\psi}_i^\dagger, \hat{\psi}_j^\dagger\} = 0 \qquad \text{(similar operators)}, \tag{3.36a}$$

$$\{\hat{\psi}_i, \hat{\psi}_j^\dagger\} = \{\hat{\psi}_i^\dagger, \hat{\psi}_j\} = \delta_{ij} \qquad \text{(different operators)}, \tag{3.36b}$$

$$\{\psi_i, \psi_j\} = \{\psi_i, \psi_j^*\} = \{\psi_i^*, \psi_j^*\} = 0 \qquad \text{(numbers)}, \tag{3.36c}$$

$$\{\psi_i, \hat{\psi}_j\} = \{\psi_i, \hat{\psi}_j^\dagger\} = \{\psi_i^*, \hat{\psi}_j\} = \{\psi_i^*, \hat{\psi}_j^\dagger\} = 0 \qquad \text{(numbers and operators)}. \tag{3.36d}$$

In other words, all field operators and all Grassmann numbers anti-commute with themselves and each other. The anti-commutators (3.36a) and (3.36b) are the discrete analogues of the continuous anti-commutators (3.30a) and (3.30b). It will be more comfortable to carry out the formalism of fermionic coherent states in the discrete case and then take the continuum limit $\psi_i \to \psi(\boldsymbol{x})$ in the end.

The Fock space of the fermionic field has a **ground state** or **vacuum state**

$$|0, 0, \ldots, 0\rangle = |0\rangle\,. \tag{3.37}$$

If we apply any annihilation operator to the ground state, we get

$$\hat{\psi}_i\,|0\rangle = 0, \quad \text{because} \quad \hat{\psi}_i\hat{\psi}_i\,|0\rangle = -\hat{\psi}_i\hat{\psi}_i\,|0\rangle = 0 \text{ by equation (3.36a).} \tag{3.38}$$

On the other hand, we can apply a creation operator to build a **one-particle state**

$$|1_i\rangle = |(n_1 = 0), \ldots, (n_i = 1), \ldots, (n_N = 0)\rangle = \hat{\psi}_i^\dagger\,|0\rangle\,. \tag{3.39}$$

If we apply the same creation operator again, we get

$$\hat{\psi}_i^\dagger\,|1_i\rangle = 0, \quad \text{because} \quad \hat{\psi}_i^\dagger\hat{\psi}_i^\dagger\,|0\rangle = -\hat{\psi}_i^\dagger\hat{\psi}_i^\dagger\,|0\rangle = 0 \text{ by equation (3.36a).} \tag{3.40}$$

Applying the corresponding annihilation operator instead, we return to the vacuum

$$\hat{\psi}_i\,|1_i\rangle = \hat{\psi}_i\hat{\psi}_i^\dagger\,|0\rangle = (1 - \hat{\psi}_i^\dagger\hat{\psi}_i)\,|0\rangle = |0\rangle\,. \tag{3.41}$$

More generally, we can apply any sequence of $n = \sum_i n_i$ different creation operators to the vacuum state to build an **n-particle state**

$$|n_1, n_2, \ldots, n_N\rangle = \left(\hat{\psi}_1^\dagger\right)^{n_1} \cdots \left(\hat{\psi}_N^\dagger\right)^{n_N} |0\rangle\,. \tag{3.42}$$

This results in a nonzero state only if all $n_i \in \{0, 1\}$, because $(\hat{\psi}_i^\dagger)^2\,|0\rangle = -(\hat{\psi}_i^\dagger)^2\,|0\rangle = 0$ by the anti-commutator (3.36a). Note that shuffling the sequence of operators in equation (3.42) can change the sign of the state. To avoid ambiguity in our definition, we simply adopt any ordering convention, such as defining the n-particle state to have operators whose indices increase from left to right, as in the equation above.

The interpretation of this analysis is that the **creation operator** $\hat{\psi}_i^\dagger$ adds a particle in the state i, while the **annihilation operator** $\hat{\psi}_i$ removes a particle from the same state. The restriction that $n_i \in \{0, 1\}$ implies that there can be at most one particle in every state and is called the *Pauli exclusion principle*. Note that the Fock space has a total of 2^N distinct states

$$|n_1, n_2, \ldots, n_N\rangle \qquad \text{where } n_i \in \{0, 1\} \text{ for all } i = 1, \ldots, N. \tag{3.43}$$

Next, define the **coherent state**

$$\begin{aligned} |\psi\rangle &= \exp\left(-\sum_i \psi_i\hat{\psi}_i^\dagger\right)|0\rangle \\ &= \prod_i \exp\left(-\psi_i\hat{\psi}_i^\dagger\right)|0\rangle \\ &= \prod_i \left(1 - \psi_i\hat{\psi}_i^\dagger\right)|0\rangle \qquad \text{(by Taylor expansion (3.34))}. \end{aligned} \tag{3.44}$$

Applying an annihilation operator to this state gives

$$\begin{aligned}
\hat{\psi}_j |\psi\rangle &= \hat{\psi}_j \prod_i \left(1 - \psi_i \hat{\psi}_i^\dagger\right) |0\rangle && \text{(by (3.44))} \\
&= \prod_{i\neq j} \left(1 - \psi_i \hat{\psi}_i^\dagger\right) \hat{\psi}_j \left(1 - \psi_j \hat{\psi}_j^\dagger\right) |0\rangle && \text{(by (3.36b) and (3.36d))} \\
&= \prod_{i\neq j} \left(1 - \psi_i \hat{\psi}_i^\dagger\right) \psi_j |0\rangle && \text{(by (3.36d), (3.38) and (3.41))} \\
&= \prod_{i\neq j} \left(1 - \psi_i \hat{\psi}_i^\dagger\right) \psi_j \left(1 - \psi_j \hat{\psi}_j^\dagger\right) |0\rangle && \text{(by (3.36c))} \\
&= \psi_j \prod_i \left(1 - \psi_i \hat{\psi}_i^\dagger\right) |0\rangle && \text{(by (3.36c) and (3.36d))} \\
&= \psi_j |\psi\rangle && \text{(by (3.44))}.
\end{aligned} \tag{3.45}$$

In other words, the coherent state $|\psi\rangle$ is an eigenstate of every annihilation operator $\hat{\psi}_j$ with eigenvalue ψ_j! This is analogous to the bosonic eigenvalue equation (3.5). It is the coherent states that we wish to use when taking the trace, inner product and inserting identity operators in the path integral.

First, let us find the inner product between two coherent states. It is

$$\begin{aligned}
\langle\psi|\psi'\rangle &= \langle\psi| \prod_i (1 + \psi_i^* \psi_i') |0\rangle && \text{(by (3.44), (3.36d) and (3.45))} \\
&= \langle 0| \prod_i (1 + \psi_i^* \psi_i') |0\rangle && \text{(by orthogonality)} \\
&= \exp\left(\sum_i \psi_i^* \psi_i'\right) && \text{(by } \langle 0|0\rangle = 1 \text{ and (3.34))}.
\end{aligned} \tag{3.46}$$

Next, we can work out that the unit operator $\mathbb{1}$ can be represented by the integral

$$\begin{aligned}
&\int \mathrm{d}\psi^* \int \mathrm{d}\psi \, \exp\left(-\sum_i \psi_i^* \psi_i\right) |\psi\rangle \langle\psi| \\
&= \int \mathrm{d}\psi^* \int \mathrm{d}\psi \prod_i \left(1 + \psi_i \psi_i^*\right) \prod_j \left(1 - \psi_j \hat{\psi}_j^\dagger\right) |0\rangle \langle 0| \prod_k \left(1 - \hat{\psi}_k \psi_k^*\right) \\
&= \sum_{n_1=0}^{1} \sum_{n_2=0}^{1} \cdots \sum_{n_N=0}^{1} |n_1, n_2, \ldots, n_N\rangle \langle n_1, n_2, \ldots, n_N| = \mathbb{1}.
\end{aligned} \tag{3.47}$$

To make the big leap across the second equality sign, stare intensely at the middle line while following the next argument. To get a nonzero contribution from the integral, the parentheses must be multiplied out in a way such that one gets terms with the particular combination

$$\int \mathrm{d}\psi^* \int \mathrm{d}\psi \, \psi_1 \psi_1^* \cdots \psi_N \psi_N^* = 1. \tag{3.48}$$

Why? Any term with duplicate fields $\psi_i^2 = -\psi_i^2 = 0$ will yield zero. Similarly, if a term has a product that does not contain *all* the factors ψ_1, ψ_1^*, …, ψ_N, ψ_N^*, then after integrating out the *present* factors with integral (3.35b), there will always be left behind a vanishing constant integral in the form (3.35a) over the *absent* factors, causing the whole integral to vanish. Based on this, we can derive three rules for what combinations of factors we can choose when multiplying out the three parentheses.

1. **For any i in the first parenthesis:** Given that we follow the two next rules, we are free to choose either the factor 1 or $\psi_i \psi_i^*$.

2. **For $j = i$ in the second parenthesis:** If we choose $\psi_i\psi_i^*$ in the first parenthesis, we *must* choose 1 in the second to avoid a duplicate factor $\psi_i^2 = 0$. Conversely, if we choose 1 in the first, we *must* choose $-\psi_j\hat{\psi}_j^\dagger$ in the second to "saturate" the product (3.48).

3. **For $k = j = i$ in the third parenthesis:** If we choose $-\psi_j\hat{\psi}_j^\dagger$ in the second, we *must* choose $-\psi_k\hat{\psi}_k^\dagger$ in the third to get $\psi_j\psi_j^*$ in the field product. Conversely, if we choose 1 in the second, then we have already included $\psi_i\psi_i^*$ in the first by rule 2, and we *must* choose 1 in the third to avoid a duplicate factor $(\psi_i^*)^2 = 0$.

Following these rules, the first parenthesis expands to all possible 2^N terms. For every one of these terms, there is precisely one combination of factors in the second and third parentheses that yields a nonzero contribution. This evaluates to 2^N terms with all possible combinations of $N_j = N_k$ creation and annihilation operators and $N_i = N - N_j$ Grassmann numbers. *These 2^N terms are therefore precisely all the 2^N states (3.43) in the Fock space!* The sign ambiguity following different orderings of operators in the n-particle states (3.42) does not cause any problems with signs in the sum over all the states, either. To understand why, note that rule 3 forces us to apply the *same* sequence of operators to both $|0\rangle$ and $\langle 0|$ in equation (3.47), and any ordering that does not follow definition (3.42) can be made to do so by anti-commuting the *same* operators in *both* sequences, introducing an *even* number of minus signs that cancel. This explains the transition to the final line.

With the same reasoning, we can work out that the trace of an operator $\hat{A}$ can be written

$$\begin{aligned}
&\int \mathrm{d}\psi^* \int \mathrm{d}\psi \, \exp\left(-\sum_i \psi_i^*\psi_i\right) \langle -\psi|\hat{A}|\psi\rangle \\
&= \int \mathrm{d}\psi^* \int \mathrm{d}\psi \, \prod_i \left(1 + \psi_i\psi_i^*\right) \langle 0| \prod_j \left(1 + \hat{\psi}_j\psi_j^*\right) \hat{A} \prod_k \left(1 - \psi_k\hat{\psi}_k^\dagger\right)|0\rangle \\
&= \sum_{n_1=0}^{1} \sum_{n_2=0}^{1} \cdots \sum_{n_N=0}^{1} \langle n_1, n_2, \ldots, n_N|\hat{A}|n_1, n_2, \ldots, n_N\rangle = \operatorname{tr}\hat{A}.
\end{aligned} \tag{3.49}$$

The rules for multiplying out the parentheses are virtually identical to those in equation (3.47). Schematically, the two last parentheses give contributions in the form $\langle 0|(\hat{\psi}_j\psi_j^*)\hat{A}(-\psi_k\hat{\psi}_k^\dagger)|0\rangle = +\psi_k\psi_j^* \langle 0|\hat{\psi}_j\hat{A}\hat{\psi}_k^\dagger|0\rangle$ and all its multi-particle generalizations, where we must set $j = k$ to get a nonzero contribution. In addition, we have *assumed* that $\hat{A}$ is a "bosonic" operator that *commutes* with the Grassmann numbers, allowing us to move the Grassmann numbers out of the inner product in this way. For example, the Dirac Hamiltonian (3.89) that we will work with later is such an $\hat{A}$, as it contains *two* field operators. *Pay special attention to the minus sign in $\langle -\psi| = \langle 0|\prod_j[1 - \hat{\psi}_j(-\psi_j^*)] = \langle 0|\prod_j[1 + \hat{\psi}_j\psi_j^*]$ in the first line!* Without it, we would not obtain the trace when multiplying out the parentheses. *We will soon see that this minus sign is perhaps the most important result of this whole chapter, yet surely the least visible one!*

As we remarked at the start, this analysis was for discrete fields that satisfy the discrete anti-commutators (3.36). We are studying fields $\psi(\boldsymbol{x})$ and $\psi^*(\boldsymbol{x})$ with an infinite number of field operators $\hat{\psi}^\dagger(\boldsymbol{x})$ and $\hat{\psi}(\boldsymbol{x})$ that satisfy the continuum generalization (3.30). Our results carry over with the substitutions $\psi_i \to \psi(\boldsymbol{x})$, as if every Grassmann number corresponds to the field at one position, and $\sum_i \to \int \mathrm{d}^3x$. The continuum version of the coherent state is therefore

$$|\psi\rangle = \exp\left[-\int \mathrm{d}^3x \, \psi(\boldsymbol{x})\hat{\psi}^\dagger(\boldsymbol{x})\right]|0\rangle\,. \tag{3.50}$$

The inner product (3.46) between two coherent states is then

$$\langle\psi|\psi'\rangle = \exp\left[\int \mathrm{d}^3x \, \psi^*(\boldsymbol{x})\psi'(\boldsymbol{x})\right], \tag{3.51a}$$

and the identity operator (3.47) becomes

$$\int \mathrm{d}\psi^* \int \mathrm{d}\psi \, \exp\left[-\int \mathrm{d}^3x \, \psi^*(\boldsymbol{x})\psi(\boldsymbol{x})\right] |\psi\rangle \langle\psi| = \mathbb{1}, \tag{3.51b}$$

while the trace (3.49) is modified to

$$\int \mathrm{d}\psi^* \int \mathrm{d}\psi \, \exp\left[-\int \mathrm{d}^3x \, \psi^*(\boldsymbol{x})\psi(\boldsymbol{x})\right] \left\langle -\psi \middle| \hat{A} \middle| \psi \right\rangle = \operatorname{tr} \hat{A}. \tag{3.51c}$$

The most important thing to note is the necessity of the *minus sign* in $\langle -\psi|$ of the trace (3.51c) – we will see that this requires fermionic fields to be *anti-periodic* in imaginary time, in contrast to the periodic bosonic fields.

Partition function

Using equations (3.51a), (3.51b) and (3.51c) as our toolbox, let us now construct the path integral for the fermionic partition function. We now revert from the above notation with single fermion fields ψ and ψ^* back to the four-component spinors ψ and $\psi^\dagger$. Accordingly, we write $\prod_{\alpha=0}^{3} \mathrm{d}\psi_\alpha = \mathrm{d}\psi$ and $\prod_{\alpha=0}^{3} \mathrm{d}\psi_\alpha^* = \mathrm{d}\psi^\dagger$ to indicate integration over all four components. The partition function (3.1) follows from the trace (3.51c) with $\hat{A} = e^{-\beta(\hat{H}-\mu\hat{N})}$ as

$$Z = \int \mathrm{d}\psi_0^\dagger \int \mathrm{d}\psi_0 \, e^{-\int \mathrm{d}^3x \, \psi_0^\dagger(\boldsymbol{x})\psi_0(\boldsymbol{x})} \left\langle -\psi_0 \middle| e^{-\beta(\hat{H}-\mu\hat{N})} \middle| \psi_0 \right\rangle. \tag{3.52}$$

Breaking up the operator $e^{-\beta(\hat{H}-\mu\hat{N})}$ as in equation (3.16) with small times $\Delta\tau = \beta\hbar/N$ and inserting one Grassmann completeness relation (3.51b) between every factor, the partition function becomes

$$Z = \prod_n \int \mathrm{d}\psi_n^\dagger \int \mathrm{d}\psi_n \, e^{-\int \mathrm{d}^3x \, \psi_{n+1}^\dagger(\boldsymbol{x})\psi_{n+1}(\boldsymbol{x})} \left\langle \psi_{n+1} \middle| e^{-(\hat{H}-\mu\hat{N})\Delta\tau/\hbar} \middle| \psi_n \right\rangle, \tag{3.53}$$

where we defined the left end state

$$\langle \psi_{N+1}| = \langle -\psi_0| \qquad (\textbf{note the minus sign!}). \tag{3.54}$$

We are hiding the minus sign to be able to write the expression in compact product notation. Do not forget it! Next, expand the Hamiltonian to first order as in equation (3.19). Then we obtain

$$Z = \prod_n \int \mathrm{d}\psi_n^\dagger \int \mathrm{d}\psi_n \, e^{-\int \mathrm{d}^3x \, \psi_{n+1}^\dagger(\boldsymbol{x})\psi_{n+1}(\boldsymbol{x})} \langle \psi_{n+1}|\psi_n\rangle \, e^{-(H_n-\mu N)\Delta\tau/\hbar}. \tag{3.55}$$

Now use the Grassmann inner product (3.51a) on $\langle \psi_{n+1}|\psi_n\rangle$ to write

$$Z = \prod_n \int \mathrm{d}\psi_n^\dagger \int \mathrm{d}\psi_n \, \exp\left[\frac{\Delta\tau}{\hbar} \sum_n \int \mathrm{d}^3x \left(-\hbar\psi_{n+1}^\dagger \frac{\psi_{n+1}-\psi_n}{\Delta\tau}\psi_n - \mathcal{H} + \mu\mathcal{N}\right)\right]. \tag{3.56}$$

Finally, take the continuum limit and introduce the functional integrals $\mathcal{D}\psi = \prod_{n=1}^{\infty} \mathrm{d}\psi_n$ and $\mathcal{D}\psi^\dagger = \prod_{n=1}^{\infty} \mathrm{d}\psi^\dagger$. We then obtain the **fermionic partition function**

$$Z = \oint_- \mathcal{D}\psi^\dagger \oint_- \mathcal{D}\psi \exp\left[\frac{1}{\hbar}\int_0^{\beta\hbar} \mathrm{d}\tau \int \mathrm{d}^3x \left(-\hbar\psi^\dagger\dot{\psi} - \mathcal{H}\left(\psi^\dagger,\psi\right) + \mu\mathcal{N}\right)\right], \tag{3.57}$$

where $\oint_-$ means to integrate over *anti-periodic* fields $\psi(\boldsymbol{x},0) = -\psi(\boldsymbol{x},\beta\hbar)$, naturally extending the symbol $\oint_+$ we introduced for bosonic fields that were *periodic*. Here, anti-periodicity follows from the negative sign in $\langle -\psi|$ in the trace (3.51c) that we hid in the end state (3.54). Remarkably, this result looks identical to the bosonic partition function (3.25) with canonical momentum $\pi = i\hbar\psi^\dagger$, despite the very different machinery with anti-periodic Grassmann fields.

3.3 Matsubara frequencies and box quantization

We have just seen that the partition function for bosons and fermions can be expressed by path integrals over fields that are periodic and anti-periodic on the time interval $\beta\hbar$, respectively. In other words, a bosonic *or* fermionic field $\phi(\boldsymbol{x}, \tau)$ satisfies the (anti-)periodicity

$$\phi(\boldsymbol{x}, \tau) = \begin{cases} +\phi(\boldsymbol{x}, \tau + \beta\hbar) & \text{for bosons} \\ -\phi(\boldsymbol{x}, \tau + \beta\hbar) & \text{for fermions.} \end{cases} \tag{3.58}$$

Accordingly, we can expand either field in a Fourier series

$$\phi(\boldsymbol{x}, \tau) = \sum_n \phi_n(\boldsymbol{x}) e^{i\omega_n \tau} \tag{3.59}$$

with **Matsubara frequencies**

$$\omega_n = \begin{cases} 2\pi n/\beta\hbar & \text{for bosons} \\ 2\pi(n + \frac{1}{2})/\beta\hbar & \text{for fermions.} \end{cases} \tag{3.60}$$

The field is not periodic in space, but let us for a moment pretend that it is by putting it in a fictitious box of volume $V = L^3$ and impose periodic boundary conditions. Then the spatial part of the field can also be represented by a Fourier series

$$\phi_n(\boldsymbol{x}) = \sum_{\boldsymbol{k}} \phi_n(\boldsymbol{k}) e^{i\boldsymbol{k}\cdot\boldsymbol{x}}, \tag{3.61}$$

where the sum runs over all wavevectors $\boldsymbol{k}$ with components $k_i = 2\pi n_i/L$ for integers n_i, each separated by the distance $\Delta k = 2\pi/L$ in $\boldsymbol{k}$-space. Since the field is not really periodic, we should take the continuum limit $V \to \infty$ at the end. Then $\Delta k \to 0$, so the sum is replaced by the integral

$$\sum_{\boldsymbol{k}} = \sum_{\boldsymbol{k}} \frac{(\Delta k)^3}{(2\pi/L)^3} \quad \to \quad \int \frac{\mathrm{d}^3 k}{(2\pi/L)^3} = V \int \frac{\mathrm{d}^3 k}{(2\pi)^3}. \tag{3.62}$$

This mathematical trick is known as **box quantization**. In the following sections, we will therefore proceed through a calculation with a finite Fourier series expansion

$$\phi(\boldsymbol{x}, \tau) = \sum_n \sum_{\boldsymbol{k}} \phi_n(\boldsymbol{k}) e^{i(\boldsymbol{k}\cdot\boldsymbol{x} + \omega_n \tau)} \tag{3.63}$$

of the field, then take the continuum limit (3.62) at the end of the calculation to make it physically correct.

The infinite volume factor V will come in handy when calculating thermodynamic observables. To obtain the pressure (3.2c), we are instructed to divide by volume. Similarly, we will need to divide by volume to convert extensive observables like the energy (3.2b) into intensive observables like the energy *density* $\epsilon = \langle E \rangle / V$ that we need in the Tolman-Oppenheimer-Volkoff equation (2.16).

The wave number $\boldsymbol{k}$ and the Matsubara frequency ω_n here arose due to geometrical considerations of the periodicity of the field. We will soon see that they have important physical consequences, too. In anticipation of this, we define the corresponding momentum and Matsubara energy

$$\boldsymbol{p} = \hbar\boldsymbol{k}, \qquad E_n = \hbar\omega_n \qquad \text{and} \qquad \sum_{\boldsymbol{p}} = \sum_{\boldsymbol{k}} = V \int \frac{\mathrm{d}^3 p}{(2\pi\hbar)^3}. \tag{3.64}$$

Note that some authors adopt the four-momentum $p = (E_n/c, \boldsymbol{p})$ and write the Fourier amplitude as $\phi(p)$. Due to the difference between the discrete nature of the Matsubara energies and the continuous nature of the momenta, we wish to maintain some "separation" between time and space and therefore choose to write $\phi_n(\boldsymbol{p})$.

3.4 The partition function for free real scalar bosons

As a first example, we apply the path integral formalism to find the partition function for a free real scalar field representing spin-zero bosons. Its Lagrangian density is

$$\mathcal{L} = \frac{1}{2}(\partial_\mu\phi)(\partial^\mu\phi) - \frac{1}{2}\frac{m^2c^2}{\hbar^2}\,\phi^2 = \frac{1}{2c^2}\dot{\phi}^2 - \frac{1}{2}(\nabla\phi)^2 - \frac{1}{2}\frac{m^2c^2}{\hbar^2}\,\phi^2. \tag{3.65}$$

To be clear, we now denote time by τ, regard the field as a function $\phi(\boldsymbol{x},\tau)$ and denote the time derivative by $\dot{} = \partial/\partial\tau$. There is no t anymore, only the τ of the path integral (3.25). The conjugate momentum (3.3) is

$$\pi = \frac{\partial\mathcal{L}}{\partial\dot{\phi}} = \frac{1}{c^2}\dot{\phi}. \tag{3.66}$$

The Hamiltonian density is therefore

$$\mathcal{H} = \pi\dot{\phi} - \mathcal{L} = \frac{1}{2}c^2\pi^2 + \frac{1}{2}(\nabla\phi)^2 + \frac{1}{2}\frac{m^2c^2}{\hbar^2}\phi^2. \tag{3.67}$$

We now calculate the partition function (3.25). To do so, we need the combination

$$\begin{aligned} i\pi\dot{\phi} - \mathcal{H} &= i\pi\dot{\phi} - \frac{1}{2}c^2\pi^2 - \frac{1}{2}(\nabla\phi)^2 - \frac{1}{2}\frac{m^2c^2}{\hbar^2}\phi^2 \\ &= -\frac{1}{2}c^2\left(\pi - \frac{i}{c^2}\dot{\phi}\right)^2 - \frac{1}{2c^2}\dot{\phi}^2 - \frac{1}{2}(\nabla\phi)^2 - \frac{1}{2}\frac{m^2c^2}{\hbar^2}\phi^2 \\ &= -\frac{1}{2}c^2\tilde{\pi}^2 + \mathcal{L}_E. \end{aligned} \tag{3.68}$$

We completed the square by defining the shifted field $\tilde{\pi} = \pi - i\dot{\phi}/c^2$, for reasons that soon will be apparent. Remember that the Legendre transformation (3.67) exchanges the independent variable $\dot{\phi}$ in $\mathcal{L} = \mathcal{L}(\phi,\dot{\phi},\nabla\phi)$ to π in $\mathcal{H} = \mathcal{H}(\phi,\pi,\nabla\phi)$. Thus, the shift can be regarded as a shift by a *constant*. We also defined the remaining terms as the Lagrangian density $\mathcal{L}_E$. It is exactly the original Lagrangian density (3.65), only with $\tau \to i\tau$. This can be interpreted as a change from Minkowski space to Euclidean space, and we therefore call $\mathcal{L}_E(\tau) = \mathcal{L}(i\tau)$ the Euclidean Lagrangian density. There is no conserved current, so the path integral (3.25) is now

$$Z = \int\mathcal{D}\pi\oint_+\mathcal{D}\phi\exp\left\{\frac{1}{\hbar}\int_0^{\beta\hbar}\mathrm{d}\tau\int_V\mathrm{d}^3x\left[-\frac{1}{2}c^2\tilde{\pi}^2 + \mathcal{L}_E\right]\right\}. \tag{3.69}$$

Since $\tilde{\pi}$ can be regarded as a constant shift of the field π, we can now use the Gaussian integral (F.3) to *integrate out* the momentum. We do not bother keeping track of the resulting constant or any other constants in front of the partition function. Physical quantities like the energy (3.2b) only involve derivatives of $\log Z$ and would be unaffected by such constants. The pressure (3.2c), however, contains $\log Z$ without derivatives and would really be shifted by an infinite constant, due to the infinite number of integrals in the functional integral (3.22). It is most correct, therefore, to disregard constants in Z with the attitude that we would have to renormalize the physical quantities in the end anyway, in order to get rid of infinities.

Thus, it only remains to tackle the ϕ-integral

$$Z = \oint_+\mathcal{D}\phi\exp\left(\frac{S_E}{\hbar}\right), \tag{3.70}$$

with the Euclidean action

$$\begin{aligned} S_E &= \int_0^{\beta\hbar}\mathrm{d}\tau\int_V\mathrm{d}^3x\,\mathcal{L}_E \\ &= \int_0^{\beta\hbar}\mathrm{d}\tau\int_V\mathrm{d}^3x\left[-\frac{1}{2c^2}\left|\frac{\partial\phi}{\partial\tau}\right|^2 - \frac{1}{2}(\nabla\phi)^2 - \frac{1}{2}\frac{m^2c^2}{\hbar^2}\phi^2\right]. \end{aligned} \tag{3.71}$$

By assumption, the action has no variation on the boundaries, so we can integrate by parts to convert $(\partial\phi/\partial\tau)^2$ into $-\phi\,\partial^2\phi/\partial\tau^2$ and forget the boundary term. It then becomes

$$S_E = \frac{1}{2}\int_0^{\beta\hbar} \mathrm{d}\tau \int_V \mathrm{d}^3x \left[\phi\left(\frac{1}{c^2}\frac{\partial^2}{\partial\tau^2} + \nabla^2 - \frac{m^2c^2}{\hbar^2}\right)\phi\right]. \tag{3.72}$$

At this point it is useful to introduce the Fourier series (3.63) of the field with bosonic Matsubara frequencies (3.60). However, we also include a prefactor and write

$$\phi(\boldsymbol{x},\tau) = \hbar c\sqrt{\frac{\beta}{V}}\sum_{n=-\infty}^{+\infty}\sum_{\boldsymbol{k}}\phi_n(\boldsymbol{k})e^{i(\boldsymbol{k}\cdot\boldsymbol{x}+\omega_n\tau)}. \tag{3.73}$$

The prefactor $\hbar c\sqrt{\beta/V}$ is chosen to have the same dimension as the field $\phi(\boldsymbol{x},\tau)$, so the Fourier amplitudes $\phi_n(\boldsymbol{k})$ are dimensionless. Without it, the Gaussian integral that we will calculate down in equation (3.77) would make the partition function Z dimensionful, which would formally make it meaningless to take its logarithm. A fully equivalent approach would be to skip the prefactor for now, but instead restore whichever factors of $\hbar$, c, β and V that is needed to make Z dimensionless before taking the logarithm down in equation (3.79). Note that the reality $\phi(\boldsymbol{x},\tau) = \phi^*(\boldsymbol{x},\tau)$ requires Fourier amplitudes with $\phi_n^*(\boldsymbol{k}) = \phi_{-n}(-\boldsymbol{k})$.

We now rewrite the Euclidean action (3.72) by inserting the Fourier expansion (3.73). Exploiting the reality $\phi(\boldsymbol{x},\tau) = \phi^*(\boldsymbol{x},\tau)$, we insert one Fourier expansion for the rightmost field and another with all quantities complex conjugated for the leftmost field. The action then becomes

$$\begin{aligned} S_E &= -\frac{1}{2}\frac{\hbar^2c^2\beta}{V}\sum_{n,n'}\sum_{\boldsymbol{k},\boldsymbol{k'}}\phi_{n'}^*(\boldsymbol{k'})\left(\frac{\omega_n^2}{c^2} + \boldsymbol{k}^2 + \frac{m^2c^2}{\hbar^2}\right)\phi_n(\boldsymbol{k})\underbrace{\int_V \mathrm{d}^3x\, e^{i(\boldsymbol{k}-\boldsymbol{k'})\cdot\boldsymbol{x}}}_{\delta(\boldsymbol{k}-\boldsymbol{k'})V}\underbrace{\int_0^{\beta\hbar}\mathrm{d}\tau\, e^{i(\omega_n-\omega_{n'})\tau}}_{\delta_{n,n'}\beta\hbar} \\ &= -\frac{1}{2}\hbar\beta^2\sum_n\sum_{\boldsymbol{p}}\left(E_n^2 + E^2(\boldsymbol{p})\right)|\phi_n(\boldsymbol{p})|^2, \end{aligned} \tag{3.74}$$

where E_n are the Matsubara energies we defined in equation (3.64), and

$$E(\boldsymbol{p}) = \sqrt{\boldsymbol{p}^2c^2 + m^2c^4} \tag{3.75}$$

is the **relativistic dispersion relation**. Ignoring the prefactor, the change of variables (3.73) is a unitary transformation with Jacobian 1, so the integral measure becomes

$$\mathcal{D}\phi(x) = \prod_i \mathrm{d}\phi(x_i) = \prod_n\prod_{\boldsymbol{p}}\mathrm{d}\phi_n(\boldsymbol{p}). \tag{3.76}$$

Integrating over the new variables (3.76) and inserting the action (3.74) into the path integral (3.70), it factors into the Gaussian integrals

$$Z = \prod_n\prod_{\boldsymbol{p}}\int \mathrm{d}\phi_n(\boldsymbol{p})\,\exp\left\{-\frac{1}{2}\beta^2\left[E_n^2 + E^2(\boldsymbol{p})\right]|\phi_n(\boldsymbol{p})|^2\right\}. \tag{3.77}$$

The integrand depends only on the magnitude of $\phi_n(\boldsymbol{p}) = |\phi_n(\boldsymbol{p})|\,e^{i\theta_n(\boldsymbol{p})}$. The reality of the field $\phi(\boldsymbol{x},\tau) = \phi^*(\boldsymbol{x},\tau)$ implies that $\phi_n^*(\boldsymbol{p}) = \phi_{-n}(-\boldsymbol{p})$ and consequently that $\theta_{-n}(-\boldsymbol{p}) = -\theta_n(\boldsymbol{p})$, so all phases in the measures $\mathrm{d}\phi_n(\boldsymbol{p})$ cancel after taking the product over all n and $\boldsymbol{p}$. Thus, we can carry out the integral using the Gaussian integral (F.3) to obtain

$$Z = \prod_n\prod_{\boldsymbol{p}}\left\{\beta^2\left[E_n^2 + E^2(\boldsymbol{p})\right]\right\}^{-1/2}. \tag{3.78}$$

We only need $\log Z$ to compute the thermodynamic observables, and now is an excellent time to take the logarithm. The product is then converted into the sum

$$\log Z = -\frac{1}{2}\sum_n \sum_{\boldsymbol{p}} \log\left\{\beta^2\left[E_n^2 + E^2(\boldsymbol{p})\right]\right\}. \tag{3.79}$$

To evaluate the sum over n, it actually turns out to be easier to differentiate every term in the sum, sum the derivatives and then integrate back to undo the differentiation. More precisely, we have that

$$\begin{aligned}\log Z &= -\frac{1}{2}\sum_{\boldsymbol{p}} \int \mathrm{d}E^2(\boldsymbol{p}) \sum_n \frac{\partial}{\partial E^2(\boldsymbol{p})} \log\left\{\beta^2\left[E_n^2 + E^2(\boldsymbol{p})\right]\right\} \\ &= -\frac{1}{2}\sum_{\boldsymbol{p}} \int \mathrm{d}E^2(\boldsymbol{p}) \sum_n \frac{1}{E_n^2 + E^2(\boldsymbol{p})}.\end{aligned} \tag{3.80}$$

We need to evaluate the **Matsubara energy sum** over n. Later we will in fact encounter the same sum over fermionic Matsubara energies. In appendix C, we devise a powerful and general method for computing such sums by contour integration in the complex plane. We even kill two birds with one stone, as the exact same procedure enables us to compute bosonic and fermionic Matsubara energy sums simultaneously! In fact, it turns out that the Bose-Einstein distribution emerges naturally from the bosonic sums, while the Fermi-Dirac distribution drops out as a byproduct of fermionic sums. Again, all of this is demonstrated in appendix C. Applying the method to the sum above yields the result (C.17). We insert this back into our expression for $\log Z$ above to find

$$\log Z = -\frac{\beta}{2}\sum_{\boldsymbol{p}} \int \mathrm{d}E^2(\boldsymbol{p}) \frac{1}{2E(\boldsymbol{p})}\left[1 + \frac{2}{e^{\beta E(\boldsymbol{p})} - 1}\right] \qquad \big(\text{by equation (C.17)}\big). \tag{3.81}$$

The integral can be evaluated by using $\mathrm{d}E^2(\boldsymbol{p}) = 2E(\boldsymbol{p})\,\mathrm{d}E(\boldsymbol{p})$. We then find

$$\begin{aligned}\log Z &= -\frac{\beta}{2}\sum_{\boldsymbol{p}} \int \mathrm{d}E(\boldsymbol{p})\left[1 + \frac{2}{e^{\beta E(\boldsymbol{p})} - 1}\right] \\ &= -\frac{\beta}{2}\sum_{\boldsymbol{p}} \left\{E(\boldsymbol{p}) + \frac{2}{\beta}\log\left[1 - e^{-\beta E(\boldsymbol{p})}\right]\right\}.\end{aligned} \tag{3.82}$$

Finally, take the continuum limit (3.62) to obtain the **partition function for a real scalar field**

$$\log Z = V\int \frac{\mathrm{d}^3 p}{(2\pi\hbar)^3}\left\{-\frac{1}{2}\beta E(\boldsymbol{p}) - \log\left[1 - e^{-\beta E(\boldsymbol{p})}\right]\right\}. \tag{3.83}$$

3.5 The partition function for free Dirac fermions

Let us now find the partition function (3.57) for **free Dirac fermions** with half-spin and Lagrangian density

$$\mathcal{L} = \bar{\psi}\Big(i\hbar c\,\partial\!\!\!/ - mc^2\Big)\psi = \bar{\psi}\Big(i\hbar\gamma^0\frac{\partial}{\partial\tau} + i\hbar c\,\boldsymbol{\gamma}\cdot\nabla - mc^2\Big)\psi. \tag{3.84}$$

Here, the four-component Dirac spinor $\psi = [\psi_0, \psi_1, \psi_2, \psi_3]$ is the basic field and $\psi^\dagger$ is its conjugate, while $\bar{\psi} = \psi^\dagger\gamma^0$ and $\partial\!\!\!/ = \gamma^\mu\partial_\mu = \gamma^0\partial_0 + \boldsymbol{\gamma}\cdot\boldsymbol{\nabla}$, where γ^μ are the 4×4 **Gamma matrices** defined by the Clifford algebra

$$\{\gamma^\mu, \gamma^\nu\} = 2\eta^{\mu\nu}. \tag{3.85}$$

There are multiple possible explicit representations of the Gamma matrices. We will use the **Dirac basis**

$$\gamma^0 = \begin{bmatrix} I_2 & 0 \\ 0 & -I_2 \end{bmatrix} \qquad \text{and} \qquad \gamma^i = \begin{bmatrix} 0 & \tau^i \\ -\tau^i & 0 \end{bmatrix}, \tag{3.86}$$

where τ^i are the **Pauli matrices**

$$\tau^1 = \begin{bmatrix} 0 & 1 \\ 1 & 0 \end{bmatrix}, \qquad \tau^2 = \begin{bmatrix} 0 & -i \\ i & 0 \end{bmatrix} \qquad \text{and} \qquad \tau^3 = \begin{bmatrix} 1 & 0 \\ 0 & -1 \end{bmatrix}. \tag{3.87}$$

The conjugate momentum (3.3) of the field ψ is

$$\pi = \frac{\partial \mathcal{L}}{\partial \dot{\psi}} = i\hbar\psi^\dagger, \tag{3.88}$$

so the Hamiltonian density is

$$\mathcal{H} = \pi\dot{\psi} - \mathcal{L} = \bar{\psi}\left(-i\hbar c\,\boldsymbol{\gamma}\cdot\boldsymbol{\nabla} + mc^2\right)\psi. \tag{3.89}$$

In addition, the Dirac Lagrangian is invariant under the symmetry transformation $\psi_\alpha \to \psi_\alpha e^{i\theta} \simeq \psi_\alpha + i\theta\psi_\alpha = \psi_\alpha + \delta\psi_\alpha$. By Noether's theorem [Kac18, equation 5.7], there is a corresponding conserved current

$$j^\mu \propto \frac{\delta\mathcal{L}}{\delta\partial_\mu\psi_\alpha}\delta\psi_\alpha = \bar{\psi}_\beta i\hbar c\,(\gamma^\mu)_{\beta\alpha} i\theta\psi_\alpha = -\hbar c\,\bar{\psi}\gamma^\mu\psi. \tag{3.90}$$

Ignoring the constant factors, we take the conserved current to be

$$j^\mu = \bar{\psi}\gamma^\mu\psi. \tag{3.91}$$

Let us now find the fermionic partition function (3.57). We need the combination

$$-\hbar\psi^\dagger\dot{\psi} - \mathcal{H} = \bar{\psi}\left(-\hbar\gamma^0\frac{\partial}{\partial\tau} + i\hbar c\,\boldsymbol{\gamma}\cdot\boldsymbol{\nabla} - mc^2\right)\psi = \mathcal{L}_E, \tag{3.92}$$

which we define as the Euclidean Lagrangian density $\mathcal{L}_E$ for reasons similar to the bosonic case that we will soon discuss. According to equation (3.29), we should also include the conserved current (3.91). Inserting this into the partition function (3.57), it becomes

$$Z = \oint_- \mathcal{D}\psi^\dagger \oint_- \mathcal{D}\psi \exp\left(\frac{S_E}{\hbar}\right) \tag{3.93}$$

with the Euclidean action

$$\begin{aligned} S_E &= \int_0^{\beta\hbar} \mathrm{d}\tau \int_V \mathrm{d}^3x\ \left(\mathcal{L}_E + \mu j^0\right) \\ &= \int_0^{\beta\hbar} \mathrm{d}\tau \int_V \mathrm{d}^3x\,\bar{\psi}\left(-\hbar\gamma^0\frac{\partial}{\partial\tau} + i\hbar c\,\boldsymbol{\gamma}\cdot\boldsymbol{\nabla} - mc^2 + \mu\gamma^0\right)\psi. \end{aligned} \tag{3.94}$$

Comparing the combination (3.92) to the original Lagrangian (3.84), we see that it is exactly the original Lagrangian, only with $\tau \to i\tau$, and we therefore call it the Euclidean Lagrangian density $\mathcal{L}_E(\tau) = \mathcal{L}(i\tau)$. We encountered a similar situation in the bosonic case in equation (3.68), but with an additional contribution from a shifted momentum that we integrated out from the path integral (3.69). This time, however, the correspondence to the Euclidean Lagrangian occurs immediately without need of integrating out any fields. Notice in particular the similarity of the fermionic path integral (3.93) to the bosonic path integral (3.70).

As in the bosonic case, we now Fourier expand the field. The fermionic anti-periodicity (3.58) enables us to expand the Dirac field and its conjugate in the Fourier series

$$\psi(\boldsymbol{x},\tau) = \frac{1}{\sqrt{V}}\sum_n\sum_{\boldsymbol{k}} e^{i(\boldsymbol{k}\cdot\boldsymbol{x}+\omega_n\tau)}\psi_n(\boldsymbol{k}), \tag{3.95a}$$

$$\psi^\dagger(\boldsymbol{x},\tau) = \frac{1}{\sqrt{V}}\sum_n\sum_{\boldsymbol{k}} e^{-i(\boldsymbol{k}\cdot\boldsymbol{x}+\omega_n\tau)}\psi_n^\dagger(\boldsymbol{k}), \tag{3.95b}$$

with fermionic Matsubara frequencies (3.60). As with the bosonic field, we have made the Fourier amplitudes $\psi_n(\boldsymbol{k})$ dimensionless by pulling out a factor $1/\sqrt{V}$. The factor differs from the one in the bosonic Fourier series (3.73) due to the different dimension of the fermionic field $\psi(\boldsymbol{x},\tau)$ and the bosonic field $\phi(\boldsymbol{x},\tau)$. Note that we are expanding *each component* of the four-component Dirac spinor $\psi(\boldsymbol{x},\tau)$, so the Fourier amplitudes $\psi_n(\boldsymbol{k})$ are also vectors with four components. With the Fourier series, the Euclidean action (3.94) can be rewritten

$$\begin{aligned} S &= \frac{1}{V}\sum_{n,n'}\sum_{\boldsymbol{k},\boldsymbol{k'}} \psi^\dagger_{n'}(\boldsymbol{k'})\gamma^0\left(-\hbar\gamma^0 i\omega_n + i\hbar c\,\boldsymbol{\gamma}\cdot i\boldsymbol{k} - mc^2 + \mu\gamma^0\right)\psi_n(\boldsymbol{k}) \\ &\times \underbrace{\int_0^{\beta\hbar} \mathrm{d}\tau\, e^{i(\omega_n-\omega_{n'})\tau}}_{\delta_{n,n'}\beta\hbar} \underbrace{\int_V \mathrm{d}^3x\, e^{i(\boldsymbol{k}-\boldsymbol{k'})\cdot\boldsymbol{x}}}_{\delta(\boldsymbol{k}-\boldsymbol{k'})V} \\ &= i\beta\hbar\sum_n\sum_{\boldsymbol{p}} \psi^\dagger_n(\boldsymbol{p})\left(-E_n + ic\,\gamma^0\boldsymbol{\gamma}\cdot\boldsymbol{p} + imc^2\gamma^0 - i\mu\right)\psi_n(\boldsymbol{p}). \end{aligned} \tag{3.96}$$

We now change variables from $\psi(\boldsymbol{x},\tau)$ and $\psi^\dagger(\boldsymbol{x},\tau)$ to $\psi_n(\boldsymbol{k})$ and $\psi^\dagger_n(\boldsymbol{k})$ as in the bosonic case (3.76). To be consistent with treating the field and its conjugate as independent variables, we continue to treat the Fourier amplitudes and their conjugates independently. The partition function (3.93) now becomes

$$Z = \prod_n\prod_{\boldsymbol{p}}\int \mathrm{d}\psi^\dagger_n(\boldsymbol{p})\int \mathrm{d}\psi_n(\boldsymbol{p})\exp\left\{\psi^\dagger_n(\boldsymbol{p})\left[i\beta(-E_n + ic\gamma^0\boldsymbol{\gamma}\cdot\boldsymbol{p} + imc^2\gamma^0 - i\mu)\right]\psi_n(\boldsymbol{p})\right\}, \tag{3.97}$$

analogous to the bosonic Gaussian integral (3.77). Do not forget that $\psi^\dagger_n(\boldsymbol{p})$ and $\psi_n(\boldsymbol{p})$ are four-*vectors*, sandwiching the *matrix* in the square brackets to create a *scalar* action in the exponent! Using the Grassmann exponential integral (F.5), we obtain

$$Z = \prod_n\prod_{\boldsymbol{p}} \det\Big(i\beta D_n(\boldsymbol{p})\Big) \qquad \text{with} \qquad D_n(\boldsymbol{p}) = -E_n + ic\gamma^0\boldsymbol{\gamma}\cdot\boldsymbol{p} + imc^2\gamma^0 - i\mu. \tag{3.98}$$

Let us calculate the determinant of the 4×4 matrices $D_n(\boldsymbol{p})$ explicitly. First, let us use the Dirac basis representation (3.86) of the Gamma matrices to write the 4×4 matrix as a block matrix of 2×2 matrices. This gives the block matrix

$$D_n(\boldsymbol{p}) = \begin{bmatrix} -E_n - i\mu + imc^2 & ic\,\boldsymbol{\tau}\cdot\boldsymbol{p} \\ ic\,\boldsymbol{\tau}\cdot\boldsymbol{p} & -E_n - i\mu - imc^2 \end{bmatrix}. \tag{3.99}$$

Calculating the determinant becomes easier by applying the formula [Sil00, theorem 3]

$$\det\begin{bmatrix} A & B \\ C & D \end{bmatrix} = \det(AD - BC), \tag{3.100}$$

which is familiar for a non-block 2×2 matrix, but in fact also valid for a block matrix if $CD = DC$. This is applicable in our situation, where D is diagonal. Matching the block matrices A, B, C and D with those in equation (3.99), we then have $AD = (E_n + i\mu)^2 + (mc^2)^2$ and $BC = -(\boldsymbol{\tau}\cdot\boldsymbol{p})^2c^2$. From the Pauli matrices (3.87), it is straightforward to verify the property $(\boldsymbol{\tau}\cdot\boldsymbol{p})^2 = \boldsymbol{p}^2$. Introducing the relativistic dispersion relation (3.75) again, we then get the simple diagonal 2×2 matrix $AD - BC = (E_n + i\mu)^2 + E^2(\boldsymbol{p})$. The determinant then becomes

$$\det\Big(i\beta D_n(\boldsymbol{p})\Big) = \beta^4\left[(E_n + i\mu)^2 + E^2(\boldsymbol{p})\right]^2. \tag{3.101}$$

The logarithm of the partition function (3.98) is now the sum

$$\begin{aligned} \log Z &= \sum_n\sum_{\boldsymbol{p}} \det\Big(i\beta D_n(\boldsymbol{p})\Big) \\ &= \sum_n\sum_{\boldsymbol{p}} \log\left\{\beta^4\left[(E_n + i\mu)^2 + E^2(\boldsymbol{p})\right]^2\right\}. \end{aligned} \tag{3.102}$$

The i in front of μ is awkward and can certainly not appear in the physical quantities that are derived from $\log Z$. Let us see if we can make it disappear. The logarithm involves a sum $\sum_n s(E_n)$ of some function $s(E_n)$ over all Matsubara energies E_n. Because the Matsubara energies satisfy $E_n = -E_{-n}$ by definitions (3.60) and (3.64), we have $\sum_n s(E_n) = \sum_n s(E_{-n}) = \sum_n s(-E_n)$ for any function $s(E_n)$ of the energies. We can then split up the logarithm of the square into *two* logarithms and exchange $E_n \to -E_n$ in *one* sum without changing the value:

$$\begin{aligned}
\log Z &= \sum_n \sum_{\boldsymbol{p}} \log\left\{\beta^4\left[(E_n + i\mu)^2 + E^2(\boldsymbol{p})\right]^2\right\} \\
&= \sum_n \sum_{\boldsymbol{p}} \log\left\{\beta^2\left[(E_n + i\mu)^2 + E^2(\boldsymbol{p})\right]\right\} + \sum_n \sum_{\boldsymbol{p}} \log\left\{\beta^2\left[(+E_n + i\mu)^2 + E^2(\boldsymbol{p})\right]\right\} \\
&= \sum_n \sum_{\boldsymbol{p}} \log\left\{\beta^2\left[(E_n + i\mu)^2 + E^2(\boldsymbol{p})\right]\right\} + \sum_n \sum_{\boldsymbol{p}} \log\left\{\beta^2\left[(-E_n + i\mu)^2 + E^2(\boldsymbol{p})\right]\right\} \\
&= \sum_n \sum_{\boldsymbol{p}} \log\left\{\beta^4\left[(E_n + i\mu)^2 + E^2(\boldsymbol{p})\right]\left[(-E_n + i\mu)^2 + E^2(\boldsymbol{p})\right]\right\}.
\end{aligned} \tag{3.103}$$

By multiplying out all parentheses, it is straightforward to verify that

$$\left[(\pm E_n + i\mu)^2 + E^2(\boldsymbol{p})\right] = \left[E_n \pm i(E(\boldsymbol{p}) + \mu)\right]\left[E_n \mp i(E(\boldsymbol{p}) - \mu)\right]. \tag{3.104}$$

We can use this to rewrite the product in the partition function (3.103) as

$$\begin{aligned}
&\left[(E_n + i\mu)^2 + E^2(\boldsymbol{p})\right]\left[(-E_n + i\mu)^2 + E^2(\boldsymbol{p})\right] \\
&= \left[E_n + i(E(\boldsymbol{p}) + \mu)\right]\left[E_n + i(E(\boldsymbol{p}) - \mu)\right]\left[E_n - i(E(\boldsymbol{p}) + \mu)\right]\left[E_n - i(E(\boldsymbol{p}) - \mu)\right] \\
&= \left[E_n^2 + (E(\boldsymbol{p}) - \mu)^2\right]\left[E_n^2 + (E(\boldsymbol{p}) + \mu)^2\right].
\end{aligned} \tag{3.105}$$

Inserting this back into the partition function (3.103), we find that it can be written

$$\begin{aligned}
\log Z &= \sum_n \sum_{\boldsymbol{p}} \log\left\{\beta^4\left[E_n^2 + (E(\boldsymbol{p}) - \mu)^2\right]\left[E_n^2 + (E(\boldsymbol{p}) + \mu)^2\right]\right\} \\
&= \sum_n \sum_{\boldsymbol{p}} \log\left\{\beta^2\left[E_n^2 + (E(\boldsymbol{p}) - \mu)^2\right]\right\} + \sum_n \sum_{\boldsymbol{p}} \log\left\{\beta^2\left[E_n^2 + (E(\boldsymbol{p}) + \mu)^2\right]\right\}
\end{aligned} \tag{3.106}$$

We have accomplished our mission of removing the awkward i from the partition function (3.102), manifesting it as a real quantity. Moreover, the two sums over n are now in the same form as the bosonic sum (3.80), but this time over fermionic Matsubara energies. Defining the energies $\tilde{E}_\pm(\boldsymbol{p}) = E(\boldsymbol{p}) \pm \mu$ relative to the chemical potential, we can use the same method as we did back there to rewrite it as the two integrals

$$\log Z = \sum_{\boldsymbol{p}} \left[\int \mathrm{d}\tilde{E}_+^2(\boldsymbol{p}) \sum_n \frac{1}{E_n^2 + \tilde{E}_+^2(\boldsymbol{p})} + \int \mathrm{d}\tilde{E}_-^2(\boldsymbol{p}) \sum_n \frac{1}{E_n^2 + \tilde{E}_-^2(\boldsymbol{p})}\right]. \tag{3.107}$$

Like in (3.80), the sums over n can be performed using the Matsubara energy sum (C.17), but this time over the fermionic energies. Then the integrals become

$$\begin{aligned}
\log Z &= \beta \sum_{\boldsymbol{p}} \left\{\int \frac{\mathrm{d}\tilde{E}_+^2(\boldsymbol{p})}{2\tilde{E}_+(\boldsymbol{p})}\left[1 - \frac{2}{e^{\beta\tilde{E}_+(\boldsymbol{p})} + 1}\right] + \int \frac{\mathrm{d}\tilde{E}_-^2(\boldsymbol{p})}{2\tilde{E}_-(\boldsymbol{p})}\left[1 - \frac{2}{e^{\beta\tilde{E}_-(\boldsymbol{p})} + 1}\right]\right\} \quad \Big(\text{by (C.17)}\Big) \\
&= \beta \sum_{\boldsymbol{p}} \left\{\int \mathrm{d}\tilde{E}_+(\boldsymbol{p})\left[1 - \frac{2}{e^{\beta\tilde{E}_+(\boldsymbol{p})} + 1}\right] + \int \mathrm{d}\tilde{E}_-(\boldsymbol{p})\left[1 - \frac{2}{e^{\beta\tilde{E}_-(\boldsymbol{p})} + 1}\right]\right\} \\
&= \beta \sum_{\boldsymbol{p}} \left\{E_+(\boldsymbol{p}) + \frac{2}{\beta}\log\left[1 + e^{-\beta E_+(\boldsymbol{p})}\right] + E_-(\boldsymbol{p}) + \frac{2}{\beta}\log\left[1 + e^{-\beta E_-(\boldsymbol{p})}\right]\right\} \\
&= 2\sum_{\boldsymbol{p}} \left\{\beta E(\boldsymbol{p}) + \log\left[1 + e^{-\beta E_+(\boldsymbol{p})}\right] + \log\left[1 + e^{-\beta E_-(\boldsymbol{p})}\right]\right\}.
\end{aligned} \tag{3.108}$$

Taking the continuum limit (3.62), we finally obtain the **partition function for Dirac fermions**

$$\log Z = 2V \int \frac{\mathrm{d}^3 p}{(2\pi\hbar)^3} \left\{ \beta E(\boldsymbol{p}) + \log\left[e^{-\beta(E(\boldsymbol{p})-\mu)} + 1\right] + \log\left[e^{-\beta(E(\boldsymbol{p})+\mu)} + 1\right] \right\}. \tag{3.109}$$

3.6 Summary

Having evaluated $\log Z$ for both a real scalar field and Dirac fermions, it is insightful to conclude this chapter by comparing some similarities and differences of the two cases:

- The bosonic and fermionic path integrals (3.25) and (3.57) that we started with look very similar on the outside, yet are very different on the inside due to the algebra of commuting complex numbers in the bosonic case being replaced by anti-commuting Grassmann numbers for fermions.
- The periodicity of the bosonic field and the anti-periodicity of the fermionic field allowed us to expand both as Fourier series, but with different Matsubara frequencies (3.60).
- Only the Dirac field has a conserved charge that let us introduce a chemical potential μ. The *real* scalar field that we considered has no conserved current, unlike a *complex* scalar field, for example.
- In the bosonic case, we could integrate out the momentum π, leaving the Gaussian integrals (3.77) over *one* variable that we tackled using $\int \mathrm{d}x\, e^{-ax^2} \propto a^{-1/2}$. In the fermionic case, we could not integrate out the momentum $\pi = i\hbar\psi^\dagger$. This resulted in the Gaussian integrals (3.97) over *pairs* of Grassmann numbers that we handled with $\int \mathrm{d}\psi^\dagger \int \mathrm{d}\psi\, e^{-\psi^\dagger A \psi} = \det A$. The integrals effectively differ by the power $-1/2$.
- We managed to bring $\log Z$ into the similar sums (3.79) and (3.106) over the Matsubara energies E_n in both cases. In appendix C we described a general framework for computing both sums, with the Bose-Einstein and Fermi-Dirac distributions $1/[e^{\beta E(\boldsymbol{p})} \mp 1]$ arising naturally in the bosonic and fermionic case, respectively.
- The results (3.83) and (3.109) for $\log Z$ have very similar structure. In particular, the first terms essentially differ by the factor -4. Physically, we can attribute the factor 4 to from four separate contributions from particles, antiparticles, spin up and spin down for the fermions, compared to the bosons with only one value of spin and no antiparticles.

Now that we have $\log Z$ for free Dirac fermions, we can move on to calculate the particle number density, energy density and pressure in the next chapter.

Chapter 4

Ideal Neutron Stars

In chapter 3, we found the partition function $Z = Z(T, \mu, V)$ for two sample systems, and in particular a gas of free Dirac fermions, referred to as an **ideal Fermi gas**. From the partition function, we can derive the pressure $P = P(T, \mu)$ and energy density $\epsilon = \langle E \rangle / V = \epsilon(T, \mu)$ as functions of the temperature and chemical potential using equation (3.2a), (3.2b) and (3.2c), eliminating the volume dependence as P and ϵ are turned into intensive quantities by division. At some fixed temperature T, we can therefore eliminate μ to express ϵ in terms of P. This gives us an equation of state $\epsilon = \epsilon(T, P)$ for the energy density. In this chapter, we will see that inside neutron stars it is valid to consider the zero-temperature limit $T = 0$, making the Fermi gas completely degenerate and directly relating pressure to energy density in the resulting temperature-independent equation of state $\epsilon = \epsilon(P)$. With this equation of state, we can finally solve the Tolman-Oppenheimer-Volkoff system (2.38) for some central pressure $P(0) = P_c$. By doing so for a range of central pressures, we will parametrize a **mass-radius curve** of **ideal neutron stars** modeled by degenerate ideal Fermi gases of neutrons.

In the second part of this chapter, we investigate whether the stars on the mass-radius curve we find are **stable or unstable**. By applying perturbation theory to the equilibrium analysis of general relativity in chapter 2, we will derive a differential equation for radial pulsations of stars slightly outside equilibrium. We will find a general solution of this equation expressed as a sum over infinitely many normal pulsation modes and corresponding eigenfrequencies, each of which solve a Sturm-Liouville problem. From this, we will see that we can conclude whether a star is stable or not by checking the *sign* of the eigenvalue of one Sturm-Liouville problem. To conclude our stability analysis, we therefore use the **shooting method** to solve a Sturm-Liouville problem for every star on our mass-radius curve to determine their stability.

This chapter is inspired by references [And12], [Gle00], [MTW73] and [Bar+66].

4.1 Equation of state for a degenerate ideal Fermi gas

For ease of reference, the logarithm of the free Dirac fermion partition function (3.109) is

$$\log Z = 2V \int \frac{\mathrm{d}^3 p}{(2\pi\hbar)^3} \Big\{ \beta E(\boldsymbol{p}) + \log\Big[e^{-\beta(E(\boldsymbol{p})-\mu)} + 1\Big] + \log\Big[e^{-\beta(E(\boldsymbol{p})+\mu)} + 1\Big] \Big\}, \tag{4.1}$$

and the Fermi-Dirac distribution is

$$n(E-\mu) = \frac{1}{e^{\beta(E-\mu)} + 1}. \tag{4.2}$$

First, the particle number density $n = \langle N \rangle / V$ follows from the derivative (3.2a) and is

$$n = \frac{1}{\beta V} \frac{\partial \log Z}{\partial \mu} = 2 \int \frac{\mathrm{d}^3 p}{(2\pi\hbar)^3} \Big\{ n\big(E(\boldsymbol{p}) - \mu\big) - n\big(E(\boldsymbol{p}) + \mu\big) \Big\}. \tag{4.3a}$$

Do not confuse the particle density n on the left with the Fermi-Dirac distributions $n\big(E(\boldsymbol{p}) \mp \mu\big)$ on the right! We will soon perform the integral over $\boldsymbol{p}$ and get rid of $n\big(E(\boldsymbol{p}) \mp \mu\big)$, anyway. From the density (4.3a), we see that $n = n(\mu, T)$ is a function of the chemical potential μ and temperature T, so that at some fixed temperature, the value of μ determines the particle density n.

Second, we calculate the energy density $\epsilon = \langle E \rangle \,/\, V$ from equation (3.2b). Inserting the particle number density (4.3a) and taking the derivative of $\log Z$, we get

$$\epsilon = \mu n - \frac{1}{V}\frac{\partial \log Z}{\partial \beta} = 2\int \frac{\mathrm{d}^3 p}{(2\pi\hbar)^3}\Big\{ -E(\boldsymbol{p}) + E(\boldsymbol{p})\, n\big(E(\boldsymbol{p}) - \mu\big) + E(\boldsymbol{p})\, n\big(E(\boldsymbol{p}) + \mu\big)\Big\}. \quad (4.3b)$$

Third, we find that the pressure (3.2c) is

$$P = \frac{\log Z}{\beta V} = 2\int \frac{\mathrm{d}^3 p}{(2\pi\hbar)^3}\left\{ E(\boldsymbol{p}) + \frac{1}{\beta}\log\Big[e^{-\beta(E(\boldsymbol{p})-\mu)} + 1\Big] + \frac{1}{\beta}\log\Big[e^{-\beta(E(\boldsymbol{p})+\mu)} + 1\Big]\right\}. \quad (4.3c)$$

An interpretation of the terms contributing to the particle number density, energy density and pressure is in order.

1. From the particle density (4.3a) at constant temperature T, we see that the sign of n is determined by the sign of μ. The total density n is expressed as a balance between *particles* living relative to the chemical potential $+\mu$ and *antiparticles* living relative to the chemical potential $-\mu$. Thus, the chemical potential μ determines the balance between particles and antiparticles in the system. Similarly, the two last terms in the energy density (4.3b) and pressure (4.3c) can be interpreted as contributions from particles and antiparticles, respectively. We *choose* a large positive value of $\mu > 0$, so that the presence of particles dominate, while antiparticles are more or less absent. With this choice, $n\big(E(\boldsymbol{p}) - \mu\big) \gg n\big(E(\boldsymbol{p}) + \mu\big)$, and we *drop the last terms of the particle density* (4.3a)*, energy density* (4.3b) *and pressure* (4.3c).

2. The first term of the energy density (4.3b) is infinite, as the integrand increases unbounded like $\mathrm{d}^3 p\, E(\boldsymbol{p}) = 4\pi p^2 \sqrt{p^2c^2 + m^2c^4} \propto p^3$ for large p. It is like a sum over the ground state energies of an infinite number of fermionic harmonic oscillators $\hat{H} = \hbar\omega\left(a^\dagger a - \frac{1}{2}\right)$ – two for spin up and down and two more for both particles and antiparticles. Therefore, it can be interpreted as an *infinite shift of the vacuum energy*. We will make the assumption that there is no vacuum energy, or equivalently redefine the infinite contribution as a new zero-point energy. For example, in the vacuum outside a star there should be no mass density $\rho = \epsilon/c^2$, and hence no energy density ϵ. Do note, however, that the possible presence of vacuum energy is really an unresolved problem in physics – we will briefly discuss this in a moment. Either way, we will *drop the first term of the energy density* (4.3b).

3. Like the energy density, the first term of the pressure (4.3c) is also infinite. It is reasonable that if we drop the infinite contribution to the energy density, then we should drop it in the pressure, too. As we remarked on page 31, the pressure that we obtain directly from $\log Z$ is really undetermined up to the shift of a constant, anyway, justifying that we do indeed have the freedom to remove such an infinite contribution here as well. We will therefore *drop the first term of the pressure* (4.3c). Physically, the pressure should vanish when the energy density vanishes. For example, outside the surface of a star the pressure vanishes by definition, and we assume we are in vacuum with no energy or mass density. We will see below that dropping the term does indeed ensure that this condition is satisfied. If you wish, peek ahead and note that both the energy density (4.10b) and pressure (4.10c) both vanish when $x_F = 0$.

Our ad-hoc removal of the vacuum energy has no doubt sparked the curiosity of the educated reader. The *cosmological constant problem* is an unresolved problem in physics concerning

the disagreement between small *observed* values of the vacuum energy density and large – here infinite – values *predicted* by quantum field theory. The presence of a nonzero vacuum energy density is related to the appearance of the cosmological constant Λ in the Einstein field equations. However, we have used the field equations with $\Lambda = 0$ throughout. We "resolve the problem" by simply discarding the infinite contribution to the vacuum energy density, but make no attempt to conceal the deep theoretical questions underlying this ad-hoc resolution. For the interested reader, the Wikipedia article [Wiki21a] is a good starting point to learn more about the cosmological constant problem.

Before completely losing track of what we were doing, let us get back to calculating the equation of state. After dropping terms as described above, only the penultimate terms are left in the number density (4.3a), energy density (4.3b) and pressure (4.3c). Noting that all integrals only depend on the magnitude $|\boldsymbol{p}| = p$ of the momentum, we rebaptize $E(\boldsymbol{p}) = E(p)$ and are left with

$$\text{particle density} \qquad n = 2\int_0^\infty \frac{\mathrm{d}p\, 4\pi p^2}{(2\pi\hbar)^3}\, n\big(E(p)-\mu\big), \tag{4.4a}$$

$$\text{energy density} \qquad \epsilon = 2\int_0^\infty \frac{\mathrm{d}p\, 4\pi p^2}{(2\pi\hbar)^3}\, E(p)\, n\big(E(p)-\mu\big), \tag{4.4b}$$

$$\text{pressure} \qquad P = \frac{2}{\beta}\int_0^\infty \frac{\mathrm{d}p\, 4\pi p^2}{(2\pi\hbar)^3}\, \log\left[e^{-\beta(E(p)-\mu)}+1\right]. \tag{4.4c}$$

The logarithm in the third integral looks annoyingly similar to the Fermi-Dirac distribution in the two first. Let us make one partial integration on the pressure with $u' = p^2$ and $v = \log\left[e^{-\beta(E(\boldsymbol{p})-\mu)}+1\right]$. The boundary term $uv \propto p^3 \log\left[e^{-\beta(E(p)-\mu)}+1\right]$ then vanishes at $p = 0$ because $p^3 = 0$ there, and also at $p = \infty$ where $\log\left[e^{-\beta(E(p)-\mu)}+1\right] = \log\left[e^{-\infty}+1\right] = \log 1 = 0$. After the partial integration, the three integrals take the satisfyingly similar forms

$$\text{particle density} \qquad n = 2\int_0^\infty \frac{\mathrm{d}p\, 4\pi p^2}{(2\pi\hbar)^3}\, n\big(E(p)-\mu\big), \tag{4.5a}$$

$$\text{energy density} \qquad \epsilon = 2\int_0^\infty \frac{\mathrm{d}p\, 4\pi p^2}{(2\pi\hbar)^3}\, E(p)\, n\big(E(p)-\mu\big), \tag{4.5b}$$

$$\text{pressure} \qquad P = 2\int_0^\infty \frac{\mathrm{d}p\, 4\pi p^3}{3(2\pi\hbar)^3}\, E'(p)\, n\big(E(p)-\mu\big). \tag{4.5c}$$

The integrals become quite complicated after plugging in the relativistic dispersion relation (3.75) and the Fermi-Dirac distribution (4.2). In order to calculate them analytically, we will make one more approximation.

At *absolute* zero temperature $T = 0$, the Fermi-Dirac distribution

$$n(E-\mu) = \frac{1}{e^{\beta(E-\mu)}+1} = \Theta(\mu - E) = \begin{cases} 0 & (E > \mu) \\ 1 & (E < \mu) \end{cases} \tag{4.6}$$

behaves like a step function. To see this, observe that $T = 0$ corresponds to $\beta = 1/k_B T = \infty$, and that the sign of $E - \mu$ then determines whether the exponential $e^{\beta(E-\mu)}$ in the denominator blows up or vanishes, and hence whether the fraction survives. Physically, this means that the system is completely degenerate, filling momentum states with $E(\boldsymbol{p}) < \mu$ only. The occupied states with the greatest momentum p_F make up a so-called *Fermi surface* $|\boldsymbol{p}| = p_F$ in momentum space, and the corresponding maximum energy $E_F = \sqrt{p_F^2 c^2 + m^2 c^4}$ is called the *Fermi energy*, and is equal to the chemical potential when $T = 0$.

Typical neutron star core temperatures linger around $T_0 \approx 10^6\,\mathrm{K}$, [Gle00] so how is this relevant for our purposes? In the grand canonical ensemble, the temperature T and chemical potential μ are formally *independent* variables. However, we require that the total number of particles N, and thus the density $n(\mu, T)$, is *fixed*, so that if we change the temperature, we must also change

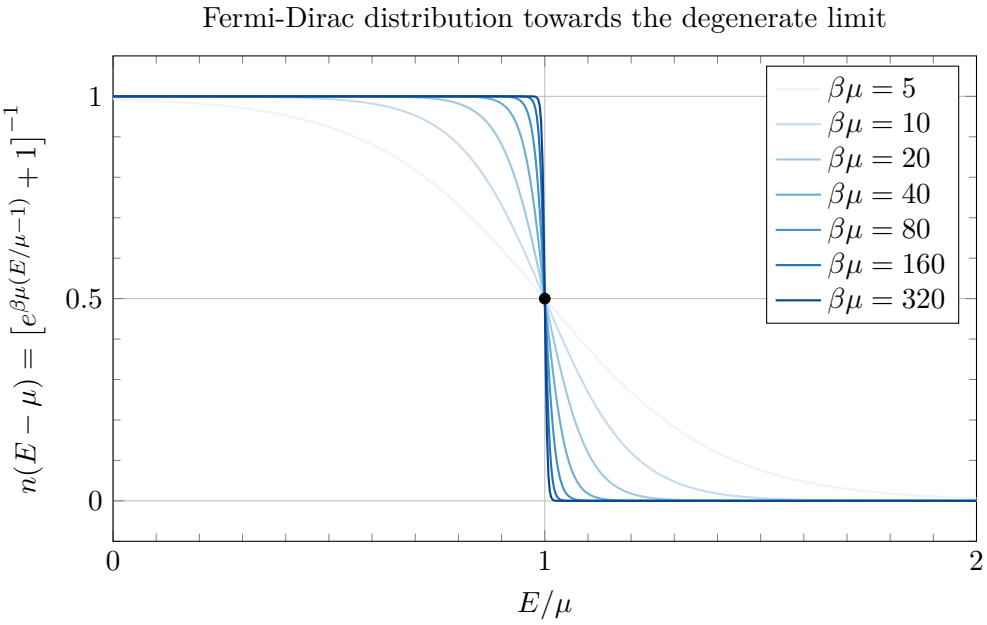

Figure 4.1: As $\beta\mu \to \infty$, the Fermi-Dirac distribution $n(E-\mu) = \left[e^{\beta\mu(E/\mu-1)}+1\right]^{-1}$ increasingly resembles the step function $\Theta(\mu - E)$.

the chemical potential to compensate. This creates an implicit dependence between μ and T. Under this constraint, it is possible to use a Sommerfeld expansion to show mathematically that the chemical potential

$$\mu(T) = E_F + \mathcal{O}\left(\left(\frac{T}{T_F}\right)^2\right) \tag{4.7}$$

is corrected from the Fermi energy by contributions of second or higher order in T/T_F, where $T_F = E_F/k_B$ is the *Fermi temperature*. For a more detailed discussion of the Sommerfeld expansion and the inter-dependence between T and μ, we recommend [Ton12, section 3.6].

In other words, if $T \ll T_F$, then $\mu \approx E_F$. Neutrons have mass $m = 1.67 \cdot 10^{-27}\,\mathrm{kg}$, so the Fermi temperature is at least $T_F = \sqrt{p_F^2c^2 + m^2c^4}/k_B > mc^2/k_B \approx 10^{13}\,\mathrm{K}$. Thus, we do indeed have $T/T_F \approx 10^{-7} \ll 1$ for a neutron star. This is equivalent to $\beta E_F \gg 1$, and since this *implies* that $E_F \approx \mu$, then it is also an excellent approximation to take the **degenerate limit**

$$\beta\mu \gg 1. \tag{4.8}$$

Let us now rewrite the Fermi-Dirac distribution as

$$n(E-\mu) = \frac{1}{e^{\beta\mu(E/\mu-1)}+1}. \tag{4.9}$$

As shown in figure 4.1, this distribution again resembles the step function $\Theta(\mu - E)$ in the degenerate limit (4.8). Thus, the zero-temperature behavior of the Fermi-Dirac distribution is restored in this limit. Although the core temperature is far from zero in everyday terms, it is small *compared to* the Fermi temperature, and this approximation is therefore also referred to as the **zero-temperature limit**.

In hindsight, since the chemical potential is an independent variable in the partition function, we do have the freedom to simply *assume* the degenerate limit (4.8) from the beginning, at the point where we said we *chose* a "large positive value" for the chemical potential.

With the zero-temperature approximation, the particle density (4.5a) is simply

$$n = 2\int_0^\infty \frac{\mathrm{d}p\,4\pi p^2}{(2\pi\hbar)^3}\,\Theta\big(\mu - E(p)\big) = 2\int_0^{p_F} \frac{\mathrm{d}p\,4\pi p^2}{(2\pi\hbar)^3} = \frac{p_F^3}{3\pi^2\hbar^3}. \tag{4.10a}$$

The energy density (4.5b) becomes

$$\begin{aligned}\epsilon &= 2\int_0^\infty \frac{\mathrm{d}p\,4\pi p^2}{(2\pi\hbar)^3}\,E(p)\,\Theta\big(\mu - E(p)\big)\\ &= 2\int_0^{p_F} \frac{\mathrm{d}p\,4\pi p^2}{(2\pi\hbar)^3}\,\sqrt{p^2c^2+m^2c^4}\\ &= \frac{m^4c^5}{\pi^2\hbar^3}\int_0^{x_F}\mathrm{d}x\,x^2\sqrt{x^2+1} && \big(x = p/mc\big)\\ &= \frac{m^4c^5}{8\pi^2\hbar^3}\left[\big(2x_F^3+x_F\big)\sqrt{x_F^2+1} - \log\left(x_F+\sqrt{x_F^2+1}\right)\right] && \big(\text{by (F.6)}\big).\end{aligned} \tag{4.10b}$$

Finally, the pressure (4.5c) is

$$\begin{aligned}P &= 2\int_0^\infty \frac{\mathrm{d}p\,4\pi p^3}{3(2\pi\hbar)^3}\,E'(p)\,\Theta\big(\mu - E(p)\big)\\ &= 2\int_0^{p_F} \frac{\mathrm{d}p\,4\pi p^3}{3(2\pi\hbar)^3}\,\frac{pc^2}{\sqrt{p^2c^2+m^2c^4}}\\ &= \frac{m^4c^5}{3\pi^2\hbar^3}\int_0^{x_F}\frac{\mathrm{d}x\,x^4}{\sqrt{x^2+1}} && \big(x = p/mc\big)\\ &= \frac{m^4c^5}{24\pi^2\hbar^3}\left[\big(2x_F^3-3x_F\big)\sqrt{x_F^2+1} + 3\log\left(x_F+\sqrt{x_F^2+1}\right)\right] && \big(\text{by (F.7)}\big).\end{aligned} \tag{4.10c}$$

At this point, let us justify the act of dropping the infinite contribution to the pressure (4.3c). Outside a star, for example, we required that the pressure should vanish when the energy density vanishes. Indeed, now we see that $\epsilon(x_F) = 0$ only if $x_F = 0$, and $P(x_F = 0) = 0$.

The equation of state $\epsilon = \epsilon(P)$ follows by eliminating x_F from the energy density (4.10b) and pressure (4.10c). Due to their complicated dependence on x_F, we will do so in three cases of increasing difficulty.

4.1.1 Ultra-relativistic limit

First, consider the ultra-relativistic limit

$$x_F \gg 1, \tag{4.11}$$

where the Fermi energy $E_F = \sqrt{p_F^2c^2+m^2c^4} \simeq p_Fc$ is dominated by the contribution from the Fermi momentum. Since $\log\left(x_F+\sqrt{x_F^2+1}\right) \simeq \log 2x_F$ diverges only logarithmically, we see that both the energy density (4.10b) and pressure (4.10c) are dominated by their first terms with $2x_F^3\sqrt{x_F^2+1} \simeq 2x_F^4$. In the ultra-relativistic limit, then,

$$\epsilon \simeq \frac{m^4c^5x_F^4}{4\pi^2\hbar^3} \qquad \text{and} \qquad P \simeq \frac{m^4c^5x_F^4}{12\pi^2\hbar^3}, \tag{4.12}$$

and x_F is easily eliminated, yielding the very simple equation of state

$$\epsilon = 3P. \tag{4.13}$$

4.1.2 Non-relativistic limit

Next, let us consider the non-relativistic limit

$$x_F \ll 1, \tag{4.14}$$

where the Fermi energy $E_F = \sqrt{p_F^2 c^2 + m^2 c^4} \simeq mc^2$ is dominated by the rest energy of the fermions. Taylor expanding the energy density (4.10b) and pressure (4.10c) around $x_F = 0$ to lowest order, we find

$$\epsilon \simeq \frac{mc^2 p_F^3}{3\pi^2\hbar^3} \qquad \text{and} \qquad P \simeq \frac{p_F^5}{15\pi^2\hbar^3 m}. \tag{4.15}$$

Note that with the density (4.10a), the energy density can be written $\epsilon = nmc^2$, as if all fermions have broken free from the Pauli exclusion principle and possess the same energy mc^2. This is only a mathematical feature of the non-relativistic limit – the fermions still occupy different states with different momentum, but the momenta are so small that the differences are negligible compared to the rest energy mc^2. Again, it is straightforward to eliminate x_F to find the equation of state, only this time there is some extra bookkeeping due to the different exponents of p_F. We find

$$\epsilon = \left(\frac{5^3 m^8 c^{10}}{3^2\pi^4\hbar^6}\right)^{\frac{1}{5}} P^{\frac{3}{5}}. \tag{4.16}$$

4.1.3 General Fermi momenta

How can we find the energy density

$$\epsilon = \frac{m^4 c^5}{8\pi^2\hbar^3}\left[\left(2x_F^3 + x_F\right)\sqrt{x_F^2+1} - \log\left(x_F + \sqrt{x_F^2+1}\right)\right] \tag{4.17a}$$

that corresponds to a given pressure

$$P = \frac{m^4 c^5}{24\pi^2\hbar^3}\left[\left(2x_F^3 - 3x_F\right)\sqrt{x_F^2+1} + 3\log\left(x_F + \sqrt{x_F^2+1}\right)\right] \tag{4.17b}$$

for general x_F? Since we will solve the Tolman-Oppenheimer-Volkoff equation on a computer anyway, we can do so by numerical root finding. Given the pressure P, we use a root finding algorithm to find the root x_F of the function

$$f(x_F) = P(x_F) - P = 0, \tag{4.18}$$

where $P(x_F)$ is the pressure (4.17b) as a function of x_F. Having found the root, we can simply calculate the corresponding energy density $\epsilon(x_F)$ from equation (4.17a). In appendix G.4, we encapsulate this whole procedure into one numerical equation of state $\epsilon(P)$.

All three equations of state (4.13), (4.16) and (4.17) are shown in figure 4.2.

4.2 Mass-radius relation for ideal neutron stars

Having obtained equations of state $\epsilon = \epsilon(P)$, we are finally in a position to solve the Tolman-Oppenheimer-Volkoff system (2.38). We will do so for all three equations of state that we found in section 4.1.

4.2.1 Ultra-relativistic equation of state

With the ultra-relativistic equation of state (4.13), the Tolman-Oppenheimer-Volkoff equation can be solved analytically with the polynomial trial solution

$$P(r) = Ar^n. \tag{4.19}$$

With $\epsilon = 3P = 3Ar^n$, the mass gradient (2.38b) reads

$$\frac{\mathrm{d}m}{\mathrm{d}r} = \frac{12\pi A}{c^2} r^{n+2}, \qquad \text{so} \qquad m(r) = \frac{12\pi A}{(n+3)c^2} r^{n+3} \quad (n \neq -3). \tag{4.20}$$

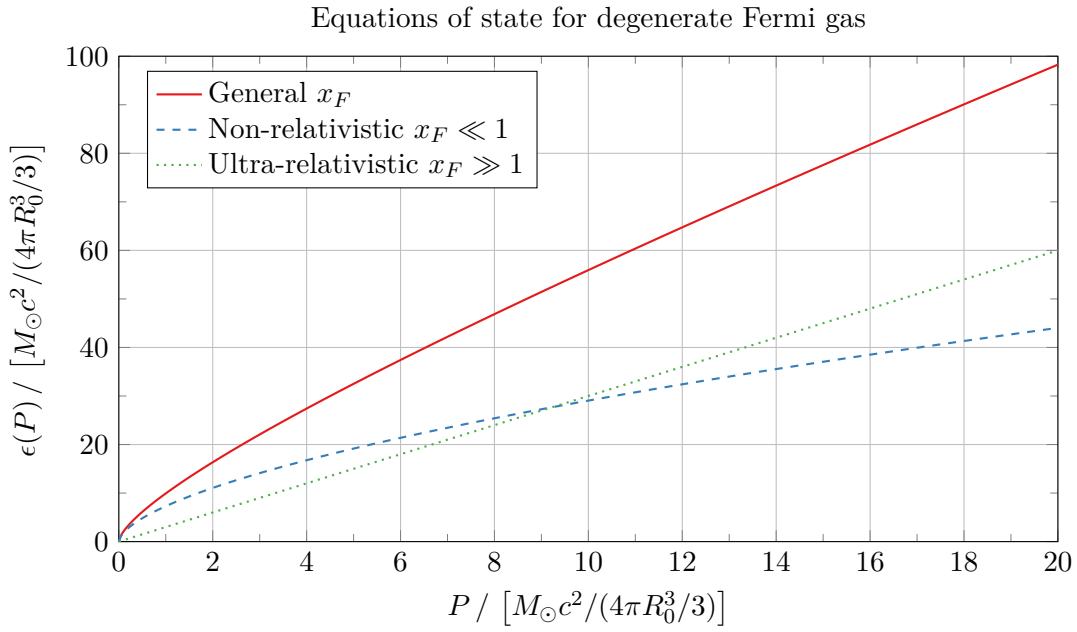

Figure 4.2: Equations of state $\epsilon(P)$ for a degenerate Fermi gas for general Fermi momenta $p_F = mc\,x_F$, non-relativistic $p_F \ll mc$ and ultra-relativistic $p_F \gg mc$. Here $M_\odot$ is the solar mass and $R_0 = 10\,\mathrm{km}$.

Inserting the mass, pressure and energy density into the Tolman-Oppenheimer-Volkoff equation (2.38a), it becomes

$$nAr^{n-1} = -\frac{48\pi G A^2 r^{2n+1}}{(n+3)c^4}\left[2+\frac{n}{3}\right]\left[1-\frac{24\pi G A r^{n+2}}{(n+3)c^4}\right]^{-1}. \tag{4.21}$$

We can attain equality for all r if we choose $n = -2$. Then the rightmost factor no longer depends on r, and both sides have the same r^{-3}-dependence

$$-2Ar^{-3} = -\frac{64\pi G A^2 r^{-3}}{c^4}\left[1-\frac{24\pi G A}{c^4}\right]^{-1}. \tag{4.22}$$

Equality is established if we match the constant factors by choosing $A = c^4/56\pi G$. Then the solutions for the pressure and mass are

$$P(r) = \frac{c^4}{56\pi G r^2} \qquad \text{and} \qquad m(r) = \frac{3c^2 r}{14G}. \tag{4.23}$$

This is a highly unphysical result. The pressure diverges at the center, so gravity cannot hold such a star together. In addition, $p(r) > 0$ for all r, so the star has no surface, and accordingly its mass $M = m(\infty) = \infty$ is infinite.

4.2.2 Non-relativistic equation of state

With the power dependence of the non-relativistic equation of state (4.16), it is not easy, if even possible, to solve the Tolman-Oppenheimer-Volkoff equation analytically. The trial solution (4.19) we employed in section 4.1.1 fails miserably, as we do not get the same fortunate cancellations of r. We therefore resort to the numerical solution method described in appendix G.2, parametrizing different stars by their central pressure P_c and integrating the Tolman-Oppenheimer-Volkoff equation until the pressure $p(R)$ vanishes, using the corresponding radius R to establish the mass $M = m(R)$ of the star. This results in the mass-radius curve shown in figure 4.3. Notably, the curve peaks at the maximum mass $M = 0.96M_\odot$ around $R = 8.11\,\mathrm{km}$ when using the full Tolman-Oppenheimer-Volkoff pressure gradient (2.38a), but not when using its Newtonian limit (2.33).

4.2.3 General equation of state

For general Fermi momenta, the equation of state $\epsilon = \epsilon(P)$ is calculated numerically as described in section 4.1.3, and the Tolman-Oppenheimer-Volkoff equation is again integrated numerically as described in section 4.2.2. The resulting mass-radius curve is also shown in figure 4.3. Again, the curve peaks at a maximum mass $M = 0.71 M_\odot$ only for the relativistic pressure gradient. This is the most accurate equation of state, and it is therefore the bottom curve in figure 4.3 that we should pay most attention to. In addition, we show the pressure profiles for some stars on this curve in figure 4.4. Notice that the normalized profiles are quite similar for central pressures below that corresponding to the maximum mass, but begin to change dramatically once it is exceeded!

4.3 Stability analysis

The mass-radius curves in figure 4.3 display some interesting behavior. In particular, the curves obtained with the relativistic pressure gradient enter spirals for central pressures greater than those corresponding to their maximum masses. As we derived the Tolman-Oppenheimer-Volkoff equation, we assumed the star to be in hydrostatic equilibrium. Our use of statistical mechanics in the grand canonical ensemble to obtain the equation of state is consistent with this, as it describes a system in thermal and chemical equilibrium. So all stars on the mass-radius curve are in *equilibrium*, but just like a pendulum can be in a stable or unstable equilibrium, the equilibrium state of a star can also be either *stable* or *unstable* with respect to small perturbations. Let us investigate the stability of the sequences of stars in figure 4.3.

4.3.1 Necessary conditions for stability

We will start by presenting a few *necessary* conditions for stability from simple physical considerations. However, neither of the conditions are *sufficient* for a star to be stable, so we can only use them to identify unstable stars.

The Buchdal limit

We have already discussed one such condition – the Buchdal limit (2.29). In fact, we have plotted the line $M = 4c^2R/9G$ in figure 4.3 – it is just so steep that it coincides with the vertical axis and is completely invisible. Only stars above this line would be unstable, and it therefore does not rule out any stars on our mass-radius curve.

Causality

However exotic life inside a star may be, it cannot break causality. In particular, the speed of sound $v = \sqrt{\mathrm{d}P/\mathrm{d}\rho} = c\sqrt{\mathrm{d}P/\mathrm{d}\epsilon}$, as derived in appendix B.5, should not exceed the speed of light c. The equation of state $\epsilon = \epsilon(P)$ must therefore satisfy

$$\frac{\mathrm{d}P}{\mathrm{d}\epsilon} < 1 \qquad \text{(necessary condition)}. \tag{4.24}$$

How does the equation of state for a free Fermi gas hold up in this regard? Recall that the equation of state for general Fermi momenta p_F followed by eliminating x_F from the energy density (4.10b) to express it in terms of the pressure (4.10c). It is straightforward to calculate the derivatives

$$\frac{\mathrm{d}P}{\mathrm{d}x_F} = \frac{m^4c^5}{3\pi^2\hbar^3}\frac{x_F^4}{\sqrt{x_F^2+1}} \quad \text{and} \quad \frac{\mathrm{d}\epsilon}{\mathrm{d}x_F} = \frac{m^4c^5}{\pi^2\hbar^3}x_F^2\sqrt{x_F^2+1}. \tag{4.25}$$

Then we can apply the chain rule and the rule of inverse derivatives to obtain

$$\frac{\mathrm{d}P}{\mathrm{d}\epsilon} = \frac{\mathrm{d}P}{\mathrm{d}x_F}\frac{\mathrm{d}x_F}{\mathrm{d}\epsilon} = \frac{\mathrm{d}P/\mathrm{d}x_F}{\mathrm{d}\epsilon/\mathrm{d}x_F} = \frac{1}{3}\frac{1}{1+1/x_F^2}. \tag{4.26}$$

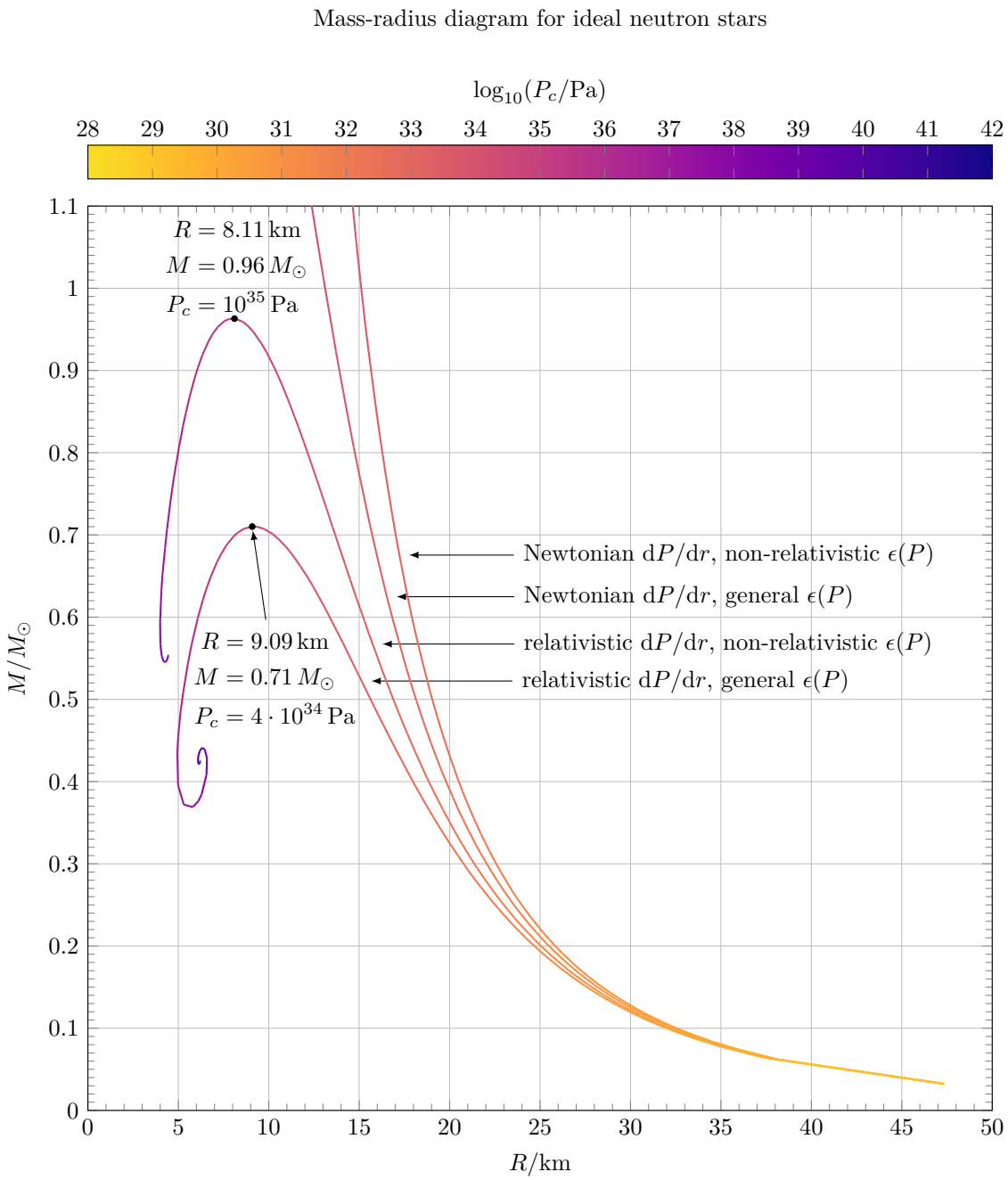

Figure 4.3: Mass-radius curve for ideal neutron stars parametrized by their central pressure P_c. The curve is obtained by numerically integrating the Tolman-Oppenheimer-Volkoff equation (2.38) with both the relativistic pressure gradient (2.38a) ("relativistic $\mathrm{d}P/\mathrm{d}r$") and its Newtonian limit (2.33) ("Newtonian $\mathrm{d}P/\mathrm{d}r$") from the center $r = 0$ with pressure $P(0) = P_c$ until the pressure $P(r) = 0$ vanishes at the surface $r = R$. The numerical integration is carried out using both the explicit non-relativistic equation of state (4.16) ("non-relativistic $\epsilon(P)$"), and using a root-finding algorithm to calculate the general equation of state (4.17) ("general $\epsilon(P)$"). Consult appendix G for the implementation of the computer program. Stars are parametrized by central pressures $4.27 \cdot 10^{28}\,\mathrm{Pa} \leq P_c \leq 4.27 \cdot 10^{41}\,\mathrm{Pa}$, and $M_\odot$ is the mass of the sun.

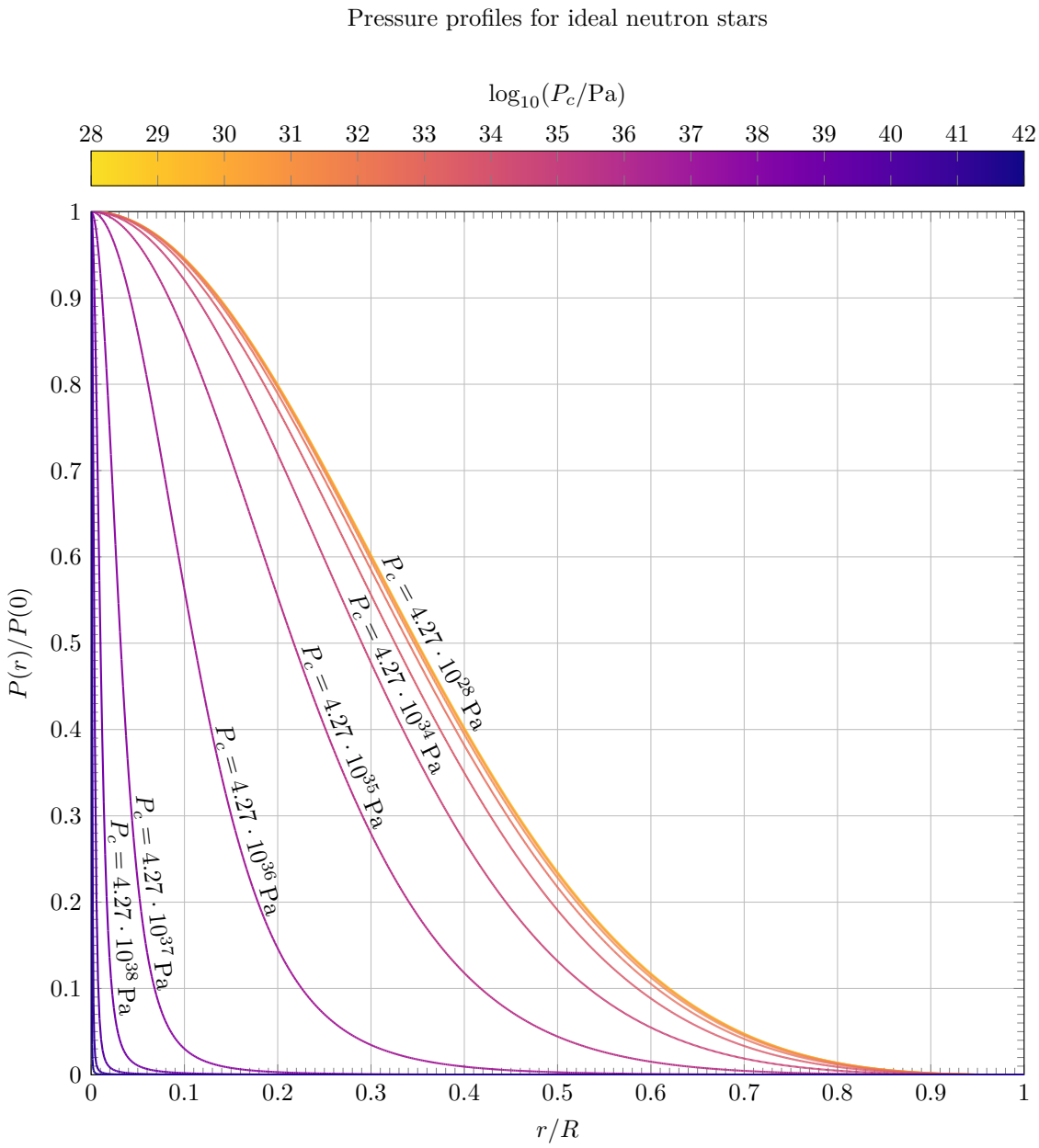

Figure 4.4: Normalized pressure profiles $P(r)/P(0)$ for the 14 neutron stars with central pressures $P_c = P(0) = 4.27 \cdot 10^{28}\,\mathrm{Pa}$, $4.27 \cdot 10^{29}\,\mathrm{Pa}$, …, $4.27 \cdot 10^{41}\,\mathrm{Pa}$ along the bottom sequence in figure 4.3. Where there is sufficient space, the central pressure is written above the pressure profile of the star it corresponds to.

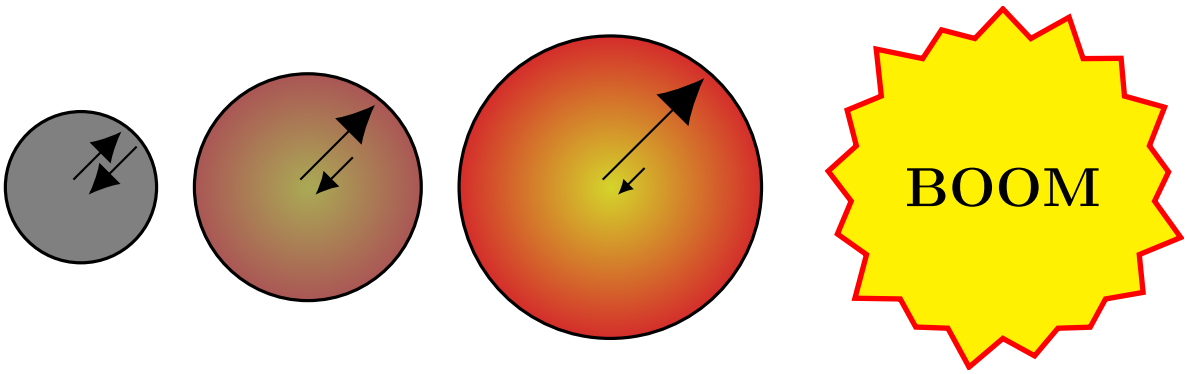

Figure 4.5: A slight decrease $\mathrm{d}\epsilon < 0$ in energy density weakens the gravitational force pulling a star in. If the equation of state $\epsilon = \epsilon(P)$ in a star satisfies $\mathrm{d}P/\mathrm{d}\epsilon < 0$, such a change in energy density would cause an increase $\mathrm{d}P > 0$ in the pressure pushing the star out. The greater pressure then causes the star to expand, which in turn causes another decrease in energy density. Repeated application of the same argument shows that the star continues to expand while the pressure grows indefinitely, so the star ultimately explodes.

We see that $\mathrm{d}P/\mathrm{d}\epsilon < 1$ for all x_F and approaches $1/3$ in the ultra-relativistic limit $x_F \to \infty$, as we should expect from the corresponding equation of state (4.13). Alternatively, this can be seen by inspecting the slopes $\mathrm{d}\epsilon/\mathrm{d}P > 1$ of the equations of state in figure 4.2. Hence, all the stars in figure 4.3 satisfy this condition, so it does not rule out any of them.

Real speed of sound

From the expression $v = c\sqrt{\mathrm{d}P/\mathrm{d}\epsilon}$ of the speed of sound, it also seems reasonable to require that

$$\frac{\mathrm{d}P}{\mathrm{d}\epsilon} > 0 \qquad \text{(necessary condition)} \tag{4.27}$$

for it to be a real quantity. Violation of this condition would in fact have dramatic consequences. First, note that an increase in energy density $\mathrm{d}\epsilon > 0$ is *always* accompanied by an increase in the gravitational force attempting to pull the star inwards. If such an increase implied a *decrease* $\mathrm{d}P < 0$ in the pressure that pushes the star outwards, then the gravitational force would automatically "win", causing the star to contract, and hence the energy density to increase further. Repeating the argument, we understand that the star collapses. This process is illustrated in figure 4.5. Likewise, if a decrease $\mathrm{d}\epsilon < 0$ caused an increase $\mathrm{d}P > 0$, the same argument shows that the pressure wins and the star explodes. However, if the changes $\mathrm{d}\epsilon$ and $\mathrm{d}P$ are of the same sign, then the pressure and gravitational force will at the very least counteract each other instead of driving apart. In this case the star *can* be stable, but the precise balance between the forces would have to be investigated in detail to conclude if it *really is*. In our case, the derivative (4.26) is already positive, so this criterion does not let us rule out any of our stars, either. However, this result is not completely useless, as it will be useful to assert that condition (4.27) is satisfied as we continue our stability analysis.

Mass increase for rising central pressure

A fourth necessary condition for stars parametrized by their central pressure P_c is

$$\frac{\mathrm{d}M(P_c)}{\mathrm{d}P_c} > 0 \qquad \text{(necessary condition)}. \tag{4.28}$$

To understand it, consider a star E_1^+ in equilibrium on the increasing part of the mass-pressure curve in figure 4.6, where condition (4.28) is satisfied. Now compress this star to the non-equilibrium star C^+ with the same mass, and let E_2^+ be the star in equilibrium with the same central pressure as C^+. Then C^+ has less mass than E_2^+, and hence *weaker gravitational forces*

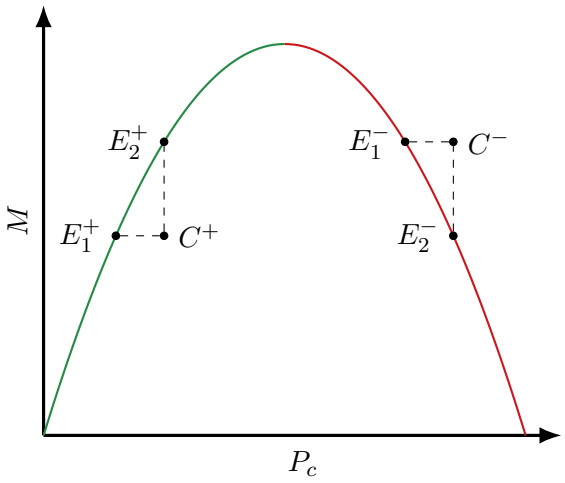

Figure 4.6: Suppose an equilibrium star E_1^+ on an *increasing* part of the mass-pressure curve $M(P_c)$ is compressed to a non-equilibrium star C^+ with the same mass. Compared to the *more massive* equilibrium star E_2^+ with the increased central pressure, it experiences *less* gravitational attraction, causing it to expand back towards the original equilibrium configuration E_1^+. In contrast, suppose an equilibrium star E_1^- on a *decreasing* part of the mass-pressure curve is compressed to a non-equilibrium star C_- with the same mass. Compared to the *less massive* equilibrium star E_2^- with the increased central pressure, it experiences *more* gravitational attraction, causing it to compress even more and ultimately implode.

but the *same central pressure* as E_2^+. As a result, C^+ will expand and hence relieve the central pressure, causing it to return towards the equilibrium star E_1^+.

Let us repeat the argument on the decreasing part of the curve, where condition (4.28) does not hold. After compressing E_1^- to C^-, we see that C^- has more mass, and hence *stronger gravitational forces* but the *same central pressure* as E_2^-. As a result, C^+ contracts, and repeating the argument then shows that it drifts away from the equilibrium curve in figure 4.6 and collapses.

Criterion (4.28) shows that the stars located between the maximum mass and the bottom of the spiral in figure 4.3 are unstable! Moreover, it suggests that there is a change in character of stability across a stationary point $\mathrm{d}M(P_c)/\mathrm{d}P_c = 0$ on the mass-radius curve. We will now investigate this further.

4.3.2 General stability analysis

The arguments presented above were necessary, but not sufficient for stellar stability. Let us analyze the stability of the stars in a more rigorous way by finding a necessary *and* sufficient criterion for stability. We will follow the path of Chandrasekhar [Cha64] and [MTW73, §26].

Perturbation theory for the fluid displacement

In section 2.1, we showed that in the spherically symmetric metric

$$\mathrm{d}s^2 = e^{2\alpha_0(r)}c^2\,\mathrm{d}t^2 - e^{2\beta_0(r)}\,\mathrm{d}r^2 - r^2\left(\mathrm{d}\theta^2 + \sin^2\theta\,\mathrm{d}\phi^2\right), \tag{4.29}$$

for a perfect fluid with energy-momentum

$$T_{\mu\nu} = \frac{1}{c^2}u_\mu u_\nu(\epsilon_0 + P_0) - g_{\mu\nu}P_0 \qquad \text{where} \qquad P_0 = P_0(r) \text{ and } \epsilon_0 = \epsilon_0(r) \tag{4.30}$$

that is in *equilibrium* with four-velocity

$$u^\mu = (u^0, 0, 0, 0), \tag{4.31}$$

the Einstein field equations (2.1) reduce to

$$\frac{1}{r^2}e^{-2\beta_0}\left(2r\beta_0' - 1 + e^{2\beta_0}\right) = \frac{8\pi G}{c^4}\epsilon_0 \qquad \left(G_{00} = \frac{8\pi G}{c^4}T_{00}\right), \tag{4.32a}$$

$$\frac{1}{r^2}e^{-2\beta_0}\left(2r\alpha_0' + 1 - e^{2\beta_0}\right) = \frac{8\pi G}{c^4}P_0 \qquad \left(G_{11} = \frac{8\pi G}{c^4}T_{11}\right), \tag{4.32b}$$

$$\alpha_0' = \frac{-1}{\epsilon_0 + P_0}P_0' \qquad \left(\nabla_\mu T^\mu{}_1 = 0\right), \tag{4.32c}$$

where $' = \partial/\partial r$.

Now we suppose that the fluid is no longer in equilibrium, but rather allow for a small radial velocity component u^1 in the four-velocity

$$u^\mu = (u^0, u^1, 0, 0). \tag{4.33}$$

By the spherical symmetry, we still assume that there is only radial motion of fluid elements. In a rotating neutron star – a pulsar – for example, the situation would be more complicated. The metric should therefore still be spherically symmetric, but $\alpha_0(r) \to \alpha(r,t)$ and $\beta_0(r) \to \beta(r,t)$ are now promoted to time-dependent functions, and therefore so are the pressure $P_0(r) \to P(r,t)$ and energy density $\epsilon_0(r) \to \epsilon(r,t)$. We therefore have the new metric

$$\mathrm{d}s^2 = e^{2\alpha(t,r)}c^2\,\mathrm{d}t^2 - e^{2\beta(t,r)}\,\mathrm{d}r^2 - r^2\left(\mathrm{d}\theta^2 + \sin^2\theta\,\mathrm{d}\phi^2\right). \tag{4.34}$$

To make calculations tractable, we assume that the fluid is only *slightly perturbed* from equilibrium. Following [Cha64], let us use perturbation theory and express the new functions

$$\begin{aligned} \alpha(t,r) &= \alpha_0(r) + \delta\alpha(t,r), & P(t,r) &= P_0(r) + \delta P(t,r), \\ \beta(t,r) &= \beta_0(r) + \delta\beta(t,r), & \epsilon(t,r) &= \epsilon_0(r) + \delta\epsilon(t,r), \end{aligned} \tag{4.35}$$

with small perturbations $\delta\alpha$, $\delta\beta$, δP and $\delta\epsilon$ around their equilibrium values. We will now perform all calculations only to first order in these quantities.

We want to determine how these variations displace fluid elements from the unperturbed star to the perturbed star. Evolution of this quantity should give us insight into how the star responds to perturbations. Let us therefore define $\xi(t,r)$ so that if we attach a tracker to some fixed fluid element in the star, then

$$\begin{aligned} &\text{in the unperturbed star, the fluid element is at } \big(ct, r, \theta, \phi\big), \\ &\text{while in the perturbed star, the fluid element is at } \big(ct, r + \xi(r,t), \theta, \phi\big). \end{aligned} \tag{4.36}$$

Like $\delta\alpha$, $\delta\beta$, δP and $\delta\epsilon$, we treat ξ as a small quantity. We have chosen to name the displacement ξ instead of, say, δr, to avoid some confusion that can arise with the radial *coordinate* r, hoping to increase readability at the cost of some consistency.

What is the relation between the fluid element displacement $\xi(r,t)$ and the fluid's four-velocity? By our definition, $\partial\xi/\partial t = \mathrm{d}r/\mathrm{d}t$, where the right side is to be interpreted as the derivative of the fluid element's radial coordinate taken *along its worldline* – or *streamline* – $x(\tau)$. The chain rule then gives

$$\dot\xi = \frac{\partial\xi}{\partial t} = \frac{\mathrm{d}r}{\mathrm{d}t} = \frac{\mathrm{d}r/\mathrm{d}\tau}{\mathrm{d}t/\mathrm{d}\tau} = c\,\frac{u^1}{u^0}. \tag{4.37}$$

We can now express u^0 and u^1 in terms of $\dot\xi$ by combining this equation with the normalization condition $u_\mu u^\mu = e^{2\alpha}\left(u^0\right)^2 - e^{2\beta}\left(u^1\right)^2 = c^2$. To first order in $\dot\xi$ and $\delta\alpha$, we then find

$$u^0 = \frac{c\,e^{-\alpha}}{\sqrt{1 - \left(e^{\beta-\alpha}\dot\xi/c\right)^2}} \simeq c\,e^{-\alpha_0}\left(1 - \delta\alpha\right), \tag{4.38a}$$

$$u^1 = \frac{\dot\xi\,e^{-\alpha}}{\sqrt{1 - \left(e^{\beta-\alpha}\dot\xi/c\right)^2}} \simeq \dot\xi\,e^{-\alpha_0}. \tag{4.38b}$$

In the perturbed system, the field equations (4.32) also change and must be rederived from the Einstein equations (2.1) in the new metric (4.34) subject to the energy-momentum (4.30) with the non-equilibrium velocity (4.38). As always, the field equations follow from the machinery of equations (A.24), (A.30), (A.32) and (A.33). This time we calculate the field equations only to first order in the small quantities and subtract the equilibrium equations (4.32) to simplify them. This calculation is easy in principle, but definitely harder in practice. We therefore borrow the results obtained by [MTW73, §26.4d], who find that two of the new field equations are

$$\frac{2}{r}e^{-(\beta_0+\alpha_0)}\dot{\delta\beta} = -\frac{8\pi G}{c^4}(\epsilon_0+P_0)e^{\beta_0-\alpha_0}\dot{\xi} \qquad \left(G_{01}=\frac{8\pi G}{c^4}T_{01}\right), \tag{4.39a}$$

$$\frac{2}{r}e^{-2\beta_0}\left(\delta\alpha' - \alpha_0' - \frac{\delta\beta}{r}\right) = \frac{8\pi G}{c^4}\delta P \qquad \left(G_{11}=\frac{8\pi G}{c^4}T_{11}\right). \tag{4.39b}$$

We can erase the two dots in the first equation by performing a time integration, forgetting about the integration constant because we should have $\delta\beta = 0$ when we are back in equilibrium with $\xi = 0$. The simplest form of the field equations is therefore

$$\frac{1}{r}e^{-2\beta_0}\delta\beta = -\frac{4\pi G}{c^4}(\epsilon_0+P_0)\xi, \tag{4.40a}$$

$$\frac{1}{r}e^{-2\beta_0}\left(\delta\alpha' - \alpha_0' - \frac{\delta\beta}{r}\right) = \frac{4\pi G}{c^4}\delta P. \tag{4.40b}$$

The non-equilibrium equations (4.40a) and (4.40b) are analogous to the equilibrium equations (4.32a) and (4.32b). What is the third equation corresponding to equation (4.32c), which we found from conservation of energy-momentum $\nabla_\mu T^{\mu\nu} = 0$ back in section 2.1? In appendix B, we study relativistic fluid mechanics and start from $\nabla_\mu T^{\mu\nu} = 0$ to derive the relativistic generalization of the Euler equation,

$$\frac{1}{c^2}\Big(\epsilon+P\Big)u^\mu\nabla_\mu u^\alpha = \nabla^\alpha P - \frac{1}{c^2}u^\alpha u^\mu\nabla_\nu P \qquad \Big(\nabla_\mu T^{\mu\nu}=0\Big).$$

By inserting the new four-velocity components (4.38) and the perturbation expansions (4.35) into the relativistic Euler equation and performing calculations in the new metric (4.34) to first order, [MTW73, §26.5] finds

$$\Big[\epsilon_0+P_0\Big]e^{2\beta_0-2\alpha_0}\ddot{\xi} = -c^2\Big[\delta P' - (\delta\epsilon+\delta P)\,\alpha_0' - (\epsilon_0+P_0)\,\delta\alpha'\Big]. \tag{4.40c}$$

The non-equilibrium system (4.40) is analogous to equilibrium system (4.32) and consists of *three* equations for the *five* unknowns ξ, δP, $\delta\epsilon$, $\delta\alpha$ and $\delta\beta$. To complete the set, we will make use of two further results of our study of relativistic fluid mechanics in appendix B.

In order to make use of the results of appendix B in our context, we must first learn to distinguish between *Eulerian* and *Lagrangian* changes in fluids. The quantities

$$\delta f(t,r) = f(t,r) - f_0(r) \tag{4.41a}$$

that we defined in equation (4.35) are **Eulerian changes** in the quantities f, measured by an observer who is sitting duck at some *fixed position* $x^\mu = (ct, r, \theta, \phi)$. In contrast, we define the **Lagrangian changes**

$$\Delta f(r,t) = f(r+\xi(r,t),t) - f_0(r) \tag{4.41b}$$

as the changes in the same quantities, but measured by an observer who is *moving with the fluid element* as it flows from r to $r+\xi(r,t)$. One type of change can always be converted into the other through the Taylor expansion

$$\begin{aligned}\Delta f(r,t) &\simeq f(r,t) + \xi(r,t)\,f'(r,t) - f_0(r)\\ &= \delta f(r,t) + \xi(r,t)\,f'(r,t).\end{aligned} \tag{4.42}$$

In words, δ measures changes at a fixed position but of different fluid elements, while Δ measures changes of fixed fluid elements but at different positions. The former stems from our use of perturbation theory, while the latter is a natural tool in fluid mechanics.

In our study of relativistic fluid mechanics in appendix B, we also derive the relativistic generalization of conservation of energy in the flow of a fluid,

$$\frac{\mathrm{d}\epsilon}{\mathrm{d}\tau} = u^\mu \nabla_\mu \epsilon = -(\epsilon + P)\nabla_\mu u^\mu. \tag{4.43}$$

On the left side, note that because the equilibrium energy density $\epsilon_0(r)$ is independent of time, we have $\mathrm{d}\epsilon/\mathrm{d}\tau = \mathrm{d}\Delta\epsilon/\mathrm{d}\tau$. At first sight, it may sound more correct to write $\mathrm{d}\delta\epsilon/\mathrm{d}\tau$ instead of $\mathrm{d}\Delta\epsilon/\mathrm{d}\tau$. However, since the derivative $\mathrm{d}/\mathrm{d}\tau$ is *along the streamline* of the fluid element, it is more accurate to use a Lagrangian change over an Eulerian change to first order in perturbation theory. Since the radial velocity component (4.38b) is already a first-order quantity, only the time component (4.38a) contributes to

$$\frac{\mathrm{d}\epsilon}{\mathrm{d}\tau} = \frac{\mathrm{d}\Delta\epsilon}{\mathrm{d}\tau} = u^\mu \nabla_\mu \Delta\epsilon = u^0 \nabla_0 \Delta\epsilon + u^1 \nabla_1 \Delta\epsilon \simeq u^0 \frac{\partial \Delta\epsilon}{\partial t} = u^0 \dot{\Delta\epsilon} = e^{-\alpha_0} \dot{\Delta\epsilon}. \tag{4.44}$$

The right side of equation (4.43) can be calculated with the identity [Car19, equation 3.34]

$$\nabla_\mu u^\mu = \frac{1}{\sqrt{-|g|}} \partial_\mu \left(\sqrt{-g}\, u^\mu\right) = e^{-\alpha_0} \left[\dot{\delta\beta} + \frac{e^{-\beta_0}}{r^2}\left(e^{\beta_0} r^2 \dot{\xi}\right)'\right]. \tag{4.45}$$

To first order in the small quantities, equation (4.43) then says

$$\dot{\Delta\epsilon} = -(\epsilon_0 + P_0)\left[\dot{\delta\beta} + \frac{e^{-\beta_0}}{r^2}\left(e^{\beta_0} r^2 \dot{\xi}\right)'\right]. \tag{4.46}$$

Again, integrate with respect to time to get rid of the dots and set the integration constant to zero, so $\Delta\epsilon = 0$ when $\delta\beta = 0$ and $\xi = 0$. We then find our fourth main equation

$$\Delta\epsilon = -(\epsilon_0 + P_0)\left[\delta\beta + \frac{e^{-\beta_0}}{r^2}\left(e^{\beta_0} r^2 \xi\right)'\right]. \tag{4.47}$$

We have four equations down, and only one to go. The last result of appendix B that we make use of is adiabaticity of the flow. In appendix B.4, we show that the flow of a perfect fluid is adiabatic with the **adiabatic index**

$$\gamma = \frac{\epsilon + P}{P}\left(\frac{\mathrm{d}P}{\mathrm{d}\epsilon}\right)_s, \tag{4.48}$$

where the derivative should be taken at constant specific entropy s, that is *along the flow*. The above expression can be calculated entirely from the fluid's equation of state $\epsilon = \epsilon(P)$, although in its current form, it is the *unknown* perturbed quantities ϵ and P that enter – not the known equilibrium quantities ϵ_0 and P_0. However, since the derivative should be taken *along the flow*, we can rewrite it as the ratio of *Lagrangian* changes, so the adiabatic index becomes

$$\gamma = \frac{\epsilon + P}{P}\frac{\Delta P}{\Delta\epsilon}, \quad \text{or} \quad \Delta P = \frac{P}{\epsilon + P}\,\gamma\,\Delta\epsilon. \tag{4.49}$$

The latter is a relation between two first-order quantities, and so for the purpose of perturbation theory, *the only relevant part of γ is the known zeroth-order part*

$$\gamma_0 = \frac{\epsilon_0 + P_0}{P_0}\frac{\mathrm{d}P_0}{\mathrm{d}\epsilon_0} = \frac{\epsilon_0 + P_0}{P_0}\frac{\Delta P}{\Delta\epsilon}. \tag{4.50}$$

The two forms in equation (4.50) are very similar, but serve distinct uses. The first version allows us to *calculate* γ_0 from the equation of state $\epsilon_0(P_0)$ in equilibrium, while the latter gives us our fifth and final main equation

$$\Delta P = \frac{P_0}{\epsilon_0 + P_0}\,\gamma_0\,\Delta\epsilon = \frac{\mathrm{d}P_0}{\mathrm{d}\epsilon_0}\,\Delta\epsilon. \tag{4.51}$$

Final system of perturbation equations

We have made quite a big mess by now, but we finally have all the information we need, and it remains only to clean up after ourselves. Together, equations (4.40a), (4.40b), (4.40c), (4.47) and (4.51) constitute the system of five equations

$$\frac{1}{r}e^{-2\beta_0}\delta\beta = -\frac{4\pi G}{c^4}\Big[\epsilon_0 + P_0\Big]\xi, \tag{4.52a}$$

$$\frac{1}{r}e^{-2\beta_0}\Big[\delta\alpha' - \alpha_0' - \frac{\delta\beta}{r}\Big] = \frac{4\pi G}{c^4}\delta P, \tag{4.52b}$$

$$\Big[\epsilon_0 + P_0\Big]e^{2\beta_0 - 2\alpha_0}\ddot{\xi} = -c^2\Big[\delta P' - (\delta\epsilon + \delta P)\,\alpha_0' - (\epsilon_0 + P_0)\,\delta\alpha'\Big], \tag{4.52c}$$

$$\Delta\epsilon = -(\epsilon_0 + P_0)\left[\delta\beta + \frac{e^{-\beta_0}}{r^2}\left(r^2 e^{\beta_0}\xi\right)'\right], \tag{4.52d}$$

$$\Delta P = \frac{P_0}{\epsilon_0 + P_0}\,\gamma_0\,\Delta\epsilon, \tag{4.52e}$$

for the five unknowns ξ, $\delta\alpha$, $\delta\beta$, δP and $\delta\epsilon$. Remember that any occurrence of ΔP and $\Delta\epsilon$ can be traded for δP and $\delta\epsilon$ by the Taylor expansion (4.42). Except for the independent variables t and r, the only other quantities are the equilibrium values α_0, β_0, P_0 and ϵ_0 and derivatives thereof, all of which are obtained by solving the Tolman-Oppenheimer-Volkoff equation (2.38)!

It is the displacement $\xi(t, r)$ we want to calculate, so let us reduce the system (4.52) to a differential equation involving it as the only dependent variable. Along the way, it is convenient to define

$$\zeta(t, r) = r^2 e^{\beta_0(r)}\xi(t, r), \tag{4.53}$$

because the only spatial derivative of ξ in the system (4.52) appears through this combination in equation (4.52d). Never forget that we are doing perturbation theory, so we can still neglect any product of two small quantities, and we can simplify expressions using any equilibrium equation from above. Again, the work before us is easy in principle and hard in practice. In the end, [MTW73, equation 26.19] find that ζ obeys the differential equation

$$W(r)\ddot{\zeta}(r, t) = \big[\Pi(r)\zeta'(r)\big]' + Q(r)\zeta(r), \tag{4.54}$$

where the coefficient functions are

$$\Pi = \frac{1}{r^2}e^{\beta_0 + 3\alpha_0}\gamma_0 P_0, \tag{4.55a}$$

$$Q = -\frac{4}{r^3}e^{\beta_0 + 3\alpha_0}P_0' - \frac{8\pi G}{c^4}\frac{1}{r^2}e^{3\beta_0 + 3\alpha_0}P(\epsilon_0 + P_0) + \frac{e^{\beta_0 + 3\alpha_0}}{r^2(\epsilon_0 + P_0)}\left(P_0'\right)^2, \tag{4.55b}$$

$$W = \frac{1}{c^2 r^2}e^{3\beta_0 + \alpha_0}(\epsilon_0 + P_0). \tag{4.55c}$$

This differential equation governs the displacement $\xi(t, r)$ through definition (4.53).

General Sturm-Liouville solution for the fluid displacement

We can find a solution to the differential equation (4.54) using separation of variables. Let us assume a solution of the form

$$\zeta(t, r) = T(t)\,U(r). \tag{4.56}$$

Substituting the trial solution (4.56) into the differential equation (4.54) and dividing by WUT, we see that

$$\frac{\ddot{T}(t)}{T(t)} = \frac{[\Pi(r)\,U'(r)]' + Q(r)\,U(r)}{W(r)\,U(r)} = -\omega^2 \tag{4.57}$$

must be a constant $-\omega^2$, which can be any complex number at this stage. We then find the temporal solutions $T(t) = e^{\pm i\omega t}$, while the spatial function $U(r)$ and ω^2 must solve

$$\frac{\mathrm{d}}{\mathrm{d}r}\left[\Pi(r)\frac{\mathrm{d}U(r)}{\mathrm{d}r}\right] + \Big[Q(r) + \omega^2 W(r)\Big]U(r) = 0. \tag{4.58}$$

What are the boundary equations for $U(r)$? At the center $r = 0$, spherical symmetry implies that there can be no flow, so the physical boundary condition there is

$$\xi(t, 0) = 0. \tag{4.59}$$

In addition, [Bar+66] argues that $\xi'(t, 0) > 0$ must be finite at the center. From definitions (4.53) and (4.56), we see that these two requirements are satisfied only if

$$U(r) \propto r^3 \qquad \text{near } r = 0. \tag{4.60}$$

At the surface $r = R$, there can be no change in pressure as one follows a fluid element, just like at the interface between water and air down on Earth. Here, the boundary condition is therefore the vanishing of the *Lagrangian* pressure change

$$\Delta P = 0 \qquad \text{at } r = R. \tag{4.61}$$

From equation (4.51), we see that this is equivalent to

$$\Delta P = \frac{\mathrm{d}P_0}{\mathrm{d}\epsilon_0}\Delta\epsilon = \left(\frac{v_0}{c}\right)^2 \Delta\epsilon, \tag{4.62}$$

where we recognize the speed of sound $v_0 = c\sqrt{\mathrm{d}P_0/\mathrm{d}\epsilon_0}$. The surface $r = R$ is defined by $P_0(r) = 0$, and where there is no pressure, there can be no sound, so we should have $v_0 = 0$. This can be confirmed from the equation of state. Close to the surface, the density (4.10a) is small, so x_F is small, and $\mathrm{d}P_0/\mathrm{d}\epsilon_0 \to 0$ as $x_F \to 0$ by equation (4.26). Hence, the first factor $\mathrm{d}P_0/\mathrm{d}\epsilon_0$ of the product (4.62) is zero, and the whole product will vanish *provided that* the second factor $\Delta\epsilon$ is finite. Glancing back at expression (4.52e) for $\Delta\epsilon$, it then follows that the boundary condition (4.61) is *automatically* satisfied *provided that*

$$\Delta\epsilon = -(\epsilon_0 + P_0)\left[\delta\beta + \frac{e^{-\beta_0}}{r^2}\frac{\mathrm{d}U}{\mathrm{d}r}e^{i\omega t}\right] \quad \text{is finite at } r = R. \tag{4.63}$$

By definition, $P_0 = 0$ and $\epsilon_0 = 0$ at the surface. By assumption, $\delta\beta$ is a small and thus finite quantity, and $e^{-\beta_0(R)} = \big(1 - 2GM/Rc^2\big)^{-1/2}$ is also finite at the surface. The translation of the boundary condition (4.61) at the surface into a criterion on $U(r)$ is therefore *only* that

$$\frac{\mathrm{d}U(r)}{\mathrm{d}r} \quad \text{is finite at } r = R. \tag{4.64}$$

This may sound unnecessarily picky at this point, but we will soon see that the finiteness of U plays a very important role when solving the differential equation.

The differential equation (4.58) subject to the boundary conditions (4.60) and (4.64) is a **Sturm-Liouville problem** for *multiple* eigenfunctions $U(r) = U_n(r)$ with corresponding eigenvalues $\omega^2 = \omega_n^2$. It is best viewed as the eigenvalue equation

$$\frac{\mathrm{d}}{\mathrm{d}r}\left[\Pi(r)\frac{\mathrm{d}U_n(r)}{\mathrm{d}r}\right] + Q(r)\,U_n(r) = -\omega_n^2 W(r)U_n(r) \qquad \text{for } 0 \le r \le R, \tag{4.65a}$$

$$\text{subject to} \quad U_n(r) \propto r^3 \qquad \text{near } r = 0, \tag{4.65b}$$

$$\text{and} \quad \frac{\mathrm{d}U_n(r)}{\mathrm{d}r} < \infty \qquad \text{at } r = R. \tag{4.65c}$$

We will always take $U_n(r)$ to be a real solution – for if U_n is a complex solution, then so is ${U_n}^*$ and thus also $\operatorname{Re} U_n = (U_n + {U_n}^*)/2$, by linearity. Let us show that in the form above, the Sturm-Liouville equation is expressed in a self-adjoint form with respect to the inner product

$$\langle f|g\rangle = \int_0^R \mathrm{d}r\, f(r)g(r). \tag{4.66}$$

Denoting the left side of equation (4.65a) by $\hat{L}U_n = \hat{L}(r)U_n(r)$, we can integrate by parts twice to show that for two solutions $U_m(r)$ and $U_n(r)$,

$$\begin{aligned}
\left\langle \hat{L}U_m \,\middle|\, U_n \right\rangle &= \int_0^R \mathrm{d}r\, \left[\left(\Pi U_m'\right)' U_n + Q U_m U_n \right] \\
&= \left[\Pi\, U_m'\, U_n \right]_{r=0}^{r=R} + \int_0^R \mathrm{d}r\, \left[-\Pi U_m' U_n' + Q U_m U_n \right] \\
&= \left[\Pi\, U_m'\, U_n \right]_{r=0}^{r=R} - \left[\Pi\, U_m\, U_n' \right]_{r=0}^{r=R} + \int_0^R \mathrm{d}r\, \left[\left(\Pi U_n'\right)' U_m + Q U_m U_n \right] \\
&= \left[\Pi\, U_m'\, U_n \right]_{r=0}^{r=R} - \left[\Pi\, U_m\, U_n' \right]_{r=0}^{r=R} + \left\langle U_m \,\middle|\, \hat{L}U_n \right\rangle \\
&= \left\langle U_m \,\middle|\, \hat{L}U_n \right\rangle .
\end{aligned} \tag{4.67}$$

The surface terms at $r = 0$ vanish because $U_n(0) = U_m(0) = 0$ there by boundary condition (4.60), while the surface terms at $r = R$ vanish because $P_0(R) = 0$ there, causing $\Pi(R) = 0$ from its definition (4.55a). Using the inner product (4.66) and property (4.67), one can dive into the field of Sturm-Liouville theory, where one will discover the following important properties:

1. The eigenvalues ω_n^2 are real and form an infinite, discrete sequence

$$\omega_0^2 < \omega_1^2 < \omega_2^2 < \cdots \tag{4.68a}$$

   that is bounded from below, but not from above.

2. The eigenfunction $U_n(r)$ corresponding to the eigenvalue ω_n^2 has exactly

$$n \text{ zeros } U_n(r) = 0 \quad \text{for} \quad 0 < r < R. \tag{4.68b}$$

3. Eigenfunctions $U_n(r)$ corresponding to different eigenvalues ω_n^2 are different, and constitute an orthonormal basis for the Hilbert space of real, square integrable functions on $[0, R]$ under the W-weighted inner product

$$\langle U_m|U_n\rangle_W = \langle WU_m|U_n\rangle = \delta_{mn}. \tag{4.68c}$$

The property that the eigenvalues are real is possible for us to prove, and we should, because we will take it as an assumption when we solve the Sturm-Liouville problem numerically. Applying property (4.67) with $U_m = U_n$, we have $\langle \hat{L}U_n|U_n\rangle = \langle \hat{L}U_n|U_n\rangle^*$. Exchanging the left side of $\hat{L}U_n = -\omega_n^2 W U_n$ with the right and noting that $\langle WU_n|U_n\rangle$ is real because W and $|U_n|^2$ are real, this is equivalent to $-\omega_n^2 \langle WU_n|U_n\rangle = \left(-\omega_n^2\right)^* \langle WU_n|U_n\rangle$, so ω_n^2 is real.

We can also understand intuitively why the number of zeros must increase with ω_n^2. By rewriting the Sturm-Liouville equation as $\left(\Pi U_n'\right)' / U_n = -\left(Q + \omega_n^2 W\right)$ and noting that $W > 0$ by its definition (4.55c), it is apparent that as ω_n^2 increases, so does the curvature of U_n towards 0, and hence the number of zeros.

For a greater overview of Sturm-Liouville theory and proofs of the other properties, we recommend [Mor+99]. Perhaps, it can also be comforting to think of a more familiar example of applied Sturm-Liouville theory, namely the time-independent Schrödinger equation $\left[\left(-\hbar^2/2m\right) \mathrm{d}^2/\mathrm{d}x^2 + V(x)\right] \psi_n(x) = E_n \psi_n(x)$. Here, the energies E_n play the role of the eigenvalues ω_n^2 and the wave functions $\psi_n(x)$ are analogous to the eigenfunctions $U_n(r)$. In one dimension, normalizable solutions to the Schrödinger equation possess precisely the same three properties as above.

Necessary and sufficient criterion for stellar stability

At long last, we are now in position to state a rigorous mathematical criterion of stellar stability. Property 3 implies that any physically reasonable displacement $\xi(t, r)$ can be written as a linear combination

$$\xi(t, r) = \frac{e^{-\beta_0(r)}}{r^2} \sum_n c_n U_n(r) e^{i\omega_n t} \tag{4.69}$$

for some constants c_n. The superposition will still satisfy the physical boundary conditions (4.59) and (4.61), provided that each $U_n(r)$ separately satisfies the boundary conditions (4.60) and (4.64). Property 1 ensures all ω_n^2 are real, *but there is no restriction on the sign of* ω_n^2.

- If $\omega_0^2 > 0$, then all vibration modes have real frequencies $\omega_n > 0$. Then all terms in the displacement (4.69) merely oscillate back and forth like $\xi \propto e^{i\omega_n t}$, so the star attempts to return to equilibrium, and it is **stable**.
- If $\omega_0^2 < 0$, then one or more vibration modes have imaginary frequencies $\omega_n = \pm i\,|\omega_n|$. Then some term in the displacement (4.69) takes off exponentially like $\xi \propto e^{\pm|\omega_n|t}$, so the star either implodes or explodes, and it is **unstable**.

A prerequisite for the above criterion is that it is sufficient for *one* mode in the displacement (4.69) to be unstable for the star as a whole to be unstable. To understand this, suppose a star is exposed to some external perturbation $\xi(t, r)$. Whatever the source of this perturbation – be it the touch of a finger, an imperfection in the star's material or the blast from a nearby supernova explosion – it is the initial state $\xi(t, r)$ of this *external* perturbation that determines the contribution c_n from each mode in the sum (4.69), and subsequently the *response* of the star to the perturbation. In the real world, we expect that any external perturbation will activate *all* modes $U_n(r)$ to some extent – for one would need remarkable finger precision to perturb the star in an *exact* superposition of only a finite selection of modes. Given that all modes have even the slightest nonzero contribution $c_n \neq 0$, the presence of *any* exponential term is sufficient for the whole sum to collapse or grow unbounded towards 0 or ∞.

A clever and perhaps slightly nitpicky objection to our criterion, is that the perturbative exponential growth should not be valid once the perturbation has grown outside the domain where it is valid. Either way, we would still say that the star is *locally* unstable in the immediate vicinity of the equilibrium. *If* a star were to reach another state of equilibrium once it has grown outside this domain of validity, then that new state must necessarily also be either stable or unstable. If it is stable, then it is either a neutron star on a different part of the mass-radius curve we have found, or it has evolved to a completely different type of star on a mass-radius curve that we do not know about. If it is unstable, then we would recursively enter the beginning of this argument again. Ultimately, what is physically interesting to us are the (locally) stable configurations, as any unstable star will either explode, collapse, evolve to one of the stable configurations or transition to a completely different type of star.

Numerical solution of the Sturm-Liouville problem with the shooting method

Multiple methods for determining the stability of stars through the criterion above are catalogued by [Bar+66]. The **shooting method** is a particularly fun numerical technique for finding the eigenfunctions $U_n(r)$ and eigenvalues ω_n^2 of the Sturm-Liouville problem (4.65). Let us put it to use, so we can determine the stability of the stars along the curve in figure 4.3.

We describe the shooting method and our implementation of it in detail in appendix G.3. It is also possible to understand the gist of it from figure 4.7, where we show how it establishes the fundamental vibration mode $U_0(r)$ and ω_0^2 for some star by an intelligent form of "trial and error". In figure 4.8, we display the eight lowest modes obtained with the shooting method for one particular star. It is meant to demonstrate the boundary conditions (4.65b) and (4.65c), and that the eigenfunction $U_n(r)$ has exactly n nodes.

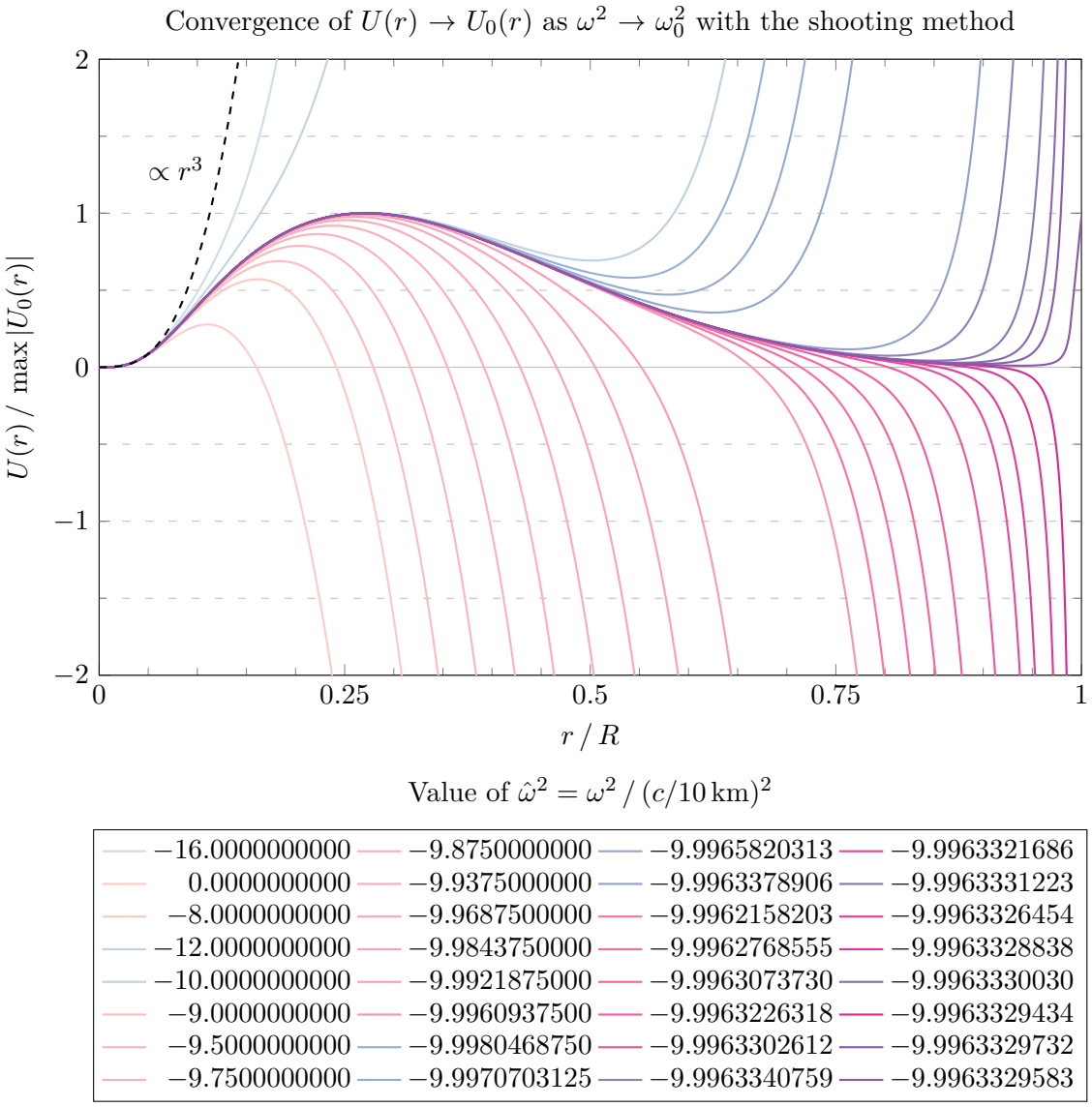

Figure 4.7: The shooting method finds the eigenvalue ω_n^2 and corresponding eigenfunction $U_n(r)$ with $n = 0$ of a Sturm-Liouville problem (4.65). It guesses the eigenvalue ω^2, imposes the boundary condition (4.65b) near $r = 0$, "shoots" across to $r = R$ by integrating the differential equation (4.65a) and checks whether $U(r)$ "hits" boundary condition (4.65c) there. By comparing the number of nodes $n(\omega^2)$ of $U(r)$ to n, the guess is intelligently improved and the process repeated, arriving ever closer to the true eigenvalue ω_n^2. First, the algorithm establishes two bounds $\hat{\omega}_-^2 = -16$ and $\hat{\omega}_+^2 = 0$ whose corresponding solutions have $n(\omega_-^2) \leq n$ and $n(\omega_+^2) > n$ nodes. The exact squared frequency is then guaranteed to lie in $\omega_-^2 < \omega_n^2 < \omega_+^2$. Next, the algorithm finds the number of nodes corresponding to $\hat{\omega}^2 = (\hat{\omega}_-^2 + \hat{\omega}_+^2)/2 = -8$. Here, it is found to have $n(\omega^2) > n$ nodes, so the process is repeated with the tighter upper bound $\hat{\omega}_+^2 = -8$. In the opposite case $n(\omega^2) \leq n$, -8 would rather be a better lower bound $\hat{\omega}_-^2$. The algorithm continues to split the $[\omega_-^2, \omega_+^2]$ in this fashion until the bounds are so close that any value in the interval is satisfactory. In the plot, blue lines correspond to lower bounds ω_-^2, red lines to upper bounds ω_+^2, and increasingly mixed colors to later guesses.

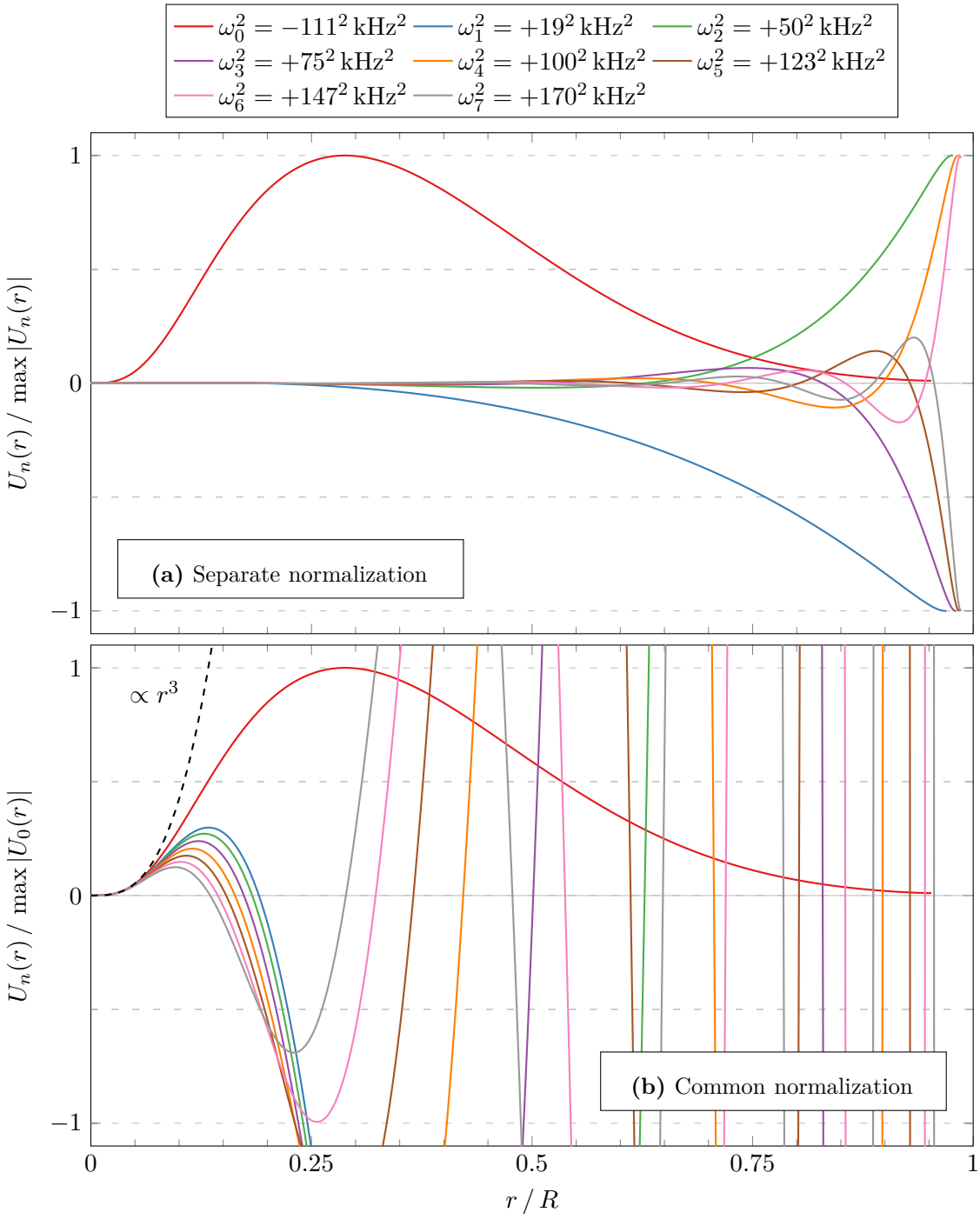

Figure 4.8: Eight lowest vibration modes $U_n(r)$ and squared eigenfrequencies ω_n^2 for an unstable ideal neutron star with central pressure $P = 1.28 \cdot 10^{37}\,\mathrm{Pa}$. In **(a)**, eigenfunctions are normalized to their own maxima, making their shape throughout the star and the boundary condition $U_n(R) < \infty$ clear. In **(b)**, they are instead normalized to a common scale, highlighting the boundary condition $U_n(r \to 0) \propto r^3$ and their number of nodes. We have cut away the divergent parts as $r \to R$ from the final iteration of the shooting method.

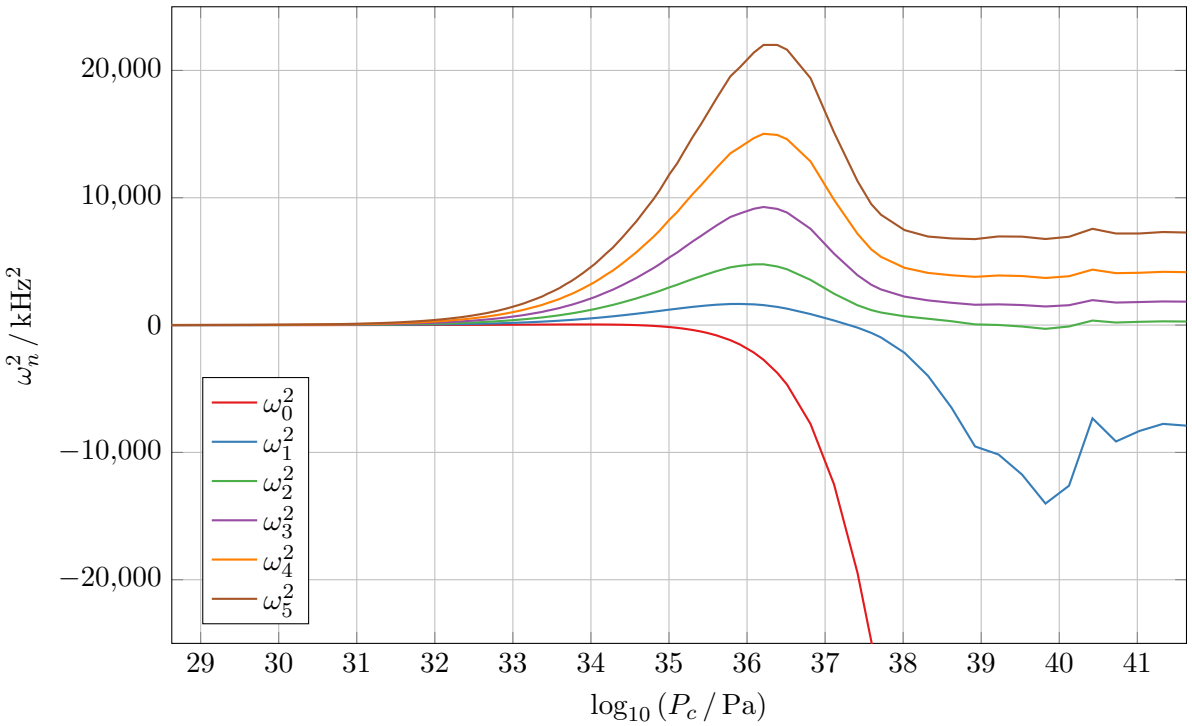

Figure 4.9: Squared eigenfrequencies ω_n^2 of the six lowest vibration modes for all stars on the bottom sequence in figure 4.3 obtained with the shooting method. As the central pressure rises, numerical difficulties of integrating the Sturm-Liouville equation makes the curves shaky.

Finally, we use the shooting method to examine the stability of every star along the curve in figure 4.3. In figure 4.9, we show the six lowest squared eigenvalues ω_n^2 for all stars on the curve. As the central pressure increases, we see that more squared eigenvalues become negative. We then simply count the number of unstable modes with $\omega_n^2 < 0$ for every star, and display this number in figure 4.10. The results are very interesting.

1. Starting from the lowest central pressure, and hence lowest central energy and mass densities, all stars are *stable* up until the maximum mass. The part on this segment with the lowest central energy density is the territory of Newtonian theory, where we should already expect stars to be stable, but that the situation remains so as relativistic effects take over is not necessarily obvious.

2. At the point of maximum mass, stars gain *one unstable mode*, and the number stays constant as we follow the curve down to the point of the spiral with minimal mass. From the necessary stability condition (4.28), we already know that stars on this segment should indeed be unstable.

3. Beyond the spiral's point of minimal mass, stars acquire a *second unstable mode*.

4. In the innermost parts of the spiral after the next local mass maximum, there even seems to be some stars with a *third unstable mode*. The effect is not as crystal clear as it is with the previous segments, however.

Our computations suggest that at every local mass extremum point where $\mathrm{d}M(P_c)/\mathrm{d}P_c = 0$, stars acquire one additional unstable vibration mode, starting with zero unstable modes for the lowest pressures $P_c \to 0$. In fact, [Bar+66] presents a method for determining stability of stars based on this principle! For a sequence of *cold* stars – like ours – in a mass-radius diagram like figure 4.3, they claim that:

- For the lowermost central energy densities $\epsilon(P_c)$, we know from classical theory that stars are *stable*.

- At every local mass extremum $\mathrm{d}M(P_c)/\mathrm{d}P_c = 0$ where the curve bends *counterclockwise* as the central pressure increases, one *stable* mode becomes *unstable*.

- At every local mass extremum $\mathrm{d}M(P_c)/\mathrm{d}P_c = 0$ where the curve bends *clockwise* as the central pressure increases, one *unstable* mode becomes *stable*.

Our curve only includes a spiral turning counterclockwise and seem consistent with the first two rules. A detailed discussion and proofs of these three rules is given by [Tho66]. As we speculated when we derived the necessary stability criterion (4.28), stability does indeed change of character at the mass extrema of the mass-radius curve. Thus, the maximum mass is not only a limit on *massiveness*, but also on *stability*.

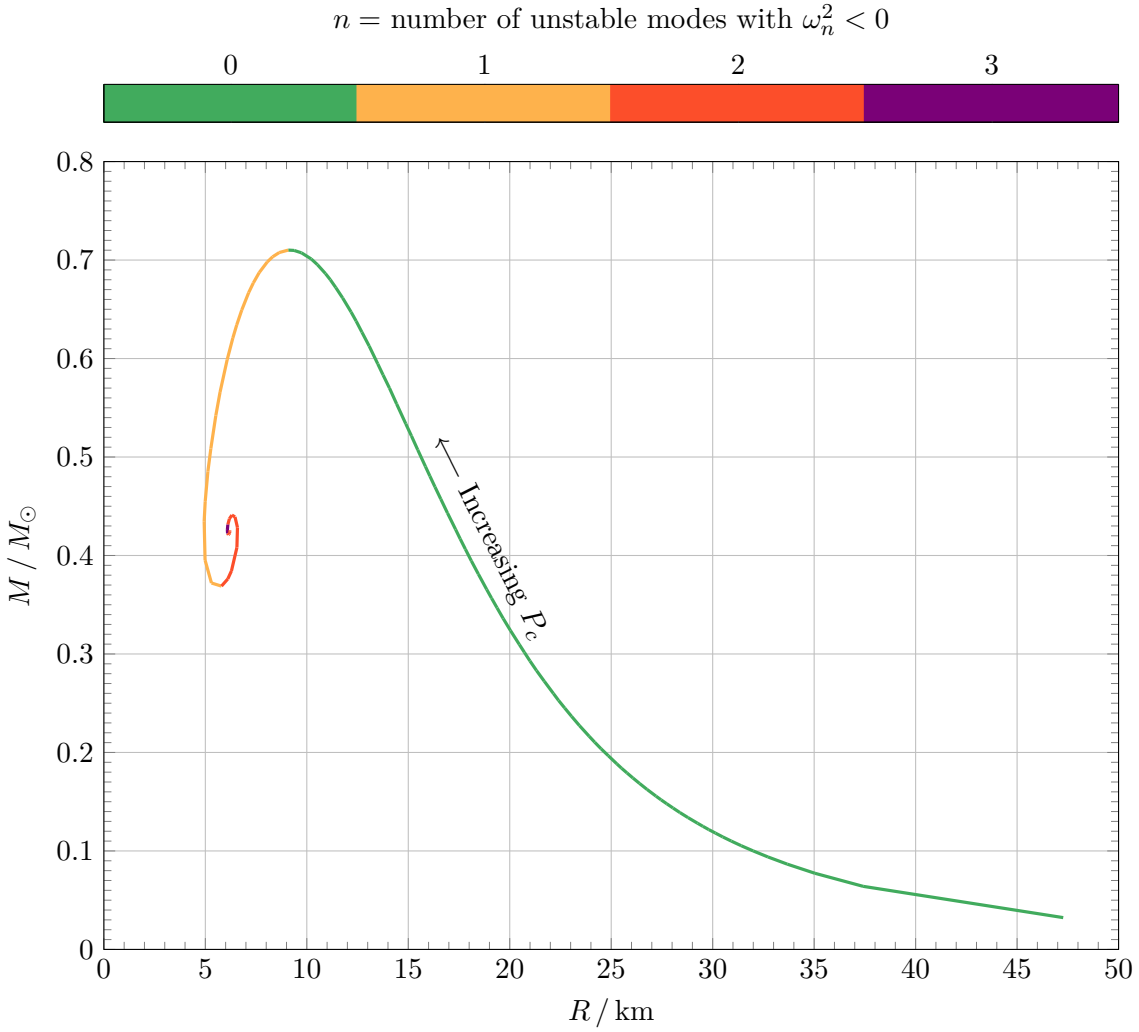

Figure 4.10: Stability analysis of the relativistic neutron star sequence with the general equation of state in figure 4.3. For each star, squared eigenfrequencies ω_n^2 of the Sturm-Liouville problem (4.65) are computed numerically with shooting method, and the number of unstable modes n with $\omega_n^2 < 0$ displayed. For $n \geq 1$ unstable modes, it is *theoretically* possible for a star to vibrate in a greater-than-n-th stable normal mode. However, in *practice* any real-world vibration should activate *all* vibration modes to some extent. Therefore, we say that a star is stable only if it has $n = 0$ unstable modes.

4.4 Summary

The main result of this chapter is the bottom sequence of ideal neutron stars in figure 4.3 that we obtained by numerically integrating the Tolman-Oppenheimer-Volkoff equation (2.38) with the general equation of state (4.17). Unlike the Newtonian curves, general relativity produces an upper mass limit $M \approx 0.71 M_{\odot}$. Finally, we used the shooting method to solve a Sturm-Liouville problem describing stars perturbed from equilibrium, yielding the number of unstable normal pulsation modes for all stars on the sequence. Figure 4.10 showed that the only stable neutron stars are those with central pressure below that corresponding to the maximum mass.

Chapter 5

Conclusions and Outlook

5.1 Conclusions

In this thesis, we have laid a solid foundation for continued study of neutron stars and other kinds of compact stars, starting from first principles of general relativity and quantum field theory. We have derived the Tolman-Oppenheimer-Volkoff equation from general relativity, and shown how the partition function for a quantum field theory with some specified Lagrangian can be expressed as a path integral in the framework of thermal field theory. In particular, we calculated the partition function for a cold Fermi gas composed of free Dirac neutrons and solved the Tolman-Oppenheimer-Volkoff equation with the resulting equation of state. Finally, we applied perturbation theory to general relativity and performed a detailed analysis of stellar stability. Equipped with our numerical "machine" that solves the Tolman-Oppenheimer-Volkoff equation for arbitrary equations of state and even analyzes the stability of the solutions, we are ready to take on new stellar models!

Our main results are the computed mass-radius curve in figure 4.3 and the computed stability analysis in figure 4.10. Together, they show that neutron stars are stable up to the maximum central pressure $P_c \approx 10^{35}\,\text{Pa}$ with a corresponding maximum mass $M = 0.71 M_\odot$ and minimum radius $R = 9.1\,\text{km}$, but become unstable for greater central pressures. In comparison, [Opp+39], building upon the work of [Tol34], studied the same model in 1939 and obtained the same limit $M_{\text{TOV}} = 0.71 M_\odot$ with the slightly different radius $R = 9.5\,\text{km}$ by approximate analytical techniques. Our computational stability analysis is also consistent with a set of qualitative rules established by [Bar+66] based on curvature and extrema in the mass-radius diagram.

However, most observed neutron stars exceed the mass limit we have found. Even slowly rotating pulsars, for whom our results are comparable, [Pot10, section 2.1] are typically observed with masses in the range $1.0 M_\odot < M < 2.2 M_\odot$. [Öze+16, figure 2 and 3] The recent observation of the gravitational wave GW170817 from the merging of two neutron stars even suggests that the true value of the upper mass limit M_{TOV} for neutron stars, named in honor of Tolman, Oppenheimer and Volkoff, is at least $M_{\text{TOV}} \gtrsim 2.3 M_\odot$. [Shi+19]

Observations of massive neutron stars give a lower bound on M_{TOV}, and hence impose constraints on stellar equations of state. Viewed the other way around, equations of state are benchmarked by the maximum masses they produce. Although our model performs poorly in this regard, it can in hindsight still be viewed as an interesting result because it should be close to a *lower* bound on M_{TOV}. Why? Due to the zero-temperature approximation, *all* resistance against gravitational collapse in our model is provided by the degeneracy pressure of neutrons. As the density increases, *repulsive* nuclear effects become more important and provides *additional* pressure and hence greater resistance against collapse in a real neutron star. [Gle00, section 3.9.8] Nevertheless, it is impressive that a model of a neutron star as a simple sphere of non-interacting neutrons give estimates within the right order of magnitude!

5.2 Outlook

From the mismatch between our results and observations, it is clear that we should seek improvements to our model. Instead of going further in the same direction, it is also possible to turn around and pursue a different path by studying other types of stars, for example. Let us take a look at some options available to us at the current crossroads.

More advanced models with additional particles

There is little doubt that the greatest simplification in our free Fermi gas model is that a neutron star consists *only* of neutrons. This is not true, and we should expect different results by accounting for a greater variety of particles with more advanced models. In order to keep the model simple enough for accurate calculations, it is of practical importance to include only the particles that are most relevant. When adding several types of charged particles, one must impose additional constraints of chemical equilibrium and charge neutrality, neither of which we have needed to worry about for the neutral neutron. For example, [Gle00, chapter 4] studies relativistic nuclear field theory and outlines a series of successive improvements to our model:

0. Our original model includes only neutrons n with the free Dirac Lagrangian

$$\mathcal{L}_\psi = \bar{\psi}\left(i\gamma^\mu\partial_\mu - m\right)\psi \qquad \big(\text{with } \hbar = c = 1 \text{ from here on}\big).$$

1. One improvement is to account for inverse beta decay $n \to e^- + p + \bar{\nu}_e$ of neutrons into electrons, protons and (anti)neutrinos. It can be shown that (anti)neutrinos will diffuse out of the star, so a simple extension is then to make the Lagrangian a sum

$$\mathcal{L}_{\psi_n} + \mathcal{L}_{\psi_p} + \mathcal{L}_{\psi_n}$$

of three Dirac Lagrangians of the form (0), with one independent field and mass corresponding to neutrons, protons and electrons. The partition function then separates into a product of three factors, and the energy density and pressure accordingly becomes a sum of three terms of the form that we have found here. Numerical results show that this only gives a *softer* equation of state with a slightly *lower* maximum mass $M_{\text{TOV}} = 0.70 M_\odot$, and although it is a more accurate description, it really takes us in the wrong direction. [Gle00, section 3.9.8]

2. Yet another improvement is made by appending the $\sigma - \omega$ model, also referred to as the Walecka model. It consists of a scalar meson ω and a vector meson ω_μ with

$$\text{free scalar meson Lagrangian} \qquad \mathcal{L}_\sigma = \frac{1}{2}\left[(\partial_\mu\sigma)(\partial^\mu\sigma) - m_\sigma^2\sigma^2\right], \tag{5.1a}$$

$$\text{free vector meson Lagrangian} \qquad \mathcal{L}_\omega = -\frac{1}{4}\omega_{\mu\nu}\omega^{\mu\nu} + \frac{1}{2}m_\omega^2\omega_\mu\omega^\mu, \tag{5.1b}$$

$$\text{scalar meson-nucleon interaction} \qquad \mathcal{L}_{\sigma\psi} = g_\sigma\sigma\bar{\psi}\psi, \tag{5.1c}$$

$$\text{vector meson-nucleon interaction} \qquad \mathcal{L}_{\omega\psi} = g_\omega\omega^\mu\bar{\psi}\gamma_\mu\psi, \tag{5.1d}$$

$$\text{scalar self-interactions} \qquad \mathcal{L}_{\sigma\sigma} = -\frac{1}{3}bm\left(g_\sigma\sigma\right)^3 - \frac{1}{4}c\left(g_\sigma\sigma\right)^4. \tag{5.1e}$$

3. The $\sigma - \omega$ model is extended to the $\sigma - \omega - \rho$ model by including a ρ meson with

$$\text{free Lagrangian} \qquad \mathcal{L}_\rho = -\frac{1}{4}\boldsymbol{\rho}_{\mu\nu}\cdot\boldsymbol{\rho}^{\mu\nu} + \frac{1}{2}m_\rho^2\boldsymbol{\rho}_\mu\cdot\boldsymbol{\rho}^\mu, \tag{5.1f}$$

$$\text{isospin force} \qquad \mathcal{L}_{\rho\psi} = -\frac{1}{2}g_\rho\gamma_\mu\boldsymbol{\rho}^\mu\cdot\boldsymbol{\tau}\psi. \tag{5.1g}$$

4. Finally, the presence of neutrons, protons and electrons is generalized to that of other baryons and leptons. Protons and neutrons are generalized to the full baryon octet

$$(n,\, p) \quad \to \quad \left(n,\, p,\, \Lambda,\, \Sigma^+,\, \Sigma^-,\, \Sigma^0,\, \Xi^-,\, \Xi^0\right),$$

while a muon is added to the lepton range

$$\left(e^-\right) \quad \to \quad \left(e^-,\, \mu^-\right).$$

This extension is straightforward to apply to the Lagrangians above. For each baryon B, a free Dirac Lagrangian $\mathcal{L}_{\psi_B}$ and additional interaction Lagrangians with distinct couplings g_B from above are added. For each lepton L, only a free Dirac Lagrangian $\mathcal{L}_{\psi_L}$ is added – their most important job is only to meet the charge neutrality constraint.

Several fields are treated approximately in a relativistic mean field approach. Throwing all these particles into the mix, one ends up with the quite complicated Lagrangian

$$\mathcal{L} = \sum_B \left(\mathcal{L}_{\psi_B} + \mathcal{L}_{\sigma\psi_B} + \mathcal{L}_{\omega\psi_B} + \mathcal{L}_{\rho\psi_B}\right) + \mathcal{L}_\sigma + \mathcal{L}_\omega + \mathcal{L}_{\sigma\sigma} + \mathcal{L}_\rho + \sum_L \mathcal{L}_{\psi_L}.$$

With all these effects, numerical results give a maximum mass in the range $1.42M_\odot < M_{\text{TOV}} < 2.02M_\odot$ depending on the values chosen for the coupling constants. [Jia+02, table 1] This is much more in line with observations. For a gradual, step-by-step exposure to these successive improvements, see also the theses [Bra17; Pog17].

Rotating neutron stars

Since observed neutron stars are pulsars, another relevant path of study is that of rotating neutron stars. A rotating neutron star breaks spherical symmetry, but retains axial symmetry about its rotation axis. This requires a more advanced treatment of general relativity, where the spherically symmetric metric (2.4) must be replaced with the axially symmetric metric [Gle00, section 6]

$$\mathrm{d}s^2 = e^{2\nu(r,\theta)}c^2\,\mathrm{d}t^2 - e^{2\lambda(r,\theta)}\,\mathrm{d}r^2 - r^2e^{2\mu(r,\theta)}\left\{\mathrm{d}\theta^2 + \sin^2\theta\,[\mathrm{d}\theta - \omega(r,\theta)\,\mathrm{d}t]^2\right\},$$

and the fluid's four-velocity $u^\mu = (u^0, 0, 0, u^3)$ gains an angular component $u^3 = \mathrm{d}\phi/\mathrm{d}\tau$ in equilibrium. The star is then no longer governed by the familiar Tolman-Oppenheimer-Volkoff equation, which were derived under the assumption of no rotation. Study of rotating neutron stars is useful because it is directly comparable to observations of pulsars.

Hybrid stars and quark stars

Neutrons are composed of quarks, and quarks are described by quantum chromodynamics. This theory features *asymptotic freedom*. At extreme density, it causes quarks to become free of interactions, resulting in a new state of matter known as *quark matter*. As illustrated in figure 5.1, neutrons lose their individuality, and it is instead free quarks that make up the fundamental degrees of freedom. It is speculated that the conditions in the cores of neutron stars are so extreme that it allows for the presence of quark matter. If this is true, some or all neutron stars may really be *hybrid stars* with a phase transition between a central quark matter core surrounded by a nuclear matter envelope. *Quark stars* refer to such hypothetical stars composed of pure quark matter only, with no nuclear envelope. [Gle00, chapter 8]

Indeed, there have been observed objects of unknown nature whose mass exceeds the currently accepted value of Tolman-Oppenheimer-Volkoff limit, but falls short of the least massive known black holes. [Wiki21d] These objects may turn out to be neutron stars or black holes after all, but they are also candidates for hybrid stars and quark stars – both of which are hypothetical objects yet to be observed.

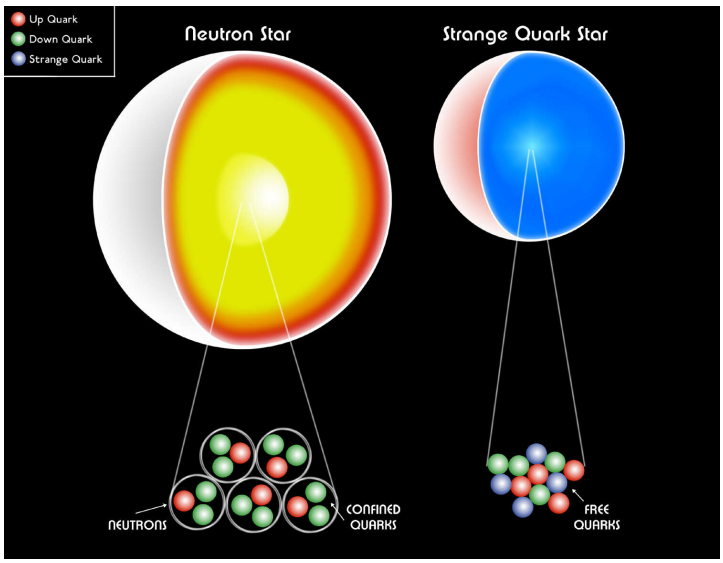

Figure 5.1: In a neutron star, quarks are confined in neutrons. In a hypothetical quark star, the density is so extreme that quarks are deconfined from neutrons. **Credit:** Chandra X-ray Observatory / M. Weiss (https://chandra.harvard.edu/photo/2002/0211/more.html).

Unfortunately, it is notoriously difficult to make practical computations of quantum chromodynamics. Therefore, alternative and more practical models such as the *MIT bag model* have been developed to study quark stars.

It is this path that I aim to study in my master thesis following this specialization project.

Part II

Quark and Hybrid Stars with the Quark-Meson Model

(master thesis)

Chapter 6

Introduction

In chapter 1 and figure 1.1 we reviewed how the currently known life cycle of a star is more or less predetermined by the initial mass M_0 of the embryonic **protostar** that is born from its parent **giant molecular cloud**. Provided that $M_0 \gtrsim 0.08 M_\odot$, the temperature in a protostar reaches the point necessary to ignite fusion of hydrogen, and the star becomes a **main-sequence star** – otherwise it retires early as a **brown dwarf**. First, if $0.08 M_\odot \lesssim M_0 \lesssim 8 M_\odot$, the main-sequence star eventually explodes in a **planetary nebula** and leaves behind a core that collapses under gravity until it stabilizes as a **white dwarf** (figure 6.1a) supported by the electron degeneracy pressure. Second, if $8 M_\odot \lesssim M_0 \lesssim 40 M_\odot$, the main-sequence star instead explodes in a **supernova** and becomes a **neutron star** (figure 6.1b) that is squeezed by gravity beyond the maximum supported pressure of white dwarfs, reaching a new equilibrium mainly supported by the degeneracy pressure of baryons. Third, if $M_0 \gtrsim 40 M_\odot$, the supernova remnant cannot support itself and collapses under gravity to a **black hole** (figure 6.1d).

As proposed by [Iva+67; Iva+69], the density in the cores of the heaviest neutron stars on brink of collapse to black holes could be so high that baryons break up into deconfined quark matter. Neutron stars with such quark cores are called **hybrid (neutron) stars** (figure 6.1b). Moreover, **(strange) quark stars** (figure 6.1c) consisting *only* of (strange) quark matter could exist. While two-flavor quark matter decays to hadronic matter and *cannot* be realized in pure quark stars, the *strange matter hypothesis* of [Bod71; Wit84] suggests that hadronic matter could be only a long-lived *metastable* state and that its true ground state is three-flavor quark matter, which *could* make up stable pure quark stars with extremely sharp surfaces. [Gle00]

As explained in section 1.2, observed neutron stars are identified by radiation emitted from rapidly spinning **pulsa**ting **r**adio (**pulsar** or **PSR**) sources. However, it is hard to conclude whether they are hybrid stars with quark cores, and some could even be mistaken for strange

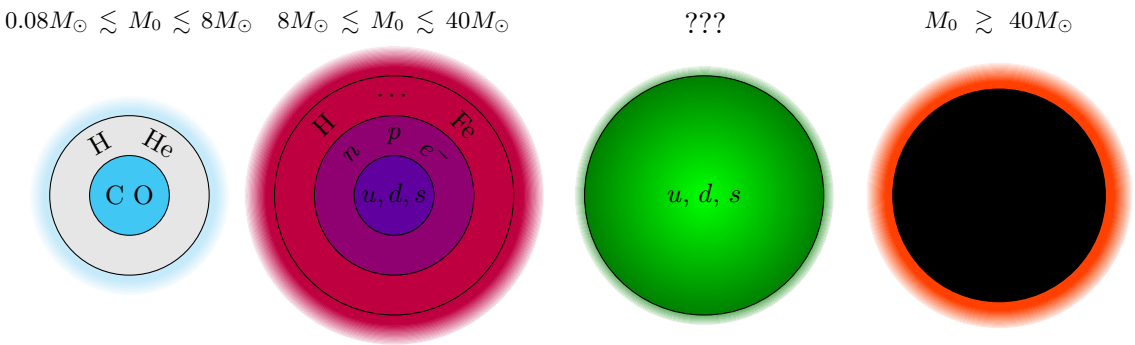

(a) White dwarf **(b)** (Hybrid) neutron star **(c)** (Strange) quark star **(d)** Black hole

Figure 6.1: Final stages of a star's life depending on its birth mass M_0. Quark matter can exist in pure **(strange) quark stars** or in the cores of the heaviest **(hybrid) neutron stars**.

quark stars. The recent observations [Ant+13; Arz+18; Fon+21] of the heavy pulsars PSR J0348+0432, PSR J1614−2230 and PSR J0740+6620 with masses $M = \{2.01 \pm 0.04, 1.91 \pm 0.02, 2.08 \pm 0.07\}\, M_\odot$ suggest that neutron stars could indeed reach sufficient densities for the formation of quark cores and be hybrid stars. Candidates for strange quark stars include RX J185635−3754 [Trü+04], 3C58 [Pra+03], ASASSN−15lh [Dai+16], PSR B0943+10 [Yue+06] and the yet unseen SN1987A remnant [Cha+09; Liu+12]. In particular, if a pulsar with a sub-millisecond rotation period is observed, it would break the theoretical speed limit for neutron star rotation, but could be naturally explained if it is a strange quark star. [Gle00]

Quarks and the mediators of the strong force between them – gluons – are described by the theory of **quantum chromodynamics**. Very roughly speaking, it predicts that quarks are confined in hadrons at low temperatures and densities due to a property called **color confinement**, but deconfined and free of all interactions at high temperatures or densities because of another property called **asymptotic freedom**. In addition to the confinement transition, quantum chromodynamics exhibits a **chiral transition**. Unfortunately, it is very hard to work analytically with the general theory of quantum chromodynamics, so one must turn to approximations and models. We will model quark and hybrid stars using the quark-meson model; elaborating, complementing and building upon earlier work by [Ber13].

This chapter is inspired by part I and references [Gle00] and [Sch14].

6.1 The Tolman-Oppenheimer-Volkoff equation and stellar stability

The structure of a spherically symmetric star is governed by the Tolman-Oppenheimer-Volkoff equation

$$\frac{\mathrm{d}P}{\mathrm{d}r} = -\frac{Gm\epsilon(P)}{r^2c^2}\left(1+\frac{P}{\epsilon(P)}\right)\left(1+\frac{4\pi r^3 P}{mc^2}\right)\left(1-\frac{2Gm}{rc^2}\right)^{-1}, \tag{6.1a}$$

$$\frac{\mathrm{d}m}{\mathrm{d}r} = \frac{4\pi r^2\epsilon(P)}{c^2}. \tag{6.1b}$$

It is a system of two differential equations for the energy density $\epsilon(r)$, pressure $P(r)$ and cumulative mass $m(r)$ as functions of the radius r from the center of the star assumed to be composed of a perfect fluid in hydrostatic equilibrium. We derived it from the Einstein field equations (2.1) and studied it in detail in chapter 2. It therefore includes relativistic corrections, which is particularly important for compact stars with high density.

To solve it, one must know the **equation of state** $\epsilon(P)$ that connects the fluid's pressure and energy density, thereby closing the system of three equations and three unknowns. It can then be integrated from the center $r = 0$ with zero initial mass $m(0) = 0$ and some central pressure $P(0) = P_c$ until reaching the surface $r = R$ defined by a vanishing pressure $P(R) = 0$. This yields the radial profiles $\epsilon(r)$, $P(r)$ and $m(r)$, and the total mass $M = m(R)$ can then be calculated. Thus, one chosen central pressure P_c corresponds to one star with a resulting mass M and radius R. As the central pressure is unknown, it is common to parametrize a sequence of stars with a range of central pressures, solve the Tolman-Oppenheimer-Volkoff equation for each of them and draw a curve connecting their masses and radii in a mass-radius diagram.

In appendix G.2 we wrote a program that integrates the Tolman-Oppenheimer-Volkoff equation for an arbitrary equation of state and generates a smooth mass-radius curve between two given central pressures. We will feed this machine with all equations of state that we encounter.

We drew a mass-radius curve for ideal neutron stars in figure 4.3. As the central pressure increases, the mass also increases up to some maximum, and then decreases as the curve enters a counterclockwise spiral. In section 4.3.2 we studied the stability of stars along this curve in detail, and found that only the stars on the mass-increasing segment up to the maximum are stable and realized in nature. This common property of mass-radius curves is the reason that we will focus our attention on the maximum mass and the part of the curve leading up to it.

6.2 Thermal field theory in compact stars

To derive equations of state for quark matter, we will study quantum field theories whose dynamics is described by some Lagrangian density $\mathcal{L}$. In chapter 3 we showed that the partition function in the grand canonical ensemble corresponding to a Lagrangian including both a fermionic Grassmann field ψ and a bosonic scalar field ϕ is given by the path integral

$$Z(V,T,\mu_i) = \oint_- \mathcal{D}\bar{\psi} \oint_- \mathcal{D}\psi \oint_+ \mathcal{D}\phi \exp\left\{ \int_0^\beta \mathrm{d}\tau \int_V \mathrm{d}^3x \left(\mathcal{L}_E\left[\bar{\psi},\psi,\phi\right] + \sum_i \mu_i j_i^0 \right) \right\}. \tag{6.2}$$

Here it is the Euclidean Lagrangian density $\mathcal{L}_E$ that enters, obtained from the original Lagrangian $\mathcal{L}$ in Minkowski space by substituting an imaginary time variable $t = -i\tau$ into all the fields and then treating τ as the new "time" variable. The volume of the system is V, while its "temporal" extent is the system's inverse temperature $\beta = 1/T$. Sign subscripts are placed on closed path integral signs to remind us of an important property that we showed: bosonic fields must be *periodic* in inverse temperature time, while fermionic fields must be *anti-periodic*. We also saw that we could couple any conserved Noether charge densities j_i^0 arising from symmetries of the Lagrangian to chemical potentials μ_i.

After computing (the logarithm of) the partition function, it is straightforward to find the grand potential (density)

$$\Omega(T,\mu_i) = -\frac{\log Z}{\beta V} \qquad \text{from} \qquad Z = e^{-\beta V \Omega}. \tag{6.3}$$

The volume dependence of the partition function is eliminated by division, turning the extensive quantity $\log Z$ into the intensive quantity Ω. From the grand potential density, we can calculate the relevant thermodynamic quantities: [Kar07, section 4.9]

$$\text{pressure} \quad P(T,\mu_i) = -\Omega, \tag{6.4a}$$

$$\text{number densities} \quad n_i(T,\mu_i) = -\frac{\partial\Omega}{\partial\mu_i}, \tag{6.4b}$$

$$\text{entropy density} \quad s(T,\mu_i) = -\frac{\partial\Omega}{\partial T} = \beta^2 \frac{\partial\Omega}{\partial\beta}, \tag{6.4c}$$

$$\text{energy density} \quad \epsilon(T,\mu_i) = \sum_i \mu_i n_i + \frac{\partial(\beta\Omega)}{\partial\beta} = \sum_i \mu_i n_i - P + Ts. \tag{6.4d}$$

Our goal is to connect a given pressure P to some energy density ϵ, so we can solve the Tolman-Oppenheimer-Volkoff equation (6.1). This is greatly simplified in compact stars, where it is common to employ the **zero-temperature approximation** $T = 0$. We justified this approximation for neutron stars in section 4.1 due to the temperature being far lower than the Fermi temperature T_f. With $T = 0$, only the dependence on the chemical potentials remains in

$$P(\mu_i) = -\Omega \qquad \text{and} \qquad \epsilon(\mu_i) = \sum_i \mu_i n_i - P. \tag{6.5}$$

If there is only one chemical potential $\mu_i = \mu$, the equation of state $\epsilon(P)$ follows by simply eliminating μ from $P(\mu)$ and $\epsilon(\mu)$, either numerically or analytically. This was the case for the neutron star equation of state (4.17). In contrast, the stars we will study now will be composed of up quarks, down quarks, strange quarks and electrons, each associated with a chemical potential. We then need *three* additional relations to constrain the *four* chemical potentials to *one* independent one, which can then be eliminated to give the equation of state.

Chemical equilibrium of weak interaction processes

We can find two relations between the chemical potentials by assuming that the nuclear processes in the star are in chemical equilibrium. According to [Lug16], quark stars may be formed as

hadronic matter in a neutron star decays to quark matter through **Urca processes**[1] like

$$u + e^- \to d + \nu_e \qquad \text{and} \qquad u + e^- \to s + \nu_e. \tag{6.6}$$

Over time, neutrinos are emitted from the star, thereby cooling it. Setting $\mu_{\nu_e} = 0$, chemical equilibrium of these two processes implies the two independent **β-equilibrium** relations

$$\mu_u + \mu_e = \mu_d = \mu_s. \tag{6.7}$$

Electric charge neutrality

The third and last relation between the four chemical potentials is provided by electric charge neutrality. By comparing Newton's law of gravity and Coulomb's law of electrostatics, we can make a simple classical argument for why there can be no *global* net electric charge in stars.

Suppose a test particle with mass m and electric charge q is placed on the surface R of a star with total mass M and electric charge Q. In an idealized situation where the test particle is affected only by the gravitational and electrostatic forces, the total outwards force on it is

$$F_{\text{out}} = -G\frac{Mm}{R^2} + k_e\frac{Qq}{R^2}. \tag{6.8}$$

If the star and test particle have opposite charges, $F_{\text{out}} < 0$ and the star binds the particle and picks up any other particles with opposite charge, seeking to neutralize itself. However, if they have like charges, $F_{\text{out}} > 0$ *provided that*

$$\frac{Q}{M} > \frac{G}{k_e}\frac{m}{q}. \tag{6.9}$$

In other words, particles leave and neutralize the star until the left side has descended to the constant right side. Even for a heavy baryon like a proton with mass $m = 1.67 \cdot 10^{-27}\,\text{kg}$ and charge $q = +e$ in a common compact star of about one solar mass $M \approx M_\odot$, the star emits particles until it has practically zero net electric charge

$$Q \lesssim 10^{-10} e. \tag{6.10}$$

In a star that consists of different particle species with charges q_i, we could implement *global* neutrality by constraining the chemical potentials $\mu_i(r)$ at every radius r such that the charge density

$$\sum_i q_i\, n_i(\mu_i(r)) = \rho(r) \tag{6.11}$$

fits some profile $\rho(r)$ that integrates to a vanishing total charge $Q = \int_0^R \rho(r) 4\pi r^2\,\mathrm{d}r = 0$. This approach would make the equation of state $\epsilon(P)$ at one radius r dependent on its value at *all radii*, and it is not obvious how one should single out one of the infinitely many possible charge density profiles $\rho(r)$. We will avoid this problem altogether by rather assuming that charge neutrality holds *locally* with $\rho(r) = 0$, eliminating the chemical potentials at any radius according to

$$\sum_i q_i\, n_i(\mu_i) = 0 \tag{6.12}$$

As shown in [dCar+14], for example, the stronger assumption of local charge neutrality can in fact modify masses and radii of stars within an order of magnitude of solar masses, but the differences become smaller as one approaches the maximum mass star. Our choice $\rho(r) = 0$ is therefore the simplest choice, but not necessarily the most accurate and physical one.

The three relations (6.7) and (6.12) constrain the four chemical potentials μ_u, μ_d, μ_s and μ_e to a single one that is eliminated from $P(\mu_i)$ and $\epsilon(\mu_i)$ to yield the equation of state $\epsilon(P)$.

[1] **Urca processes** are a general class of processes that emit neutrinos and cool neutron stars. Their discoverers George Gamow and Mário Schenberg met at the famous Casino de Urca in Rio de Janeiro in Brazil, where they "called it the Urca Process, partially to commemorate the casino in which we first met, and partially because the Urca Process results in a rapid disappearance of thermal energy from the interior of a star, similar to the rapid disappearance of money from the pockets of the gamblers on the Casino da Urca." [Gam70]

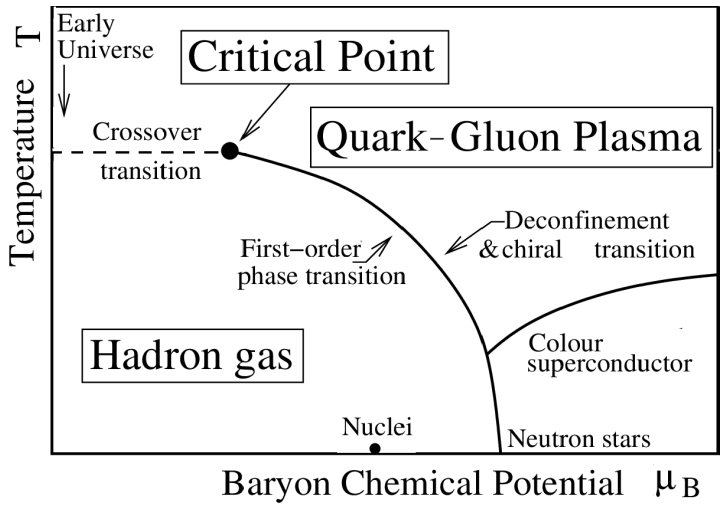

Figure 6.2: The μ_B-T-slice of the phase diagram of quantum chromodynamics, where there is no isospin $\mu_I = 0$ or strangeness $\mu_S = 0$. **Credit:** R. S. Bhalerao (https://commons.wikimedia.org/wiki/File:PhasDiagQGP.png).

6.3 Quantum chromodynamics

The theory of the strong interaction force is called **quantum chromodynamics** (**QCD**). It describes the interaction between quarks mediated by gluons through the Lagrangian density

$$\mathcal{L} = \bar{q}(i\gamma^\mu D_\mu - m)q - \frac{1}{4}G^a_{\mu\nu}G^{\mu\nu}_a \qquad \text{with} \qquad G^a_{\mu\nu} = \partial_\mu A^a_\nu - \partial_\nu A^a_\mu + g f^{abc} A^b_\mu A^c_\nu. \tag{6.13}$$

In general, the quark fields $q = q_{f,c,\alpha}(x)$ are indexed by the $N_f = 6$ flavors $f \in \{u, d, s, c, b, t\}$, the $N_c = 3$ colors $c \in \{r, g, b\}$ and 4 Dirac spinor indices $\alpha \in \{0, 1, 2, 3\}$. We will take a flavor index with the shorthand $f = q_{f,c,\alpha}(x)$. The gamma matrices (3.86) (in the Dirac basis) act in spinor space, the mass matrix $m = \text{diag}(m_u, m_d, m_s, m_c, m_b, m_t)$ in flavor space, and there are suppressed identity matrices in spinor, flavor and color space wherever needed for the Lagrangian to be a scalar. The covariant derivative is $D_\mu = \partial_\mu - igA^a_\mu T^a$ and couples the gluon gauge fields A^a_μ to the quarks with strength g. Finally, T^a are the $N_f^2 - 1$ generators of the symmetry group $SU(N_f)$. They are conventionally normalized to $\text{tr}[T^a T^b] = \delta^{ab}/2$, and their structure constants f^{abc} can be determined from the commutators $[T^a, T^b] = if^{abc}T^c$.

QCD can be viewed as a generalization of quantum electrodynamics (QED), where there is a single electron in place of multiple quarks and photons play the role of gluons. QED is a simpler *Abelian* gauge theory with symmetry group $U(1)$, whereas QCD is a *non-Abelian* gauge theory with symmetry group $SU(N_f)$ and an example of a Yang-Mills theory.

The heaviest **c**harm, **b**ottom and **t**op quarks only appear at extreme energies. In "practical applications" only the $N_f = 3$ lightest **u**p, **d**own and **s**trange flavors are needed. Their $SU(3)$ generators T^a are the *Gell-Mann matrices*, and their main properties are listed in table 6.1.

Table 6.1: Properties of the up, down and strange quarks. The lone mass is the mass of a quark by itself *excluding* any gluons, while the constituent mass refers to the effective mass of a quark in a hadron *including* the surrounding gluon fields. [PDG20; Gle00]

Quark	Electrical charge	Lone mass	Constituent mass
up (u)	$+\frac{2}{3}e$	5 MeV	$\approx$ 300 MeV
down (d)	$-\frac{1}{3}e$	7 MeV	$\approx$ 300 MeV
strange (s)	$-\frac{1}{3}e$	150 MeV	$\approx$ 500 MeV

Phase diagram and calculation methods

The phase diagram of quantum chromodynamics describes the phase of quark matter as a function of temperature T and the common quark, isospin and strangeness chemical potentials

$$\mu = \frac{1}{2}(\mu_u + \mu_d), \qquad \mu_I = \frac{1}{2}(\mu_u - \mu_d), \qquad \mu_S = \frac{1}{2}(\mu_u - \mu_d) - \mu_s. \tag{6.14}$$

Inverting these relations for the individual quark chemical potentials give

$$\mu_u = \mu + \mu_I, \qquad \mu_d = \mu - \mu_I, \qquad \mu_s = \mu - \mu_S. \tag{6.15}$$

By applying the chain rule to the density (6.4b), we can derive that the suitably named common quark chemical potential $\mu = \mu(\mu_u, \mu_d, \mu_s)$ corresponds to the total quark density

$$n = -\frac{\partial \Omega}{\partial \mu} = -\frac{\partial \Omega}{\partial \mu_u}\frac{\partial \mu_u}{\partial \mu} - \frac{\partial \Omega}{\partial \mu_d}\frac{\partial \mu_d}{\partial \mu} - \frac{\partial \Omega}{\partial \mu_s}\frac{\partial \mu_s}{\partial \mu} = n_u + n_d + n_s. \tag{6.16}$$

Some authors rather prefer to talk about the baryon chemical potential $\mu_B = 3\mu$ and the baryon density $n_B = n/3$. Although mapping out the phase diagram is an active area of research, a rough qualitative picture is known, and the μ_B-T-slice with $\mu_I = \mu_S = 0$ is shown in figure 6.2. In compact stars we have already argued that it is a good approximation to set $T = 0$, and we will later see that the chemical potential constraints (6.7) and (6.12) parametrizes a curve for the state of charge-neutral quark matter in β-equilibrium that lies close to the μ-axis. We will shortly discuss the most important qualitative properties of quantum chromodynamics and relate them to this phase diagram.

The general theory of quantum chromodynamics is notorious for being very difficult to work with, and its elegance and practicality stops not long after writing down its Lagrangian (6.13). To explore the phase diagram, one must therefore turn to alternative techniques:

- **Perturbation theory** can be used to study quantum chromodynamics analytically at *high* energy, perhaps contrary to what one might expect. As we will soon discuss in more detail, this is due to an unintuitive property called asymptotic freedom that causes the interaction strength to *decrease* with increasing energy, or decreasing distances.
- **Lattice QCD** consists of discretizing spacetime to a lattice and making numerical field calculations on it. This method has proved very useful for studying quantum chromodynamics under quite general circumstances, but in the regime of high baryon density and low temperature it is plagued by the *sign problem*, referring to the difficulty of calculating integrals of highly oscillatory functions. This is precisely the region of the phase diagram that is relevant for compact stars.
- The **N_c expansion** is a systematic scheme in which one makes expansions in the assumed small parameter $1/N_c$. Although there are only $N_c = 3$ colors in nature, this scheme is indeed widely used to gain insight into quantum chromodynamics and make predictions. [Luc+13] Specifically, sending $N_c \to \infty$ is referred to as the **large N_c-limit**. We will refer to it to justify some of our later calculations.
- **Effective theories and models** can be used to study quantum chromodynamics in some regimes of interest. The most important requirements of such a theory or model is that it includes the correct degrees of freedom (particles) and exhibits the same symmetries and symmetry breaking patterns as the theory it aims to describe in the targeted regime. Due to [Wei21], the philosophy is then to "write down the most general possible theory involving fields for these particles, including all possible interactions consistent with the symmetries". Chiral perturbation theory (χPT) is an example of an effective low-energy *theory* obtained systematically in this way, and the Nambu-Jona-Lasinio (NJL) model and the quark-extended linear sigma model (LSM), also known as the quark-meson (QM) model, are effective *models* in the same regime. This approach is applicable along the μ-axis and hence in compact stars, and is the one we will take.

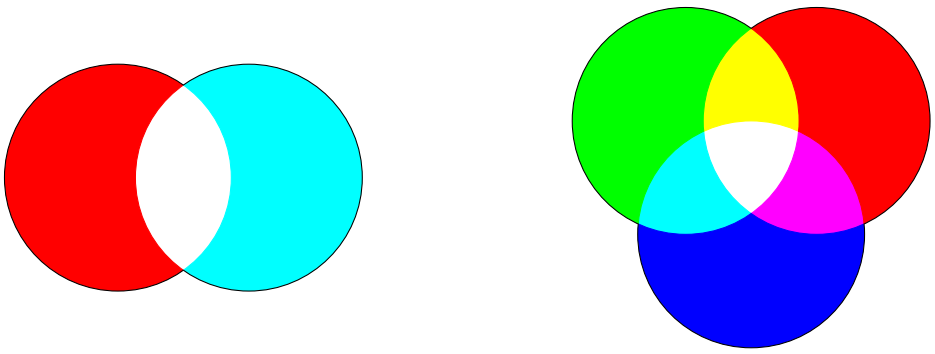

Figure 6.3: A color-charged "white" meson composed of a red quark and an antired antiquark, and a color-charged "white" baryon composed of red, blue and green quarks.

Color confinement and asymptotic freedom

One fundamental feature of quantum chromodynamics is **color confinement**. Quarks can be color-charged **red**, **green** and **blue**, while antiquarks can have the complementary anticolors **antired**, **antigreen** and **antiblue**. At low temperature and density, experiments and lattice simulations show that colored quarks never appear alone, but are always confined in "white" hadrons with no overall color. As the distance between color-charged quarks increases, the strong force between them remains *constant* – the quarks are effectively "glued" together by mediating gluons. For example, a meson consists of one quark of any color and one antiquark of its complementary color, making the meson itself colorless or "white". Similarly, a(n) (anti)baryon consists of one (anti)red, one (anti)green and one (anti)blue quark and is also "white". Such "white" bound states illustrated in figure 6.3 are also referred to as color singlets.

What if you are even stronger than the strong force and attempt to forcibly separate the color*less* quarks in a hadron to color*ful* groups of quarks? Then nature will simply create new quark–antiquark pairs so that the new groups of quarks both become new colorless hadrons, shrug back at you and ask what your next trick is. At low temperatures and densities in the lower left of figure 6.2, quarks are therefore *confined* in nuclei that make up the present world around us.

In the opposite extreme of high temperature or density in figure 6.2, quantum chromodynamics exhibits the property of **asymptotic freedom**. As the energy scale of quark interactions increases, or equivalently its length scale decreases, the interaction strength *decreases* and quarks become *deconfined*. With high temperature, experiments and calculations have shown that the deconfined phase is a **quark-gluon plasma** of free color charges and gluons. It is believed that the universe passed through this phase during the first 20 µs after the Big Bang, after which it transitioned to the present phase of hadronic matter. The situation with low temperature and high density is more uncertain: no human-made laboratory can recreate the extreme densities required for quark matter to form and be studied experimentally. On the theoretical side, calculations are difficult and done with separate models that suggest qualitatively different features. Only in the extreme limit of infinite baryon density where perturbation theory applies, it is known that the deconfined phase turns into a **color-flavor-locked phase** of superconducting color charges. [Fuk+11] Asymptotic freedom was first discovered by [Gro+73; Pol73], who were recognized with the Nobel Prize in 2004.

The *Polyakov loop* is an approximate order parameter of confinement in quantum chromodynamics. We will model quark stars that consist of deconfined quark matter, but there also exist effective models that take the Polyakov loop and confinement into account – see for example [Fol18] for an introduction.

Vector, axial and chiral symmetries and chiral symmetry breaking

The Lagrangian (6.13) has some interesting global symmetries, each of which gives rise to a conserved classical current by Noether's theorem. The simplest symmetry is the $U(1)_V$ **vector symmetry** $q \to e^{i\theta} q$, giving rise to the conserved vector current $j^\mu = \bar{q}\gamma^\mu q$ representing quark number densities. In the grand canonical ensemble, we will later couple one such conserved current to a chemical potential for each quark flavor. In the massless case $m = 0$, the Lagrangian also has the $U(1)_A$ **axial symmetry** $q \to e^{i\theta\gamma^5} q$ with the conserved axial current $j^\mu = \bar{q}\gamma^\mu\gamma^5 q$.

As its proof assumes the action to be extremized, Noether's theorem is inherently *classical*. Unlike the vector current, the axial current is in fact no longer conserved as one takes quantum effects into account, and it is therefore said to be *anomalous*. [Sch14, equation (28.20)]

Using the projection operator $P_\pm = \frac{1}{2}(1 \pm \gamma^5)$, we can introduce the left-handed $(-)$ and right-handed $(+)$ chiral fields $q_\pm = P_\pm q$. One can then show that $q = q_- + q_+$, $\bar{q}_\pm q_\pm = 0$ and $\bar{q}_\pm \gamma^\mu D_\mu q_\mp = 0$, so that the Lagrangian (6.13) can be written

$$\mathcal{L} = \bar{q}_- i\gamma^\mu D_\mu q_- + \bar{q}_+ i\gamma^\mu D_\mu q_+ - \bar{q}_- m q_+ - \bar{q}_+ m q_- - \frac{1}{4} G^a_{\mu\nu} G_a^{\mu\nu}. \tag{6.17}$$

In the massless case $m = 0$, it is invariant under the $SU(N_f)_L \times SU(N_f)_R$ **chiral symmetry** transformation $q_\pm \to U_\pm q_\pm$ where both $U_\pm \in SU(N_f)$. Moreover, it is known that the ground state of quantum chromodynamics admits a nonzero quark condensate [Sch14, chapter 28]

$$\langle \bar{q} q \rangle = \langle \bar{q}_- q_+ \rangle + \langle \bar{q}_+ q_- \rangle, \tag{6.18}$$

but this is generally *not* invariant under the chiral transformation. The fact that the ground state does not carry the same symmetry as its governing Lagrangian is the signature of **spontaneous symmetry breaking**. Only if $U_- = U_+$ is the condensate (6.18) invariant – this is an $SU(N_f)_V$ vector symmetry where both left-handed and right-handed fields are transformed in the same way. This is also a symmetry of the *massive* Lagrangian (6.17) *if* all quark masses are set equal so that the mass matrix m is proportional to the identity matrix. We therefore say that quantum chromodynamics exhibits **chiral symmetry breaking**

$$SU(N_f)_L \times SU(N_f)_R \quad (m = 0) \qquad \longrightarrow \qquad SU(N_f)_V \quad (m \neq 0). \tag{6.19}$$

Goldstone's theorem then predicts that one massless Goldstone boson arises from every broken symmetry generator. Hence, chiral symmetry breaking gives rise to $2 \times (N_f^2 - 1) - (N_f^2 - 1) = N_f^2 - 1$ Goldstone bosons. With $N_f = 2$ and $N_f = 3$ flavors, these are the three pions and the eight pseudoscalar mesons.

In the real world, however, the quarks have different masses and chiral symmetry is only *approximately* broken. We say that the different quark masses cause **explicit symmetry breaking**, in the sense that the Lagrangian changes by a small amount under the chiral transformation. The physical consequence of this is that there are no massless Goldstone bosons, but rather very light pseudo-Goldstone bosons.

The breaking of chiral symmetry leads to the **chiral phase transition** shown in figure 6.2. It is analogous to the phase transition and spontaneous symmetry breaking in a paramagnet described with the Ising model, where an external magnetic field B explicitly breaks the symmetry of spin orientations encapsulated in the order parameter of the magnetization M, just like the quark masses m explicitly breaks chiral symmetry encapsulated in the order parameter of the quark condensate $\langle \bar{q} q \rangle$.

Chapter 7

The MIT Bag Model

To illustrate some of the concepts in chapter 6 and gently familiarize ourselves with additional ones, let us first model quark stars consisting of a free Fermi gas of quarks with the **MIT bag model**. Originally introduced by [Cho+74] at MIT, this simple phenomenological model accounts for confinement of quarks in hadrons by adding a **bag constant** B on top of a normal deconfined ideal Fermi gas. We will see how B can be interpreted as an external pressure that effectively describes an enclosed *bag* that resists stretching and groups quarks, as if they are trapped in a balloon that represents a hadron. However, we will also see that this confinement effect is suppressed in the modeled quark stars, which then consist only of *deconfined* quark matter, as if the balloon has burst and the quarks have escaped. Moreover, we will discuss instability of two-flavor quark matter compared to hadronic matter and the **strange matter hypothesis** of three-flavor quark matter being its absolute ground state, and see how this can be used to determine a **bag window** of acceptable values for B.

This chapter is inspired by references [Gle00] and [Has+78].

7.1 Lagrangian, grand potential and equation of state

We will start by simply ignoring the gluon fields A^a_μ in the quantum chromodynamics Lagrangian (6.13) with the three lightest quark flavors $f = \{u, d, s\}$. In addition, we couple the conserved vector current $j^\mu_f = \bar{q}_f \gamma^\mu q_f$ to a chemical potential μ_f for each flavor, allowing us to tune the densities (6.4b) of quarks. With these modifications, the Lagrangian becomes

$$\mathcal{L} = \bar{q}(i\partial\!\!\!/ + \mu\gamma^0 - m)q = \sum_{c=1}^{N_c}\sum_{f=1}^{N_f} \bar{q}_{f,c}(i\partial\!\!\!/ + \mu_f\gamma^0 - m_f)q_{f,c}. \tag{7.1}$$

In this model the two-flavor and three-flavor analyses are very similar, so we consider them in parallel. Unless N_f is specified explicitly, we perform the general analysis with $N_f = 3$, or $f = \{u, d, s\}$, and simply drop terms or factors indexed by the strange quark s to get expressions for $N_f = 2$, or $f = \{u, d\}$. As we have simply omitted the gluons, we set the quark masses m_f to the lone quark masses in table 6.1.

With the Euclidean version $\mathcal{L}_E$ of the Lagrangian (7.1), the partition function (6.2) reads

$$\begin{aligned} Z &= \oint_- \mathcal{D}\bar{q} \oint_- \mathcal{D}q \exp\left\{ \int_0^\beta \mathrm{d}\tau \int_V \mathrm{d}^3x\, \bar{q}\big(i\partial\!\!\!/ + \mu_f\gamma^0 - m_f\big)q \right\} \\ &= \prod_{c=1}^{N_c}\prod_{f=1}^{N_f} \oint_- \mathcal{D}\bar{q}_{f,c} \oint_- \mathcal{D}q_{f,c} \exp\left\{ \int_0^\beta \mathrm{d}\tau \int_V \mathrm{d}^3x\, \bar{q}_{f,c}\big(i\partial\!\!\!/ + \mu_f\gamma^0 - m_f\big)q_{f,c} \right\} \end{aligned} \tag{7.2}$$

It decouples into a product of $N_c \times N_f$ path integrals (3.93) that we encountered back in chapter 3 and simplified to the form (3.109) for arbitrary temperature. In chapter 4 we neglected the

divergent vacuum contribution from the first term and calculated the path integral explicitly at zero temperature, arriving at the pressure (4.10c) that is related to the grand potential density Ω by the simple sign flip (6.4a). The path integrals differ only by the unique chemical potentials μ_f associated with each quark flavor. Adding a background of free electrons and reinstating $x_f = p_f/m_f = \sqrt{\mu_f^2 - m_f^2}/m_f$ for each particle species, the grand potential becomes

$$\begin{aligned}\Omega(\boldsymbol{\mu}) = &-\sum_{f=1}^{N_f} \frac{N_c}{24\pi^2}\left[\left(2\mu_f^2 - 5m_f^2\right)\mu_f\sqrt{\mu_f^2 - m_f^2} + 3m_f^4 \operatorname{asinh}\left(\sqrt{\frac{\mu_f^2}{m_f^2} - 1}\right)\right] \\ &- \frac{1}{24\pi^2}\left[\left(2\mu_e^2 - 5m_e^2\right)\mu_e\sqrt{\mu_e^2 - m_e^2} + 3m_e^4 \operatorname{asinh}\left(\sqrt{\frac{\mu_e^2}{m_e^2} - 1}\right)\right].\end{aligned} \tag{7.3}$$

This expression is only valid when $\mu_i \geq m_i$, as we assumed so when we calculated the pressure integral (4.10c) with the step function $\Theta(\mu_i - \sqrt{m_i^2 - p^2})$. In the opposite case $\mu_i < m_i$, this step function would be turned off for all p and make the integral vanish. Equivalently, we can consider the grand potential above valid for *all* μ_i if we implicitly take its *real part*. Adopting this convention, the corresponding quark and electron densities (6.4b) are

$$n_f = -\frac{\partial\Omega}{\partial\mu_f} = \frac{N_c}{3\pi^2}\left(\mu_f^2 - m_f^2\right)^{\frac{3}{2}} \qquad \text{and} \qquad n_e = -\frac{\partial\Omega}{\partial\mu_e} = \frac{1}{3\pi^2}\left(\mu_e^2 - m_e^2\right)^{\frac{3}{2}}, \tag{7.4}$$

and the pressure (6.4a) and energy density (6.4d) easily follow with $T = 0$.

We now see explicitly that Ω and hence P and ϵ are functions of the four chemical potentials μ_u, μ_d, μ_s and μ_e. As explained in section 6.2, we reduce them to a single independent chemical potential with the three constraints (6.7) and (6.12), and take it to be the quark chemical potential μ defined in equation (6.14). Inserting $N_c = 3$, the charges in table 6.1 and the densities (7.4), the system that constrains the chemical potentials is

$$0 = 2\left(\mu_u^2 - m_u^2\right)^{\frac{3}{2}} - \left(\mu_d^2 - m_d^2\right)^{\frac{3}{2}} - \left(\mu_s^2 - m_s^2\right)^{\frac{3}{2}} - \left(\mu_e^2 - m_e^2\right)^{\frac{3}{2}}, \tag{7.5a}$$

$$\mu_d = \mu_u + \mu_e, \tag{7.5b}$$

$$\mu_s = \mu_d. \tag{7.5c}$$

It is a system of three equations for four unknowns. To solve it for a given value of $\mu = (\mu_u + \mu_d)/2$, we vary μ_e with a root-finding algorithm until we have found the solution. Repeating this procedure for a range of μ, we parametrize the pressure $P(\mu)$ and energy density $\epsilon(\mu)$ as functions of μ. We then invert $P(\mu)$ to $\mu(P)$ and insert it into $\epsilon(\mu)$ to obtain the equation of state $\epsilon(P)$.

Ultra-relativistic limit

Before tackling the general solution numerically, it is instructive and in fact not far from accurate to solve this problem analytically in the ultra-relativistic limit $m_i = 0$. The grand potential (7.3) then reduces to

$$\Omega(\boldsymbol{\mu}) = -\frac{N_c\mu_u^4}{12\pi^2} - \frac{N_c\mu_d^4}{12\pi^2} - \frac{N_c\mu_s^4}{12\pi^2} - \frac{\mu_e^4}{12\pi^2}, \tag{7.6}$$

while the densities (7.4) become

$$n_f = \frac{N_c\mu_f^3}{3\pi^2} \qquad \text{and} \qquad n_e = \frac{\mu_e^3}{3\pi^2}. \tag{7.7}$$

Regardless of the relations between the chemical potentials, the equation of state is then simply

$$\epsilon \underset{\text{by (6.4d)}}{=} -P + \sum_i \mu_i n_i \underset{\text{by (7.7)}}{=} -P + \frac{1}{3\pi^2}\left(N_c\mu_u^4 + N_c\mu_d^4 + N_c\mu_s^4 + \mu_e^4\right) \underset{\text{by (7.6)}}{=} -P - 4\Omega \underset{\text{by (6.4a)}}{=} -P + 4P = 3P\,! \tag{7.8}$$

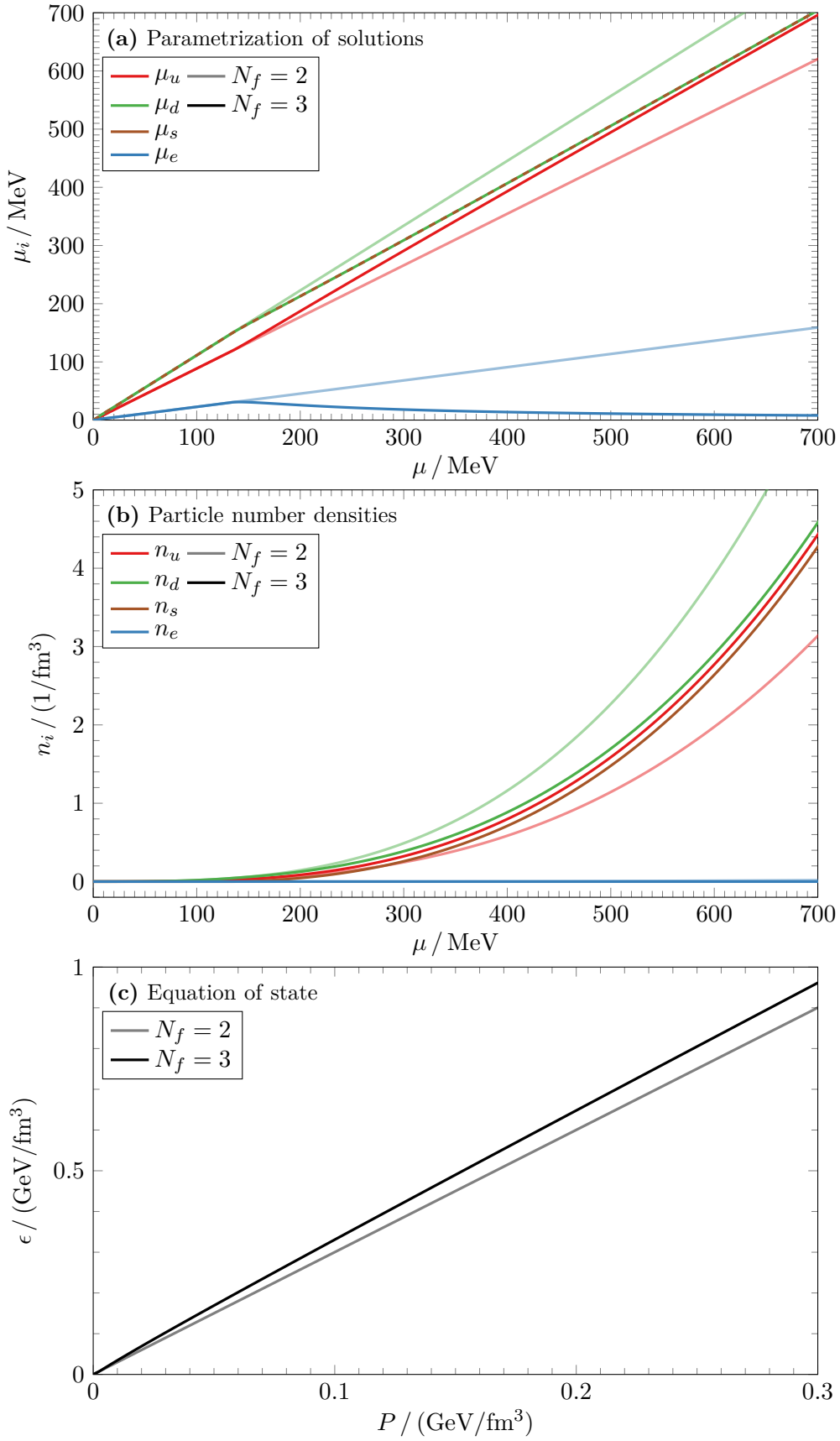

Figure 7.1: Properties of charge-neutral two-flavor (weak lines) and three-flavor (strong lines) quark matter in β-equilibrium in the MIT bag model. Upper panel **(a)** shows the relations between chemical potentials due to the constraints (7.5), middle panel **(b)** the particle number densities (7.4) and lower panel **(c)** the equation of state $\epsilon(P)$.

Although they are not needed for the equation of state, we can also find approximate analytical relations between the chemical potentials in the ultra-relativistic limit. They will be useful to compare with the general numerical solution, for which the equation of state *does* depend on these relations. To do so, we assume that the electron density in the charge neutrality condition (7.5a) can be neglected. This assumption is subject to a self-consistency check down the line.

In the two-flavor case, this simplifies the charge neutrality condition (7.5a) to $\mu_d^3 = 2\mu_u^3$, or $n_d = 2n_u$, with the solution $\mu_d = 2^{1/3}\mu_u$. According to the β-equilibrium condition (7.5b) the chemical potential of the electrons is then $\mu_e = \mu_d - \mu_u \approx (2^{1/3} - 1)\mu_u$, and the corresponding electron density (7.7) is $n_e = (2^{1/3} - 1)^3 n_u/N_c = 0.006\, n_u \ll n_u < n_d$, so neglecting it is a self-consistent approximation! Expressing the chemical potentials in terms of the quark chemical potential (6.14), we then have

$$\mu_u = \underbrace{\frac{2}{1+2^{1/3}}}_{0.88}\mu, \quad \mu_d = \underbrace{\frac{2}{1+2^{-1/3}}}_{1.12}\mu \quad \text{and} \quad \mu_e = \underbrace{\frac{2\left(2^{1/3}-2^{-1/3}\right)}{2+2^{1/3}+2^{-1/3}}}_{0.23}\mu \qquad (N_f = 2). \tag{7.9a}$$

With three flavors, the charge neutrality condition (7.5a) becomes $2n_u - n_d - n_s = 0$ after neglecting electrons. It has the very simple solution $n_u = n_d = n_s$ with

$$\mu_u = \mu_d = \mu_s = \mu \quad \text{and} \quad \mu_e = 0 \qquad (N_f = 3). \tag{7.9b}$$

As $\mu_e = \mu_d - \mu_u = 0$, neglecting the electron contribution is exact in this case.

General solution

We now calculate the general solution with massive quarks using the program in appendix G.5, solving equation (7.5) numerically for different quark chemical potentials μ. We obtain the chemical potentials, densities and equation of state shown in figure 7.1. Note that the electron density is very small, but nonzero. Indeed, the results are very close to the straight-line ultra-relativistic relations (7.7)-(7.9b) as $\mu_i \gg m_i$, thereby supporting our numerical calculations.

7.2 Bag constant and the strange matter hypothesis

For chemical potentials $\mu_i < m_i$ the (real part of the) densities (7.4) vanish, so we refer to this region of the phase diagram as the **vacuum phase**. So far we have modeled the quarks as a free Fermi gas of *deconfined* quarks. We know, however, that quarks are *confined* in hadrons at low energies. Let us see how the MIT bag model attempts to incorporate confinement with the so-called bag constant.

The pressure $P = -\Omega$ due to the grand potential density (7.3) is normalized to $P = 0$ in the vacuum. Suppose that we shift $\Omega \to \Omega + B$ by a **vacuum constant** B. This in turn shifts the pressure (6.4a) and energy density (6.4d) to

$$P(\mu) \to P(\mu) - B \qquad \text{and} \qquad \epsilon(\mu) \to \epsilon(\mu) + B, \tag{7.10}$$

effectively moving the equation of state in figure 7.1c north-west in P-ϵ-space. The vacuum constant is hence a phenomenological parameter that adjusts the normalization of the grand potential in vacuum, and hence the zero-point energy and pressure, and the equation of state.

As illustrated in figure 7.2, a positive vacuum constant B creates a negative pressure $P = -B$ in the vacuum. This is commonly interpreted as an external pressure or mechanism that *confines* quarks to *bags* or *balloons* that resemble hadrons, so B is often called the **bag constant**. With rising density, the quarks in the bag exert a counteracting outwards pressure that stabilizes the hadron at $P = 0$, like a balloon that has reached equilibrium with its surroundings. With large positive pressures $P \to \infty$, the balloon inflates and merges with nearby balloons, effectively bursting as the quarks escape to take part in a phase of deconfined quark matter.

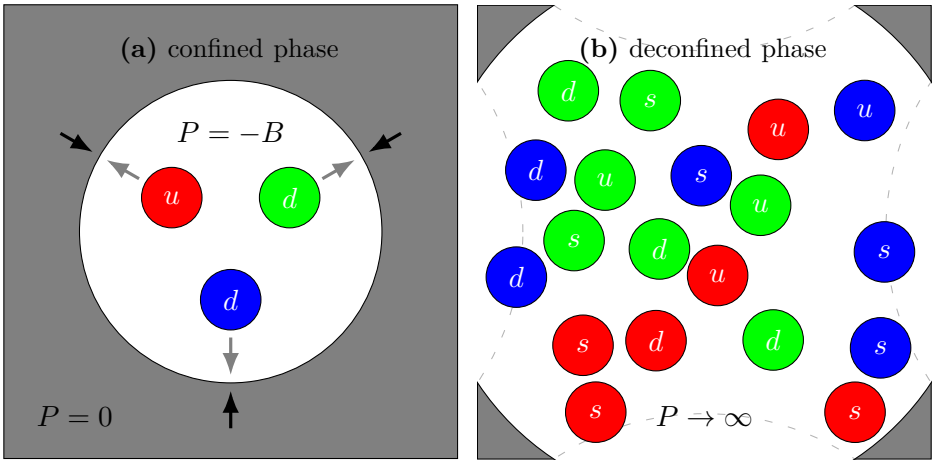

Figure 7.2: The bag constant B allows for negative pressure and is often interpreted as a confinement mechanism. A negative internal pressure is equivalent to a positive external pressure that effectively traps quarks in a hadron-resembling *bag* or *balloon* in the confined phase **(a)**. At large positive pressure, the balloon inflates and merges with adjacent balloons, effectively bursting as the quarks escape to take part in the deconfined quark matter phase **(b)**.

As another analogy, imagine a swimming pool full of water representing the gray quark-forbidden medium. It would cost an amount BV of energy to expel water from a volume V and create a confined vacuum in the pool, and a plastic bag enclosing this volume would have to generate some internal pressure to survive against the pressure from the surrounding water.

Despite the common interpretation of B as a confinement mechanism, it is very important to note that the quark stars we will model will be integrated from a positive central pressure to a vanishing pressure at the surface, and therefore have *non-negative pressure* everywhere and more or less only contain *deconfined* quark matter. As explained in section 6.1, the integration of the Tolman-Oppenheimer-Volkoff equation stops when it reaches the surface defined by $P = 0$, so the confinement-interpretable part of the equation of state with negative pressure that arises due to the shift (7.10) is *unused* in a quark star! We should therefore not take the confinement interpretation too literally in our case. Nevertheless, the bag shift (7.10) affects the equation of state even in the deconfined regime, so it is perhaps better to think of B only as a phenomenological parameter that we can vary to adjust the normalization of the grand potential and – as we will see shortly – a parameter that determines the stability of quark matter compared to hadronic matter.

What values can the bag constant take? Let us perform a heuristic calculation where we picture quarks to be confined in a spherical bag of radius R, as depicted in figure 7.2a. The vacuum energy associated with the mere existence of this bag is $E_V = 4\pi R^3 B/3$. By Heisenberg's uncertainty principle $\Delta p \Delta x \geq \hbar/2$, a quark confined to a region extending $\Delta x = 2R$ in one dimension with *mean* momentum $\langle p \rangle = 0$ has momentum $p \lesssim \hbar/4R \propto 1/R$. In the ultra-relativistic regime where we can neglect the particles' masses, the kinetic energy inside the bag is therefore $E_K = pc = C/R$ for some constant C. As a function of R, the total energy $E = E_V + E_K = 4\pi R^3 B/3 + C/R$ has a minimum at $R = (C/4\pi B)^{1/4}$ for which the bag is stable. Eliminating C, the energy of this stable configuration is $E = 16\pi R^3 B/3$. Assuming a neutron with total energy $E = mc^2 = 900\,\mathrm{MeV}$ and radius $R \approx 1\,\mathrm{fm} = 1/197\,\mathrm{MeV}$ in natural units, the "optimal" bag constant is

$$B = \frac{3E}{16\pi R^3} = (142.4\,\mathrm{MeV})^4. \tag{7.11}$$

Another approach lets us determine a *range* of values for the bag constant. In the early days with high density and temperature, the universe likely passed through a phase of deconfined quark-gluon plasma. [Gle00] Today, two-flavor quark matter is accreting in nuclei through fusion towards iron-56 in stars, which seemingly represent the ground state of nuclear matter. However, the **strange matter hypothesis** of [Bod71; Wit84] conjectures that this state is only *metastable* and could decay further to the hypothesized absolute ground state of three-flavor quark matter consisting of up, down and strange quarks. If true, the universe could turn into a very *strange* place some day.

Iron-56 is the most stable nuclide with an energy of $E/N_B = \epsilon/n_B = 930\,\text{MeV}$ per baryon. [Gle00] If we denote the energy densities of two-flavor and three-flavor quark matter by ϵ_2 and ϵ_3, then the instability of two-flavor quark matter and hypothesized stability of three-flavor quark matter at zero pressure $P = 0$, which characterizes equilibrium of a system, imply the double inequality

$$\frac{\epsilon_3(P=0)}{n_B} \leq 930\,\text{MeV} \leq \frac{\epsilon_2(P=0)}{n_B}. \tag{7.12}$$

We will now see that this yields a range of bag constants that we call a **bag window**.

Ultra-relativistic bag window

Let us first examine how the ultra-relativistic equation of state is affected by the addition of a bag constant, and how inequality (7.12) generates a corresponding bag window. The bag shift (7.10) changes the equation of state (7.8) to $\epsilon = 3P + 4B$. Neglecting electrons again, the baryon density is always $n_B = (n_u + n_d + n_s)/3 = n_u = \mu_u^3/\pi^2$, since $n_d = 2n_u$ and $n_s = 0$ in the two-flavor case and $n_u = n_d = n_s$ in the three-flavor case. With two flavors we also had $\mu_d = 2^{1/3}\mu_u$, so the grand potential density (7.6) yields the pressure $P = -\Omega - B = (1 + 2^{4/3})\mu_u^4/4\pi^2 - B$ after "bagging". With three flavors we had $\mu_s = \mu_d = \mu_u$ and instead find $P = 3\mu_u^4/4\pi^2 - B$. Setting $P = 0$, eliminating μ_u in favor of B and inserting these relations into inequality (7.12), it becomes exactly solvable and gives the bag window

$$144.4\,\text{MeV} = \frac{930\,\text{MeV}}{\left[4\pi^2 \cdot \left(1 + 2^{4/3}\right)^3\right]^{\frac{1}{4}}} \leq B^{\frac{1}{4}} \leq \frac{930\,\text{MeV}}{\left[4\pi^2 \cdot 3^3\right]^{\frac{1}{4}}} = 162.8\,\text{MeV}. \tag{7.13}$$

General bag window

Returning to the general case with nonzero masses, the program in appendix G.5 solves inequality (7.12) numerically. It calculates the baryon density $n_B = (n_u + n_d + n_s)/3$ and performs the shift (7.10) of the pressure and energy density for different bag constants B until it finds the one for which the inequality is barely satisfied. For the two-flavor and three-flavor equations of state in figure 7.1c, the program reports the bag window

$$144.3\,\text{MeV} \leq B^{\frac{1}{4}} \leq 154.9\,\text{MeV}. \tag{7.14}$$

Note that whereas inequality (7.12) has three and two flavors on its far left and right, the lower and upper bounds in all bag windows come from two and three flavors, respectively. This reverse-ordering of flavors can be understood by noting that $\epsilon \sim B$ and $n_B \sim \mu_u^3 \sim B^{3/4}$, so $\epsilon/n_B \sim B^{1/4}$ on each side of the double inequality (7.12).

Also note that the lower bounds in the analytical and numerical bag windows (7.13) and (7.14) agree not only with each other, but also with the "optimal" bag constant (7.11). In contrast, the upper bounds disagree due to the massless approximation being worse with the addition of the heavy strange quark.

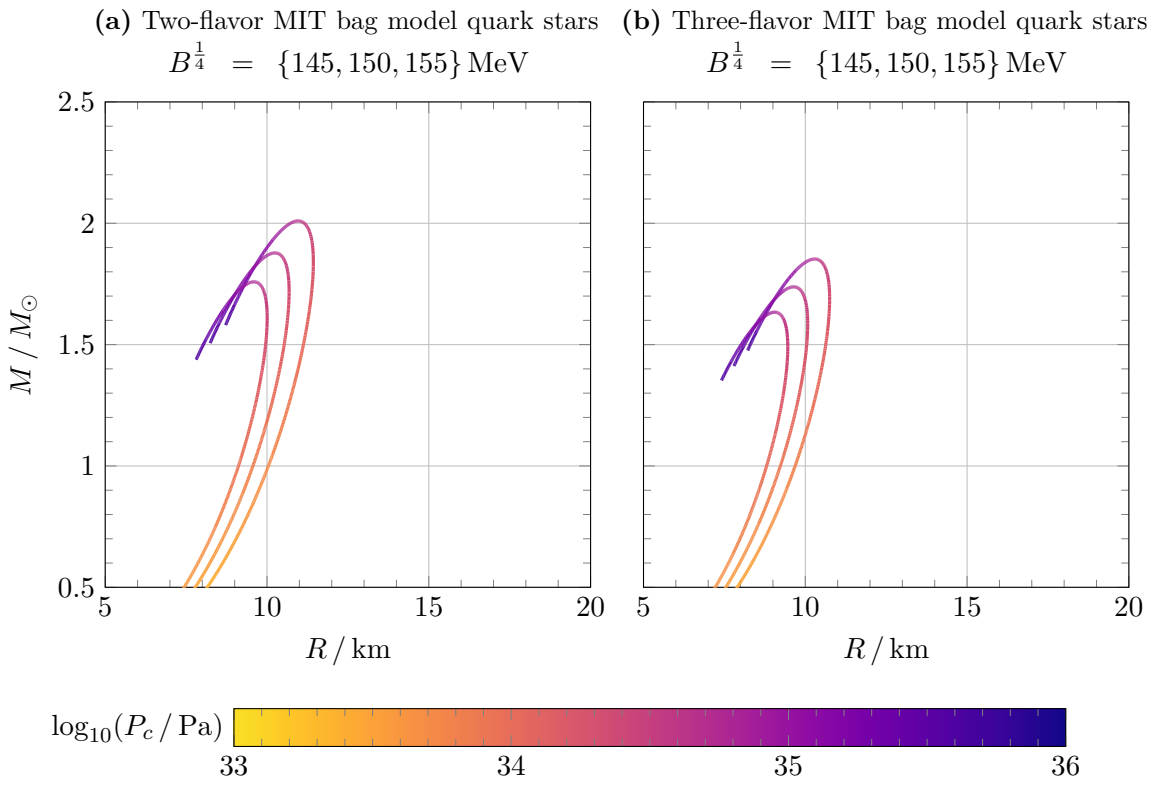

Figure 7.3: Mass-radius solutions of the Tolman-Oppenheimer-Volkoff equation (6.1) parametrized by the central pressure P_c, using the two-flavor and three-flavor MIT bag model equations of state from figure 7.1c modified by the bag shift (7.10) with bag constants B covering the bag window (7.14). Lower bag constants correspond to greater maximum masses.

7.3 Quark star solutions

Different equations of state are now finally available to us by making the shift (7.10) of the "unbagged" equation of state in figure 7.1c with multiple bag constants inside the established bag window (7.14). From the numerical implementation in appendix G.5, we then integrate the Tolman-Oppenheimer-Volkoff equation numerically by calling upon the program in appendix G.2 as described in section 6.1, obtaining the quark stars in figure 7.3:

- As mentioned in section 6.1 and studied in section 4.3, stars with central pressure exceeding that of the maximum mass star are unstable against radial perturbations, so we cut off the curve not long after the mass peak.
- The smaller the bag constant, the larger and more massive the star. The bag shift (7.10) lifts the equation of state in the P-ϵ-diagram up and to the left so that a given (energy) density corresponds to a lower pressure. This makes the star easier to compress, so we say that the equation of state is *softened*. Conversely, an equation of state where a given (energy) density corresponds to a higher pressure describes material that is harder to compress and is said to be *stiffer*. In other words, lower bag constants yield stiffer equations of state, which in turn generate more massive stars, so we pay most attention to the lowest B here and onward.

  The increase in size due to the stiffening is easy to understand: integrating the Tolman-Oppenheimer-Volkoff equation (6.1) from a fixed central pressure P_c, a stiffer equation of state yields a strictly smaller mass gradient $\mathrm{d}m/\mathrm{d}r$ and pressure gradient magnitude $|\mathrm{d}P/\mathrm{d}r|$, so the surface $P(R) = 0$ is reached at a greater radius. The increase in mass can then only be explained by the effects of the greater radius outweighing those of the smaller mass gradient.

- Notice the qualitatively similar shapes of mass-radius curves corresponding to different bag constants. As mentioned in [Gle00, equation 8.29], it is in fact possible to show that with the bagged ultra-relativistic equation of state $\epsilon = 3P + 4B$, the Tolman-Oppenheimer-Volkoff equation (6.1) admits scaling solutions where the masses $M(B)$ and radii $R(B)$ corresponding to two different bag constants $B = \{B_1, B_2\}$ are related by $M(B_2) = \sqrt{B_1/B_2}\, M(B_1)$ and $R(B_2) = \sqrt{B_1/B_2}\, R(B_1)$. These relations hold only approximately in our massive case.
- Using bag constants inside the bag window (7.14), the MIT bag model realizes quark stars with maximum masses $1.7\, M_\odot \leq M \leq 2.0\, M_\odot$ with $N_f = 2$ flavors and $1.6\, M_\odot \leq M \leq 1.9\, M_\odot$ with $N_f = 3$ flavors, in both cases with corresponding radii $9\,\text{km} \leq R \leq 11\,\text{km}$. The two-flavor stars are more massive due to their stiffer equation of state in figure 7.1c.

7.4 Summary

In this chapter we have reviewed the simplest and most well-known model of quark stars as a free Fermi gas of deconfined quarks featuring a phenomenological bag constant B. We described a method for determining a window of acceptable bag constants by assuming that at zero pressure, two-flavor quark matter is unstable and can decay to hadronic matter, which in turn can decay to three-flavor quark matter if the strange matter hypothesis of it being the ground state of nuclear matter is true. By constraining the chemical potentials associated with each particle species, we saw how to determine the equation of state $\epsilon(P)$, which in turn was used to integrate the Tolman-Oppenheimer-Volkoff equation (6.1), yielding solutions corresponding to quark stars with given masses and radii. We obtained maximum masses $1.7 M_\odot \leq M \leq 2.0 M_\odot$ with $N_f = 2$ flavors and $1.6 M_\odot \leq M \leq 1.9 M_\odot$ with $N_f = 3$ flavors. This concludes our introduction to the basic concepts to be used in the remainder of this thesis.

Chapter 8

The Two-Flavor Quark-Meson Model

At low energy the effective degrees of freedom of quantum chromodynamics are not individual quarks, but baryons composed of up and down quarks and the three pions that we saw arose from the spontaneous chiral symmetry breaking pattern (6.19). The MIT bag model that we discussed in chapter 7 modeled quark stars as a deconfined Fermi gas of quarks with a bag constant B. We will now crank up the difficulty and investigate the **linear sigma model**, which also takes chiral symmetry breaking and the pions into account by introducing an "ad–hoc" σ particle. The linear sigma model was originally introduced by [Gel+60] as an effective model for nucleons interacting with pions and scalar mesons, but the fermions have since been interpreted as quarks in what is commonly referred to as a **quark-meson model**.

We will take the quark-meson model as granted. As it combines *independent* quarks and mesons, the latter of which are fundamentally bound quark states, it may appear strange. A hypothetical first-principles approach from quantum chromodynamics would naturally give rise to hadrons by binding quarks with gluons. We cannot expect this from an effective model that excludes the gluons, in a sense trading the binding *mechanism* with the bound *product*. It is not our primary concern here to give a full physical justification of the model, but we will justify it to some extent by seeing how it gives rise to chiral symmetry breaking. To better understand its theoretical origin, we recommend studying [Res16; Fol18; Eic20].

Quark stars consisting only of two-flavor quark matter are unlikely to be found in nature, as two-flavor quark matter is observed to be unstable compared to hadronic matter. Nevertheless, they are a natural stepping stone for modeling possibly stable strange quark stars and dense hybrid neutron stars whose core could contain two-flavor quark matter.

This chapter is inspired by references [Sch+07b], [Eic20] and [Adh+17b].

8.1 Lagrangian, vacuum and symmetries

The Lagrangian density for the linear sigma model coupled to quarks is [Sch+07b]

$$\mathcal{L} = \bar{q}\Big[i\partial\!\!\!/ + \mu\gamma^0 - g\big(\sigma + i\gamma^5 \boldsymbol{\tau}\cdot\boldsymbol{\pi}\big)\Big]q + \frac{1}{2}\Big[\big(\partial_\mu\sigma\big)\big(\partial^\mu\sigma\big) + \big(\partial_\mu\boldsymbol{\pi}\big)\big(\partial^\mu\boldsymbol{\pi}\big)\Big] - \mathcal{V}(\sigma,\boldsymbol{\pi}) \tag{8.1}$$

with the meson potential

$$\mathcal{V}(\sigma,\boldsymbol{\pi}) = \frac{m^2}{2}\big(\sigma^2+\boldsymbol{\pi}^2\big) + \frac{\lambda}{4!}\big(\sigma^2+\boldsymbol{\pi}^2\big)^2 - h\sigma. \tag{8.2}$$

The quarks q behave as in the QCD Lagrangian (6.13) with $N_f = 2$ flavor indices $\{u, d\}$, $N_c = 3$ color indices and four Dirac spinor indices. They are coupled to two quark chemical potentials $\mu = \mathrm{diag}(\mu_u, \mu_d)$ in flavor space, but are now seemingly massless and coupled to a σ meson and three pions $\boldsymbol{\pi} = [\pi^+, \pi^-, \pi^0]^\mathsf{T}$ with a Yukawa coupling g and the Pauli matrices (3.87). The meson potential features three couplings $m^2 < 0$, $\lambda > 0$ and $h > 0$.

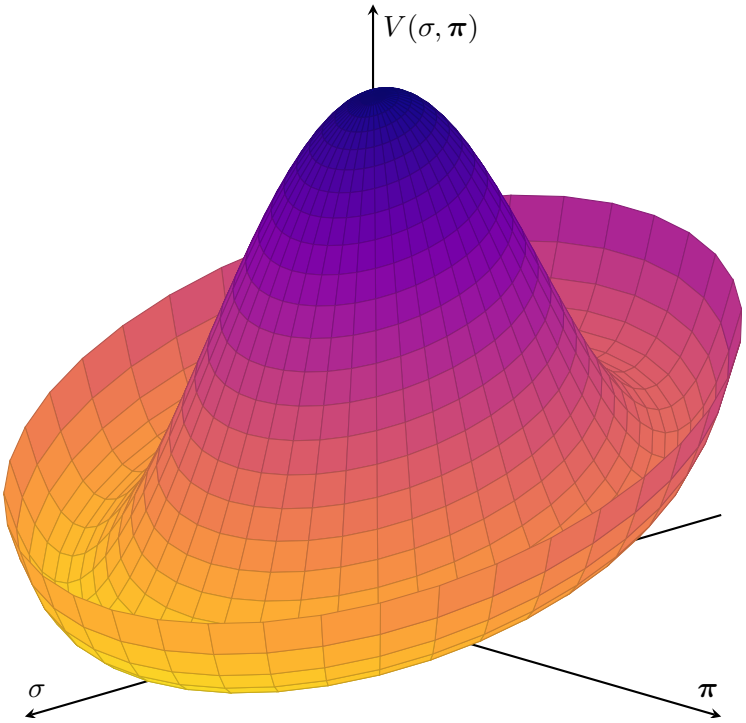

Figure 8.1: A two-dimensional realization of the meson potential (8.2) with $m^2 < 0$, $\lambda > 0$ and $h \geq 0$ looks like a Mexican hat, tilted along the σ-axis by the explicit symmetry breaking parameter h. If $h = 0$, the hat is upright with a continuous range of minima around the brim $\sigma^2 + \boldsymbol{\pi}^2 = -6m^2/\lambda$; while if $h \neq 0$, the hat is respectfully tipped towards a unique global minimum determined by equation (8.6).

Like quantum chromodynamics, the quark-meson model Lagrangian (8.1) has the vector $U(1)_V$ and the axial $U(1)_A$ symmetry shown in section 6.3. But how does the quark-meson model give rise to the chiral symmetry breaking of quantum chromodynamics?

First, express the Yukawa coupling with right-handed and left-handed chiral fields $q_\pm = P_\pm q$:

$$\begin{aligned}
\bar{q}\big[\sigma + i\gamma^5 \boldsymbol{\tau}\cdot\boldsymbol{\pi}\big]q &= \bar{q}\big[(P_+ + P_-)\sigma + (P_+ - P_-)i\boldsymbol{\tau}\cdot\boldsymbol{\pi}\big]q && \big(P_\pm = \tfrac{1}{2}(1 \pm \gamma^5)\big) \\
&= \bar{q}\big[P_+\phi + P_-\phi^\dagger\big]q && \big(\text{define } \phi = \sigma + i\boldsymbol{\tau}\cdot\boldsymbol{\pi}\big) \\
&= \bar{q}\big[P_+\phi + P_-\phi^\dagger\big]\big[P_+ + P_-\big]q && \big(P_+ + P_- = 1\big) \\
&= \bar{q}\big[P_+\phi P_+ + P_-\phi^\dagger P_-\big]q && \big(P_\pm P_\mp = 0\big) \\
&= \bar{q}_-\phi\, q_+ + \bar{q}_+\phi^\dagger q_- && \big(P_\pm q = q_\pm,\ \bar{q}P_\pm = \bar{q}_\mp\big).
\end{aligned} \tag{8.3}$$

Second, note that the meson potential (8.2) with $h = 0$ only depends on the flavor-space trace

$$\tfrac{1}{2}\operatorname{tr}\big[\phi^\dagger\phi\big] = \tfrac{1}{2}\big(\underbrace{\operatorname{tr}\big[1\big]}_{2}\sigma^2 - i^2\underbrace{\operatorname{tr}\big[\tau_a\tau_b\big]}_{2\delta_{ab}}\pi_a\pi_b\big) = \sigma^2 + \boldsymbol{\pi}^2. \tag{8.4}$$

Under the $SU(2)_L \times SU(2)_R$ transformation

$$q_\pm \to U_\pm q_\pm \qquad \text{and} \qquad \phi \to U_-\phi U_+^\dagger, \tag{8.5}$$

the Yukawa interaction (8.3), the meson potential argument (8.4) and hence the Lagrangian (8.1) are invariant when $U_- = U_+$, similarly to quantum chromodynamics. This shows that in the absence of the parameter h, the quark-meson model has $SU(2)_L \times SU(2)_R$ symmetry in the vacuum.

Since the group $SU(2)_L \times SU(2)_R$ is isomorphic to $O(4)$, the symmetry can equivalently be understood by considering the meson fields as a four-vector $[\sigma, \boldsymbol{\pi}]^\mathsf{T}$ and noting that the meson potential (8.2) with $h = 0$ is invariant under rotation of this vector in four-space.

Is this symmetry also spontaneously broken in the vacuum, like in quantum chromodynamics? In the vacuum, the fermions do not contribute to the grand potential, and the ground state values $\sigma = \langle\sigma\rangle$ and $\boldsymbol{\pi} = \langle\boldsymbol{\pi}\rangle$ are given by minima of the meson potential $\mathcal{V}(\langle\sigma\rangle, \langle\boldsymbol{\pi}\rangle)$ illustrated in figure 8.1. From its definition (8.2), we see that they are given by

$$\frac{\partial\mathcal{V}}{\partial\pi_a} = \langle\pi_a\rangle\Big[m^2 + \frac{\lambda}{6}\big(\langle\sigma\rangle^2 + \langle\boldsymbol{\pi}\rangle^2\big)\Big] = 0 \quad \text{and} \quad \frac{\partial\mathcal{V}}{\partial\sigma} = \langle\sigma\rangle\Big[m^2 + \frac{\lambda}{6}\big(\langle\sigma\rangle^2 + \langle\boldsymbol{\pi}\rangle^2\big)\Big] - h = 0. \tag{8.6}$$

The qualitative nature of the solutions depends on whether h vanishes:

- In the **chiral limit** $h = 0$, the ground state solutions are a degenerate range of minima along the circle $\langle\sigma\rangle^2 + \langle\boldsymbol{\pi}\rangle^2 = -6m^2/\lambda$, sometimes referred to as a vacuum manifold. Without any loss of generality, we pick the one at $\langle\sigma\rangle = \sqrt{-6m^2/\lambda} > 0$ and $\langle\boldsymbol{\pi}\rangle = 0$.
- At the **physical point** $h \neq 0$, the ground state of the potential is a unique global minimum at $\langle\sigma\rangle \neq 0$ and $\langle\boldsymbol{\pi}\rangle = 0$ determined implicitly by equation (8.6).

Note how the oppositely signed parameters $m^2 < 0$ and $\lambda > 0$ are needed for the minimum $\langle\sigma\rangle = \sqrt{-6m^2/\lambda} \neq 0$ to exist, and that $\langle\boldsymbol{\pi}\rangle = 0$ in both cases. To account for quantum fluctuations $\tilde{\sigma}$ and $\tilde{\boldsymbol{\pi}}$ of σ and $\boldsymbol{\pi}$ around the ground states $\langle\sigma\rangle$ and $\langle\boldsymbol{\pi}\rangle$, let us write

$$\sigma = \langle\sigma\rangle + \tilde{\sigma} \qquad \text{and} \qquad \boldsymbol{\pi} = \langle\boldsymbol{\pi}\rangle + \tilde{\boldsymbol{\pi}}. \tag{8.7}$$

Up to second order in the quantum fluctuations, the Lagrangian (8.1) becomes

$$\mathcal{L} \simeq \sum_{f=1}^{N_f}\sum_{c=1}^{N_c} \bar{q}\Big[i\partial\!\!\!/ + \mu\gamma^0 - m_q\Big]q + \frac{1}{2}\Big[\big(\partial_\mu\tilde{\sigma}\big)\big(\partial^\mu\tilde{\sigma}\big) + \big(\partial_\mu\tilde{\boldsymbol{\pi}}\big)\big(\partial^\mu\tilde{\boldsymbol{\pi}}\big)\Big] - \mathcal{V}(\sigma, \boldsymbol{\pi}), \tag{8.8}$$

where the meson potential (8.2) to the same order is

$$\mathcal{V}(\sigma, \boldsymbol{\pi}) = \mathcal{V}(\langle\sigma\rangle, \langle\boldsymbol{\pi}\rangle) + h\tilde{\sigma} + \frac{1}{2}m_\sigma^2\tilde{\sigma}^2 + \frac{1}{2}m_\pi^2\tilde{\pi}^2. \tag{8.9}$$

Here the quark and meson fields have acquired the effective masses

$$m_q = g\langle\sigma\rangle, \tag{8.10a}$$

$$m_\sigma^2 = \frac{\partial^2\mathcal{V}}{\partial\sigma^2} = m^2 + \frac{\lambda}{2}\langle\sigma\rangle^2 \overset{\text{by (8.6) with } \langle\boldsymbol{\pi}\rangle = 0}{\downarrow} \frac{3h}{\langle\sigma\rangle} - 2m^2, \tag{8.10b}$$

$$m_\pi^2 = \frac{\partial^2\mathcal{V}}{\partial\boldsymbol{\pi}^2} = m^2 + \frac{\lambda}{6}\langle\sigma\rangle^2 \underset{\text{by (8.6) with } \langle\boldsymbol{\pi}\rangle = 0}{\uparrow} \frac{h}{\langle\sigma\rangle}. \tag{8.10c}$$

Note that the up and down quarks share the degenerate mass $m_u = m_d = m_q$. In nature isospin symmetry is only slightly broken, and the up and down quark masses are indeed almost equal. The meson masses m_σ and m_π are called *curvature masses* due to their relation with the second derivative of the potential. They coincide with the physical pole masses of the particles' propagators only at tree level, where loop effects are neglected.

The qualitative nature of the pions depends on whether h vanishes:

- In the **chiral limit** $h = 0$, the $SU(2)_L \times SU(2)_R$ symmetry under the transformation (8.5) is exact, and we saw that there is a manifold of ground states. Upon committing to the minimum $\langle\sigma\rangle = \sqrt{-6m^2/\lambda} \neq 0$ and $\langle\boldsymbol{\pi}\rangle = 0$, the $O(4)$ rotation symmetry of the four original meson fields $[\sigma, \boldsymbol{\pi}]^\mathsf{T}$ is spontaneously broken to rotation of only the three pion quantum fluctuations $\boldsymbol{\pi} = \tilde{\boldsymbol{\pi}}$ in $O(3)$. Correspondingly, the pions are Goldstone bosons with vanishing masses (8.10c) associated with spontaneous symmetry breaking.
- At the **physical point** $h \neq 0$, the $SU(2)_L \times SU(2)_R$ symmetry under the transformation (8.5) is explicitly broken, and we saw above that there is a unique ground state. Correspondingly, the pions are pseudo-Goldstone bosons with small masses (8.10c).

Unlike the resulting massless pions, the σ particle is the *cause* of the symmetry breaking, and there is no reason for its mass (8.10b) to vanish. Speaking brutally to get our point across, the σ meson is merely a means to an end to generate the chiral symmetry breaking and the pions, which are our three favorite spoiled children in this group of four meson siblings.

To summarize: although the linear sigma model symmetry breaking pattern

$$SU(2) \times SU(2) \simeq O(4) \qquad \longrightarrow \qquad O(3) \tag{8.11}$$

is *different* from the quantum chromodynamics symmetry breaking pattern (6.19) "under the hood", they qualitatively give rise to the *same* spontaneous chiral symmetry breaking and pion degrees of freedom "on the outside". Practically speaking, the patterns are indistinguishable and equivalent. According to Weinberg's philosophy presented in section 6.3, the quark-meson model is thus an appropriate effective model of quantum chromodynamics at low energy. The explicit symmetry breaker $h \neq 0$ only turns the exact symmetry into an approximate one, just like the different quark masses explicitly break the chiral symmetry of quantum chromodynamics. This is our physical justification of the quark-meson model.

8.2 Grand potential

With our recently gained faith in the quark-meson model, we set out to calculate its grand potential (6.3). With the quark fields q, the meson fields σ and $\boldsymbol{\pi}$ and the coupling of conserved currents $j_f^\mu = \bar{q}_f \gamma^\mu q_f$ to chemical potentials μ already baked into the Lagrangian (8.1), the partition function (6.2) is

$$Z = \oint_- \mathcal{D}\bar{q} \oint_- \mathcal{D}q \oint_+ \mathcal{D}\sigma \oint_+ \mathcal{D}\boldsymbol{\pi} \exp\left\{ \int_0^\beta \mathrm{d}\tau \int_V \mathrm{d}^3x \, \mathcal{L}_E[\bar{q}, q, \sigma, \boldsymbol{\pi}] \right\}. \tag{8.12}$$

To calculate it we will use the **mean-field approximation** for the bosonic fields, replacing them by their *yet unknown* expectation values $\langle\sigma\rangle$ and $\langle\boldsymbol{\pi}\rangle$ in the classical ground state and simply ignoring their quantum fluctuations $\tilde{\sigma}$ and $\tilde{\boldsymbol{\pi}}$. In contrast we will give the fermions full treatment, motivated by their more dramatic behavior at zero temperature. After calculating the grand potential with unknown mean fields, their precise values are found *self-consistently* with the original assumption of them being minima of the grand potential by solving

$$\frac{\partial\Omega}{\partial\langle\sigma\rangle} = \frac{\partial\Omega}{\partial\langle\boldsymbol{\pi}\rangle} = 0. \tag{8.13}$$

We call this the **self-consistency equation** for the mean fields. For example, the mean-field approximation is also famously used in the Bardeen-Cooper-Schrieffer theory of superconductivity to determine an energy gap. There it is called the **gap equation**, and many authors continue to use this name as a relic even in other applications, such as this model.

In our treatment we will also neglect pion condensation and assume that $\langle\boldsymbol{\pi}\rangle = 0$ *always* vanishes. As shown by [And+19; And+18], for example, this is known to be true at $T = 0$ when the isospin chemical potential (6.14) does not exceed half the pion mass. This assumption is subject to a self-consistency check later. It is then only $\langle\sigma\rangle$ that needs to be determined by the self-consistency equation (8.13).

With bosonic mean fields, the partition function (8.12) with the Lagrangian (8.1) reads

$$Z = \oint_- \mathcal{D}\bar{q} \oint_- \mathcal{D}q \exp\left\{ \int_0^\beta \mathrm{d}\tau \int_V \mathrm{d}^3x \Big[\bar{q}\big(i\partial\!\!\!/ + \mu\gamma^0 - m_q\big)q - \mathcal{V}(\langle\sigma\rangle, \mathbf{0}) \Big] \right\}. \tag{8.14}$$

The meson potential is independent of the fields and can be pulled out of the integrals, while the fermionic contribution decouples into a product of identical integrals. We therefore have

$$\log Z = -\beta V \, \mathcal{V}(\langle\sigma\rangle, \mathbf{0}) + \sum_{f=1}^{N_f} \sum_{c=1}^{N_c} \log \oint_- \mathcal{D}\bar{q}_{f,c} \oint_- \mathcal{D}q_{f,c} \exp\left\{ \int_0^\beta \mathrm{d}\tau \int_V \mathrm{d}^3x \, \bar{q}_{f,c}\big(i\partial\!\!\!/ + \mu_f\gamma^0 - m_f\big)q_{f,c} \right\}. \tag{8.15}$$

We have already calculated the path integral in the last term from equation (3.93) to equation (3.109). As $q_{f,c}$ is integrated over, the color sum gives an additional factor $\sum_{c=1}^{N_c} = N_c$ because its summand is independent of c, while the flavor sum $\sum_{f=1}^{N_f}$ yields N_f terms that differ only by the chemical potential μ_f associated with each flavor. Thus, the grand potential (6.3) is

$$\Omega = \mathcal{V}(\langle\sigma\rangle, \mathbf{0}) - \frac{2N_c}{\beta} \sum_{f=1}^{N_f} \int \frac{\mathrm{d}^3 p}{(2\pi)^3} \left\{ \beta E(\boldsymbol{p}) + \log\left[e^{-\beta(E(\boldsymbol{p})-\mu_f)} + 1\right] + \log\left[e^{-\beta(E(\boldsymbol{p})+\mu_f)} + 1\right] \right\}, \tag{8.16}$$

with the dispersion relation $E(\boldsymbol{p}) = \sqrt{p^2 + m_q^2}$. We work in the zero-temperature approximation $T = 0$ and choose positive chemical potentials, so the anti-particle contribution from the third term in $\{\ldots\}$ vanishes. The integral of the second term in $\{\ldots\}$ was calculated in the zero-temperature pressure $P = -\Omega$ in equation (4.10c). This time we also include and renormalize the infinite vacuum contribution from the integral of the first term in $\{\ldots\}$. It is called the *Dirac sea*, and we renormalize it in the modified minimal subtraction scheme in appendix D, arriving at expression (D.5b). We also reinstate $x_f = p_f/m_q = \sqrt{\mu_f^2 - m_q^2}/m_q$ into expression (4.10c). Pulling all this together, the divergent grand potential (8.16) becomes

$$\begin{aligned} \Omega = \mathcal{V}(\langle\sigma\rangle, \mathbf{0}) &+ N_c N_f \frac{m_q^4}{16\pi^2} \left[\frac{1}{\epsilon} + \frac{3}{2} + \log\left(\frac{\Lambda^2}{m_q^2}\right) \right] \\ &- \sum_{f=1}^{N_f} \frac{N_c}{24\pi^2} \left[\left(2\mu_f^2 - 5m_q^2\right) \mu_f \sqrt{\mu_f^2 - m_q^2} + 3m_q^4 \operatorname{asinh}\left(\sqrt{\frac{\mu_f^2}{m_q^2} - 1}\right) \right]. \end{aligned} \tag{8.17}$$

The renormalization has introduced a renormalization scale Λ that we will determine later. It also exposes the Dirac sea vacuum divergence in the ϵ-pole $N_c N_f m_q^4/16\pi^2\epsilon$. Recalling that $m_q = g\langle\sigma\rangle$ and glancing back at the meson potential (8.2), we also see that this divergence can be removed by the term $\lambda\langle\sigma\rangle^4/24$ in $\mathcal{V}(\langle\sigma\rangle, \mathbf{0})$ if the quartic coupling is shifted to

$$\lambda \to \lambda + \delta\lambda \qquad \text{with the counterterm} \qquad \delta\lambda = -N_c N_f \frac{3g^4}{2\pi^2\epsilon}. \tag{8.18}$$

Then $N_c N_f m_q^4/16\pi^2\epsilon + \delta\lambda\langle\sigma\rangle^4/24 = 0$, demonstrating that the theory is renormalizable. Adding free electrons to the mix, the finite and renormalized grand potential is finally

$$\begin{aligned} \Omega(\langle\sigma\rangle, \boldsymbol{\mu}) = \mathcal{V}(\langle\sigma\rangle, \mathbf{0}) &+ N_c N_f \frac{m_q^4}{16\pi^2} \left[\frac{3}{2} + \log\left(\frac{\Lambda^2}{m_q^2}\right) \right] \\ &- \sum_{f=1}^{N_f} \frac{N_c}{24\pi^2} \left[\left(2\mu_f^2 - 5m_q^2\right) \mu_f \sqrt{\mu_f^2 - m_q^2} + 3m_q^4 \operatorname{asinh}\left(\sqrt{\frac{\mu_f^2}{m_q^2} - 1}\right) \right] \\ &- \frac{1}{24\pi^2} \left[\left(2\mu_e^2 - 5m_e^2\right) \mu_e \sqrt{\mu_e^2 - m_e^2} + 3m_e^4 \operatorname{asinh}\left(\sqrt{\frac{\mu_e^2}{m_e^2} - 1}\right) \right]. \end{aligned} \tag{8.19}$$

As in the MIT bag model, the particle densities (6.4b) are

$$n_f = -\frac{\partial\Omega}{\partial\mu_f} = \frac{N_c}{3\pi^2}\left(\mu_f^2 - m_q^2\right)^{\frac{3}{2}} \qquad \text{and} \qquad n_e = -\frac{\partial\Omega}{\partial\mu_e} = \frac{1}{3\pi^2}\left(\mu_e^2 - m_e^2\right)^{\frac{3}{2}}, \tag{8.20}$$

and the pressure (6.4a) and energy density (6.4d) follow at $T = 0$.

On one side, it can be argued that treating bosons and fermions to zero and one loops is *inconsistent*. However, note that the fermionic contribution to the grand potential (8.19) is of order $\mathcal{O}(N_c^1)$, while any bosonic contribution with one loop would only be of order $\mathcal{O}(N_c^0)$. On the other side, then, we can argue that our approach is *consistent* in the **one-loop large-N_c limit**. The number of loops must be restricted to one, for with two loops, for example, the $\mathcal{O}(N_c^1)$ Feynman diagram due to the $\bar{q}\sigma q$ Yukawa interaction should also be included. Despite there only being $N_c = 3$ colors in nature, we briefly mentioned the success of the large-N_c approximation in section 6.3. We will come back to this matter of consistency later.

8.3 Parameter fit at tree-level

To determine the four parameters g, m^2, λ and h in the grand potential (8.19), we use measured values of $\langle\sigma\rangle$ and the curvature masses m_σ, m_π and m_q in vacuum. Inverting equations (8.6) and (8.10), we can express the parameters entirely in terms of these variables as

$$g = \frac{m_q}{\langle\sigma\rangle}, \quad m^2 = \frac{3m_\pi^2 - m_\sigma^2}{2}, \quad \lambda = \frac{3m_\sigma^2 - 3m_\pi^2}{\langle\sigma\rangle^2} \quad \text{and} \quad h = m_\pi^2\langle\sigma\rangle. \tag{8.21}$$

According to [PDG20], in vacuum the mean field is the pion decay constant $\langle\sigma\rangle = f_\pi = 93\,\text{MeV}$, the average mass of the three pions is $m_\pi = 138\,\text{MeV}$ and the up and down quarks have almost equal masses $m_u \approx m_d \approx 300\,\text{MeV}$. All these quantities have low uncertainty.

On the other hand, the mass m_σ is very uncertain and hard to choose. Even in 2002, according to the σ meson status update [Pel14], it was only known to lie in the huge uncertainty range $400\,\text{MeV} \leq m_\sigma \leq 1200\,\text{MeV}$. Today [PDG20] places it in the tighter range $400\,\text{MeV} \leq m_\sigma \leq 550\,\text{MeV}$. Ideally we would like to use a value within this range, but there are several problems. First, the vacuum potential $\mathcal{V}(\langle\sigma\rangle, \mathbf{0})$ plotted in figure 8.2 does not have a minimum and is therefore useless for $m_\sigma \leq 500\,\text{MeV}$, and the same happens with the three-flavor model in chapter 9. We therefore operate with the three common values $m_\sigma = \{600, 700, 800\}\,\text{MeV}$ in both of the two models. This is the best we can do and must be regarded as a shortcoming of the model. Since the σ particle was introduced in an ad-hoc manner as a mere means to an end for the pions anyway, we argue that it is the most legitimate candidate for discrimination.

Table 8.1 summarizes the chosen input values for $\langle\sigma\rangle = f_\pi$, m_π, m_σ and $m_q = m_u = m_d$ in vacuum and the corresponding output parameters m^2, λ, g and h.

The renormalization procedure also introduced an undetermined renormalization scale Λ. To determine it, we require that the minimum of the grand potential (8.19) in vacuum, where $\boldsymbol{\mu} = 0$, remains at the minimum $\langle\sigma\rangle = f_\pi$ of the vacuum potential $\mathcal{V}(\langle\sigma\rangle, \mathbf{0})$. Since $\partial\mathcal{V}/\partial\langle\sigma\rangle = 0$ at $\langle\sigma\rangle = f_\pi$ already by assumption, we only need

$$\frac{\partial\Omega}{\partial\langle\sigma\rangle} = \frac{\partial}{\partial\langle\sigma\rangle}\left[N_c N_f \frac{m_q^4}{16\pi^2}\left(\frac{3}{2} + \log\frac{\Lambda^2}{m_q^2}\right)\right] = 0, \quad \text{yielding} \quad \Lambda = \frac{m_q}{\sqrt{e}} = \frac{g f_\pi}{\sqrt{e}} = 182.0\,\text{MeV}. \tag{8.22}$$

As mentioned at the end of section 8.2, our calculation of the grand potential can only be viewed as fully consistent in the one-loop large-N_c limit, so it is really inconsistent to fit parameters at tree-level using the curvature masses (8.10). The physical pole masses would really receive radiative loop corrections. In section 8.6 we will fit parameters consistently in the one-loop large-N_c limit and see that this resolves the large discrepancy in m_σ.

Table 8.1: The variables in the left table are used as **input** to determine the model parameters in the right table from equation (8.21). Three values are used for m_σ, generating three parameter sets with different m^2 and λ. Experimental measurements are taken from [PDG20].

Physical variables				
Variable	Modeled			Measured
	Set 1	Set 2	Set 3	
f_π / MeV	**93**	**93**	**93**	92-93
m_u / MeV	**300**	**300**	**300**	$\approx$ 300
m_d / MeV	**300**	**300**	**300**	$\approx$ 300
m_σ / MeV	**600**	**700**	**800**	400-550
m_π / MeV	**138**	**138**	**138**	138

Model parameters			
Parameter	Modeled		
	Set 1	Set 2	Set 3
g	3.23	3.23	3.23
m^2 / (MeV)^2	-389^2	-465^2	-540^2
λ	118	163	215
h / (MeV)^3	121^3	121^3	121^3

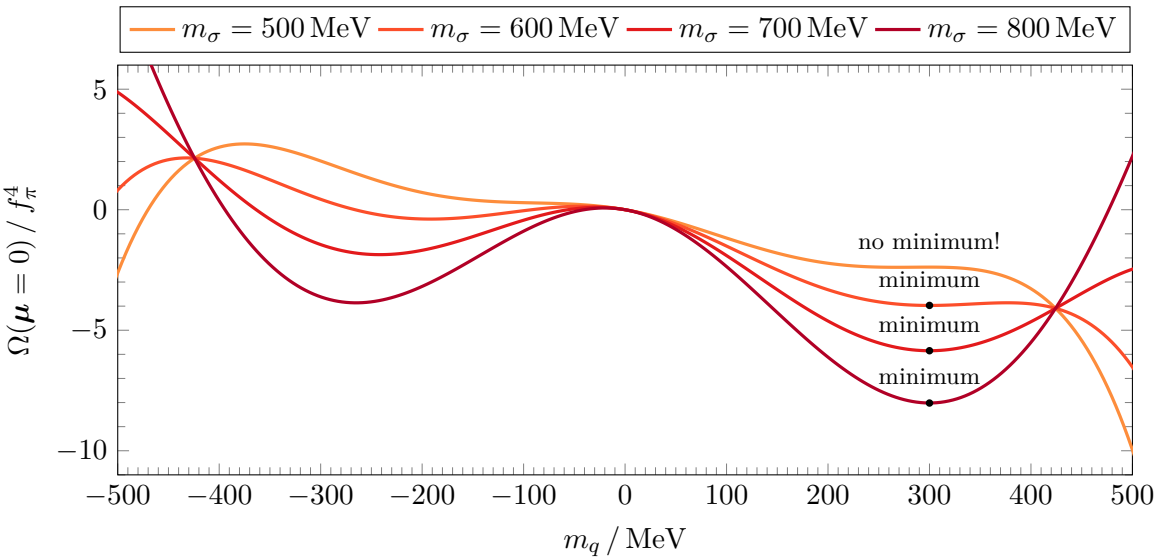

Figure 8.2: The two-flavor grand potential (8.19) admits minima for the quark mass $m_q = g\langle\sigma\rangle$ in vacuum, where $\boldsymbol{\mu} = \mathbf{0}$, only when fit to $m_\sigma \geq 600\,\mathrm{MeV}$ at tree-level.

8.4 Equation of state

Before finding the general charge neutral equation of state, it is easier and instructive to solve the special problem with imposed zero isospin $\mu_I = 0$, or $\mu_u = \mu_d = \mu$. This will give us some intuition for the shape of the grand potential in the charge-neutral case. The chemical equilibrium constraint (6.7) then says $\mu_e = 0$, so electrons are absent and only the two first lines in the grand potential (8.19) contribute. It is now a function $\Omega(\langle\sigma\rangle, \mu)$ of only two variables that is easy to visualize, as done in figure 8.3. Although we defined Ω as a function of $\langle\sigma\rangle$, we will discuss the following results in terms of $m_q = g\langle\sigma\rangle$ instead, as it is easier to compare to the chemical potentials μ_f. We see that:

- For $\mu < 300\,\mathrm{MeV} = m_q(f_\pi)$, the grand potential is independent of μ, and we are in vacuum where only the first line of the grand potential (8.19) contributes. By construction, the minimum lies at $\langle\sigma\rangle = f_\pi = 93\,\mathrm{MeV}$. The feature that a *range* of chemical potentials characterizes the vacuum is sometimes called the *Silver Blaze property*. Chiral symmetry is spontaneously broken in vacuum, as demonstrated in section 8.1.
- For $300\,\mathrm{MeV} \leq \mu \lesssim 400\,\mathrm{MeV}$, the quarks in the second line of the grand potential (8.19) begin to contribute as we leave the vacuum during the chiral transition. For $m_\sigma < 800\,\mathrm{MeV}$ the minimum jumps *discontinuously*, corresponding to a *first-order phase transition*. For $m_\sigma \geq 800\,\mathrm{MeV}$ its value changes fast and furiously but nevertheless *continuously*, and there is *no phase transition*, only what is referred to as a rapid *crossover*.
- For $\mu \gtrsim 400\,\mathrm{MeV}$, the minimum approaches the *ultra-relativistic* or *massless* limit $\langle\sigma\rangle \to 0$ asymptotically, but never quite reaches it, as chiral symmetry is gradually restored.

Our objective, however, is to determine the equation of state $\epsilon(P)$ when the chemical potentials are constrained by the charge neutrality condition (6.12) in addition to the β-equilibrium condition (6.7). This means that we must not solve only the self-consistency equation (8.13), but the *system* of equations

$$0 = \frac{\partial\Omega}{\partial\langle\sigma\rangle}, \tag{8.23a}$$

$$0 = 2\left(\mu_u^2 - m_q^2\right)^{\frac{3}{2}} - \left(\mu_d^2 - m_q^2\right)^{\frac{3}{2}} - \left(\mu_e^2 - m_e^2\right)^{\frac{3}{2}}, \tag{8.23b}$$

$$\mu_d = \mu_u + \mu_e. \tag{8.23c}$$

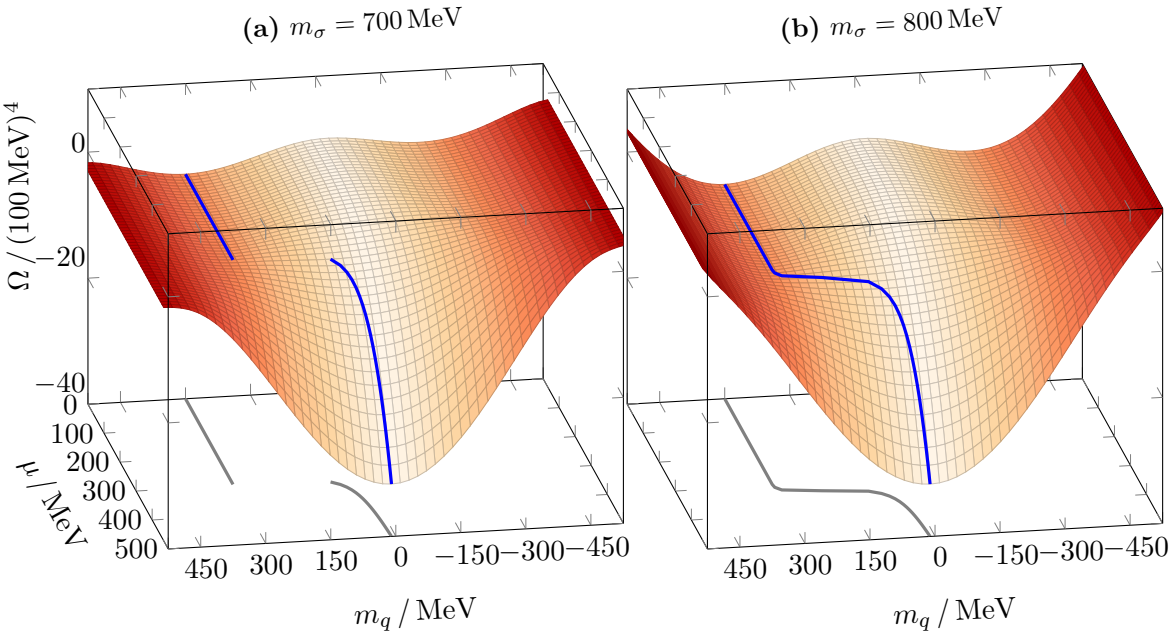

Figure 8.3: The minimum and its projection $m_q(\mu) = g\langle\sigma\rangle(\mu)$ of the grand potential (8.19) with zero isospin, or $\mu_u = \mu_d = \mu$ and $\mu_e = 0$, determined from the self-consistency equation (8.13). For **(a)** $m_\sigma < 800\,\mathrm{MeV}$ it jumps in a *discontinuous phase transition*, while for **(b)** $m_\sigma \geq 800\,\mathrm{MeV}$ it moves quickly and continuously in a *crossover* and there is no phase transition.

This is a system of three equations for the four unknowns $\langle\sigma\rangle$, μ_u, μ_d and μ_e. Do not forget that $m_q = g\langle\sigma\rangle$. We parametrize solutions with one free variable, and calculate the pressure (6.4a), densities (6.4b), energy density (6.4d) and the equation of state $\epsilon(P)$ like in chapter 7.

In particular, we now use $\langle\sigma\rangle$ as the free variable instead of μ. As revealed by peeking ahead at the results in figure 8.4a, the possible presence of a phase transition implies that one μ can correspond to multiple $\langle\sigma\rangle$, while all $\langle\sigma\rangle$ correspond to only one μ (except in the vacuum). It is therefore only the parametrization with $\langle\sigma\rangle$ that captures the multiple solutions.

How should we normalize the pressure this time? With the grand potential (8.19), the pressure $P = -\Omega$ will be nonzero in the vacuum because $\mathcal{V}(f_\pi, \mathbf{0}) \neq 0$. First, we therefore compute the pressure *relative to* vacuum by shifting

$$P \to P - P(\mu \leq 300\,\mathrm{MeV}) = P + \mathcal{V}(f_\pi, \mathbf{0}). \tag{8.24}$$

Second, and like with the MIT bag model in chapter 7, we allow for a bag constant B by making the shift (7.10). After both shifts, the pressure in the vacuum is $P(\mu \leq 300\,\mathrm{MeV}) = -B$ and the non-quark contribution to the general pressure is

$$-B(\langle\sigma\rangle) = -\big[B + \mathcal{V}(\langle\sigma\rangle, \mathbf{0}) - \mathcal{V}(f_\pi, \mathbf{0})\big] \tag{8.25}$$

from the first line of the grand potential (8.19). Unlike the constant B in the MIT bag model, we can interpret $B(\langle\sigma\rangle)$ as a dynamic bag pressure that ranges from $-B(f_\pi) = -B$ in the vacuum to $-B(0) = -\big[B - \mathcal{V}(f_\pi, \mathbf{0})\big]$ in the ultra-relativistic limit. We will come back to allowed values of the bag constant after we have found the equation of state with $B = 0$.

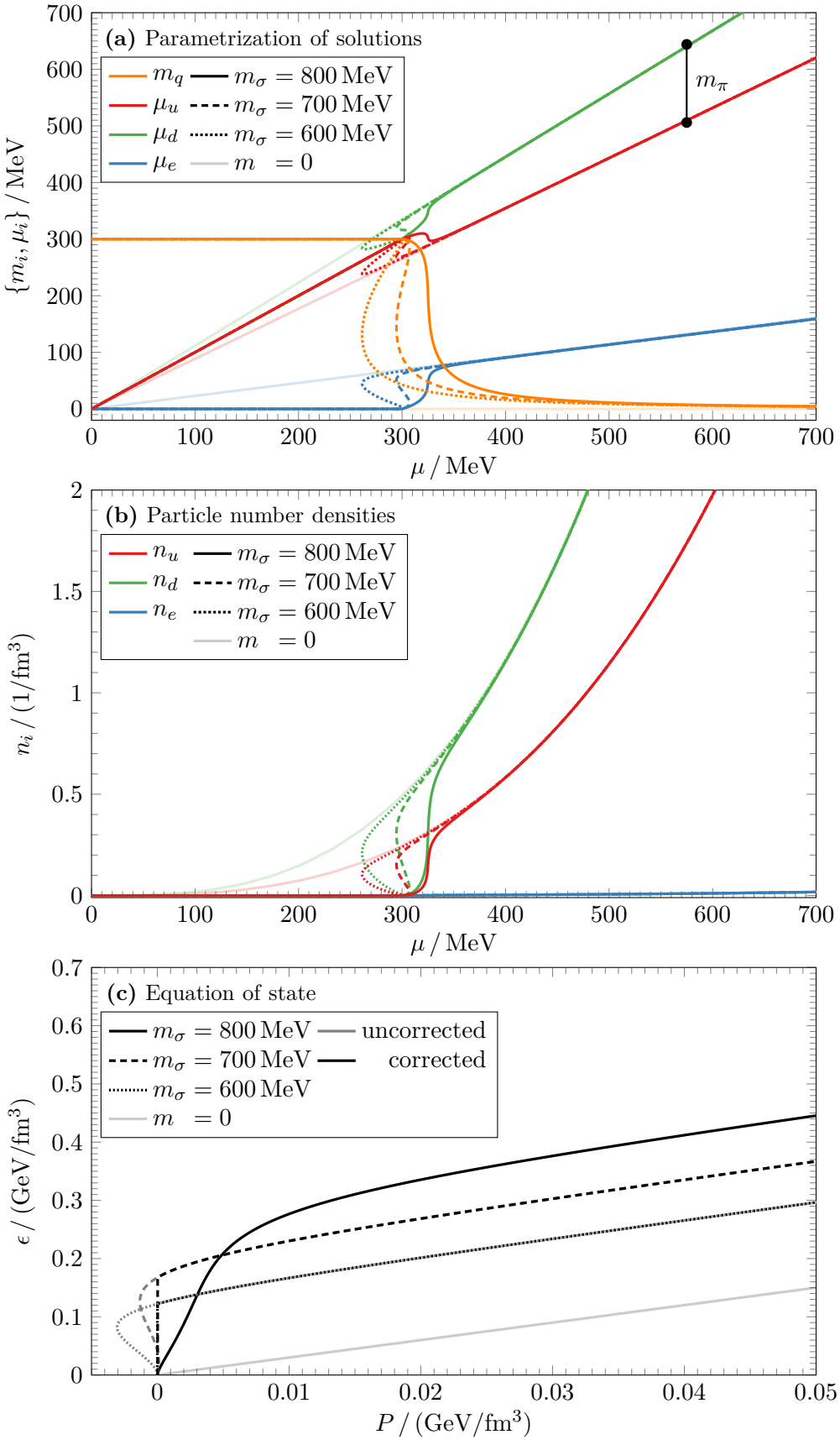

Figure 8.4: Properties of charge neutral quark matter in β-equilibrium in the two-flavor quark-meson model. Upper panel **(a)** shows solutions to equation (8.23), middle panel **(b)** the particle number densities (8.20) and lower panel **(c)** the equation of state $\epsilon(P)$ **before** and **after** the Maxwell construction. Parameter sets with $m_\sigma = \{600, 700, 800\}$MeV from table 8.1 are used. The weak lines show the solutions (7.7), (7.8) and (7.9a) in the massless limit $m = 0$.

The numerical implementation in appendix G.5 gives the equation of state in figure 8.4:

- The phase transition or crossover behaves similarly to how it did in figure 8.3: the grand potential (8.19) and its minimum $\langle\sigma\rangle = m_q/g$ is independent of $\mu = (\mu_u + \mu_d)/2$ in vacuum where $\mu < 300\,\text{MeV}$; undergoes a crossover (with $m_\sigma \geq 800\,\text{MeV}$) or a first-order phase transition (with $m_\sigma < 800\,\text{MeV}$) for $300\,\text{MeV} < \mu \lesssim 400\,\text{MeV}$; and approaches the ultra-relativistic limit $\langle\sigma\rangle \to 0$ for $\mu \gtrsim 400\,\text{MeV}$.

- The isospin chemical potential $\mu_I = (\mu_u - \mu_d)/2$ increases with no bound as μ_u and μ_d grow apart, and its magnitude exceeds the half pion mass $m_\pi/2 = 69\,\text{MeV}$ for $\mu \geq 575\,\text{MeV}$. *This means that our assumption of neglecting pion condensation is inconsistent!* A more detailed study should therefore take it into account, but this is outside our scope.

- With $m_\sigma < 800\,\text{MeV}$ and the resulting phase transition, the parametrized P-ϵ-curve corresponds to an *ambiguous equation of state* where a low pressure corresponds to *multiple* energy densities. In this case we use the Maxwell construction to produce a well-defined invertible equation of state, as described in [Pog17, equation (4.69)]. With $m_\sigma \geq 800\,\text{MeV}$ and the crossover we do not need to think about this.

- The ultra-relativistic solution obtained in section 7.1 is restored as $\langle\sigma\rangle \to 0$. In particular, the slopes $\mathrm{d}\epsilon/\mathrm{d}P = 3$ of the equations of state there and here agree, while their different relative offsets are accounted for by the bag shift (7.10).

- The equation of state always satisfies the causality condition (4.24) and the microscopic stability criterion (4.27).

- Although the electrons have an appreciable chemical potential μ_e, their density n_e is several orders of magnitude below the quark densities n_u and n_d and is hardly noticeable, like in chapter 7. Their main job is to ensure that the charge neutrality condition (8.23b) is met. Coupled with the β-equilibrium condition (8.23c), it is what causes the isospin imbalance as μ_u and μ_d grow apart.

Moreover, the program in appendix G.5 solves the two-flavor inequality (7.12) numerically and reports the lower bag bounds

$$B \geq (110.6\,\text{MeV})^4 \quad \Big(\text{or } B - \mathcal{V}(f_\pi, \mathbf{0}) \geq (145.4\,\text{MeV})^4\Big) \qquad \Big(m_\sigma = 600\,\text{MeV}\Big), \tag{8.26a}$$

$$B \geq \ (67.7\,\text{MeV})^4 \quad \Big(\text{or } B - \mathcal{V}(f_\pi, \mathbf{0}) \geq (146.3\,\text{MeV})^4\Big) \qquad \Big(m_\sigma = 700\,\text{MeV}\Big), \tag{8.26b}$$

$$B \geq \ (27.0\,\text{MeV})^4 \quad \Big(\text{or } B - \mathcal{V}(f_\pi, \mathbf{0}) \geq (156.5\,\text{MeV})^4\Big) \qquad \Big(m_\sigma = 800\,\text{MeV}\Big). \tag{8.26c}$$

In the next chapter we study the three-flavor generalization of this model and find the complementing upper bounds (9.29) due to the strange matter hypothesis. Note that these upper bounds almost coincide with the lower bounds, so the inequalities can practically speaking be squeezed into equalities *if* the strange matter hypothesis is true. On the other hand, the lower bounds are based on instability of two-flavor quark matter and are certain. We focus on the bag constants that lie *at* the lower bounds (8.26), as we saw in chapter 7 that they generate stiffer equations of state and hence greater maximum masses, and greater bag constants would be forbidden anyway *if* the strange matter hypothesis holds. The main takeaway is that B can violate the upper bounds (9.29), but certainly not the lower bounds (8.26).

Also note that it is the bounds of $B - \mathcal{V}(f_\pi, \mathbf{0})$, not B, that are comparable to the MIT bag model bound (7.14). This is because we have seen that the quark-meson model approaches the MIT bag model only in the ultra-relativistic limit $\langle\sigma\rangle \to 0$. Hence the same goes for the dynamic bag pressure (8.25), which evaluates to $-B(0) = -[B - \mathcal{V}(f_\pi, \mathbf{0})]$ in this limit.

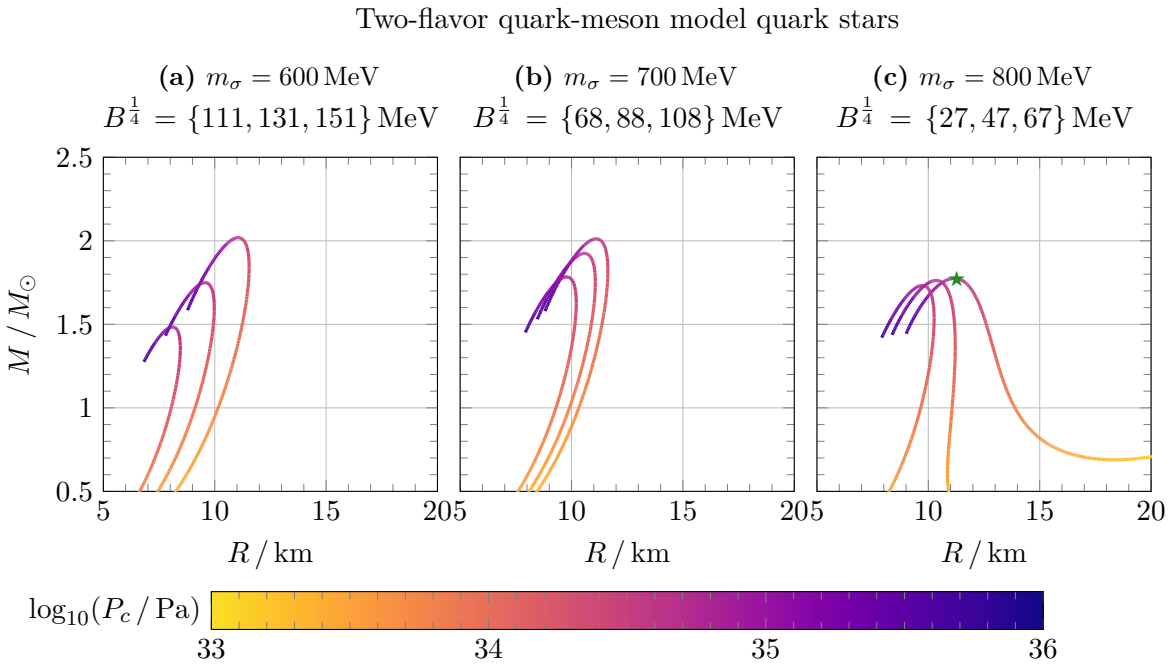

Figure 8.5: Mass-radius solutions of the Tolman-Oppenheimer-Volkoff equation (6.1) parametrized by the central pressure P_c, using equations of state for two-flavor quark matter in figure 8.4c modified by the bag shift (7.10) with bag constants at and above the bounds (8.26).

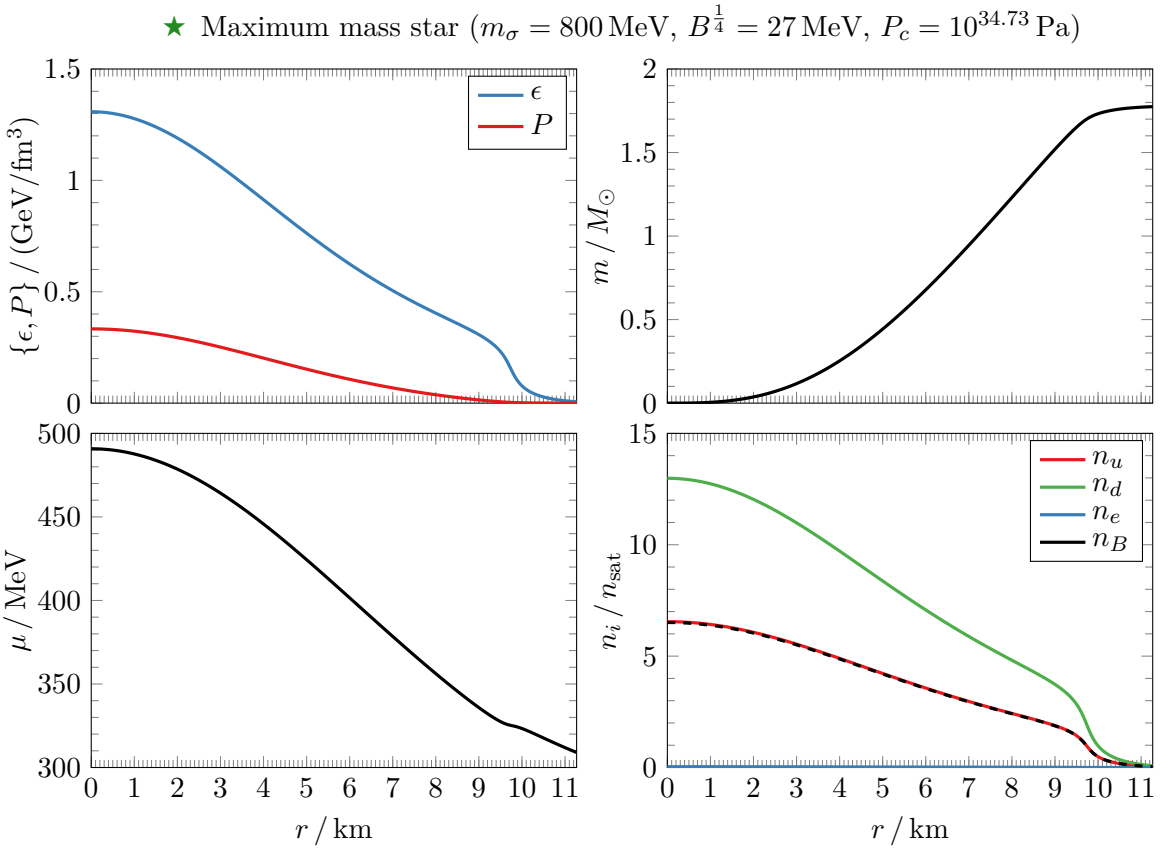

Figure 8.6: Radial profiles for the pressure P, energy density ϵ, cumulative mass m, quark chemical potential μ, particle densities n_i and baryon density $n_B = (n_u + n_d)/3$ for the maximum mass two-flavor quark star ★ in figure 8.5. The nuclear saturation density is $n_{\mathrm{sat}} = 0.165/\mathrm{fm}^3$.

8.5 Quark star solutions

Having found the minimum allowed bag constants, we now modify the equation of state with the shift (7.10) using bag constants at and above the lower bounds (8.26) and solve the corresponding Tolman-Oppenheimer-Volkoff equations (6.1). From the numerical implementation in appendix G.5, we find the mass-radius relations in figure 8.5:

- For bag constants that just satisfy the lower bounds (8.26) for $600\,\text{MeV} \leq m_\sigma \leq 800\,\text{MeV}$, stars have maximum masses $1.7\,M_\odot \leq M \leq 2.0\,M_\odot$ and corresponding radii $R \approx 11\,\text{km}$. The heaviest star has an average mass density of $\rho = M/(4\pi R^3/3) = 7 \cdot 10^{14}\,\text{kg/L}$!
- For greater bag constants, the strange matter hypothesis and corresponding upper bounds (9.29) are violated. We pay special attention to the lowest bag constants that respect both the lower and upper bounds, as the stellar masses and radii decrease with increasing bag constants anyway.
- As m_σ increases, the maximum mass decreases and becomes more resilient to changes in B, and stars tend to inflate up to larger sizes for low pressures.
- The results are generally comparable to the MIT bag model solutions in figure 7.3.

Let us also examine the radial profiles of interesting quantities in a star. The solution of the Tolman-Oppenheimer-Volkoff equation (6.1) yields $P(r)$ and $m(r)$ directly, and $\epsilon(r)$ is then easily computed from the equation of state $\epsilon(P)$. Meanwhile, $\mu(r)$ can be obtained from $P(r)$ after inverting $P(\mu)$ to $\mu(P)$, and $n_i(r)$ and other properties can then be looked up in figure 8.4. In figure 8.6 we take an in-depth look at the maximum mass star without a phase transition:

- By definition, the pressure $P(R) = 0$ vanishes at the surface $R = 11.3\,\text{km}$, and the corresponding cumulative mass $m(R) = M = 1.77\,M_\odot$ evaluates to the total mass.
- The quark chemical potential $\mu(R)$ at the surface exceeds the vacuum value 300 MeV because of the bag shift (7.10). Fortunately, the central value $\mu(0) = 490\,\text{MeV}$ does not exceed 575 MeV, beyond which neglecting pion condensation was inconsistent.
- The kink around $\mu \approx 320\,\text{MeV}$ corresponds to the chiral crossover and takes place very close to the surface of the star, and the star has a thin crust in which the particle densities rapidly drops to near-vanishing values and the cumulative mass flattens out.

8.6 Consistent parameter fit in the one-loop large-N_c limit

As explained at the end of section 8.3, fitting parameters at tree-level is inconsistent because our calculation of the grand potential (8.19) can only be considered consistent in the one-loop large-N_c limit. In a fully consistent treatment, the parameters should be fit at the same level to which the grand potential is calculated. The inconsistent method is, however, the conventional approach taken in the literature. [Zsc+07; Sch+07b; Sch+09; Zac+15].

To conclude this chapter we examine the effects of using such a consistent approach. In the chiral limit $h = 0$, [Adh+17a] has consistently matched the parameters in the one-loop large-N_c limit by relating the physical masses to the pion decay constant and running couplings with the minimal subtraction renormalization scheme. Their work is generalized to the physical point $h \neq 0$ that we consider here in [Adh+17b], where their generalized inhomogeneous chiral condensate q can simply be set to $q = 0$ to recover our homogeneous condensate. They find the grand potential

$$\Omega = \frac{1}{2}\frac{m_R^2(\lambda)}{g_R^2(\lambda)}\Delta^2 + \frac{\lambda_R(\lambda)}{24 g_R(\lambda)^4}\Delta^4 - \frac{h_R(\lambda)}{g_R(\lambda)}\Delta + \frac{N_c N_f}{16\pi^2}\Delta^4\left[\frac{3}{2} + \log\frac{\Lambda^2}{\Delta^2}\right] + \Omega_q + \Omega_e, \tag{8.27}$$

where $\Omega_q + \Omega_e$ is the same contribution from quarks and electrons as in the two last lines of our grand potential (8.19). Here all the couplings $m_R^2(\Lambda)$, $\lambda_R(\Lambda)$, $g_R(\Lambda)$ and $h_R(\Lambda)$ run with

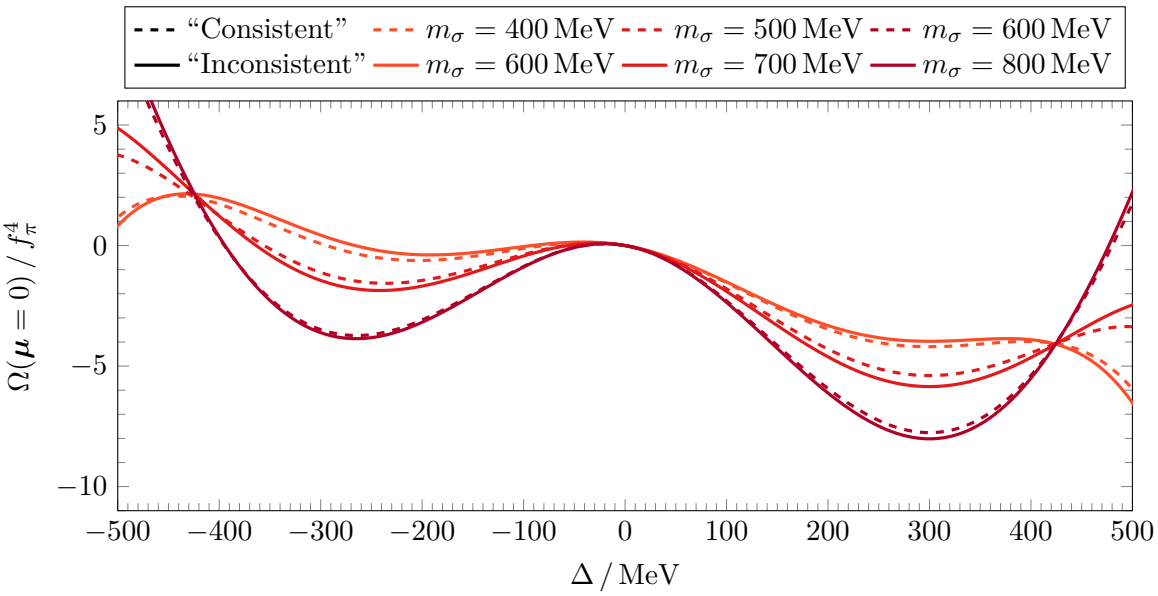

Figure 8.7: Compared to the inconsistently fit grand potential in figure 8.2, the consistently fit two-flavor grand potential (8.28) admits minima for $m_\sigma \geq 400\,\text{MeV}$ in vacuum, where $\boldsymbol{\mu} = \mathbf{0}$.

the renormalization scale Λ. After solving their renormalization group equations and inserting their solutions into the above expression, they find the following explicit grand potential in equation (7):

$$\begin{aligned}
\Omega = {} & \frac{3m_\pi^2 f_\pi^2}{4}\left\{1 - \frac{4m_q^2 N_c}{(4\pi)^2 f_\pi^2} m_\pi^2 F'(m_\pi^2)\right\}\frac{\Delta^2}{m_q^2} \\
& - \frac{m_\sigma^2 f_\pi^2}{4}\left\{1 + \frac{4m_q^2 N_c}{(4\pi)^2 f_\pi^2}\left[\left(1 - \frac{4m_q^2}{m_\sigma^2}\right)F(m_\sigma^2) + \frac{4m_q^2}{m_\sigma^2} - F(m_\pi^2) - m_\pi^2 F'(m_\pi^2)\right]\right\}\frac{\Delta^2}{m_q^2} \\
& + \frac{m_\sigma^2 f_\pi^2}{8}\left\{1 - \frac{4m_q^2 N_c}{(4\pi)^2 f_\pi^2}\left[\frac{4m_q^2}{m_\sigma^2}\log\frac{\Delta^2}{m_q^2} - \left(1 - \frac{4m_q^2}{m_\sigma^2}\right)F(m_\sigma^2) + F(m_\pi^2) + m_\pi^2 F'(m_\pi^2)\right]\right\}\frac{\Delta^4}{m_q^4} \\
& - \frac{m_\pi^2 f_\pi^2}{8}\left\{1 - \frac{4m_q^2 N_c}{(4\pi)^2 f_\pi^2} m_\pi^2 F'(m_\pi^2)\right\}\frac{\Delta^4}{m_q^4} - m_\pi^2 f_\pi^2\left\{1 - \frac{4m_q^2 N_c}{(4\pi)^2 f_\pi^2} m_\pi^2 F'(m_\pi^2)\right\}\frac{\Delta}{m_q} + \frac{3N_c}{(4\pi)^2}\Delta^4 \\
& + \Omega_q + \Omega_e,
\end{aligned} \tag{8.28}$$

where they have defined

$$F(p^2) = 2 - 2r\,\text{atan}\left(\frac{1}{r}\right), \qquad F'(p^2) = \frac{4m_q^2}{p^4 r}\,\text{atan}\left(\frac{1}{r}\right) - \frac{1}{p^2}, \qquad r = \sqrt{\frac{4m_q^2}{p^2} - 1}. \tag{8.29}$$

Note that in contrast to our dynamic masses (8.10), their m_q, m_π and m_σ refer exclusively to *vacuum masses*, and the dynamic quark mass is denoted Δ, equivalent to our $m_q = g\langle\sigma\rangle$. In our opinion, it is easiest to simply adopt their convention temporarily in this section, as any attempt to reconcile it with our convention would only clutter the already cluttered expression (8.28). Also note that the renormalization scale Λ has coincidentally disappeared from the original expression (8.27) upon substitution of the renormalized couplings!

Like before, we will fix m_q, m_π and f_π to the vacuum values in table 8.1, but vary m_σ. Whereas figure 8.2 shows that our original inconsistently fit grand potential only had stable minima for $m_\sigma \geq 600\,\text{MeV}$ in vacuum, figure 8.7 shows that it appears for $m_\sigma \geq 400\,\text{MeV}$ with the consistently fit grand potential. This allows us to set m_σ to values within its measured range $400\,\text{MeV} \leq m_\sigma \leq 550\,\text{MeV}$ without breaking the model!

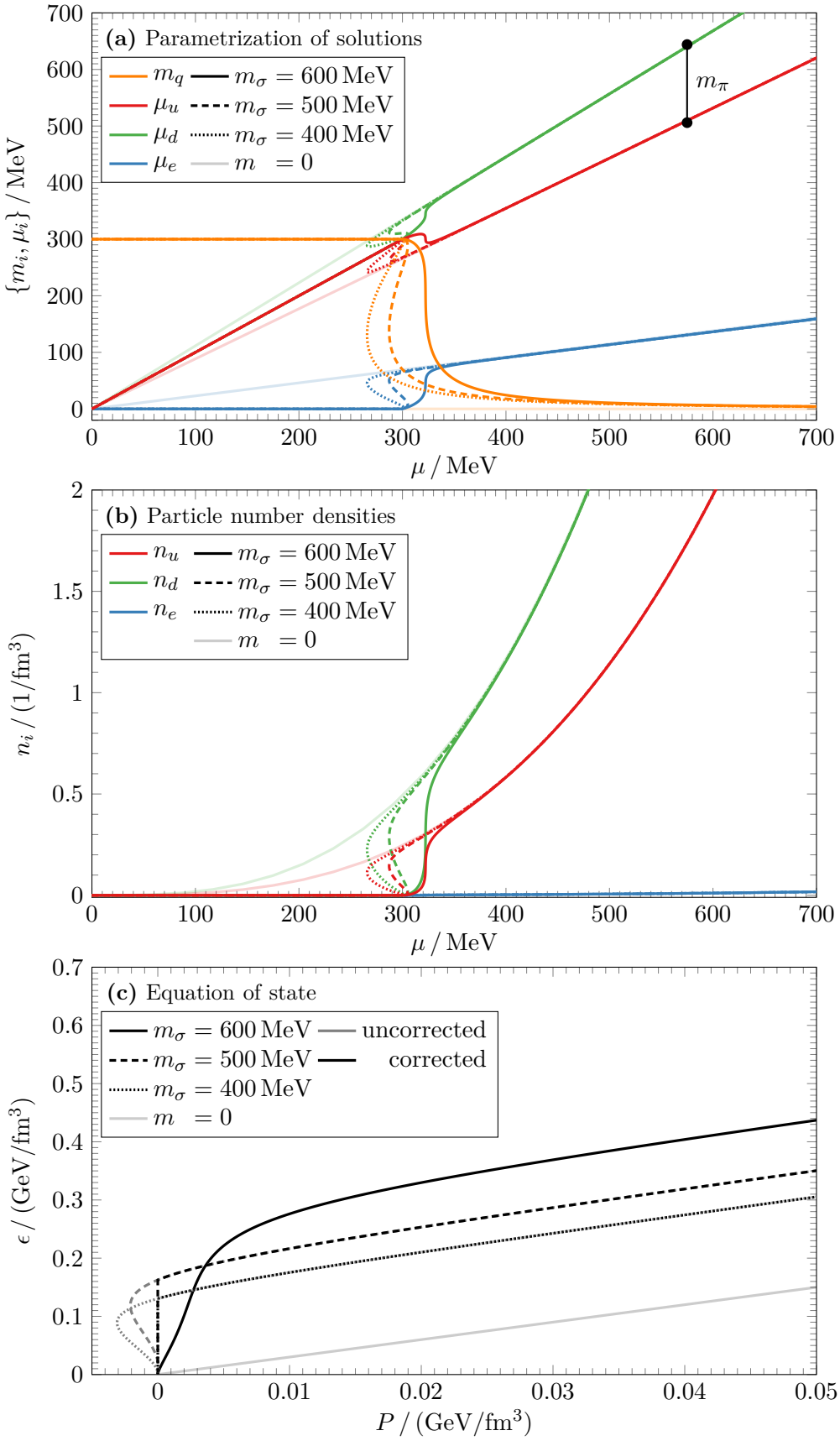

Figure 8.8: Results like those in figure 8.4, but with the consistently fit one-loop and large-N_c grand potential (8.28) and $m_\sigma = \{400, 500, 600\}\,\mathrm{MeV}$.

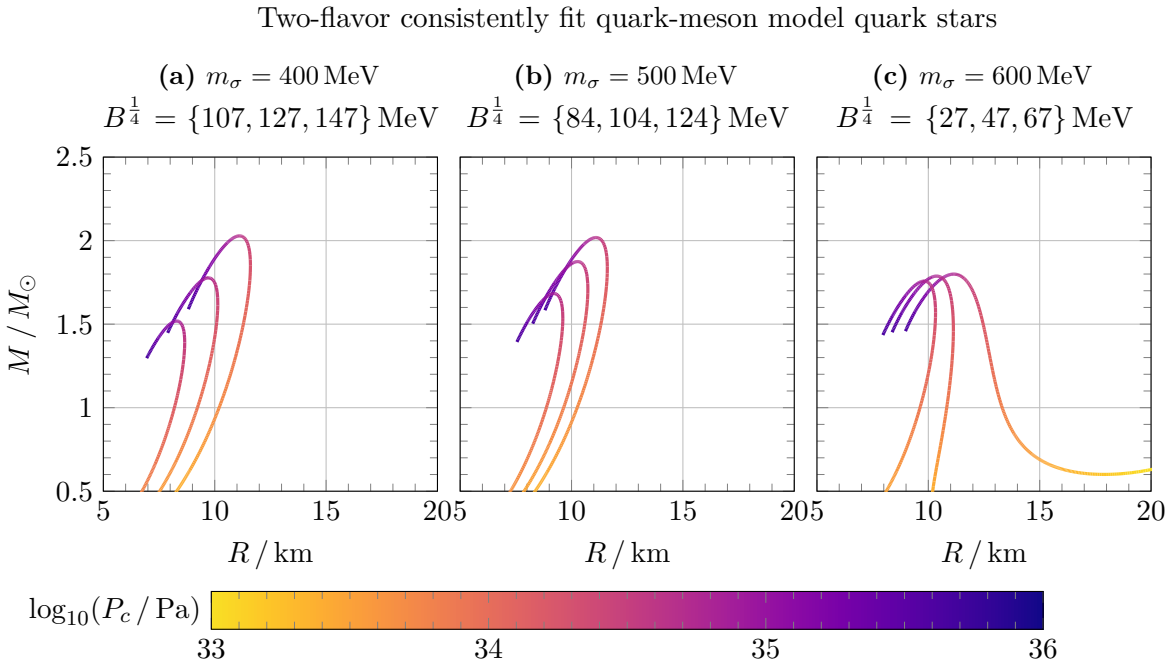

Figure 8.9: Results like those in figure 8.5, but with the equations of state in figure 8.4c from the consistently fit one-loop and large-N_c grand potential (8.28) and $m_\sigma = \{400, 500, 600\}\,\mathrm{MeV}$.

Repeating our earlier calculations with the new grand potential (8.28) for lower values of m_σ, we find the equation of state in figure 8.8, the lower bag constant bounds

$$B \geq (107.3\,\mathrm{MeV})^4 \quad \Big(\text{or } B - \mathcal{V}(f_\pi, \mathbf{0}) \geq (145.4\,\mathrm{MeV})^4\Big) \quad \Big(m_\sigma = 400\,\mathrm{MeV}\Big), \tag{8.30a}$$

$$B \geq \ (83.9\,\mathrm{MeV})^4 \quad \Big(\text{or } B - \mathcal{V}(f_\pi, \mathbf{0}) \geq (145.9\,\mathrm{MeV})^4\Big) \quad \Big(m_\sigma = 500\,\mathrm{MeV}\Big), \tag{8.30b}$$

$$B \geq \ (27.2\,\mathrm{MeV})^4 \quad \Big(\text{or } B - \mathcal{V}(f_\pi, \mathbf{0}) \geq (155.3\,\mathrm{MeV})^4\Big) \quad \Big(m_\sigma = 600\,\mathrm{MeV}\Big), \tag{8.30c}$$

and the mass-radius solutions in figure 8.9.

The "consistent" results with $m_\sigma = \{400, 500, 600\}\,\mathrm{MeV}$ are virtually identical to the "inconsistent" results with $m_\sigma = \{600, 700, 800\}\,\mathrm{MeV}$. This can be seen by comparing the individual features in figures 8.8 and 8.9 to those in figures 8.4 and 8.5, or more easily by noting that the vacuum potentials in figure 8.7, *which is the only difference between the two approaches*, more or less coincide with those in figure 8.2 that have about 200 MeV larger values of m_σ.

This approach shows the importance of fitting the parameters of the model consistently in order to achieve correspondence between experimental and model parameters. In our original inconsistent approach we had no other choice but to use too large values of m_σ to avoid breaking the model and generate any results at all, leaving us with a doubtful and unsatisfactory feeling. However, comparison with the consistent approach restores our trust in these results and tells us that we should not be too worried about fitting values of m_σ at tree-level that are about 200 MeV too large.

8.7 Summary

In this chapter we have modeled pure quark stars consisting of deconfined up and down quarks with the two-flavor quark-meson model. Our main results were the equation of state in figure 8.4, mass-radius solutions in figure 8.5 and the radial profile of a representative maximum mass star in figure 8.6. For $600\,\mathrm{MeV} \leq m_\sigma \leq 800\,\mathrm{MeV}$ and the corresponding lowest bag constants that respect the lower bounds (8.26) and hence instability of two-flavor quark matter, we obtained quark stars with maximum masses $1.7\,M_\odot \leq M \leq 2.0\,M_\odot$ and corresponding radii $R \approx 11\,\mathrm{km}$.

Chiral symmetry was restored in a crossover for $m_\sigma \geq 800\,\mathrm{MeV}$ and in a discontinuous phase transition for $m_\sigma < 800\,\mathrm{MeV}$. Our heart rates increased momentarily when we saw that neglecting pion condensation was an inconsistent approximation for $\mu \geq 575\,\mathrm{MeV}$, but stabilized when we saw that the chemical potential in the inspected maximum mass star did not exceed this. We found it difficult to fit measured values $400\,\mathrm{MeV} \leq m_\sigma \leq 550\,\mathrm{MeV}$ for the σ meson without breaking the model and had to make do with larger values, but later regained trust in our results when we explained this with the inconsistency of fitting parameters at tree-level to a grand potential that is calculated to one fermion loop.

Due to the previously discussed instability of two-flavor quark matter with respect to hadronic matter, pure two-flavor quark stars are unlikely to be realized in nature. Nevertheless, their analysis is a natural stepping stone for discussing possibly stable strange quark stars and hybrid stars with quark matter in the core.

Chapter 9

The Three-Flavor Quark-Meson Model

With three flavors, the effective low-energy degrees of freedom of quantum chromodynamics are the scalar and pseudoscalar mesons. In this chapter we will study the generalization of the quark-meson model in chapter 8 to three flavors, thereby throwing the strange quark into the mix. Most features of this model behave as natural and somewhat more complex generalizations of those in the two-flavor model. For example, we will handle the strange quark condensate in parallel with the common up and down quark condensate. Whereas there is a unique way of fixing the parameters in the two-flavor model, however, we will see that the three-flavor model presents us with a multitude of ways of doing it, so that some experimental values must be predicted rather than fitted.

Three-flavor models are particularly interesting for quark stars. While two-flavor quark matter is unstable with respect to hadronic matter, pure quark stars consisting only of strange quark matter would be stable and more likely to exist *if* the strange matter hypothesis is true. Due to the heavier mass of the strange quark, we expect its effects to become important in the mass-radius diagram only for stars that have a high central pressure and thus large chemical potentials.

This chapter is inspired by references [Sch+09] and [Len+00].

9.1 Lagrangian, vacuum and symmetries

The Lagrangian density of the three-flavor quark-meson model is [Sch+09; Len+00]

$$\mathcal{L} = \bar{q}\Big[i\partial\!\!\!/ + \mu\gamma^0 - g\big(\sigma_a + i\gamma^5\pi_a\big)T_a\Big]q + \operatorname{tr}\Big[(\partial_\mu\phi)^\dagger(\partial^\mu\phi)\Big] - \mathcal{V}(\sigma,\pi) \tag{9.1}$$

with the meson potential

$$\mathcal{V}(\sigma,\pi) = m^2\operatorname{tr}\Big[\phi^\dagger\phi\Big] + \lambda_1\Big[\operatorname{tr}(\phi^\dagger\phi)\Big]^2 + \lambda_2\operatorname{tr}\Big[(\phi^\dagger\phi)^2\Big] - \operatorname{tr}\Big[H(\phi+\phi^\dagger)\Big]. \tag{9.2}$$

The quark fields q and chemical potential matrix $\mu = \operatorname{diag}(\mu_u, \mu_d, \mu_s)$ now have the $N_f = 3$ flavors $\{u, d, s\}$, while σ_a and π_a are members of the scalar ($J^P = 0^+$) and pseudoscalar ($J^P = 0^-$) meson nonets, packed into the $N_f \times N_f$ meson matrix $\phi = \phi_a T_a = (\sigma_a + i\pi_a)T_a$. The eight $SU(3)$ generators $T_a = \lambda_a/2$ in flavor space are extended with the identity in the

common normalization $\operatorname{tr}[T_a T_b] = \delta_{ab}/2$ of the Gell-Mann matrices

$$\lambda_0 = \begin{bmatrix} \sqrt{\frac{2}{3}} & 0 & 0 \\ 0 & \sqrt{\frac{2}{3}} & 0 \\ 0 & 0 & \sqrt{\frac{2}{3}} \end{bmatrix}, \quad \lambda_1 = \begin{bmatrix} 0 & 1 & 0 \\ 1 & 0 & 0 \\ 0 & 0 & 0 \end{bmatrix}, \quad \lambda_2 = \begin{bmatrix} 0 & -i & 0 \\ i & 0 & 0 \\ 0 & 0 & 0 \end{bmatrix},$$
$$\lambda_3 = \begin{bmatrix} 1 & 0 & 0 \\ 0 & -1 & 0 \\ 0 & 0 & 0 \end{bmatrix}, \quad \lambda_4 = \begin{bmatrix} 0 & 0 & 1 \\ 0 & 0 & 0 \\ 1 & 0 & 0 \end{bmatrix}, \quad \lambda_5 = \begin{bmatrix} 0 & 0 & -i \\ 0 & 0 & 0 \\ i & 0 & 0 \end{bmatrix}, \tag{9.3}$$
$$\lambda_6 = \begin{bmatrix} 0 & 0 & 0 \\ 0 & 0 & 1 \\ 0 & 1 & 0 \end{bmatrix}, \quad \lambda_7 = \begin{bmatrix} 0 & 0 & 0 \\ 0 & 0 & -i \\ 0 & i & 0 \end{bmatrix}, \quad \lambda_8 = \begin{bmatrix} \frac{1}{\sqrt{3}} & 0 & 0 \\ 0 & \frac{1}{\sqrt{3}} & 0 \\ 0 & 0 & -\frac{2}{\sqrt{3}} \end{bmatrix}.$$

Like before, the Lagrangian has $U(1)_V \times U(1)_A \times SU(N_f)_L \times SU(N_f)_R$ symmetry in the absence of the explicit symmetry breakers h_a in the matrix $H = h_a T_a$. Moreover, there are now *two* quartic couplings λ_1 and λ_2, not to be confused with the Gell-Mann matrices (9.3). This can be understood from the *Cayley-Hamilton theorem* [Hon+08, equation (1) and (2)], which links the N traces $\operatorname{tr} A, \ldots, \operatorname{tr} A^N$ of any $N \times N$ matrix A. With three flavors we can therefore form *two* independent coupling terms $\lambda_1 \operatorname{tr}[(\phi^\dagger \phi)]^2$ and $\lambda_2 \operatorname{tr}[(\phi^\dagger \phi)^2]$ up to quadratic order[1] in the fields, while only one can be constructed with two flavors. Every other feature of the Lagrangian is identical to or a natural generalization of that in the corresponding two-flavor Lagrangian (8.1).

This general form of the model has thirteen undetermined parameters g, m^2, λ_1, λ_2 and $\{h_0, \ldots, h_8\}$. We continue to neglect pion condensation by setting $\langle \pi_a \rangle = 0$, so a nonzero symmetry breaker h_a creates a non-vanishing vacuum expectation value of the corresponding scalar field $\langle \sigma_a \rangle$, which in turn creates a nonzero quark condensate $\langle \bar{q} T_a q \rangle$ in vacuum through the Yukawa interaction in the Lagrangian (9.1). In particular, this vacuum expectation value should have the same vanishing electrical charge as the vacuum. We therefore only allow for flavor-like charge-neutral condensates such as $\langle \bar{u} u \rangle$ in the vacuum, and no mixed-flavor charged condensates like $\langle \bar{u} d \rangle$. To accomplish this, we set all symmetry breakers to zero *except* those that correspond to diagonal flavor-space matrices (9.3), or T_a, namely $\{h_0, h_3, h_8\} \neq 0$.

Using different combinations of the three remaining nonzero symmetry breakers $\{h_0, h_3, h_8\}$, one can study different symmetry breaking patterns among the u, d and s quarks. By setting only $h_0 \neq 0$, we see that the first Gell-Mann matrix λ_0 weighs all three quarks equally with common mass $m_u = m_d = m_s$. If we also unlock $h_8 \neq 0$, the last matrix λ_8 separates the strange and non-strange quarks with $m_u = m_d \neq m_s$. Including all three symmetry breakers with $h_3 \neq 0$, too, the fourth matrix λ_3 also distinguishes the non-strange quarks and treats all flavors with separate masses $m_u \neq m_d \neq m_s$. These different symmetry breaking patterns are discussed in more detail in [Len+00, section III]. Since we treated up and down quarks with degenerate mass in chapter 8, we will set $h_3 = 0$ and keep $\{h_0, h_8\} \neq 0$ to account for the heavier strange quark separately from the non-strange quarks. This leaves the six unknown parameters g, m^2, λ_1, λ_2, h_0 and h_8 that will later be fit to as many experimental values.

The explicit symmetry breakers $\{h_0, h_8\} \neq 0$ dig a global minimum for the vacuum at

$$\sigma_a = \langle \sigma_a \rangle \quad \text{and} \quad \pi_a = \langle \pi_a \rangle = 0, \quad \text{where only } \langle \sigma_0 \rangle \neq 0 \text{ and } \langle \sigma_8 \rangle \neq 0 \text{ are nonzero.} \tag{9.4}$$

Like before, we jump down into the hole (9.4) and study the quantum fluctuations $\tilde{\sigma}_a$ and $\tilde{\pi}_a$ of the meson fields by writing

$$\sigma_a = \langle \sigma_a \rangle + \tilde{\sigma}_a \qquad \text{and} \qquad \pi_a = \langle \pi_a \rangle + \tilde{\pi}_a. \tag{9.5}$$

[1] That precisely fourth order is the target implies that the theory is renormalizable, in the sense that divergences can be removed by shifting the couplings already in the Lagrangian with counterterms. Divergences from, say, sixth-order terms in the Lagrangian could only have been removed by counterterms in higher-order terms and would make the theory non-renormalizable.

We will shortly come back to the precise location of the vacuum, but first examine how it couples to the quarks. Coupled to the nonzero expectation values (9.4), the Yukawa term in the Lagrangian (9.1) reads

$$\begin{aligned} &- g\bar{q}\big(\langle\sigma_0\rangle T_0 + \langle\sigma_8\rangle T_8\big)q \\ &= -\frac{g}{2}\begin{bmatrix} u^\dagger\gamma^0 \\ d^\dagger\gamma^0 \\ s^\dagger\gamma^0 \end{bmatrix}^{\mathsf{T}} \begin{bmatrix} \sqrt{\frac{2}{3}}\langle\sigma_0\rangle + \frac{1}{\sqrt{3}}\langle\sigma_8\rangle & 0 & 0 \\ 0 & \sqrt{\frac{2}{3}}\langle\sigma_0\rangle + \frac{1}{\sqrt{3}}\langle\sigma_8\rangle & 0 \\ 0 & 0 & \sqrt{\frac{2}{3}}\langle\sigma_0\rangle - \frac{2}{\sqrt{3}}\langle\sigma_8\rangle \end{bmatrix} \begin{bmatrix} u \\ d \\ s \end{bmatrix}. \end{aligned} \tag{9.6}$$

In particular, it mixes σ_0 and σ_8 interactions with all three quarks. For conceptual cleanliness, we seek a transformation from the mixed σ_0-σ_8-basis to a strangeness-separated σ_x-σ_y-basis in which the up and down quarks couple only to σ_x and the strange quark only to σ_y. This is accomplished by

$$\begin{bmatrix} \sigma_x \\ \sigma_y \end{bmatrix} = M \begin{bmatrix} \sigma_0 \\ \sigma_8 \end{bmatrix}, \qquad \text{where} \qquad M = M^{-1} = M^{\mathsf{T}} = \frac{1}{\sqrt{3}}\begin{bmatrix} \sqrt{2} & 1 \\ 1 & -\sqrt{2} \end{bmatrix}. \tag{9.7}$$

We also define the transformed symmetry breakers $[h_x, h_y]^{\mathsf{T}} = M[h_0, h_8]^{\mathsf{T}}$ using the same transformation. In the new basis (9.7), the Yukawa coupling (9.6) takes our sought-after form

$$-\sum_{f=\{u,d,s\}} m_f \bar{q}_f q_f \quad \text{with quark masses} \quad m_u = m_d = m_x = \frac{g\langle\sigma_x\rangle}{2} \quad \text{and} \quad m_s = m_y = \frac{g\langle\sigma_y\rangle}{\sqrt{2}}. \tag{9.8}$$

Finally, we examine how the meson potential (9.2) behaves in and around the minimum (9.4) by looking for its mass-generating expansion

$$\mathcal{V}(\sigma,\pi) \simeq \mathcal{V}(\langle\sigma\rangle,\langle\pi\rangle) + \frac{1}{2}\big(m^2_{\sigma\sigma}\big)_{ab}\tilde{\sigma}_a\tilde{\sigma}_b + \frac{1}{2}\big(m^2_{\pi\pi}\big)_{ab}\tilde{\pi}_a\tilde{\pi}_b. \tag{9.9}$$

Like in chapter 8, we will use $\mathcal{V}(\langle\sigma\rangle,\langle\pi\rangle)$ in the grand potential, relate $\partial\mathcal{V}/\partial\sigma_x = \partial\mathcal{V}/\partial\sigma_y = 0$ to the minima $\{\langle\sigma_x\rangle,\langle\sigma_y\rangle\}$ and $\{h_x, h_y\}$, and fit the (squared) curvature masses $\partial^2\mathcal{V}/\partial\sigma_a\,\partial\sigma_b = \big(m^2_{\sigma\sigma}\big)_{ab}$ and $\partial^2\mathcal{V}/\partial\pi_a\,\partial\pi_b = \big(m^2_{\pi\pi}\big)_{ab}$ to particle masses. To do so, we need the flavor-space traces

$$\operatorname{tr}\big[\phi^\dagger\phi\big] = (\sigma_a - i\pi_a)(\sigma_b + i\pi_b)\operatorname{tr}\big[T_aT_b\big] = \frac{1}{2}\big(\sigma_a^2 + \pi_a^2\big), \tag{9.10a}$$

$$\operatorname{tr}\big[(\phi^\dagger\phi)^2\big] = (\sigma_a - i\pi_a)(\sigma_b + i\pi_b)(\sigma_a - i\pi_c)(\sigma_b + i\pi_d)\operatorname{tr}\big[T_aT_bT_cT_d\big], \tag{9.10b}$$

$$\operatorname{tr}\big[H(\phi + \phi^\dagger)\big] = 2h_a\sigma_b\operatorname{tr}\big[T_aT_b\big] = h_a\sigma_a. \tag{9.10c}$$

The quadruple product traces $\operatorname{tr}[T_aT_bT_cT_d]$ are more challenging than the double product traces $\operatorname{tr}[T_aT_b] = \delta_{ab}/2$. If one figures out the structure constants f_{abc} and d_{abc} defined by the commutators $[T_a, T_b] = if_{abc}T_c$ and anti-commutators $\{T_a, T_b\} = d_{abc}T_c$, these traces can be done with pen, paper and painkillers by bootstrapping traces of the Gell-Mann matrices like

$$\operatorname{tr}\Big[T_aT_b\Big] = \frac{1}{2}\delta_{ab}, \tag{9.11a}$$

$$\operatorname{tr}\Big[T_aT_bT_c\Big] = \frac{1}{2}\operatorname{tr}\Big[T_a\Big(\overbrace{[T_b,T_c]}^{if_{bcd}T_d} + \overbrace{\{T_b,T_c\}}^{d_{bcd}T_d}\Big)\Big] \overset{\text{use (9.11a)}}{=} \frac{1}{2^2}\Big(if_{bca} + d_{bca}\Big), \tag{9.11b}$$

$$\operatorname{tr}\Big[T_aT_bT_cT_d\Big] = \frac{1}{2}\operatorname{tr}\Big[T_aT_b\Big(\underbrace{[T_c,T_d]}_{if_{cde}T_e} + \underbrace{\{T_c,T_d\}}_{d_{cde}T_e}\Big)\Big] \underset{\text{use (9.11b)}}{=} \frac{1}{2^3}\Big(if_{cde} + d_{cde}\Big)\Big(if_{bea} + d_{bea}\Big). \tag{9.11c}$$

However, with our explicit knowledge (9.3) of the matrices, it is easier and less error-prone to simply calculate all the traces by brute force with a symbolic computer program. Using the

program in appendix E, we create a long explicit representation of $\mathcal{V}(\sigma,\pi)$. Evaluated in the minimum (9.4), its value is

$$\mathcal{V}(\langle\sigma\rangle,\langle\pi\rangle) = \frac{m^2}{2}\Big[\langle\sigma_x\rangle^2+\langle\sigma_y\rangle^2\Big] + \frac{\lambda_1}{4}\Big[\langle\sigma_x\rangle^2+\langle\sigma_y\rangle^2\Big]^2 + \frac{\lambda_2}{8}\Big[\langle\sigma_x\rangle^4+2\langle\sigma_y\rangle^4\Big] - h_x\langle\sigma_x\rangle - h_y\langle\sigma_y\rangle. \tag{9.12}$$

The locations of the nonzero minima $\langle\sigma_x\rangle$ and $\langle\sigma_y\rangle$ are determined by taking first derivatives of the explicit representation before evaluating it in the minimum (9.4). We find that all $\partial\mathcal{V}/\partial\pi_a = 0$ and $\partial\mathcal{V}/\partial\sigma_a = -h_a = 0$ for $a \neq \{0,8\}$ vanish by themselves, while we demand

$$0 = \frac{\partial\mathcal{V}}{\partial\sigma_x} = \langle\sigma_x\rangle\Big[m^2+\lambda_1\Big(\langle\sigma_x\rangle^2+\langle\sigma_y\rangle^2\Big)+\frac{\lambda_2}{2}\langle\sigma_x\rangle^2\Big] - h_x, \tag{9.13a}$$

$$0 = \frac{\partial\mathcal{V}}{\partial\sigma_y} = \langle\sigma_y\rangle\Big[m^2+\lambda_1\Big(\langle\sigma_x\rangle^2+\langle\sigma_y\rangle^2\Big)+\lambda_2\langle\sigma_y\rangle^2\Big] - h_y. \tag{9.13b}$$

Things get messier and our computational approach really comes in handy when evaluating the mass-generating second derivatives

$$\big(m^2_{\sigma\sigma}\big)_{ab} = \frac{\partial^2\mathcal{V}}{\partial\sigma_a\,\partial\sigma_b} \qquad \text{and} \qquad \big(m^2_{\pi\pi}\big)_{ab} = \frac{\partial^2\mathcal{V}}{\partial\pi_a\,\partial\pi_b} \tag{9.14}$$

in the minimum (9.4). All mixed derivatives $\partial^2\mathcal{V}/\partial\sigma_a\,\partial\pi_b = 0$ automatically vanish. Grouped by common values, the nonzero entries of the scalar mass matrix are

$$\left.\begin{aligned}
\big(m^2_{\sigma\sigma}\big)_{00} &= m^2 + \frac{\lambda_1}{3}\Big(4\sqrt{2}\langle\sigma_x\rangle\langle\sigma_y\rangle + 7\langle\sigma_x\rangle^2 + 5\langle\sigma_y\rangle^2\Big) + \lambda_2\Big(\langle\sigma_x\rangle^2+\langle\sigma_y\rangle^2\Big),\\
\big(m^2_{\sigma\sigma}\big)_{11}\\
\big(m^2_{\sigma\sigma}\big)_{22}\\
\big(m^2_{\sigma\sigma}\big)_{33}
&= m^2 + \lambda_1\Big(\langle\sigma_x\rangle^2+\langle\sigma_y\rangle^2\Big) + \frac{3}{2}\lambda_2\langle\sigma_x\rangle^2,\\
\big(m^2_{\sigma\sigma}\big)_{44}\\
\big(m^2_{\sigma\sigma}\big)_{55}\\
\big(m^2_{\sigma\sigma}\big)_{66}\\
\big(m^2_{\sigma\sigma}\big)_{77}
&= m^2 + \lambda_1\Big(\langle\sigma_x\rangle^2+\langle\sigma_y\rangle^2\Big) + \frac{\lambda_2}{2}\Big(\sqrt{2}\langle\sigma_x\rangle\langle\sigma_y\rangle + \langle\sigma_x\rangle^2 + 2\langle\sigma_y\rangle^2\Big),\\
\big(m^2_{\sigma\sigma}\big)_{88} &= m^2 - \frac{\lambda_1}{3}\Big(4\sqrt{2}\langle\sigma_x\rangle\langle\sigma_y\rangle - 5\langle\sigma_x\rangle^2 - 7\langle\sigma_y\rangle^2\Big) + \frac{\lambda_2}{2}\Big(\langle\sigma_x\rangle^2 + 4\langle\sigma_y\rangle^2\Big),\\
\big(m^2_{\sigma\sigma}\big)_{08}\\
\big(m^2_{\sigma\sigma}\big)_{80}
&= \frac{2}{3}\lambda_1\Big(\sqrt{2}\langle\sigma_x\rangle^2 - \sqrt{2}\langle\sigma_y\rangle^2 - \langle\sigma_x\rangle\langle\sigma_y\rangle\Big) + \frac{\lambda_2}{\sqrt{2}}\Big(\langle\sigma_x\rangle^2 - 2\langle\sigma_y\rangle^2\Big).
\end{aligned}\right. \tag{9.15a}$$

The nonzero entries of the pseudoscalar mass matrix are

$$\left.\begin{aligned}
\big(m^2_{\pi\pi}\big)_{00} &= m^2 + \lambda_1\Big(\langle\sigma_x\rangle^2+\langle\sigma_y\rangle^2\Big) + \frac{\lambda_2}{3}\Big(\langle\sigma_x\rangle^2+\langle\sigma_y\rangle^2\Big),\\
\big(m^2_{\pi\pi}\big)_{11}\\
\big(m^2_{\pi\pi}\big)_{22}\\
\big(m^2_{\pi\pi}\big)_{33}
&= m^2 + \lambda_1\Big(\langle\sigma_x\rangle^2+\langle\sigma_y\rangle^2\Big) + \frac{\lambda_2}{2}\langle\sigma_x\rangle^2,\\
\big(m^2_{\pi\pi}\big)_{44}\\
\big(m^2_{\pi\pi}\big)_{55}\\
\big(m^2_{\pi\pi}\big)_{66}\\
\big(m^2_{\pi\pi}\big)_{77}
&= m^2 + \lambda_1\Big(\langle\sigma_x\rangle^2+\langle\sigma_y\rangle^2\Big) - \frac{\lambda_2}{2}\Big(\sqrt{2}\langle\sigma_x\rangle\langle\sigma_y\rangle - \langle\sigma_x\rangle^2 - 2\langle\sigma_y\rangle^2\Big),\\
\big(m^2_{\pi\pi}\big)_{88} &= m^2 + \lambda_1\Big(\langle\sigma_x\rangle^2+\langle\sigma_y\rangle^2\Big) + \frac{\lambda_2}{6}\Big(\langle\sigma_x\rangle^2 + 4\langle\sigma_y\rangle^2\Big),\\
\big(m^2_{\pi\pi}\big)_{08}\\
\big(m^2_{\pi\pi}\big)_{80}
&= \frac{\lambda_2}{6}\Big(\sqrt{2}\langle\sigma_x\rangle^2 - 2\sqrt{2}\langle\sigma_y\rangle^2\Big).
\end{aligned}\right. \tag{9.15b}$$

Notice that both matrices are non-diagonal due to the nonzero $\{08, 80\}$ corner entries. However, it is only fields corresponding to diagonal masses that represent true mass eigenstates of physically propagating particles: [Len+00]

- The three diagonal masses $\big(m^2_{\sigma\sigma}\big)_{11} = \big(m^2_{\sigma\sigma}\big)_{22} = \big(m^2_{\sigma\sigma}\big)_{33} = m^2_{a_0}$ correspond to one degenerate mass of the charged $a_0^\pm = (\sigma_1 \pm i\sigma_2)/\sqrt{2}$ and neutral $a_0^0 = \sigma_3$ mesons.
- The three diagonal masses $\big(m^2_{\pi\pi}\big)_{11} = \big(m^2_{\pi\pi}\big)_{22} = \big(m^2_{\pi\pi}\big)_{33} = m^2_{\pi}$ correspond to one degenerate mass of the charged $\pi^\pm = (\pi_1 \pm i\pi_2)/\sqrt{2}$ and neutral $\pi^0 = \pi_3$ mesons.
- The four diagonal masses $\big(m^2_{\sigma\sigma}\big)_{44} = \big(m^2_{\sigma\sigma}\big)_{55} = \big(m^2_{\sigma\sigma}\big)_{66} = \big(m^2_{\sigma\sigma}\big)_{77} = m^2_{\kappa}$ correspond to one degenerate mass of the charged $\kappa^\pm = (\sigma_4 \pm i\sigma_5)/\sqrt{2}$ and neutral $\kappa^0 = (\sigma_6 + i\sigma_7)/\sqrt{2}$ and $\bar\kappa^0 = (\sigma_6 - i\sigma_7)/\sqrt{2}$ mesons.
- The four diagonal masses $\big(m^2_{\pi\pi}\big)_{44} = \big(m^2_{\pi\pi}\big)_{55} = \big(m^2_{\pi\pi}\big)_{66} = \big(m^2_{\pi\pi}\big)_{77} = m^2_{K}$ correspond to one degenerate mass of the charged $K^\pm = (\pi_4 \pm i\pi_5)/\sqrt{2}$ and neutral $K^0 = (\pi_6 + i\pi_7)/\sqrt{2}$ and $\bar K^0 = (\pi_6 - i\pi_7)/\sqrt{2}$ mesons.
- The *diagonalization* $\{m^2_\sigma, m^2_{f_0}\}$ of the non-diagonal matrix sector $\{\big(m^2_{\sigma\sigma}\big)_{00}, \big(m^2_{\sigma\sigma}\big)_{88}, \big(m^2_{\sigma\sigma}\big)_{08}, \big(m^2_{\sigma\sigma}\big)_{80}\}$ corresponds to two different masses of the f_0 and σ mesons.
- The *diagonalization* $\{m^2_\eta, m^2_{\eta'}\}$ of the non-diagonal matrix sector $\{\big(m^2_{\pi\pi}\big)_{00}, \big(m^2_{\pi\pi}\big)_{88}, \big(m^2_{\pi\pi}\big)_{08}, \big(m^2_{\pi\pi}\big)_{80}\}$ corresponds to two different masses of the η and η' mesons.

The two diagonalizations are achieved by two rotations

$$\begin{bmatrix} f_0 \\ \sigma \end{bmatrix} = \begin{bmatrix} \cos\theta_\sigma & -\sin\theta_\sigma \\ \sin\theta_\sigma & \cos\theta_\sigma \end{bmatrix} \begin{bmatrix} \sigma_8 \\ \sigma_0 \end{bmatrix} \qquad \text{and} \qquad \begin{bmatrix} \eta \\ \eta' \end{bmatrix} = \begin{bmatrix} \cos\theta_\pi & -\sin\theta_\pi \\ \sin\theta_\pi & \cos\theta_\pi \end{bmatrix} \begin{bmatrix} \pi_8 \\ \pi_0 \end{bmatrix} \tag{9.16}$$

of the $\{\sigma_0, \sigma_8\}$ and $\{\pi_0, \pi_8\}$ fields parametrized by two mixing angles $\{\theta_\sigma, \theta_\pi\}$. To find the pseudoscalar angle θ_π, for example, we invert transformation (9.16) and use the trigonometric identities $\cos^2\theta_\pi - \sin^2\theta_\pi = \cos 2\theta_\pi$ and $2\sin\theta_\pi\cos\theta_\pi = \sin 2\theta_\pi$ to expand

$$\begin{aligned} \sum_{\substack{a=\{0,8\}\\ b=\{0,8\}}} \big(m^2_{\pi\pi}\big)_{ab}\tilde\pi_a\tilde\pi_b = &\Big\{\big(m^2_{\pi\pi}\big)_{00}\sin^2\theta_\pi + \big(m^2_{\pi\pi}\big)_{88}\cos^2\theta_\pi + \big(m^2_{\pi\pi}\big)_{08}\sin 2\theta_\pi\Big\}\,\tilde\eta^2 \\ &+ \Big\{\big(m^2_{\pi\pi}\big)_{00}\cos^2\theta_\pi + \big(m^2_{\pi\pi}\big)_{88}\sin^2\theta_\pi - \big(m^2_{\pi\pi}\big)_{08}\sin 2\theta_\pi\Big\}\,\tilde\eta'^2 \\ &+ \underbrace{\Big\{2\Big[\big(m^2_{\pi\pi}\big)_{00} - \big(m^2_{\pi\pi}\big)_{88}\Big]\sin 2\theta_\pi + 2\big(m^2_{\pi\pi}\big)_{08}\cos 2\theta_\pi\Big\}}_{\text{0 by demand!}}\,\tilde\eta\tilde\eta', \end{aligned} \tag{9.17}$$

and then require the indicated coefficient of $\tilde\eta\tilde\eta'$ to vanish. The scalar angle θ_σ is found in the same way, only with $\{m^2_{\pi\pi}, \eta, \eta'\} \to \{m^2_{\sigma\sigma}, f_0, \sigma\}$. Thus, the third line gives the mixing angles

$$\theta_\sigma = \frac{1}{2}\arctan\left[\frac{2\big(m^2_{\sigma\sigma}\big)_{08}}{\big(m^2_{\sigma\sigma}\big)_{88} - \big(m^2_{\sigma\sigma}\big)_{00}}\right] \quad \text{and} \quad \theta_\pi = \frac{1}{2}\arctan\left[\frac{2\big(m^2_{\pi\pi}\big)_{08}}{\big(m^2_{\pi\pi}\big)_{88} - \big(m^2_{\pi\pi}\big)_{00}}\right]. \tag{9.18}$$

This in turn fixes the curvature masses of the pseudoscalar $\{\eta, \eta'\}$ mesons as their coefficients on the two first lines in the sum (9.17), and analogously for the scalar $\{f_0, \sigma\}$ mesons. To be very clear, the diagonalized mass-generating meson potential (9.9) can now be explicitly written

$$\begin{aligned} \mathcal{V}(\sigma,\pi) \simeq \mathcal{V}(\langle\sigma\rangle,\langle\pi\rangle) &+ \frac{1}{2}m^2_{f_0}\tilde f_0{}^2 + \frac{1}{2}m^2_\sigma\tilde\sigma^2 \;+ \frac{1}{2}m^2_{a_0}\sum_{a_0=\{a_0^+,a_0^-,a_0^0\}}\tilde a_0^2 \;+ \frac{1}{2}m^2_\kappa\sum_{\kappa=\{\kappa^+,\kappa^-,\kappa^0,\bar\kappa^0\}}\tilde\kappa^2 \\ &+ \frac{1}{2}m^2_\eta\tilde\eta^2 \;+ \frac{1}{2}m^2_{\eta'}\tilde\eta'^2 + \frac{1}{2}m^2_\pi\sum_{\pi=\{\pi^+,\pi^-,\pi^0\}}\tilde\pi^2 \;+ \frac{1}{2}m^2_K\sum_{K=\{K^+,K^-,K^0,\bar K^0\}}\tilde K^2. \end{aligned} \tag{9.19}$$

This shows very elaborately how the three couplings $\{m^2, \lambda_1, \lambda_2\}$, through the mass matrices

(9.15) and the mixing angles (9.18), generate the eight scalar and pseudoscalar particle masses

$$
\begin{aligned}
m_{f_0}^2 &= \left(m_{\sigma\sigma}^2\right)_{00} \sin^2\theta_\sigma + \left(m_{\sigma\sigma}^2\right)_{88} \cos^2\theta_\sigma + \left(m_{\sigma\sigma}^2\right)_{08} \sin 2\theta_\sigma, && \text{(9.20a)}\\
m_{\sigma}^2 &= \left(m_{\sigma\sigma}^2\right)_{00} \cos^2\theta_\sigma + \left(m_{\sigma\sigma}^2\right)_{88} \sin^2\theta_\sigma - \left(m_{\sigma\sigma}^2\right)_{08} \sin 2\theta_\sigma, && \text{(9.20b)}\\
m_{a_0}^2 &= \left(m_{\sigma\sigma}^2\right)_{11} = \left(m_{\sigma\sigma}^2\right)_{22} = \left(m_{\sigma\sigma}^2\right)_{33}, && \text{(9.20c)}\\
m_{\kappa}^2 &= \left(m_{\sigma\sigma}^2\right)_{44} = \left(m_{\sigma\sigma}^2\right)_{55} = \left(m_{\sigma\sigma}^2\right)_{66} = \left(m_{\sigma\sigma}^2\right)_{77}, && \text{(9.20d)}\\
m_{\eta}^2 &= \left(m_{\pi\pi}^2\right)_{00} \sin^2\theta_\pi + \left(m_{\pi\pi}^2\right)_{88} \cos^2\theta_\pi + \left(m_{\pi\pi}^2\right)_{08} \sin 2\theta_\pi, && \text{(9.20e)}\\
m_{\eta'}^2 &= \left(m_{\pi\pi}^2\right)_{00} \cos^2\theta_\pi + \left(m_{\pi\pi}^2\right)_{88} \sin^2\theta_\pi - \left(m_{\pi\pi}^2\right)_{08} \sin 2\theta_\pi, && \text{(9.20f)}\\
m_{\pi}^2 &= \left(m_{\pi\pi}^2\right)_{11} = \left(m_{\pi\pi}^2\right)_{22} = \left(m_{\pi\pi}^2\right)_{33}, && \text{(9.20g)}\\
m_{K}^2 &= \left(m_{\pi\pi}^2\right)_{44} = \left(m_{\pi\pi}^2\right)_{55} = \left(m_{\pi\pi}^2\right)_{66} = \left(m_{\pi\pi}^2\right)_{77}. && \text{(9.20h)}
\end{aligned}
$$

These relations will come in handy when we fit the parameters of the model in section 9.3.

9.2 Grand potential

Let us calculate the grand potential Ω in the same way as we did with two flavors in section 8.2, integrating over one fermion loop and neglecting pion condensation by setting $\langle\pi\rangle = 0$ while using the mean-field approximation for $\langle\sigma_x\rangle$ and $\langle\sigma_y\rangle$, determining them retrospectively according to the self-consistency equations

$$
\frac{\partial\Omega}{\partial\langle\sigma_x\rangle} = \frac{\partial\Omega}{\partial\langle\sigma_y\rangle} = 0. \tag{9.21}
$$

As explained in chapter 8, this is inconsistent in terms of the number of loops considered for the fermionic and bosonic fields, but consistent in the **one-loop large-N_c limit**.

The calculation proceeds more or less identically up to the non-renormalized grand potential (8.17), only with a different vacuum potential $\mathcal{V}(\langle\sigma\rangle, 0)$, $N_f = 3$ flavors and $m_u = m_d = m_x \neq m_y = m_s$. In addition, instead of using one common renormalization scale Λ, we operate with two separate scales Λ_x and Λ_y for the non-strange and strange quarks. We comment on this in the next section. This gives the divergent grand potential

$$
\begin{aligned}
\Omega(\langle\sigma\rangle, \boldsymbol{\mu}) = \mathcal{V}(\langle\sigma\rangle, 0) &+ \frac{N_c m_x^4}{8\pi^2}\left[\frac{1}{\epsilon} + \frac{3}{2} + \log\left(\frac{\Lambda_x^2}{m_x^2}\right)\right] + \frac{N_c m_y^4}{16\pi^2}\left[\frac{1}{\epsilon} + \frac{3}{2} + \log\left(\frac{\Lambda_y^2}{m_y^2}\right)\right]\\
&- \sum_{f=1}^{N_c} \frac{N_c}{24\pi^2}\left[\left(2\mu_f^2 - 5m_f^2\right)\mu_f\sqrt{\mu_f^2 - m_f^2} + 3m_f^4 \operatorname{asinh}\left(\sqrt{\frac{\mu_f^2}{m_f^2} - 1}\right)\right].
\end{aligned} \tag{9.22}
$$

The divergence $N_c(2m_x^4 + m_y^2)/16\pi^2\epsilon = N_c g^4(\langle\sigma_x\rangle^4 + 2\langle\sigma_y\rangle^4)/128\epsilon$ from the pole in ϵ can again be absorbed by $\lambda_2(\langle\sigma_x\rangle^4 + 2\langle\sigma_y\rangle^4)/8$ in the meson potential (9.12) if we shift

$$
\lambda_2 \to \lambda_2 + \delta\lambda_2 \qquad \text{with the counterterm} \qquad \delta\lambda_2 = -\frac{N_c g^4}{16\pi^2\epsilon}. \tag{9.23}
$$

Then $N_c(2m_x^4 + m_y^2)/16\pi^2\epsilon + \delta\lambda_2(\langle\sigma_x\rangle^4 + 2\langle\sigma_y\rangle^4) = 0$, so this theory is also renormalizable. Adding electrons, we obtain the natural three-flavor generalization of the renormalized and finite grand potential (8.19),

$$
\begin{aligned}
\Omega(\langle\sigma\rangle, \boldsymbol{\mu}) = \mathcal{V}(\langle\sigma\rangle, 0) &+ N_c\frac{m_x^4}{8\pi^2}\left[\frac{3}{2} + \log\left(\frac{\Lambda_x^2}{m_x^2}\right)\right] + N_c\frac{m_y^4}{16\pi^2}\left[\frac{3}{2} + \log\left(\frac{\Lambda_y^2}{m_y^2}\right)\right]\\
&- \sum_{f=1}^{N_c} \frac{N_c}{24\pi^2}\left[\left(2\mu_f^2 - 5m_f^2\right)\mu_f\sqrt{\mu_f^2 - m_f^2} + 3m_f^4 \operatorname{asinh}\left(\sqrt{\frac{\mu_f^2}{m_f^2} - 1}\right)\right]\\
&- \frac{1}{24\pi^2}\left[\left(2\mu_e^2 - 5m_e^2\right)\mu_e\sqrt{\mu_e^2 - m_e^2} + 3m_e^4 \operatorname{asinh}\left(\sqrt{\frac{\mu_e^2}{m_e^2} - 1}\right)\right].
\end{aligned} \tag{9.24}
$$

9.3 Parameter fit at tree-level

We are now in position to fit the six parameters g, m^2, λ_1, λ_2, h_x and h_y. In vacuum, the pion and kaon decay constants f_π and f_K are related to the nonzero expectation values [Len+00]

$$\langle\sigma_x\rangle = f_\pi \qquad \text{and} \qquad \langle\sigma_y\rangle = \sqrt{2}f_K - \frac{f_\pi}{\sqrt{2}}. \tag{9.25}$$

With vacuum measurements of the two decay constants and one of the quark masses (9.8), we determine the parameter g, then use it to predict the other quark masses. Likewise, we use vacuum measurements of three of the eight meson masses (9.20) to determine the three parameters $\{m^2, \lambda_1, \lambda_2\}$, then use them to predict the five remaining meson masses. With $\langle\sigma_x\rangle$, $\langle\sigma_y\rangle$, m^2, λ_1 and λ_2 in hand, the two symmetry breakers h_x and h_y follow from equation (9.13).

Table 9.1 shows values for the fitted and predicted particle masses. In general there are $8!/3!5! = 56$ ways of selecting three of the eight meson masses (9.20), each returning different values for $\{m^2, \lambda_1, \lambda_2\}$. We keep using m_σ and m_π for continuity from chapter 8 and include m_K as the third mass, thereby obtaining the unique selection of mesons with the lowest masses and energies. This is the same selection used by [Sch+09] and [Len+00], for example.

Note the particularly large discrepancy between the modeled and experimental η' mass. This can be improved by including a term $c\,(\det\phi + \det\phi^\dagger)$ in the Lagrangian that models the anomalous axial $U(1)_A$ current of quantum chromodynamics discussed in section 6.3. How to do so is also shown in [Sch+09] and [Len+00], but we leave it out in order to keep the two-flavor and three-flavor models as similar and comparable as possible. In particular, they find that it drives the chiral transition closer to a discontinuous phase transition than a crossover.

Like in section 8.3, we keep all parameters fixed except m_σ, due to its large experimental uncertainty. As shown in the lasagna of different vacuum potentials in figure 9.1, they still admit minima only for $m_\sigma \geq 600\,\text{MeV}$, so we continue to use $m_\sigma = \{600, 700, 800\}\,\text{MeV}$.

With two flavors we determined the renormalization scale (8.22) by requiring the minimum to remain at $\langle\sigma\rangle = f_\pi$ in vacuum. The natural generalization of this procedure to three flavors is to determine Λ_x and Λ_y so the minimum remains at (9.25) in vacuum. This is accomplished by

$$\frac{\partial\Omega}{\partial\langle\sigma_x\rangle} = \frac{\partial\Omega}{\partial\langle\sigma_y\rangle} = 0, \quad \text{so} \quad \Lambda_x = \frac{m_x}{\sqrt{e}} = 182.0\,\text{MeV} \quad \text{and} \quad \Lambda_y = \frac{m_y}{\sqrt{e}} = 260.2\,\text{MeV}. \tag{9.26}$$

This is not the only way to do it. Like [Ber13], we could rather operate with one common scale $\Lambda = \Lambda_x = \Lambda_y$ in the grand potential, for example chosen as the flavor-weighted average $\Lambda = (2 \cdot 182.0\,\text{MeV} + 260.2\,\text{MeV})/3 = 208.0\,\text{MeV}$ of the two we have found. In particular, this means that the minimum of Ω in vacuum is no longer at the minimum of $\mathcal{V}$. This is unsatisfying and has surprising consequences. For example, if Ω is fit to some quark mass $m_x = gf_\pi/2$, its minimum $\langle\sigma_x\rangle \neq f_\pi$ moves *away* from f_π because $\partial\Omega/\partial\langle\sigma_x\rangle \neq 0$ at f_π, in turn generating a *different* vacuum quark mass $g\langle\sigma_x\rangle/2 \neq gf_\pi/2$ than the one that was fitted! Of course, our approach also has its caveats, as it is not apparent how to interpret the presence of two different renormalization scales, let alone one. But it does not behave in this unpredictable way, and it permits using the same masses $m_\sigma \geq 600\,\text{MeV}$ as in chapter 8 without breaking the potential. Ideally, a more consistent calculation such as the one in section 8.6 should be done anyway, where one preferable renormalization scale appears, and we even saw that it dropped out in that specific case. It is hard to say whether our or [Ber13]'s approach is better, but this is only another argument to at the very least take the unexplored path over an already paved way.

Recall from the consistently fit two-flavor model in section 8.6 that our way of fitting parameters at tree-level to a grand potential calculated in the one-loop large-N_c limit is really inconsistent. However, we know of no consistent calculation with three flavors like the one presented there. The lesson we learned back there was that inconsistently fit $600\,\text{MeV} \leq m_\sigma \leq 800\,\text{MeV}$ is representative of physically measured masses $400\,\text{MeV} \leq m_\sigma \leq 600\,\text{MeV}$, so we can only hope that the same is true with three flavors.

Table 9.1: Variables in the left table are used as **input** to determine the six model parameters in the right table from equations (9.8), (9.13) and (9.20), which in turn are used to predict the remaining non-bold masses in the left table with the same equations. Three values are used for m_σ, generating three parameter sets with different m^2, λ_1 and m_{f_0}. Experimental measurements are taken from [PDG20].

Physical variables					Model parameters			
Variable	Modeled			Measured	Parameter	Modeled		
	Set 1	Set 2	Set 3			Set 1	Set 2	Set 3
f_π / MeV	**93**	**93**	**93**	92-93	g	6.45	6.45	6.45
f_K / MeV	**113**	**113**	**113**	113	m^2 / (MeV)^2	-178^2	-351^2	-492^2
m_u / MeV	**300**	**300**	**300**	$\approx$ 300	λ_1	-18.2	-13.0	-6.2
m_d / MeV	**300**	**300**	**300**	$\approx$ 300	λ_2	85.3	85.3	85.3
m_s / MeV	429	429	429	$\approx$ 500	h_x / (MeV)^3	121^3	121^3	121^3
m_{f_0} / MeV	1294	1315	1347	1200-1500	h_y / (MeV)^3	336^3	336^3	336^3
m_σ / MeV	**600**	**700**	**800**	400-550				
m_{a_0} / MeV	870	870	870	980				
m_κ / MeV	1141	1141	1141	1414				
m_η / MeV	636	636	636	548				
$m_{\eta'}$ / MeV	138	138	138	958				
m_π / MeV	**138**	**138**	**138**	138				
m_K / MeV	**496**	**496**	**496**	496				

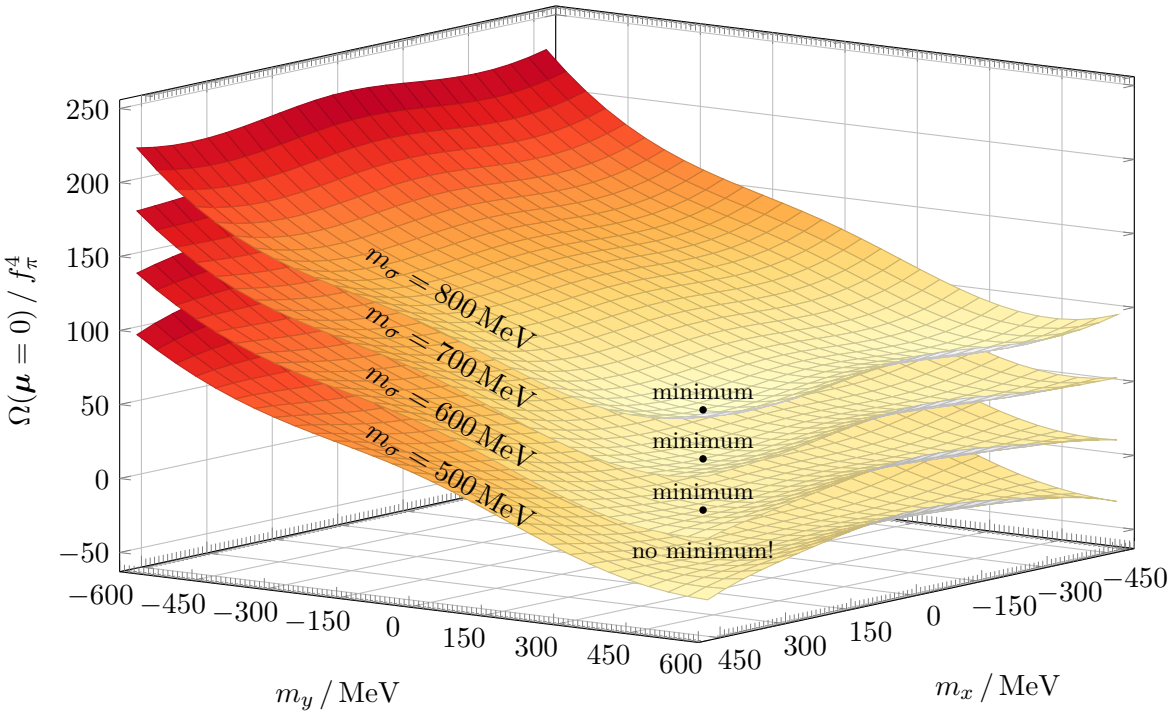

Figure 9.1: The three-flavor grand potential (9.24), here offset by constants into a human-digestible lasagna, admits minima for the quark masses $m_x = g\langle\sigma_x\rangle/2$ and $m_y = g\langle\sigma_y\rangle/\sqrt{2}$ in vacuum, where $\boldsymbol{\mu} = 0$, only when fit to $m_\sigma \geq 600\,\mathrm{MeV}$ at tree-level.

9.4 Equation of state

To find the equation of state we will follow the same procedure as in chapter 8. The generalization of the system of equations (8.23) with strange quarks that we need to solve, subject to the constraints of chemical equilibrium (6.7) and charge neutrality (6.12), is

$$0 = \frac{\partial\Omega}{\partial\langle\sigma_x\rangle}, \tag{9.27a}$$

$$0 = \frac{\partial\Omega}{\partial\langle\sigma_y\rangle}, \tag{9.27b}$$

$$0 = 2\left(\mu_u^2 - m_u^2\right)^{\frac{3}{2}} - \left(\mu_d^2 - m_d^2\right)^{\frac{3}{2}} - \left(\mu_s^2 - m_s^2\right)^{\frac{3}{2}} - \left(\mu_e^2 - m_e^2\right)^{\frac{3}{2}}, \tag{9.27c}$$

$$\mu_d = \mu_u + \mu_e, \tag{9.27d}$$

$$\mu_s = \mu_d. \tag{9.27e}$$

This is a system of five equations for the six unknowns $\langle\sigma_x\rangle$, $\langle\sigma_y\rangle$, μ_u, μ_d, μ_s and μ_e. Like in chapter 8, we parametrize solutions with $\langle\sigma_x\rangle$, evaluate the particle densities (6.4b) as

$$n_f = -\frac{\partial\Omega}{\partial\mu_f} = \frac{N_c}{3\pi^2}\left(\mu_f^2 - m_f^2\right)^{\frac{3}{2}} \qquad \text{and} \qquad n_e = -\frac{\partial\Omega}{\partial\mu_e} = \frac{1}{3\pi^2}\left(\mu_e^2 - m_e^2\right)^{\frac{3}{2}}, \tag{9.28}$$

then calculate them, the pressure (6.4a) and the energy density (6.4d), and finally eliminate the free variable to get the equation of state $\epsilon(P)$. The numerical implementation in appendix G.5 yields the solutions, particle densities and equation of state shown in figure 9.2:

- There is a non-strange crossover (for $m_\sigma \geq 800\,\text{MeV}$) or discontinuous phase transition (for $m_\sigma < 800\,\text{MeV}$) after $\mu = 300\,\text{MeV}$, as in the two-flavor case in figure 8.4. Even the strange minimum $\langle\sigma_y\rangle$ moves a bit during this transition due to the cross term $\lambda_1\langle\sigma_x\rangle^2\langle\sigma_y\rangle^2/2$ in the meson potential (9.12) changing. Accordingly, the equations of state for the two-flavor and three-flavors models are quite similar up to $P \leq 0.05\,\text{GeV/fm}^3$.
- There is a strange crossover after the non-strange crossover or phase transition. For example, for $m_\sigma = 800\,\text{MeV}$, it starts at $\mu \approx 370\,\text{MeV}$ or $\mu_s = m_y \approx 410\,\text{MeV}$. This is *below* the fitted vacuum mass $m_s = 429\,\text{MeV}$ because *both* m_x and m_y drop during the non-strange transition, as explained above. Moreover, it is *always* a crossover and *never* a phase transition, is significantly slower than the non-strange transition, and the strange quark retains a noticeable mass when the non-strange quarks have lost theirs. During this crossover, the equation of state gently ramps up from the two-flavor level towards a second plateau and softens compared to the two-flavor equation of state.
- Before the strange crossover, the up and down quark chemical potentials μ_u and μ_d spread in order to ensure charge neutrality together with the electrons. After the strange crossover, however, the strange quark kicks out the electron and provides charge neutrality together with the up and down quarks, as the quark chemical potentials find back to each other in the ultra-relativistic limit $\mu_u \to \mu_d = \mu_s \to \mu$. In contrast to the two-flavor case, the isospin chemical potential $\mu_I = (\mu_u - \mu_d)/2$ never exceeds half the pion mass, so neglecting pion condensation is a consistent assumption for all μ with three flavors.
- As shown in figure 9.3, each quark density converges towards a third of the total quark density $n = 3n_B$ as it increases. At low density the strange quark is absent and there are twice as many down quarks as up quarks, like in chapter 8, and the strange quark enters for $n_B \geq 4n_{\text{sat}}$. The fraction of up quarks is the same at all densities.
- The ultra-relativistic solution in section 7.1 is recovered as $\langle\sigma_x\rangle \to \langle\sigma_y\rangle \to 0$,
- The equation of state satisfies the criteria of causality (4.24) and stability (4.27).
- Like in chapter 8, we use the Maxwell construction to correct the ambiguous equations of state with phase transitions as described in [Pog17, equation (4.69)].

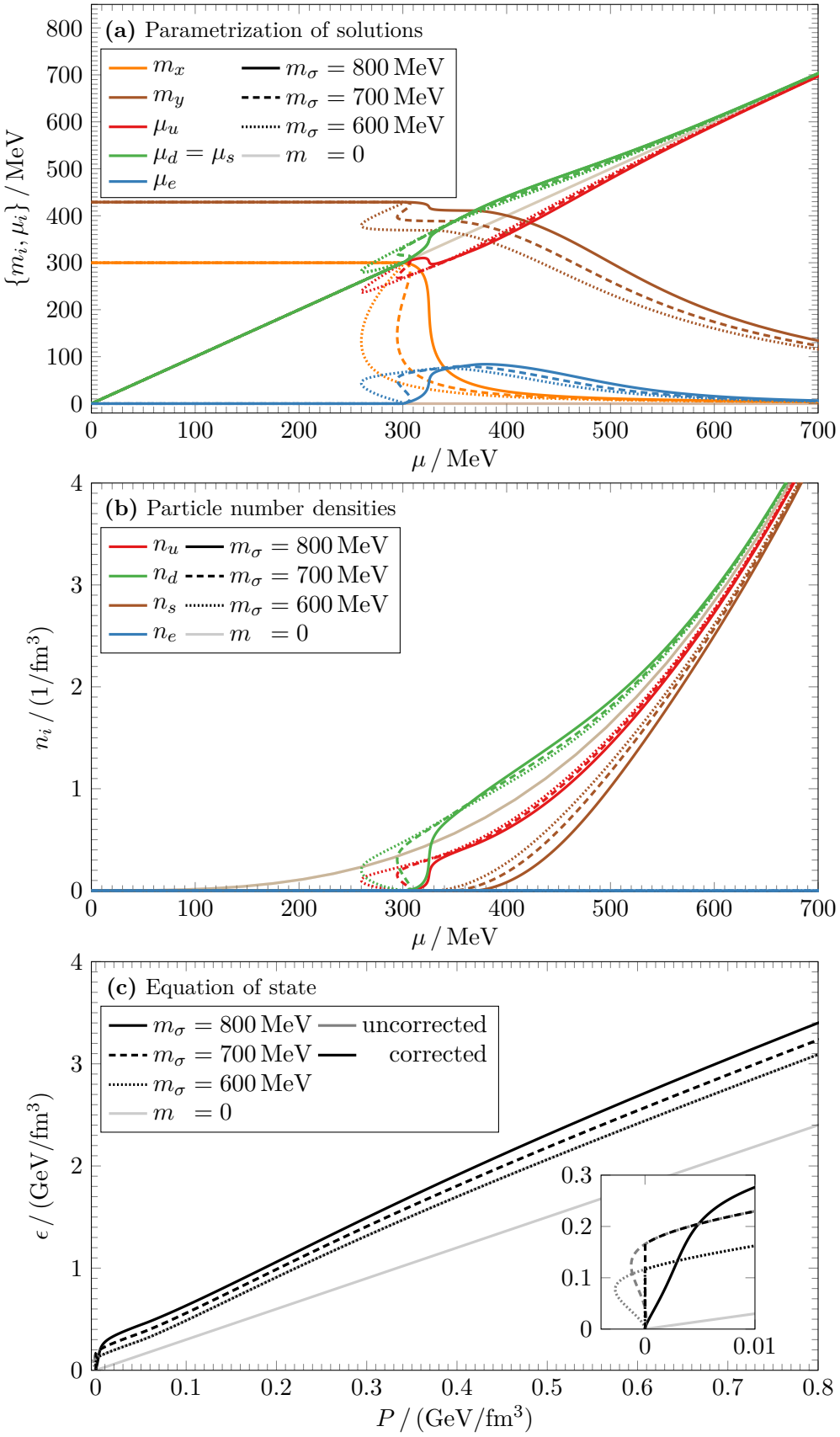

Figure 9.2: Properties of charge-neutral quark matter in β-equilibrium in the three-flavor quark meson model. Upper panel **(a)** shows solutions to equation (9.27), middle panel **(b)** the particle number densities (9.28) and lower panel **(c)** the equation of state $\epsilon(P)$ **before** and **after** the Maxwell construction. Parameter sets with $m_\sigma = \{600, 700, 800\}$MeV from table 9.1 are used. The weak lines show the solutions (7.7), (7.8) and (7.9b) in the massless limit $m = 0$.

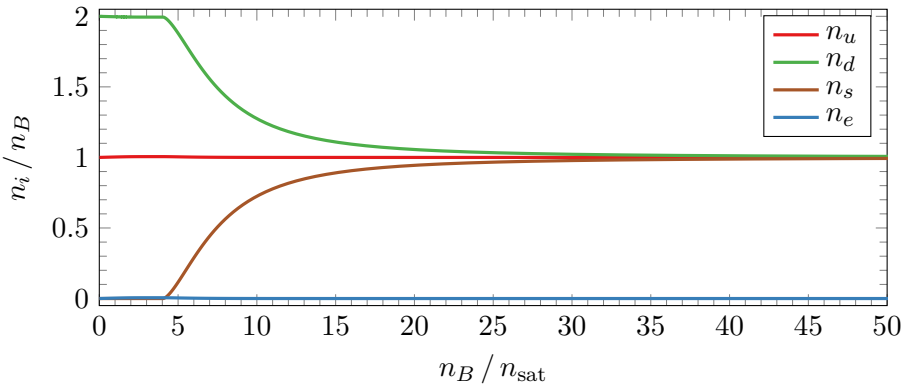

Figure 9.3: Fractions of each particle density n_i to the baryon density $n_B = (n_u + n_d + n_s)/3$ as a function of n_B for the charge-neutral three-flavor quark matter in figure 9.2. The nuclear saturation density is $n_{\text{sat}} = 0.165/\text{fm}^3$.

We again modify the equation of state with bag constants B with the shift (7.10) and determine their upper bounds by solving the three-flavor inequality (7.12), owing to the strange matter hypothesis. This yields the upper bag constant bounds

$$B \leq (112.0\,\text{MeV})^4 \quad \Big(\text{or } B - \mathcal{V}_0 \leq (226.4\,\text{MeV})^4\Big) \qquad \Big(m_\sigma = 600\,\text{MeV}\Big), \tag{9.29a}$$

$$B \leq \ (68.2\,\text{MeV})^4 \quad \Big(\text{or } B - \mathcal{V}_0 \leq (231.4\,\text{MeV})^4\Big) \qquad \Big(m_\sigma = 700\,\text{MeV}\Big), \tag{9.29b}$$

$$B \leq \ (27.0\,\text{MeV})^4 \quad \Big(\text{or } B - \mathcal{V}_0 \leq (241.3\,\text{MeV})^4\Big) \qquad \Big(m_\sigma = 800\,\text{MeV}\Big). \tag{9.29c}$$

These are so close to the lower bounds (8.26) that the inequalities practically become equalities, and the bag constant is more or less fixed for a given m_σ *if* the strange matter hypothesis holds, but can take greater values if it does not. Like before, we focus on the lowest bag constants since they generate stiffer equations of state and greater maximum masses.

Note that if one uses a single renormalization scale Λ and let the vacuum quark masses move from their fit values, like [Ber13] and as discussed in section 9.3, one obtains the rather different bounds $B^{\frac{1}{4}} \leq \{6.3, 48.2\}\,\text{MeV}$ for $m_\sigma = \{700, 800\}\,\text{MeV}$, whereas the potential is broken for $m_\sigma = 600\,\text{MeV}$. These results are impossible to reconcile with the lower bag bounds (8.26) and is one of the reasons for why we choose to go with two separate renormalization scales here.

9.5 Quark star solutions

With the numerical implementation in appendix G.5, we now modify the equations of state in figure 9.2c with the bag shift (7.10) using bag constants above the lower bounds (8.26) and solve the corresponding Tolman-Oppenheimer-Volkoff equations (6.1). This produces the mass-radius solutions in figure 9.4:

- For stars with low central pressure, the quark chemical potential μ does not reach large enough levels to activate the strange quark. Then the three-flavor equation of state and mass-radius curve track their two-flavor siblings almost perfectly. As the two models use different vacuum potentials, it is somewhat surprising that the correspondence is so good.
- For stars with greater central pressure, μ reaches sufficient levels and the strange quark is present in the core. Exactly at the threshold, we see that the mass-radius curve grows apart from the two-flavor curve into a new branch. This branch has lower masses because of the softening of the equation of state as it ramps up during the strange crossover.
- The masses and radii are comparable to the two-flavor results in section 8.5, except that the mass is lowered for stars with strange quarks. For stars that just satisfy the lower

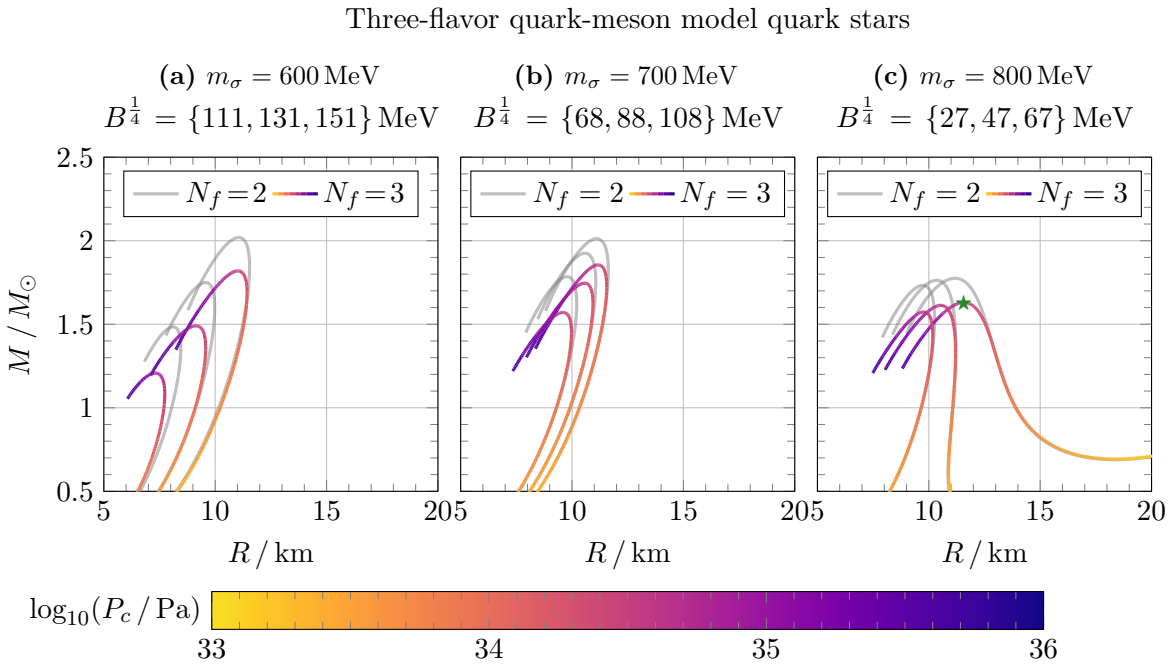

Figure 9.4: Mass-radius solutions of the Tolman-Oppenheimer-Volkoff equation (6.1) parametrized by the central pressure P_c, using equations of state for three-flavor quark matter in figure 9.2c modified by the bag shift (7.10) with bag constants at and above the bounds (8.26).

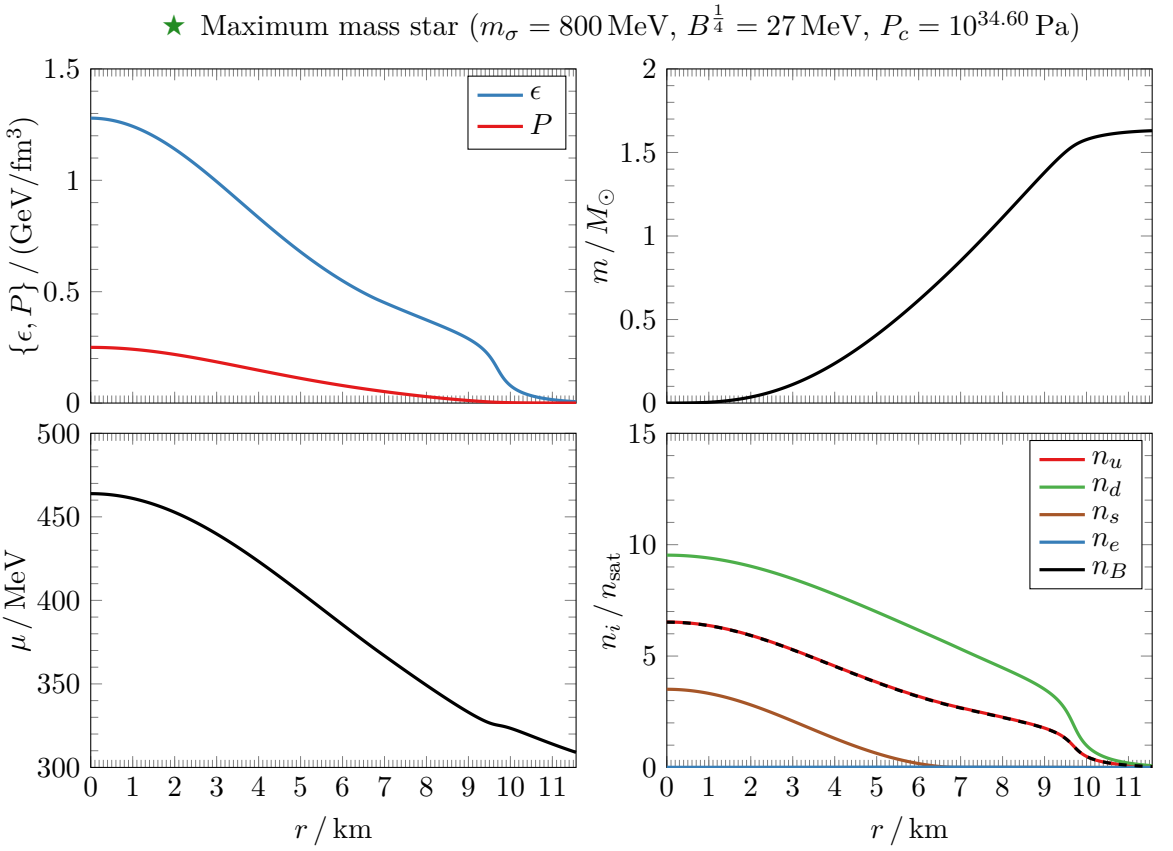

Figure 9.5: Radial profiles for the pressure P, energy density ϵ, cumulative mass m, quark chemical potential μ, particle densities n_i and baryon density $n_B = (n_u + n_d + n_s)/3$ for the maximum mass three-flavor quark star ★ in figure 9.4. The nuclear saturation density is $n_{\mathrm{sat}} = 0.165/\mathrm{fm}^3$.

bag bounds (8.26) and hence respect instability of two-flavor quark matter with respect to hadronic matter, we find maximum masses $1.6\,M_\odot \leq M \leq 1.8\,M_\odot$ and corresponding radii $11\,\text{km} \leq R \leq 12\,\text{km}$ depending on the precise mass m_σ. Greater bag constants violate the strange matter hypothesis and result in only lighter and smaller stars.

In figure 9.5 we take a more detailed look at the maximum mass star that has no phase transition and respects the strange matter hypothesis:

- Apart from the presence of strange quarks, many features are similar to that of the two-flavor star we discussed on page 96.
- The star is composed of three-flavor quark matter including strange quarks for $r \leq 6.5\,\text{km}$ and two-flavor quark matter for $r \geq 6.5\,\text{km}$ out to the surface $R = 11.6\,\text{km}$.
- With a maximum chemical potential $\mu = 465\,\text{MeV}$, the strange quark is much heavier than the up and down quarks at the center, as seen from figure 9.2a. Thus, the star is far from realizing ultra-relativistic three-flavor quark matter.
- The maximum central chemical potential is comparable in the two-flavor and three-flavor models. If we assert that this carries over to a four-flavor model that also includes the charm quark with constituent mass $m_c > 1\,\text{GeV}$ [PDG20], it would only be present for extreme central pressures far beyond that of the maximum mass star. This is why we only need to include the three lightest $\{u, d, s\}$ quarks when modeling stable quark stars.

Since these pure quark stars consist of three-flavor quark matter only in the core and two-flavor quark matter out to the surface, and the latter is unstable with respect to hadronic matter, they are unlikely to be found in nature. The only hope of realizing pure three-flavor quark stars is if the strange matter hypothesis is true and they consist of strange quark matter *everywhere*. Looking back at figure 9.2b, the strange quark is present for all m_σ only when $\mu \geq 350\,\text{MeV}$. The only way of creating a strange quark star with our model is to increase B so much that after the bag shift (7.10), we have $\mu \geq 350\,\text{MeV}$ at the surface defined by $P = 0$. Now look at $P(\mu)$ in figure 9.6; in order for $P(\mu \geq 350\,\text{MeV}) \leq 0$, we need to shift $P(\mu) \to P(\mu) - B$ with $B^{1/4} \geq 120\,\text{MeV}$. This is the minimum required bag constant for the strange quark to appear out to the surface for all m_σ. Unfortunately, this *exceeds* even the greatest upper bound (9.29a), *which was calculated precisely by assuming the strange matter hypothesis.* This means that *it is not possible to self-consistently describe pure strange quark stars with this model!*

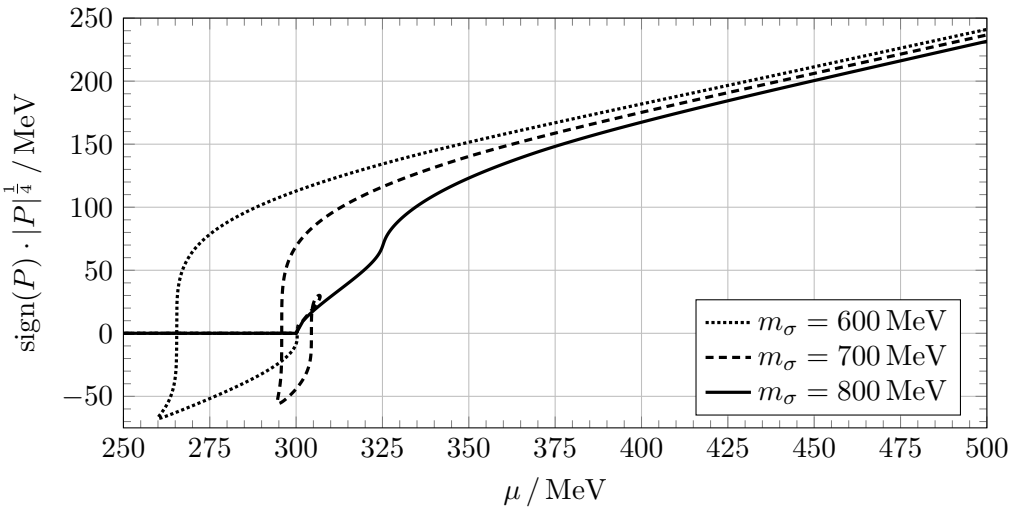

Figure 9.6: Signed fourth root of the pressure $P(\mu)$ as a function of the quark chemical potential μ for the equations of state in figure 9.2c, before the Maxwell construction and the bag shift (7.10). The funny behavior in the lower left is caused by the phase transition, and is corrected with a boring straight line after the Maxwell construction.

9.6 Summary

In this chapter we have modeled quark stars with the three-flavor quark-meson model. We found that the addition of the strange quark lowered the maximum masses of pure quark stars to $1.6\,M_\odot \leq M \leq 1.8\,M_\odot$ with corresponding radii $11\,\text{km} \leq R \leq 12\,\text{km}$, using $600\,\text{MeV} \leq m_\sigma \leq 800\,\text{MeV}$ and the lowest instability-respecting bag constants (8.26). If the strange matter hypothesis is violated, one can use greater bag constants and produce smaller and less massive stars. The three-flavor stars are less massive than their two-flavor counterparts due to their softer equations of state. Only close to the maximum mass star does the pressure and density become sufficiently high to activate the presence of the strange quark.

As with the two-flavor model, chiral symmetry restoration happens in a crossover for $m_\sigma \geq 800\,\text{MeV}$, but a first-order phase transition for $m_\sigma < 800\,\text{MeV}$. The non-strange transition is followed by a much slower strange crossover for all m_σ.

At tree-level, it was again impossible to fit measured masses $400\,\text{MeV} \leq m_\sigma \leq 550\,\text{MeV}$ without breaking the grand potential. Ideally, a fully consistent calculation in the one-loop large-N_c limit like the one presented in section 8.6 should be carried out also for the three-flavor model, where loop effects are taken into account when fitting the parameters. Unfortunately, no such calculation has been done yet, and we rely on the lesson learned back there: that inconsistently fit $600\,\text{MeV} \leq m_\sigma \leq 800\,\text{MeV}$ are representative of consistently fit masses $400\,\text{MeV} \leq m_\sigma \leq 600\,\text{MeV}$ that are compatible with measurements.

Unfortunately, we fail to model pure strange quark stars consistently with this model. The stars we found consisted of unstable two-flavor quark matter out to the surface. For them to be stable, the strange matter hypothesis must be true and the strange quark must exist out to the surface. This could only be achieved by increasing the bag constant beyond its upper bound (9.29) that was calculated precisely by *assuming the strange matter hypothesis*.

Chapter 10

A Hybrid Quark-Hadron Model

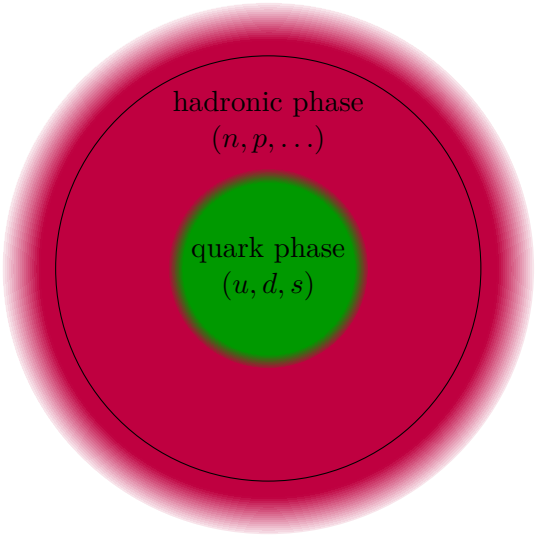

Figure 10.1: A hybrid star with a strange quark core surrounded by a hadronic envelope. Compared to the hadronic phase, quark cores are thought to be much smaller than shown here.

In the preceding chapters we modeled pure quark stars consisting of deconfined quark matter out to the surface. These models accounted for the chiral symmetry breaking of quantum chromodynamics. They also featured a bag constant that generally allowed for negative pressure in the equation of state, therefore often interpreted as a confinement mechanism. However, the pressure in the stars were restricted to *non-negative* values, so they contained only *deconfined* quarks. According to quantum chromodynamics, quarks are confined in hadrons at low density and temperature, so with the possible exception of pure strange quark stars, they are unlikely to be seen in nature.

More realistically, quark matter can be found in high-density cores of **hybrid (neutron) stars** surrounded by envelopes of low-density hadronic matter. The recent observations [Ant+13; Arz+18; Fon+21] of the heavy pulsars PSR J0348+0432, PSR J1614−2230 and PSR J0740+6620 with masses $M = \{2.01 \pm 0.04, 1.91 \pm 0.02, 2.08 \pm 0.07\}\, M_\odot$ suggest that real neutron stars could indeed reach sufficient densities for deconfined quark matter to form in the core. Due to these observations, hybrid star models are benchmarked by their ability to pass the $2M_\odot$-limit.

In our final undertaking, we assemble hybrid stars with the **quark-meson models** from chapters 8 and 9 in the core, surrounded by a phase governed by the representative **Akmal-Pandharipande-Ravenhall** (**APR**) hadronic equation of state from [APR98]. All equations of state are found at zero temperature, in β-equilibrium and subject to local charge neutrality.

This chapter is inspired by reference [Bay+18].

10.1 Construction of hybrid equations of state

The individual equations of state for the quark and hadronic phases are available to us from two different sources: the two-flavor and three-flavor quark-meson models from chapters 8 and 9, and the APR equation of state from data points at [APR15]. Both sources give us the baryon chemical potential μ_B, baryon density n_B, pressure P and energy density ϵ.

To join the two equations of state for the hadronic phase H and quark phase Q into one hybrid version, we apply the coarsest procedure outlined in [Bay+18, section V-C]:

1. Plot the pressures $P_H(\mu_B)$ and $P_Q(\mu_B)$ as functions of the baryon chemical potential μ_B.
2. Find the chemical potential μ_B^0 at which the curves $P_Q(\mu_B^0) = P_H(\mu_B^0)$ intersect. It typically corresponds to baryon densities $n_B^0 = n_B(\mu_B^0)$ in the range $2n_{\text{sat}} \lesssim n_B^0 \lesssim 5n_{\text{sat}}$.
3. Compute the hybrid pressures and energy densities
$$P(\mu_B) = \begin{cases} P_H(\mu_B) & (\mu_B \leq \mu_B^0) \\ P_Q(\mu_B) & (\mu_B > \mu_B^0) \end{cases} \quad \text{and} \quad \epsilon(\mu_B) = \begin{cases} \epsilon_H(\mu_B) & (\mu_B \leq \mu_B^0) \\ \epsilon_Q(\mu_B) & (\mu_B > \mu_B^0) \end{cases}. \tag{10.1}$$
4. Eliminate μ_B from $P(\mu_B)$ and $\epsilon(\mu_B)$ to obtain the hybrid equation of state $\epsilon(P)$.

By definition, different phases have greater pressure before and after the intersection point. The philosophy behind the method is that at any baryon chemical potential μ_B, nature prefers the phase with lower grand potential $\Omega = -P$. Effectively, $\epsilon_H(P \leq P^0)$ and $\epsilon_Q(P > P^0)$ are concatenated into one common equation of state $\epsilon(P)$.

Figure 10.2 shows an example of the step-by-step construction of a hybrid equation of state that joins the three-flavor quark-meson model with the hadronic APR equation of state. The pressures intersect at $\mu_B \approx 1300\,\text{MeV}$, which corresponds to the density $n_{BH}^0 \approx 4n_{\text{sat}}$ in the hadronic phase and $n_{BQ}^0 \approx 5.5n_{\text{sat}}$ in the quark phase. The energy density drops by $\Delta\epsilon = \epsilon_Q^0 - \epsilon_H^0 = 0.3\,\text{GeV/fm}^3$ in a discontinuous phase transition at $P = 0.2\,\text{GeV/fm}^3$. The transition takes the form of a line of constant vapor pressure, like in a Maxwell construction. The construction is virtually identical with the two-flavor quark-meson model, only with a lower drop $\Delta\epsilon$.

The biggest problem with this rough splicing method is that it assumes the equations of state for both phases to be valid near the intersection point. In reality, it is unreliable to compare them across the entire range of densities from hadronic to quark matter. A more sophisticated approach described in [Bay+18, section V-F] is to restrict each equation of state to its domain of validity, and then smoothly interpolate between them in a clever way in the intermediate range where neither of them are trustworthy. We restrict ourselves to the simpler method above, aiming only to investigate the mere possibility of using the quark-meson model in a hybrid star.

In our case, the issue of comparing the two phases is emphasized by the presence of a *second* intersection point at a lower baryon chemical potential $\mu_B \approx 1100\,\text{MeV}$. This means that the hadronic phase does not have the greatest pressure for all chemical potentials below the first intersection point! Assuming that the quark equation of state is unreliable in this regime anyway, we simply gloss over this small inconsistency. It would be utterly insane to go back to the quark phase near the surface.

In figure 10.3 we gather six equations of state constructed in this way for $N_f = \{2, 3\}$ and $m_\sigma = \{600, 700, 800\}\,\text{MeV}$ with the corresponding lowest bag constants satisfying the lower bounds (8.26). These are the same parameters we considered in chapters 8 and 9 that generated the most massive quark stars. Note that the phase transition generally becomes more severe with three quark flavors and increasing m_σ, which are accompanied by decreasing lowermost instability-respecting B above the lower bounds (8.26).

The detailed numerical implementation can be found in appendix G.5.

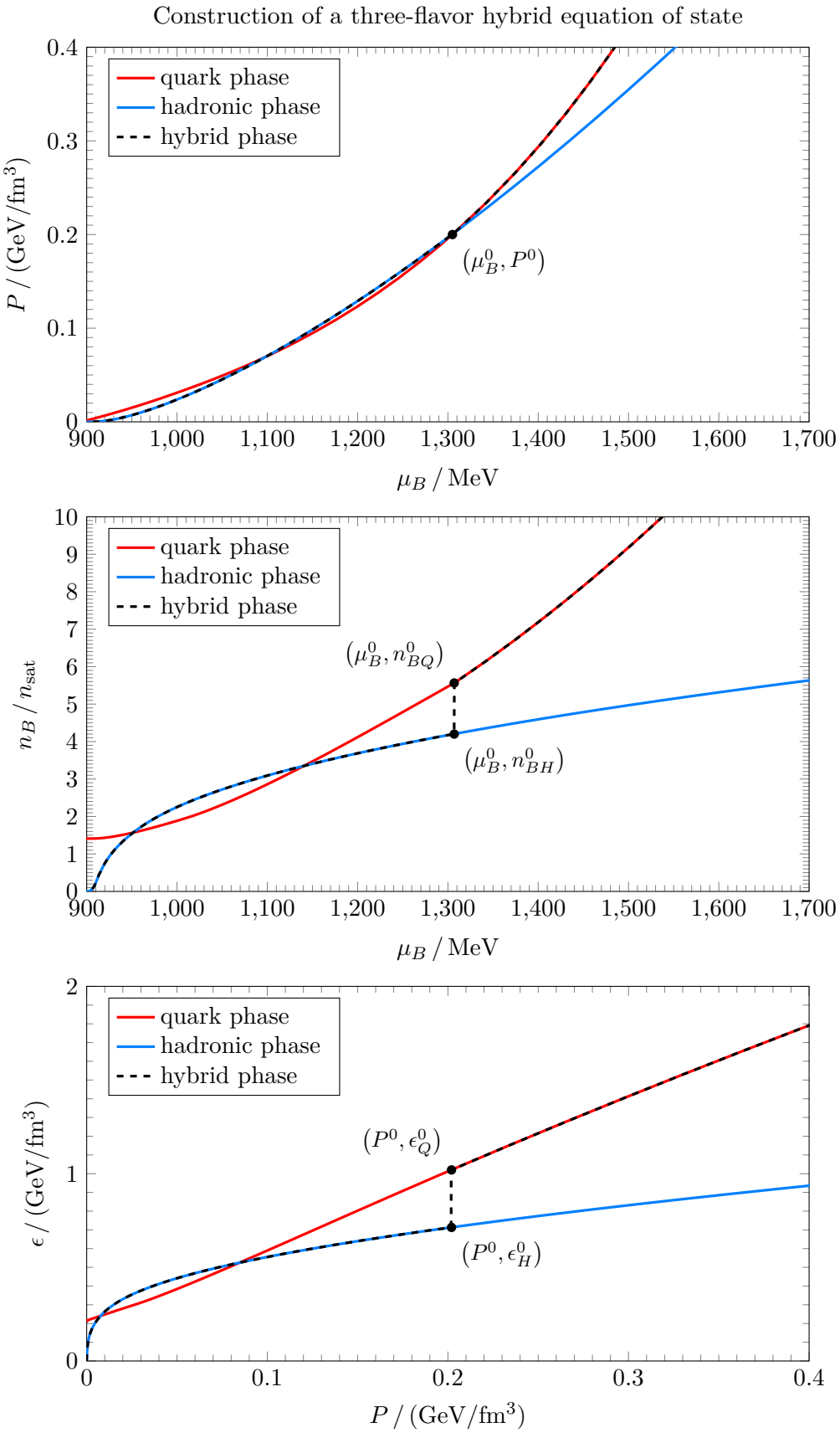

Figure 10.2: A hybrid equation of state built with steps 1–4 in section 10.1, joining the three-flavor quark-meson model in chapter 9 with $m_\sigma = 600\,\text{MeV}$ and $B^{\frac{1}{4}} = 111\,\text{MeV}$ to the hadronic Akmal-Pandharipande-Ravenhall equation of state from [APR98; APR15].

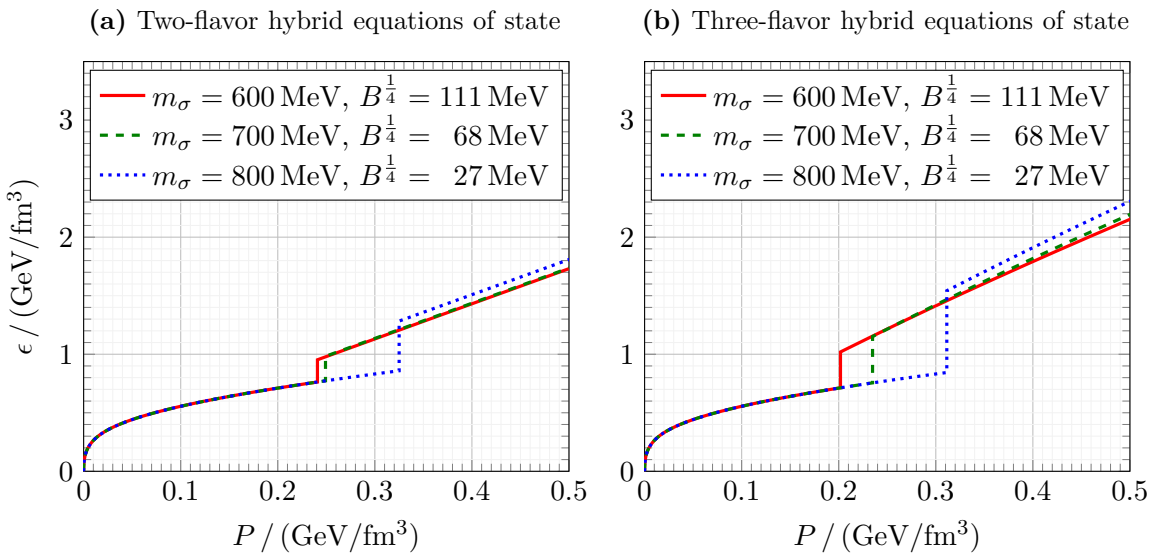

Figure 10.3: Six hybrid equations of state constructed like the one in figure 10.2 using the three parameter sets that generated the most massive quark stars with the two-flavor and three-flavor quark-meson models in chapters 8 and 9.

10.2 Hybrid star solutions

With the numerical implementation in appendix G.5, we solve the Tolman-Oppenheimer-Volkoff equation (6.1) with the hybrid equations of state in figure 10.3, obtaining the mass-radius relations in figure 10.4:

- For low central pressures the quark phase is never activated, so the stars are neutron stars modeled only with the hadronic APR equation of state.
- After onset of the quark phase, the mass-radius curve develops hybrid star branches below the neutron stars. They have maximum masses $2.00M_\odot \leq M \leq 2.09M_\odot$ with two flavors in the core and $1.90M_\odot \leq M \leq 2.07M_\odot$ with three flavors.
- At first glance, the hybrid branches in the left panels seem to plummet in mass immediately after diverging from the mass-increasing hadronic curve. As discussed in section 4.3 and particularly criterion (4.28), this indicates that all the hybrid stars are unstable. However, close inspection of the right panels shows that the dives are preceded by *small segments* of mass-increasing and thus *stable hybrid stars*! Such a stable segment is visible on all six branches, if only a very tiny one, and they are longer with two flavors and smaller m_σ. This supports the claim in [Bay+18] that quark cores are very small, if they exist at all.
- In fact, [Ran+16, equation 15] and references within show that under general circumstances and no matter how small the quark core is, the energy density drop $\Delta\epsilon = \epsilon_Q^0 - \epsilon_H^0$ in the phase transition immediately destabilizes the hybrid branch *if and only if*

$$\Delta\epsilon > \frac{1}{2}\epsilon_H^0 + \frac{3}{2}P^0. \tag{10.2}$$

  It is straightforward to verify that *none* of the six equations of state in figure 10.3 satisfy this criterion, although the three-flavor equation of state with $m_\sigma = 800\,\text{MeV}$ comes close. Relatively to the energy densities, the transition pressures P^0 are similar with two and three flavors, so the higher drop $\Delta\epsilon$ in the three-flavor model explains its shorter stable hybrid segments. Our findings are indeed consistent with the general criterion (10.2).
- Like before, we focus on the lowest bag constants respecting the lower bounds (8.26) because they generate more interesting results with longer branches of stable hybrid stars.

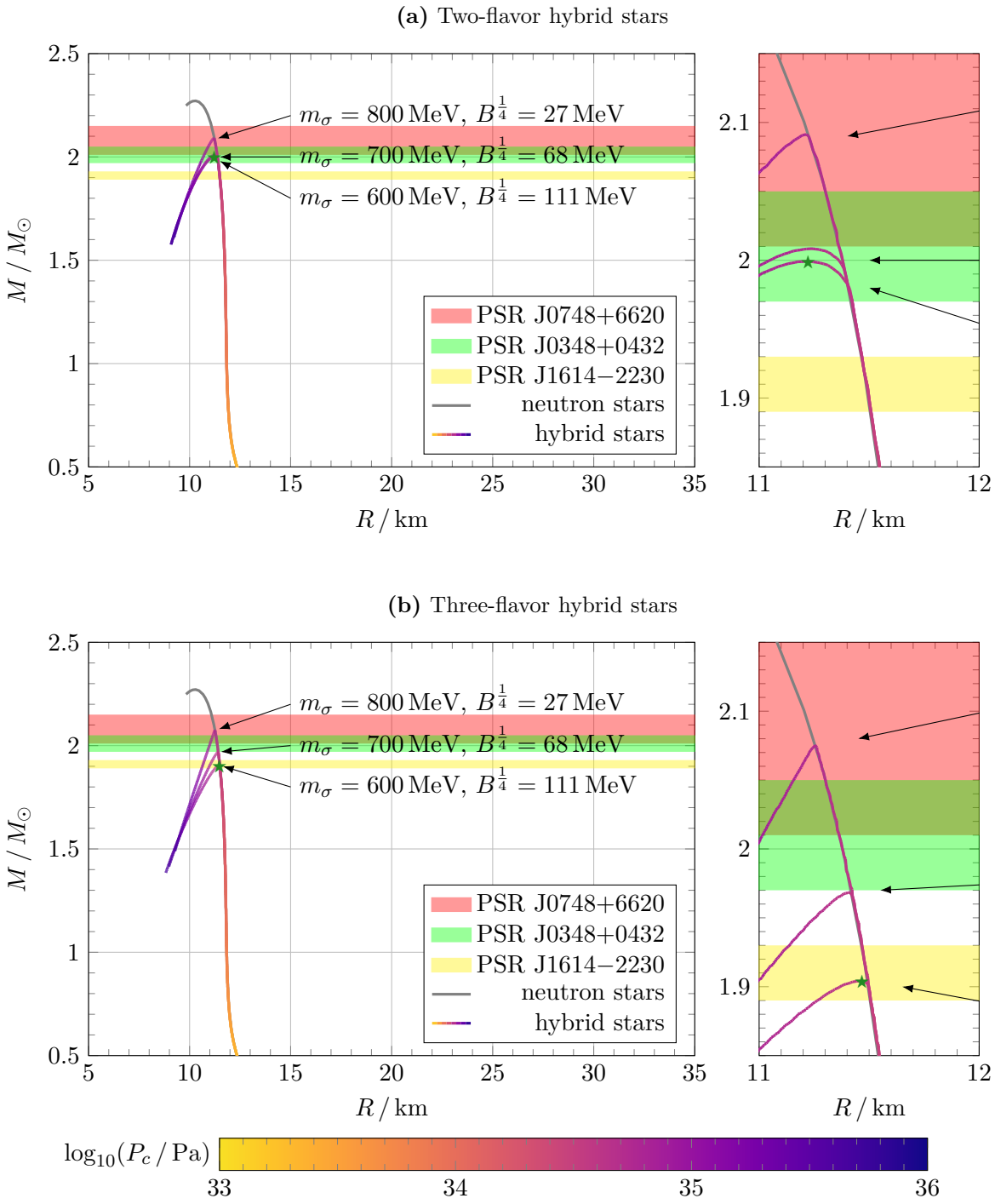

Figure 10.4: Mass-radius solutions of the Tolman-Oppenheimer-Volkoff equation (6.1) parametrized by the central pressure P_c, using the hybrid equations of state in figure 10.3. The colored bands show measured masses of three heavy pulsars from [Ant+13; Arz+18; Fon+21].

For a *fixed* value of m_σ, a greater B in the bag shift (7.10) would lower the quark pressure curve in the upper panel of figure 10.2, moving its intersection with the hadronic curve to a greater baryon chemical potential μ_B^0 and pressure P^0. The hybrid mass-radius curve would then branch off the hadronic curve for higher central pressures and closer to the maximum mass, where the stable hybrid segment shortens. This effect is shown clearly in [Zac+16, figure 14], for example.

- The modeled maximum mass hybrid stars are certainly compatible with observations of the heavy pulsars PSR J0348+0432, PSR J1614−2230 and PSR J0740+6620.

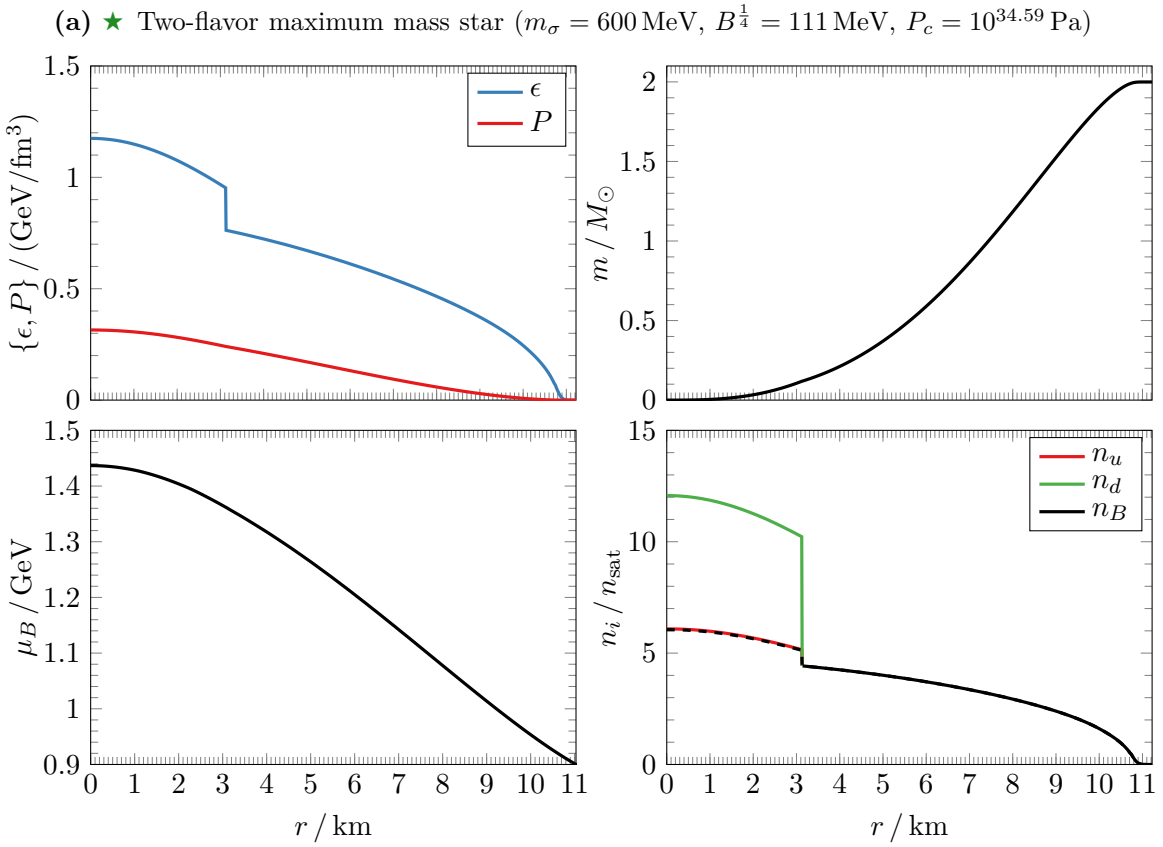

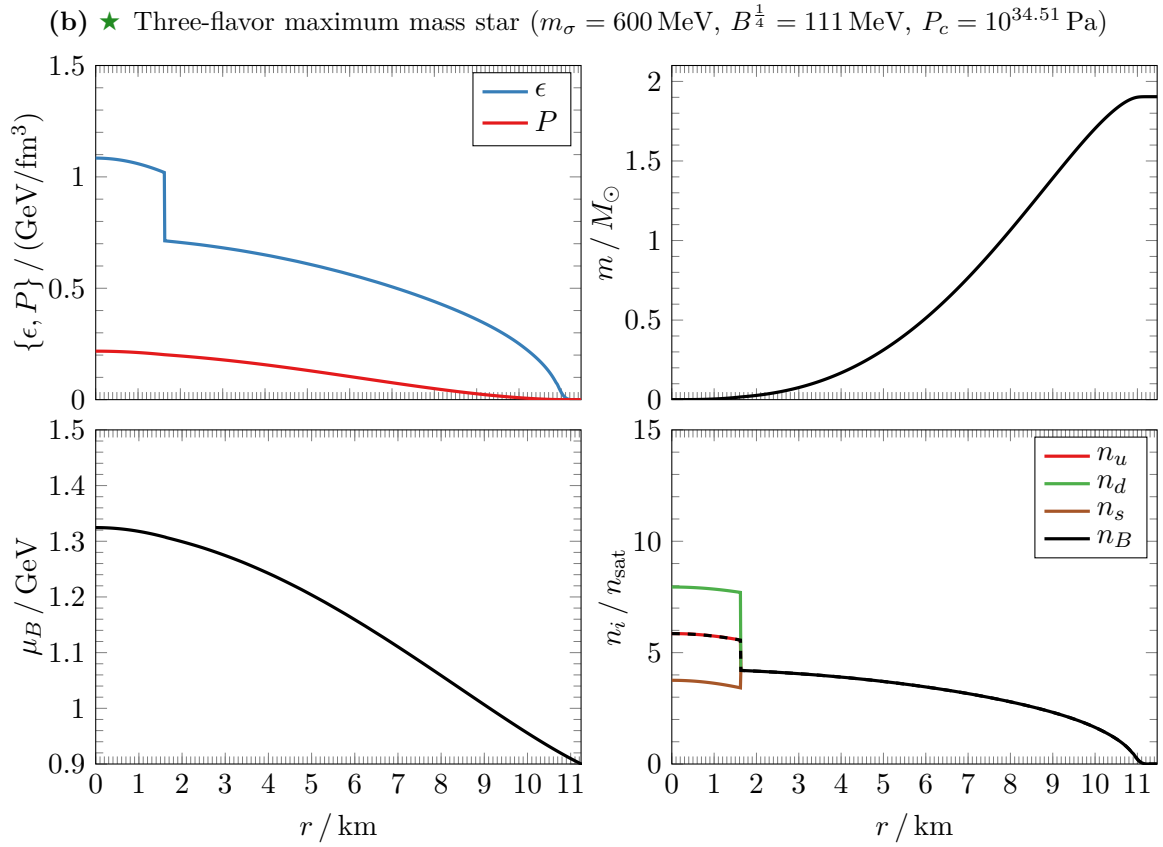

Figure 10.5: Radial profiles for the pressure P, energy density ϵ, cumulative mass m, baryon chemical potential μ_B, particle densities n_i and baryon density $n_B = (n_u + n_d + n_s)/3$ for the maximum mass hybrid stars ★ in figure 10.4.

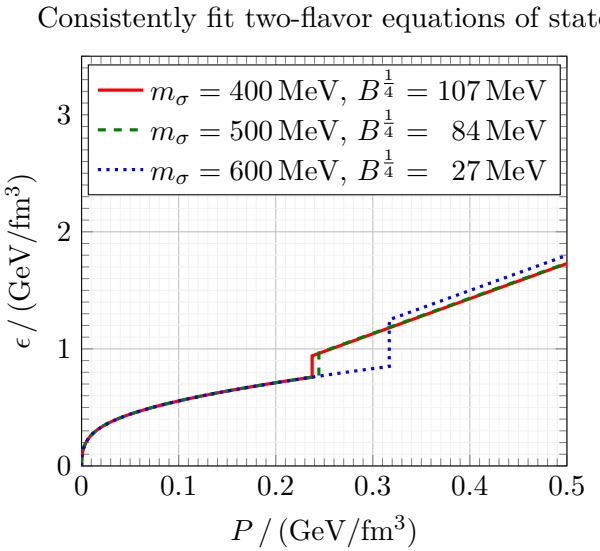

Figure 10.6: Hybrid equations of state like in figure 10.3, but with the consistently fit two-flavor quark-meson model from section 8.6.

We inspect maximum mass stars on hybrid branches with both two and three flavors in the core in figure 10.5:

- With both $N_f = \{2, 3\}$, the quark core has a central baryon density $n_B = 6n_{\mathrm{sat}}$. It extends $R' = \{3.1, 1.6\}\,\mathrm{km}$ and has masses $M_{\mathrm{core}} = \{0.12, 0.02\}\,M_\odot$. Like the pure quark stars in chapters 7 to 9, hybrid star quark cores with two flavors are generally larger and heavier than those with three flavors due to their stiffer equations of state.
- The hadronic phase dominates with both $N_f = \{2, 3\}$, making up $\{98.0, 99.7\}\,\%$ of the stars' volumes and $\{94, 99\}\,\%$ of their masses.

For completeness and to round everything off, we pay one last visit to our consistently fit two-flavor quark-meson model in section 8.6. Recall that the quark star results with inconsistently fit $600\,\mathrm{MeV} \leq m_\sigma \leq 800\,\mathrm{MeV}$ practically speaking coincided with those from consistently fit $400\,\mathrm{MeV} \leq m_\sigma \leq 600\,\mathrm{MeV}$, so we should expect nothing different when using this model for the quark core in a hybrid star. Using the slightly modified lower bag constant bounds (8.30) that we found with the consistently fit model, we repeat our calculations and find the results in figures 10.6 to 10.8. Indeed, we see that they agree very well with the results using inconsistently fit $600\,\mathrm{MeV} \leq m_\sigma \leq 800\,\mathrm{MeV}$, and we only hope the same is true in the three-flavor situation.

10.3 Summary

In this chapter we have constructed hybrid stars modeled with the two-flavor and three-flavor quark-meson models in the core, and the hadronic Akmal-Pandharipande-Ravenhall equation of state in the outer region. Using σ meson masses $600\,\mathrm{MeV} \leq m_\sigma \leq 800\,\mathrm{MeV}$ in the quark-meson models, we saw that the hadronic mass-radius relation developed short branches of hybrid stars up to maximum masses $2.00M_\odot \leq M \leq 2.09M_\odot$ with two flavors in the core and $1.90M_\odot \leq M \leq 2.07M_\odot$ with three flavors. In general, the two-flavor cores are both more massive and stable than three-flavor cores due to their stiffer equations of state. The maximum masses overlap with recent mass measurements of the heavy pulsars PSR J0348+0432, PSR J1614−2230 and PSR J0740+6620 around and above the $2M_\odot$-limit. For central pressures beyond that of the maximum mass star, the discontinuous transition between the quark and hadronic phases becomes so severe that it destabilizes the hybrid stars. This transition is generally more dramatic with three flavors, so the stable segments are longer with two flavors.

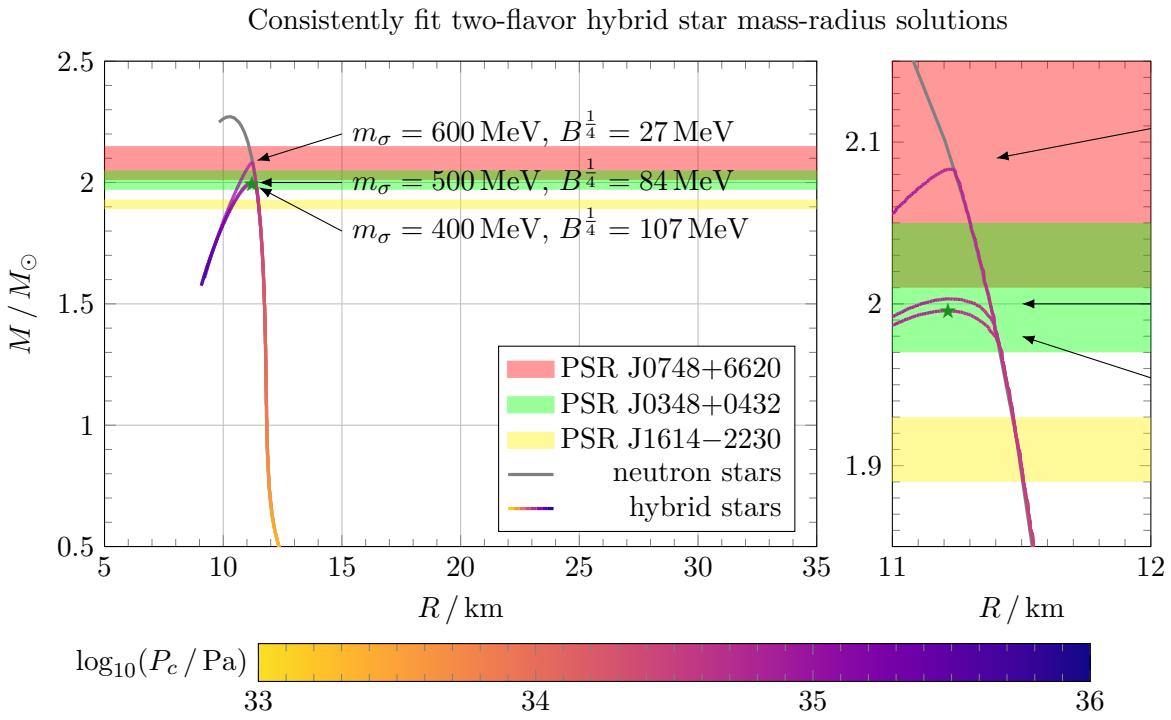

Figure 10.7: Mass-radius solutions like in figure 10.4, but with the consistently fit two-flavor hybrid equations of state from figure 10.6.

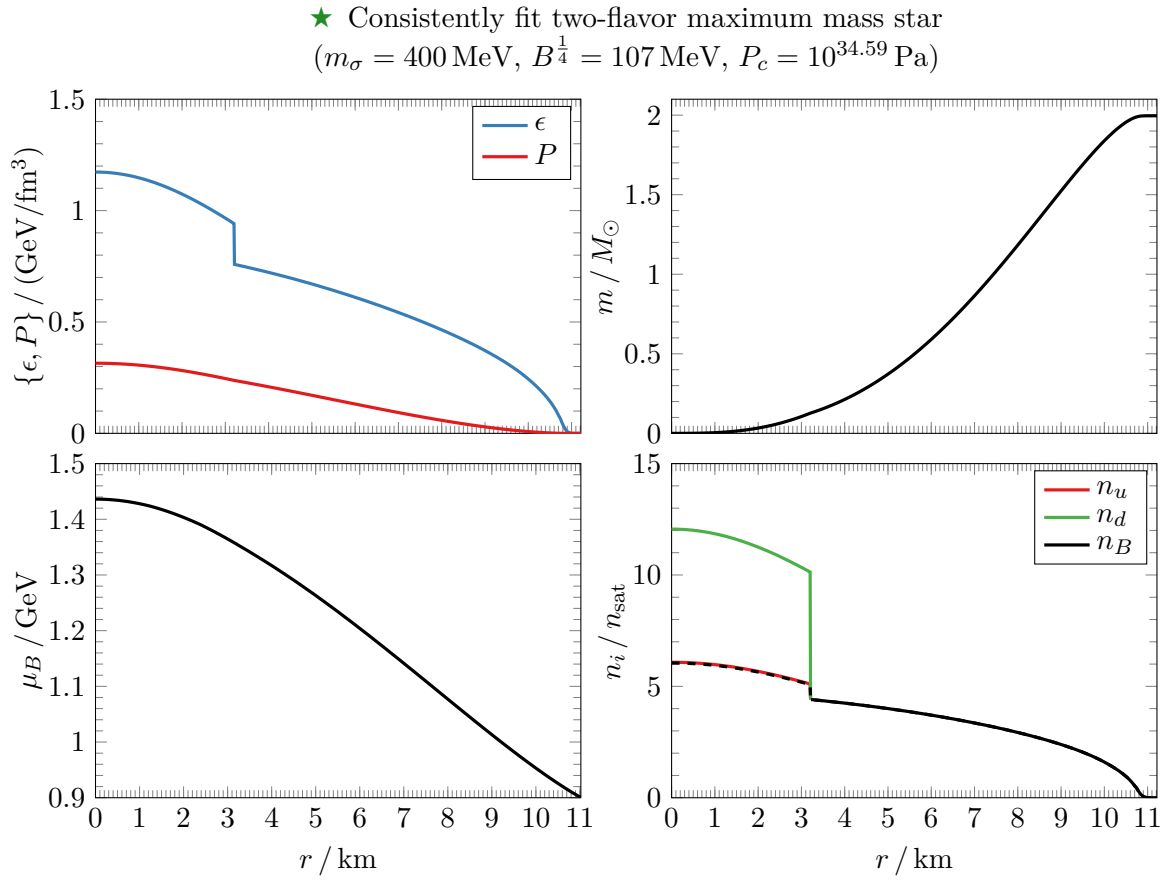

Figure 10.8: Radial profiles like in figure 10.5, but for the maximum mass star ★ in figure 10.7.

Chapter 11

Conclusions and Outlook

11.1 Conclusions

In this thesis we have modeled quark stars using the MIT bag model and the quark-meson model with two and three flavors, and finally hybrid stars by joining the quark-meson models with the hadronic Akmal-Pandharipande-Ravenhall equation of state from [APR98; APR15]. All resulting mass-radius relations, their maximum masses and corresponding radii are summarized in figure 11.1 and table 11.1.

With the quark-meson model we could create pure quark stars with two flavors up to $M \leq 2.0\,M_\odot$ and with three flavors up to $M \leq 1.8\,M_\odot$. Due to their softer equations of state, we saw that three-flavor stars are generally less massive than two-flavor stars. As two-flavor quark matter is unstable compared to hadronic matter, pure two-flavor quark stars are unlikely to be found in nature. However, *if* the strange matter hypothesis of [Bod71; Wit84] is true, strange quark stars consisting of three-flavor quark matter out to the surface would be stable and could exist. We fail to model strange quark stars self-consistently with the three-flavor quark-meson model, as the bag constant must exceed its upper bound calculated precisely by *assuming* the strange matter hypothesis if the strange quark is to exist out to surface.

We calculated the grand potential of the quark-meson models to tree-level in bosons and one-loop in fermions. This is *inconsistent* in terms of the number of loops, but can be regarded *consistent* in the one-loop large-N_c limit. The equations of state were then found at zero temperature, in β-equilibrium and subject to local electrical charge neutrality.

In particular, the parameter space of the quark-meson model is plagued by the "ad-hoc" σ meson, whose mass is only known to lie in $400\,\mathrm{MeV} \leq m_\sigma \leq 550\,\mathrm{MeV}$. [PDG20] Depending on its value, we saw that chiral symmetry restoration occurred in a rapid crossover for $m_\sigma \geq 800\,\mathrm{MeV}$, but a discontinuous phase transition for $m_\sigma < 800\,\mathrm{MeV}$. Moreover, we could only fit masses $m_\sigma \geq 600\,\mathrm{MeV}$ that exceed the measurements to prevent the minimum of the grand potential from disappearing in the vacuum phase. With two flavors, we nailed this problem down to the inconsistency of fitting parameters at tree-level to a potential that is calculated in the one-loop large-N_c limit. Repeating our calculation with a consistently fit potential in this limit found by [Adh+17a; Adh+17b], we learned that we could still trust our original results, as if inconsistently fit $600\,\mathrm{MeV} \leq m_\sigma \leq 800\,\mathrm{MeV}$ correspond to consistently fit $400\,\mathrm{MeV} \leq m_\sigma \leq 600\,\mathrm{MeV}$.

Using the quark-meson models in the core, we could also form short ranges of stable hybrid stars up to $M \leq 2.1\,M_\odot$ with both two and three flavors, where the two-flavor stars are generally somewhat heavier due to their stiffer equations of state. The hybrid stars contained very small quark cores no more massive than $0.12 M_\odot$ and $0.02 M_\odot$ with two and three flavors, respectively. This resonates with the claim in [Bay+18] that hybrid star quark cores are very small, if they exist at all. Beyond the maximum mass star, the discontinuous phase transition between the

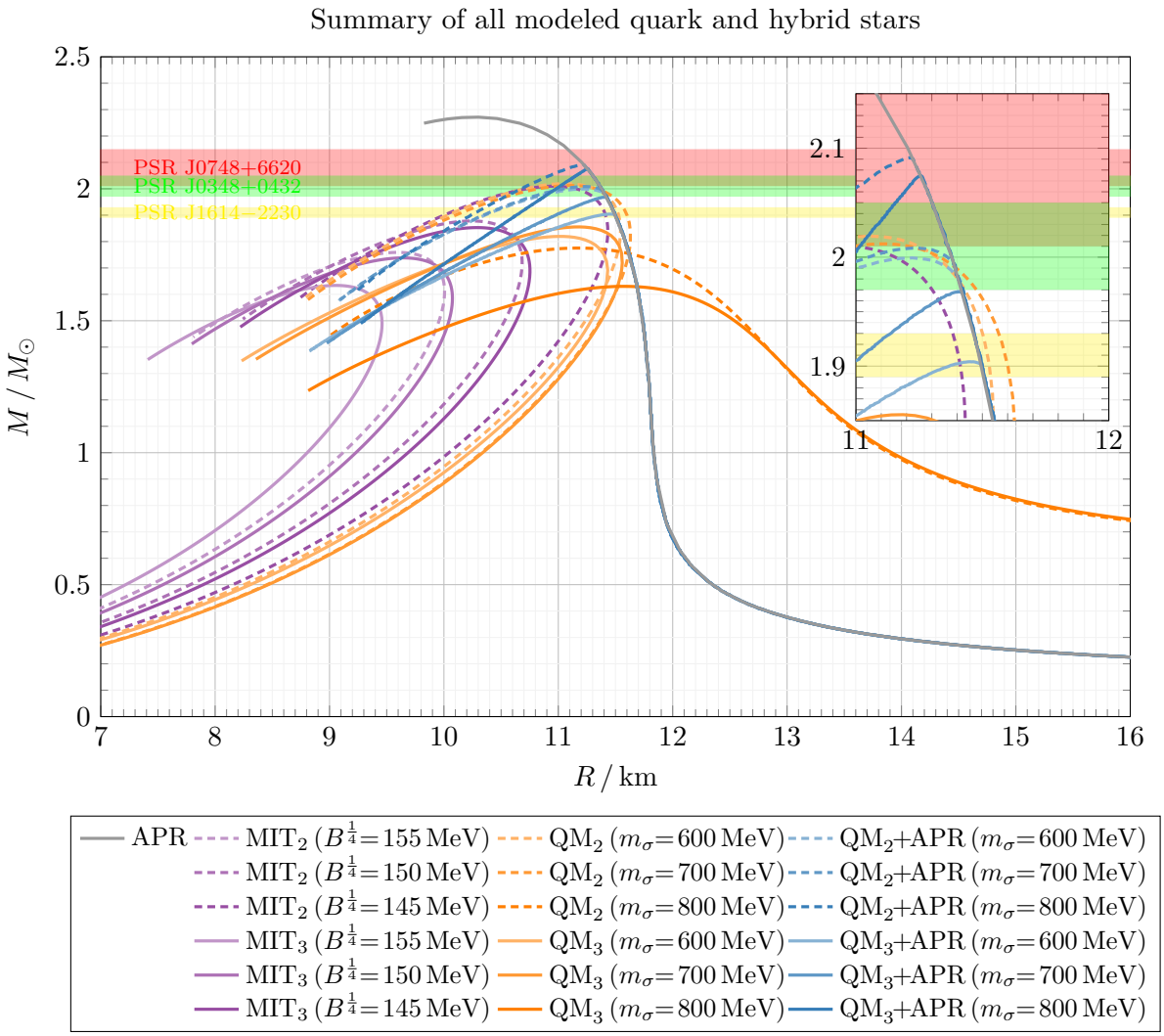

Figure 11.1: Summary of all mass-radius relations obtained in this thesis: neutron stars with the hadronic Akmal-Pandharipande-Ravenhall equation of state (APR); quark stars with the two-flavor and three-flavor MIT bag models (MIT_2 and MIT_3) and quark-meson models (QM_2 and QM_3); and hybrid stars joining QM_2 + APR and QM_3 + APR. In the MIT_2 and MIT_3 models, we have used bag constants covering the bag window (7.14). In the QM_2 and QM_3 models, we vary $600\,\mathrm{MeV} \leq m_\sigma \leq 800\,\mathrm{MeV}$ and use the corresponding lowest bag constants at the lower bounds (8.26), as greater bag constants only generate less massive stars. The colored bands show measured masses of the heavy pulsars PSR J0348+0432, PSR J1614−2230 and PSR J0740+6620 from [Ant+13; Arz+18; Fon+21]. For clearer presentations of the results with each model, please consult figures 7.3, 8.5, 9.4 and 10.4.

Table 11.1: Maximum masses and corresponding radii of the stellar sequences in figure 11.1.

Flavors	Chapter	Model	Maximum masses	Corresponding radii
$N_f = 2$	Chapter 7	MIT bag model	$1.7\,M_\odot \leq M \leq 2.0\,M_\odot$	$9.6\,\mathrm{km} \leq R \leq 11.0\,\mathrm{km}$
$N_f = 2$	Chapter 8	Quark-meson model	$1.8\,M_\odot \leq M \leq 2.0\,M_\odot$	$10.9\,\mathrm{km} \leq R \leq 11.2\,\mathrm{km}$
$N_f = 2$	Chapter 10	Hybrid model	$2.0\,M_\odot \leq M \leq 2.1\,M_\odot$	$11.2\,\mathrm{km} \leq R \leq 11.2\,\mathrm{km}$
$N_f = 3$	Chapter 7	MIT bag model	$1.6\,M_\odot \leq M \leq 1.9\,M_\odot$	$9.0\,\mathrm{km} \leq R \leq 10.3\,\mathrm{km}$
$N_f = 3$	Chapter 9	Quark-meson model	$1.6\,M_\odot \leq M \leq 1.8\,M_\odot$	$11.0\,\mathrm{km} \leq R \leq 11.6\,\mathrm{km}$
$N_f = 3$	Chapter 10	Hybrid model	$1.9\,M_\odot \leq M \leq 2.1\,M_\odot$	$11.2\,\mathrm{km} \leq R \leq 11.5\,\mathrm{km}$

quark and hadronic phases becomes so severe that it destabilizes stars with larger quark cores against radial perturbations. We succeed in modeling hybrid stars with small quark cores around the recent mass observations [Ant+13; Arz+18; Fon+21] of the heavy pulsars PSR J1614−2230, PSR J0348+0432 and PSR J0748+6620 around and above $2M_\odot$.

The indication that hybrid stars can have only small quark cores suggests that they are hard to observe decisively in nature. With future advances in our theoretical understanding and observational techniques, such as the **N**eutron **S**tar **I**nterior **C**omposition **E**xplore**r** (**NICER**) mission [NICER17], heavy observed neutron stars could one day turn out to have quark cores.

In earlier work, [Zac+15] have modeled pure quark stars with a vector meson-extended three-flavor quark-meson model, and this was incorporated into hybrid stars in [Zac+16]. With the vector meson interaction turned off and using parameters comparable to ours, they find hybrid stars with similar maximum masses $M \leq 1.9M_\odot$, and greater masses can be reached if this interaction is enabled. Quark stars have also been modeled with the Nambu-Jona-Lasinio model in [Li+20] and generalized to hybrid stars in [Con+17], for example. They also find maximum hybrid star masses $1.9M_\odot \leq M \leq 2.1M_\odot$ with reasonable parameter choices. Even [Ott+20] find hybrid stars in the band $2.0M_\odot \leq M \leq 2.1M_\odot$ using a non-perturbative functional renormalization group approach with the quark-meson model. Despite using different models for both the quark and hadronic phases, our results are in good agreement with these works.

11.2 Outlook

A natural extension of our work would be to explore the parameter space of the quark-meson model more thoroughly. Our philosophy has been to keep almost all parameters fixed, but vary the most uncertain parameter m_σ and focus on the corresponding lowest instability-respecting bag constants B because it generates stiffer equations of state and thus greater maximum masses. A more detailed treatment could also vary the quark masses, other meson masses and use larger bag constants. For example, [Zac+15] find that the maximum mass increases with the quark masses $m_u = m_d$ in the variation of our model mentioned above. One can also include more parameters by adding terms describing the axial anomaly of quantum chromodynamics and studying more complex symmetry breaking patterns, as described at length in [Len+00].

A consistent parameter fitting method in the one-loop large-N_c limit is only available for the two-flavor quark-meson model. It would be interesting to generalize it to the three-flavor model and see if the ability to fit experimental values of m_σ carries over from the two-flavor case.

It is natural to expect that our greatest source of error lies neither in the calculation of the grand potential nor its parameter fitting, but in the quark-meson model *itself*. First-principle approaches of studying quark matter from quantum chromodynamics remains difficult, as the sign problem plagues lattice calculations at finite baryon chemical potentials and perturbation theory is applicable only at high energies. Of course, other and more sophisticated effective models could be examined. For example, confinement could be incorporated with Polyakov-loop extended quark-meson models (PQM models, see for example [Sch+07a; Sch+10; Fol18]) and NJL models (PNJL models, see for example [Fuk04; Fu+08; Mat+21]). One could also examine the effects of modeling the color-superconducting phase of the phase diagram in figure 6.2.

More effort could also be put into handling the phase transition in hybrid stars more carefully. For example, the interpolation techniques described in [Bay+18] can be used near the intersection point of the transition, where both the quark and hadronic equations of state are unreliable. This method constructs a unified equation of state that bridges the gap between the two phases, constrained by physical requirements like retaining a causal speed of sound.

One can also refine calculations to nonzero temperature and beyond mean fields, investigate effects of non-local charge neutrality, and solve the axially symmetric generalization of the spherically symmetric Tolman-Oppenheimer-Volkoff to model realistic spinning pulsars.

Part III

Appendices

(project and master thesis)

Appendix A

General Relativity

This appendix is inspired by references [Car19], [MTW73] and [Kac20].

A.1 The geometry of curved spacetime

In this section, we review the geometrical aspects of general relativity. We make no attempt to be mathematically rigorous, but rather focus on listing important quantities and equations and the intuitive connections between them. For more details, we refer to the references listed above which this summary is based on.

A.1.1 Coordinates and tensors

In general relativity, 3-dimensional space and 1-dimensional time are no longer regarded separate as they are in Newtonian mechanics. They are rather intertwined into *spacetime* – a $(3+1)$-dimensional construct with **coordinates**

$$x^\mu = (x^0, x^1, x^2, x^3). \tag{A.1}$$

In flat Minkowski space, the coordinates can be taken as $x^\mu = (ct, x, y, z)$. Mathematically, the geometry of spacetime is described by a *Riemannian manifold* that generalizes flat Minkowski space to *curved space*. At every point on such a manifold, spacetime locally resembles Minkowski space in the *tangent space* located at that point, and all such tangent spaces vary smoothly from point to point. For example, figure A.1 pictures the tangent space at a point of the 2-sphere manifold. Familiar concepts like angles, lengths, area and volume apply locally in the tangent space at each point in infinitesimal form, and one can generalize such concepts to the full manifold by integrating the local contributions from one point on the manifold to another.

We will place vector fields $V^\mu(x^\nu)$, and later tensor fields, that associate a vector V^μ to every point x^ν on a manifold. As explained in figure A.1, such a vector lies in the tangent vector space at every point on the manifold. To motivate the transformation properties of tensors on a manifold, we can use the fact that the set of directional derivatives constitute a vector space with basis vectors given by the partial derivatives. Suppose $\phi(x)$ is a scalar function and $x(\tau)$ and $x(\lambda)$ are two paths on the manifold with directional derivatives given by the chain rule as

$$\frac{\mathrm{d}\phi}{\mathrm{d}\tau} = \frac{\mathrm{d}x^\mu}{\mathrm{d}\tau}\frac{\partial\phi}{\partial x^\mu} = \frac{\mathrm{d}x^\mu}{\mathrm{d}\tau}\partial_\mu\phi \qquad \text{and} \qquad \frac{\mathrm{d}\phi}{\mathrm{d}\lambda} = \frac{\mathrm{d}x^\mu}{\mathrm{d}\lambda}\frac{\partial\phi}{\partial x^\mu} = \frac{\mathrm{d}x^\mu}{\mathrm{d}\lambda}\partial_\mu\phi. \tag{A.2}$$

Like $\mathrm{d}/\mathrm{d}\tau$ and $\mathrm{d}/\mathrm{d}\lambda$, the linear combination $(a\,\mathrm{d}/\mathrm{d}\tau + b\,\mathrm{d}/\mathrm{d}\lambda)$ is a perfectly good derivative operator, as it is both linear and satisfies the product rule

$$\left(a\frac{\mathrm{d}}{\mathrm{d}\tau} + b\frac{\mathrm{d}}{\mathrm{d}\lambda}\right)(fg) = \left(a\frac{\mathrm{d}f}{\mathrm{d}\tau} + b\frac{\mathrm{d}f}{\mathrm{d}\lambda}\right)g + \left(a\frac{\mathrm{d}g}{\mathrm{d}\tau} + b\frac{\mathrm{d}g}{\mathrm{d}\lambda}\right)f. \tag{A.3}$$

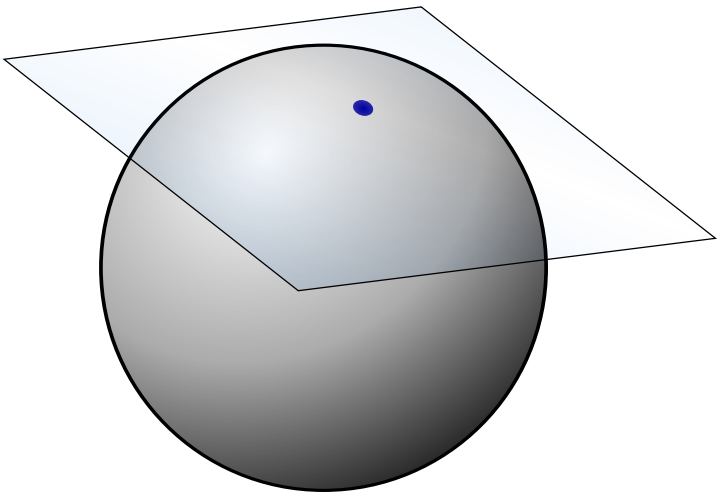

Figure A.1: The tangent space at a point on the 2-sphere manifold can be pictured as the tangent plane at that point. If a vector field is placed on the manifold, then one vector would lie in such a tangent space at every point on the manifold. **Credit:** "BenFrantzDale" (https://commons.wikimedia.org/wiki/File:Image_Tangent-plane.svg).

One can verify that the set of all differential operators, implicitly assumed to work on some scalar function, satisfy all criteria for being a vector space. Thus, like one can regard $\boldsymbol{V} = V^\mu \boldsymbol{e}_\mu$ as a vector with components V^μ and basis vectors $\boldsymbol{e}_\mu$, one can regard

$$\frac{\mathrm{d}}{\mathrm{d}\lambda} = \frac{\mathrm{d}x^\mu}{\mathrm{d}\lambda}\partial_\mu \tag{A.4}$$

as a vector with components $\mathrm{d}x^\mu/\mathrm{d}\lambda$ and basis vectors $\partial_\mu = \partial/\partial x^\mu$. To see this clearly, make a coordinate transformation

$$x \to x'(x) \qquad \text{with inverse} \qquad x' \to x(x'). \tag{A.5}$$

The product of the Jacobian matrices for a transformation and its inverse is the identity

$$\frac{\partial x'^\alpha}{\partial x^\gamma}\frac{\partial x^\gamma}{\partial x'^\beta} = \delta^\alpha_\beta. \tag{A.6}$$

Using the chain rule and the Jacobian property, the directional derivative transforms as

$$\frac{\mathrm{d}}{\mathrm{d}\lambda} = \frac{\mathrm{d}x^{\mu'}}{\mathrm{d}\lambda}\partial_{\mu'} = \underbrace{\left(\frac{\mathrm{d}x^\alpha}{\mathrm{d}\lambda}\frac{\partial x^{\mu'}}{\partial x^\alpha}\right)}_{\text{components}}\underbrace{\left(\frac{\partial x^\beta}{\partial x^{\mu'}}\partial_\beta\right)}_{\text{basis}} = \frac{\mathrm{d}x^\mu}{\mathrm{d}\lambda}\partial_\mu. \tag{A.7}$$

We see that the transformation of the components and the basis vectors exactly cancel each other, so the directional derivative is unchanged – consistent with it being a vector.

Note that we almost always use the convention $x^{\mu'} = x'^\mu$ of placing the prime on the *index* rather than the underlying object, but defined to mean the same. This makes it easy to see which indices are associated with transformed quantities. This is a matter of taste. For example, we find it easier to read, remember and reason about the index operations in the left version of the transformation

$$x^{\mu'} = \frac{\partial x^{\mu'}}{\partial x^\mu}x^\mu \qquad \text{compared to} \qquad x'^\mu = \frac{\partial x'^\mu}{\partial x^\nu}x^\nu. \tag{A.8}$$

We define an n-dimensional **covariant vector** as an n-tuple V_μ that transforms with the *same* matrix $\partial x^\mu \Big/ \partial x^{\mu'}$ as the change of basis in transformation (A.7) as

$$V_{\mu'} = \frac{\partial x^\mu}{\partial x^{\mu'}}V_\mu. \tag{A.9a}$$

Oppositely, we define an n-dimensional **contravariant vector** as an n-tuple V^μ that transforms with the *inverse* matrix $\partial x^{\mu'} \big/ \partial x^\mu$ as

$$V^{\mu'} = \frac{\partial x^{\mu'}}{\partial x^\mu} V_\mu. \tag{A.9b}$$

More generally, we define an n-dimensional **tensor** of rank (r, s) as an array composed of r n-dimensional contravariant indices and s n-dimensional covariant indices that transforms as

$$T^{\mu'_1 \cdots \mu'_r}_{\nu'_1 \cdots \nu'_s} = \frac{\partial x^{\mu'_1}}{\partial x^{\mu_1}} \cdots \frac{\partial x^{\mu'_r}}{\partial x^{\mu_r}} \frac{\partial x^{\nu_1}}{\partial x^{\nu'_1}} \cdots \frac{\partial x^{\nu_s}}{\partial x^{\nu'_s}} T^{\mu_1 \cdots \mu_r}_{\nu_1 \cdots \nu_s} \tag{A.9c}$$

under the coordinate transformation (A.5).

A.1.2 Metric tensor

The **metric tensor**

$$g_{\mu\nu}(x) = \boldsymbol{e}_\mu(x) \cdot \boldsymbol{e}_\nu(x) \tag{A.10}$$

is defined as the inner products between basis vectors $\boldsymbol{e}_\mu$ that span the tangent spaces at each point x on the manifold. It thus encodes lengths of the basis vectors and angles between them, and is therefore a fundamental object that describes the geometry of the manifold. For example, in Minkowski space with coordinates $x^\mu = (ct, x, y, z)$, the metric is $\eta_{\mu\nu} = \mathrm{diag}(+1, -1, -1, -1)$.

In addition, we define the **inverse metric tensor** $g^{\mu\nu}$ as the inverse matrix satisfying

$$g^{\mu\nu} g_{\nu\sigma} = \delta^\mu_\sigma. \tag{A.11}$$

Using the metric and its inverse, we can **raise and lower indices** on tensors. For example, the object $g_{\mu\nu} V^\nu$, according to definition (A.9c), transforms as a covariant vector

$$g_{\mu'\nu'} V^{\nu'} = \left(\frac{\partial x^\alpha}{\partial x^{\mu'}} \frac{\partial x^\beta}{\partial x^{\nu'}} g_{\alpha\beta} \right) \left(\frac{\partial x^{\nu'}}{\partial x^\nu} V^\nu \right) = \frac{\partial x^\alpha}{\partial x^{\mu'}} \Big(g_{\alpha\nu} V^\nu \Big), \tag{A.12}$$

so it is meaningful to label it as a covariant vector with a lower index $V_\mu = g_{\mu\nu} V^\nu$. Similarly, we can use the inverse metric $g^{\mu\nu}$ to raise indices.

A.1.3 Line and volume elements

From the metric tensor, one defines the **line element**

$$\mathrm{d}s = \sqrt{g_{\mu\nu} \, \mathrm{d}x^\mu \, \mathrm{d}x^\nu} \tag{A.13a}$$

that extends the concept of distance locally to every point on the manifold. By integrating the line element from one point on the manifold to another, one can compute the total distance

$$s = \int_1^2 \mathrm{d}s = \int_1^2 \sqrt{g_{\mu\nu} \, \mathrm{d}x^\mu \, \mathrm{d}x^\nu} \tag{A.13b}$$

between two points 1 and 2. Similarly, one can compute the **volume** of a region

$$V = \int \mathrm{d}V = \int \sqrt{-|\gamma|} \, \mathrm{d}x^1 \, \mathrm{d}x^2 \, \mathrm{d}x^3, \tag{A.13c}$$

where γ is the induced metric on the surface and $|\gamma| < 0$ its determinant. The factor $\sqrt{-|\gamma|}$ arises to make the volume element $\mathrm{d}^n x \sqrt{-|\gamma|}$ invariant under coordinate transformations.

A.1.4 Covariant derivative and connection coefficients

Knowing how vectors and general tensors transform, let us generalize the concept of derivatives to curved space. By the transformation rules we have found so far and the product rule, the normal partial derivative of a vector transforms like

$$\partial_{\mu'} V^{\nu'} = \left(\frac{\partial x^{\mu}}{\partial x^{\mu'}}\partial_{\mu}\right)\left(\frac{\partial x^{\nu'}}{\partial x^{\nu}} V^{\nu}\right) = \frac{\partial x^{\mu}}{\partial x^{\mu'}}\frac{\partial x^{\nu'}}{\partial x^{\nu}}\partial_{\mu} V^{\nu} + \frac{\partial x^{\mu}}{\partial x^{\mu'}}\frac{\partial^2 x^{\nu'}}{\partial x^{\mu}\,\partial x^{\nu}} V^{\nu}. \tag{A.14}$$

The first term respects the tensor transformation law (A.9c), but the second does not, so $\partial_{\mu} V^{\nu}$ is *not a tensor*. We define a tensorial derivative ∇_{μ} by *demanding* that it adheres to the tensorial transformation

$$\nabla_{\mu'} V^{\nu'} = \frac{\partial x^{\mu}}{\partial x^{\mu'}}\frac{\partial x^{\nu'}}{\partial x^{\nu}}\nabla_{\mu} V^{\nu}. \tag{A.15}$$

It turns out that our requirements can be met if we define the **covariant derivative** as

$$\nabla_{\mu} V^{\nu} = \partial_{\mu} V^{\nu} + \Gamma^{\nu}_{\sigma\mu} V^{\sigma}. \tag{A.16}$$

[Car19, equation 3.6-3.10] shows that it obeys the tensorial transformation (A.15) if the so-called **connection coefficients** $\Gamma^{\nu}_{\sigma_{\mu}}$ transform according to

$$\Gamma^{\nu'}_{\mu'\lambda'} = \frac{\partial x^{\mu}}{\partial x^{\mu'}}\frac{\partial x^{\lambda}}{\partial x^{\lambda'}}\frac{\partial x^{\nu'}}{\partial x^{\nu}}\Gamma^{\nu}_{\mu\lambda} + \frac{\partial x^{\mu}}{\partial x^{\mu'}}\frac{\partial x^{\lambda}}{\partial x^{\lambda'}}\frac{\partial^2 x^{\nu'}}{\partial x^{\mu}\,\partial x^{\lambda}}. \tag{A.17}$$

It is possible to generalize the covariant derivative to an arbitrary tensor $T^{\alpha_1\ldots\alpha_r}_{\beta_1\ldots\beta_s}$ of rank (r, s) by adding more terms with connection coefficients. [Car19, equation 3.11-3.16] shows that the general **covariant derivative** that respects the tensorial transformation law (A.9c) is

$$\begin{aligned}\nabla_{\mu} T^{\alpha_1\ldots\alpha_r}_{\beta_1\ldots\beta_s} &= \partial_{\mu} T^{\alpha_1\ldots\alpha_r}_{\beta_1\ldots\beta_s} \\ &+ \Gamma^{\alpha_1}_{\sigma\mu} T^{\sigma\alpha_2\ldots\alpha_r}_{\beta_1\ldots\beta_s} + \cdots + \Gamma^{\alpha_r}_{\sigma\mu} T^{\alpha_1\ldots\alpha_{r-1}\sigma}_{\beta_1\ldots\beta_s} \\ &- \Gamma^{\sigma}_{\beta_1\mu} T^{\alpha_1\ldots\alpha_r}_{\sigma\beta_2\ldots\beta_s} - \cdots - \Gamma^{\sigma}_{\beta_s\mu} T^{\alpha_1\ldots\alpha_r}_{\beta_1\ldots\beta_{s-1}\sigma}.\end{aligned} \tag{A.18}$$

That is, for each upper index α_i, add $+\Gamma^{\alpha_i}_{\sigma\mu} T^{\alpha_1\ldots\alpha_{i-1}\sigma\alpha_{i+1}\ldots\alpha_r}_{\beta_1\ldots\beta_s}$, and for each lower index β_i, subtract $\Gamma^{\sigma}_{\beta_i\mu} T^{\alpha_1\ldots\alpha_r}_{\beta_1\ldots\beta_{i-1}\sigma\beta_{i+1}\ldots\beta_s}$.

Note that the connection coefficients (A.17) *do not* transform like tensors – the whole point is to stash the non-tensorial behavior into the connection coefficients so that the *covariant derivative* (A.18) transforms as a tensor. However, since $\nabla_{\mu} V^{\nu}$ and $\hat{\nabla}_{\mu} V^{\nu}$ for two different connection coefficients $\Gamma^{\alpha}_{\beta\mu}$ and $\hat{\Gamma}^{\alpha}_{\beta\mu}$ are tensors by definition, subtracting them shows that the *difference*

$$S^{\alpha}{}_{\beta\gamma} = \Gamma^{\alpha}_{\beta\gamma} - \hat{\Gamma}^{\alpha}_{\beta\gamma} \tag{A.19}$$

between two connection coefficients *does* transform like a tensor.

There are many possible choices of the connection coefficients that satisfy equation (A.17). However, it turns out that we can find a set of *unique* connection coefficients from the *metric* if we impose two additional requirements. First, we demand that the **torsion tensor**

$$T^{\alpha}{}_{\beta\gamma} = \Gamma^{\alpha}_{\beta\gamma} - \Gamma^{\alpha}_{\gamma\beta} = 0 \tag{A.20}$$

vanishes. Equivalently, the connection coefficients $\Gamma^{\alpha}_{\beta\gamma} = \Gamma^{\alpha}_{\beta\gamma}$ are symmetric in the lower indices. Second, we require **metric compatibility**

$$\nabla_{\rho} g_{\mu\nu} = 0, \tag{A.21}$$

expressing that the metric is covariantly constant. One can show that this guarantees that lengths of vectors and angles between them are preserved under parallel transport, which we will study in the next section, making this a reasonable demand. [Heh+76, equation 2.10] The

covariantly constant nature of the metric implies that we can view spacetime as a continuum of flat Minkowski spacetimes, "sewn together" by the connection $\Gamma^{\alpha}_{\beta\gamma}$. Metric compatibility implies that

$$g_{\mu\lambda}\nabla_\rho V^\lambda = \nabla_\rho(g_{\mu\lambda}V^\lambda) = \nabla_\rho V_\mu, \tag{A.22}$$

so we can raise and lower indices inside covariant derivatives, even if the metric is outside. Using both of these assumptions, we can write out the metric compatibility requirement (A.21) for three permutations of the indices:

$$\nabla_\rho g_{\mu\nu} = \partial_\rho g_{\mu\nu} - \Gamma^\lambda_{\rho\mu} g_{\lambda\nu} - \Gamma^\lambda_{\rho\nu} g_{\mu\lambda} = 0, \tag{A.23a}$$

$$\nabla_\mu g_{\nu\rho} = \partial_\mu g_{\nu\rho} - \Gamma^\lambda_{\mu\nu} g_{\lambda\rho} - \Gamma^\lambda_{\mu\rho} g_{\nu\lambda} = 0, \tag{A.23b}$$

$$\nabla_\nu g_{\rho\mu} = \partial_\nu g_{\rho\mu} - \Gamma^\lambda_{\nu\rho} g_{\lambda\mu} - \Gamma^\lambda_{\nu\mu} g_{\rho\lambda} = 0. \tag{A.23c}$$

By subtracting the second and third equation from the first and solving the resulting equation for the connection, we find the **Christoffel symbols** or **metric connection**

$$\Gamma^\sigma_{\mu\nu} = \frac{1}{2} g^{\sigma\rho} \left(\partial_\mu g_{\nu\rho} + \partial_\nu g_{\rho\mu} - \partial_\rho g_{\mu\nu} \right). \tag{A.24}$$

In general relativity, we will *always* use this unique representation of the connection coefficients given in terms of the metric only. With this choice, the metric single-handedly determines the geometry of spacetime, as it is the only fundamental object that all the other geometric quantities we have looked at depends on. In fact, the requirements of zero torsion and metric compatibility that led to this metric can be viewed as defining features of general relativity. By relaxing either of these requirements, one can come up with various generalizations of general relativity. For example, by allowing for nonzero torsion (A.20), one obtains the *Einstein-Cartan theory* of gravitation. According to [Heh+76], the inclusion of torsion is equivalent to accounting for the *spin* of the microscopic particles that make up the macroscopic matter. However, general relativity is concerned with describing *macroscopic* objects, which justifies our demand of zero torsion.

A.1.5 Parallel transport and the geodesic equation

Now that we know how to take proper derivatives of vector fields and general tensor fields on manifolds, we can discuss how to *parallel transport* vectors on the manifold. In flat space, we can move a vector around, and it will keep pointing in the same direction. But on a curved 2-sphere, a vector that is parallel transported will end up different depending on the route taken, as illustrated in figure A.2. Generalizing the directional derivative $\mathrm{d}/\mathrm{d}\tau = (\mathrm{d}x^\mu/\mathrm{d}\tau)\partial_\mu$ from calculus, we define the **directional covariant derivative** along a path $x(\tau)$ as

$$\frac{D}{\mathrm{d}\tau} = \frac{\mathrm{d}x^\mu}{\mathrm{d}\tau}\nabla_\mu, \tag{A.25}$$

where ∇_μ is the covariant derivative (A.18). We say that a tensor is **parallel transported** if its components are kept constant during transport, as expressed by

$$\frac{D}{\mathrm{d}\tau} T^{\mu_1\ldots\mu_m}_{\nu_1\ldots\nu_n} = 0. \tag{A.26}$$

For the special case of a vector V^μ we get the **equation of parallel transport**

$$\frac{\mathrm{d}V^\mu}{\mathrm{d}\tau} + \Gamma^\mu_{\sigma\rho}\frac{\mathrm{d}x^\sigma}{\mathrm{d}\tau}V^\rho = 0. \tag{A.27}$$

The solution of this first-order differential equation is the continuation $V^\mu(\tau)$ from an initial vector $V^\mu(0)$ along the path such that its components are constant.

In Euclidean space, a straight line is the shortest path between two points. In curved space, we call the shortest path between two points on a manifold a **geodesic**. An equivalent definition

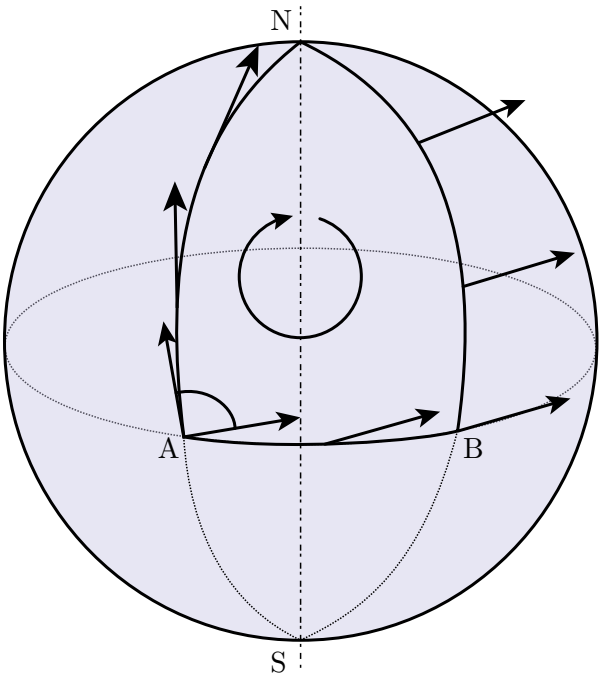

Figure A.2: When a vector is parallel transported around the closed loop $A \to N \to B \to A$ on the 2-sphere, its final direction depends on the path taken. **Credit:** "Fred the Oyster" (https://commons.wikimedia.org/wiki/File:Parallel_Transport.svg).

of both a straight line and a geodesic is that it is the path $x(\tau)$ that parallel transports its own tangent vector $\mathrm{d}x^\mu/\mathrm{d}\tau$. Inserting this vector into the equation of parallel transport (A.27), we find the **geodesic equation**

$$\frac{\mathrm{d}^2x^\mu}{\mathrm{d}\tau^2} + \Gamma^\mu_{\rho\sigma}\frac{\mathrm{d}x^\rho}{\mathrm{d}\tau}\ \frac{\mathrm{d}x^\sigma}{\mathrm{d}\tau} = 0. \tag{A.28}$$

In flat spacetime, it reduces to the equation of a straight line $\mathrm{d}^2x^\mu/\mathrm{d}\tau^2 = 0$. One of Einstein's profound insights of general relativity was that gravity does not simply alter the path of a freely falling particle away from the straight line it would follow in Euclidean space in the absence of gravity. Instead, gravity presents itself in the geometry of spacetime, as the presence of energy-momentum curves spacetime and lays geodesic "tracks" according to equation (A.28) that any freely falling particle is destined to follow. *Gravity is geometry.*

A.1.6 Riemann curvature tensor, Ricci tensor and Ricci scalar

So far we have used the term "curvature" quite informally – let us now formalize this. We already saw that parallel transporting a vector along different paths on a curved manifold like the 2-sphere yield different results. We have also seen that the covariant derivative measures the rate of change of a vector along some direction compared to what it would have been if it was parallel transported. Thus, the commutator $[\nabla_\mu, \nabla_\nu]V^\rho = \nabla_\mu\nabla_\nu V^\rho - \nabla_\nu\nabla_\mu V^\rho$ measures the difference of parallel transporting a vector along two different directions. Explicitly inserting the covariant derivative (A.18), this commutator can be written

$$[\nabla_\mu, \nabla_\nu]V^\rho = R^\rho{}_{\sigma\mu\nu}V^\sigma - T^\lambda{}_{\mu\nu}\nabla_\lambda V^\rho, \tag{A.29}$$

where $T^\lambda{}_{\mu\nu}$ is the torsion tensor (A.20) that we assume to vanish, and we define the **Riemann curvature tensor**

$$R^\rho{}_{\sigma\mu\nu} = \partial_\mu\Gamma^\rho_{\nu\sigma} - \partial_\nu\Gamma^\rho_{\mu\sigma} + \Gamma^\rho_{\mu\lambda}\Gamma^\lambda_{\nu\sigma} - \Gamma^\rho_{\nu\lambda}\Gamma^\lambda_{\mu\sigma}. \tag{A.30}$$

We expect that if space is flat, then a parallel transported vector should not depend on the path taken, so the commutator (A.29) and thus the Riemann tensor (A.30) should vanish. If there exists *any* choice of coordinates in which the curvature tensor vanishes, then it vanishes in *all*

coordinates by its tensorial nature, and this is our ultimate definition of **flat space**. In fact, it turns out that at any point x_0 we can find **normal coordinates** x^μ in which the metric locally resembles Minkowski space with $g_{\mu\nu} = \eta_{\mu\nu}$ and $\partial_\sigma g_{\mu\nu} = 0$ to first order in the displacement. To second order in the displacement, [KKK12] shows that the metric can be written

$$g_{\mu\nu}(x) = \eta_{\mu\nu} - \frac{1}{2} R_{\alpha\mu\beta\nu}(x^\alpha - x_0^\alpha)(x^\beta - x_0^\beta). \tag{A.31}$$

This shows that the Riemann tensor is a *very* appropriate measure of curvature. Moreover, **Einstein's equivalence principle** and the related **principle of general covariance** states that a physical law that is expressed by a tensor equation in Minkowski space *also* holds in any reference frame in the presence of gravity. [Wei72, chapter 4]

From the curvature tensor, we can form tensors of lower rank by contracting some of its indices. With the Christoffel connection (A.24), the only independent contraction we can make is the **Ricci tensor**

$$R_{\mu\nu} = R^\lambda{}_{\mu\lambda\nu}. \tag{A.32}$$

The two other possible contractions either vanish or are related to the Ricci tensor. Thus, the simplest scalar quantity we can form that says something about curvature is the **Ricci scalar**

$$R = R^\mu{}_\mu. \tag{A.33}$$

In the next section, we will use the Ricci scalar to derive the Einstein field equations.

A.2 Least-action derivation of the Einstein field equations

Following [Car19, section 4.3], we will derive the Einstein field equations

$$R_{\mu\nu} - \frac{1}{2} R g_{\mu\nu} = \frac{8\pi G}{c^4} T_{\mu\nu} \tag{A.34}$$

from the principle of least action. We will *postulate* the action

$$S[g_{\mu\nu}, \nabla_\sigma g_{\mu\nu}] = \int \mathrm{d}^n x \, \mathcal{L}(g_{\mu\nu}, \nabla_\sigma g_{\mu\nu}) = \int \mathrm{d}^n x \, \sqrt{-|g|}\hat{\mathcal{L}}(g_{\mu\nu}, \nabla_\sigma g_{\mu\nu}) \tag{A.35}$$

that, when varied with respect to the metric $g_{\mu\nu}$ and subject to the principle of least action $\delta S = 0$, yields the Einstein field equations. Here $\mathcal{L}$ and $\hat{\mathcal{L}}$ are Lagrangian densities with and without the metric determinant $|g| < 0$. As the strategy simply involves *guessing* the correct action that produces the desired equations, this derivation is not based on any physical first principles, so its consequences would ultimately have to be experimentally verified. Nevertheless, [Car19, page 160-161] explains how one can at the very least narrow down the choice of action based on scalar quantities that are relevant for describing curved space.

We postulate the **Hilbert action**

$$S_H = \frac{c^3}{16\pi G} \int \mathrm{d}^n x \sqrt{-|g|}\, R. \tag{A.36}$$

It is not an unreasonable guess, for the Lagrangian is a scalar quantity, and we showed that the simplest scalar quantity we could create that somehow describes curvature is the Ricci scalar (A.33). The factor $\sqrt{-|g|}$ ensures that the volume element is invariant. The prefactor has been conveniently chosen to yield correct result (A.57) in the end, which we will see in appendix A.3.2 leads to Newtonian gravity in the Newtonian limit. From an ignorant point of view, we could instead regard the prefactor as an arbitrary constant at this point, and eventually replace it with whichever combination of constants that reproduces Newtonian gravity in the Newtonian limit.

We *could* get the corresponding equations of motion by plugging the Lagrangian density $\hat{\mathcal{L}} = Rc^3/16\pi G$ into the Euler-Lagrange equations

$$\frac{\partial \hat{\mathcal{L}}}{\partial \phi} - \nabla_\mu \left(\frac{\partial \hat{\mathcal{L}}}{\partial \left(\nabla_\mu \phi\right)} \right) = 0. \tag{A.37}$$

In fact Hilbert himself did this, [Hil24] but doing so requires a great deal of effort. Instead, we will vary the action with respect to the metric and express the variation in the form

$$\delta S_H = \int \mathrm{d}^n x \sqrt{-|g|}\ \ F(g_{\mu\nu}, \nabla_\sigma g_{\mu\nu})\, \delta g^{\mu\nu} = 0. \tag{A.38}$$

Then we can conclude that the equations of motion are $F(g_{\mu\nu}, \nabla_\sigma g_{\mu\nu}) = 0$.

It may sound more natural to express the variation in terms of the ordinary metric $g_{\mu\nu}$ instead of its inverse $g^{\mu\nu}$, like we did above. But since $g^{\mu\lambda} g_{\lambda\nu} = \delta^\mu_\nu$, varying both sides with the product rule relates the two by

$$\delta g_{\mu\nu} = -g_{\mu\rho} g_{\nu\sigma} \delta g^{\rho\sigma}. \tag{A.39}$$

Thus, the stationary points are the same regardless of which one we vary with respect to. We vary with respect to the inverse metric, as it makes the derivation flow more naturally.

Using $R = R^\mu{}_\mu = g^{\mu\nu} R_{\mu\nu}$ and varying the action (A.36) with the product rule, we obtain

$$\delta S_H = \frac{c^3}{16\pi G} \Bigg[\underbrace{\int \mathrm{d}^n x \sqrt{-|g|}\, g^{\mu\nu} \delta R_{\mu\nu}}_{\delta S_1} + \underbrace{\int \mathrm{d}^n x \sqrt{-|g|}\, R_{\mu\nu} \delta g^{\mu\nu}}_{\delta S_2} + \underbrace{\int \mathrm{d}^n x\, R\, \delta \sqrt{-|g|}}_{\delta S_3} \Bigg]. \tag{A.40}$$

The second term δS_2 is already in the desired form (A.38), but we must do some work to bring δS_1 and δS_3 to the same form.

First, let us take care of δS_1 by reexpressing $\delta R_{\mu\nu}$ in terms of metric variations in a top-down manner. The Ricci tensor $R_{\mu\nu} = R^\lambda{}_{\mu\lambda\nu}$ is the contraction of the Riemann tensor (A.30). Varying it, we get

$$\delta R^\rho{}_{\sigma\mu\nu} = \partial_\mu \delta\Gamma^\rho_{\nu\sigma} - \partial_\nu \delta\Gamma^\rho_{\mu\sigma} + \left(\delta\Gamma^\rho_{\mu\lambda}\right) \Gamma^\lambda_{\nu\sigma} + \Gamma^\rho_{\mu\lambda} \left(\delta\Gamma^\lambda_{\nu\sigma}\right) - \left(\delta\Gamma^\rho_{\nu\lambda}\right) \Gamma^\lambda_{\mu\sigma} - \Gamma^\rho_{\nu\lambda} \left(\delta\Gamma^\lambda_{\mu\sigma}\right). \tag{A.41}$$

Now reexpress the variations of the Christoffel symbols. Instead of hammering straight through their definition (A.24), we observe that while single Christoffel symbols do not transform as a tensor, their *variation* is the difference between two Christoffel symbols and *do*, as in equation (A.19). It is therefore meaningful to use equation (A.18) to take its covariant derivative

$$\nabla_\lambda \delta\Gamma^\rho_{\nu\mu} = \partial_\lambda \delta\Gamma^\rho_{\nu\mu} + \Gamma^\rho_{\lambda\sigma} \delta\Gamma^\sigma_{\nu\mu} - \Gamma^\sigma_{\lambda\nu} \delta\Gamma^\rho_{\sigma\mu} - \Gamma^\sigma_{\lambda\mu} \delta\Gamma^\rho_{\nu\sigma}. \tag{A.42}$$

Flipping this equation around for $\partial_\lambda \delta\Gamma^\rho_{\nu\mu}$ and substituting the result into the variation of the Riemann tensor (A.41), we witness an avalanche of cancellations, leaving only the terms

$$\delta R^\rho{}_{\mu\lambda\nu} = \nabla_\lambda \delta\Gamma^\rho_{\nu\mu} - \nabla_\nu \delta\Gamma^\rho_{\lambda\mu}. \tag{A.43}$$

The variation of the Ricci tensor follows by contracting ρ and λ. Then the first term in the variation of the action becomes

$$\begin{aligned} \delta S_1 &= \int \mathrm{d}^n x \sqrt{-|g|}\, g^{\mu\nu} \left(\nabla_\lambda \delta\Gamma^\lambda_{\mu\nu} - \nabla_\nu \delta\Gamma^\lambda_{\lambda\mu} \right) \\ &= \int \mathrm{d}^n x \sqrt{-|g|}\, \nabla_\sigma \left(g^{\mu\nu} \delta\Gamma^\sigma_{\mu\nu} - g^{\mu\sigma} \delta\Gamma^\lambda_{\lambda\mu} \right). \end{aligned} \tag{A.44}$$

We still have not brought the variation to the form (A.38), but it does not matter. By **Stokes theorem** [Car19, equation 3.35]

$$\int_M \mathrm{d}^n x \sqrt{|g|} \nabla_\mu V^\mu = \int_{\partial M} \mathrm{d}^{n-1} \sqrt{|\gamma|} n_\mu V^\mu, \tag{A.45}$$

our integral for δS_1 over n-space can be converted into a boundary integral over $(n-1)$-space at infinity. But the variational method that we have used here asserts that there is no variation on the boundary, so

$$\delta S_1 = 0. \tag{A.46}$$

Let us now express δS_3 in terms of $\delta g^{\mu\nu}$. We will need the matrix identity

$$\log |M| = \operatorname{tr} \log M \qquad \big(\text{where } |M| = \det M\big). \tag{A.47}$$

This is trivial for diagonal matrices M. By using the property $|AB| = |A|\,|B|$, we can easily extend it to diagonalizable matrices $M = PDP^{-1}$. Varying both sides of equation (A.47), we obtain

$$\frac{\delta |M|}{|M|} = \operatorname{tr}\left(M^{-1} \delta M\right). \tag{A.48}$$

For details on variations of matrix functions, we recommend working through [Bla09]. Taking M to be the metric $g_{\mu\nu}$ and M^{-1} its inverse $g^{\mu\nu}$, we find

$$\delta |g| = |g|\, g^{\mu\nu} \delta g_{\mu\nu} = -\,|g|\, g_{\mu\nu} \delta g^{\mu\nu}, \tag{A.49}$$

where we used equation (A.39) to convert $\delta g_{\mu\nu}$ to $\delta g^{\mu\nu}$. Now the chain rule gives

$$\delta \sqrt{-|g|} = -\frac{1}{2} \frac{\delta |g|}{\sqrt{-|g|}} = -\frac{1}{2} \sqrt{-|g|} g_{\mu\nu} \delta g^{\mu\nu}, \tag{A.50}$$

so the third contribution to the variation of the action (A.40) is

$$\delta S_3 = \int \mathrm{d}^n x \sqrt{-|g|} \left(-\frac{1}{2} R g_{\mu\nu}\right) \delta g^{\mu\nu}. \tag{A.51}$$

At last, we have brought the variation of the action to the form (A.38) with

$$\delta S_H = \frac{c^3}{16\pi G} \int \mathrm{d}^n x \sqrt{-|g|} \left(R_{\mu\nu} - \frac{1}{2} R g_{\mu\nu}\right) \delta g^{\mu\nu} = 0. \tag{A.52}$$

The variation of the integral can only vanish if the integrand vanishes, so we have found the **Einstein field equations in vacuum**,

$$\frac{c^3}{16\pi G} \frac{1}{\sqrt{-|g|}} \frac{\delta S_H}{\delta g^{\mu\nu}} = R_{\mu\nu} - \frac{1}{2} R g_{\mu\nu} = 0. \tag{A.53}$$

To unveil the Einstein field equations in the presence of matter, we add a contribution $S_M = \int \mathrm{d}^n x \sqrt{-|g|}\, \mathcal{L}_M$ that represents matter to a new total action

$$S = S_H + S_M. \tag{A.54}$$

Repeating the same procedure as above then yields the equations of motion

$$\frac{c^3}{16\pi G} \frac{1}{\sqrt{-|g|}} \frac{\delta S}{\delta g^{\mu\nu}} = \left(R_{\mu\nu} - \frac{1}{2} R g_{\mu\nu}\right) + \frac{c^3}{16\pi G} \frac{1}{\sqrt{-|g|}} \frac{\delta S_M}{\delta g^{\mu\nu}} = 0. \tag{A.55}$$

If we now *define* the energy-momentum tensor $T_{\mu\nu}$ by

$$\frac{c^3}{16\pi G} \frac{1}{\sqrt{-|g|}} \frac{\delta S_M}{\delta g^{\mu\nu}} = -\frac{8\pi G}{c^4} T_{\mu\nu}, \tag{A.56}$$

we uncover the **Einstein field equations in the presence of matter**,

$$R_{\mu\nu} - \frac{1}{2} R g_{\mu\nu} = \frac{8\pi G}{c^4} T_{\mu\nu}. \tag{A.57}$$

A.3 The Newtonian limit

In Newtonian gravity, the presence of mass density $\rho(\boldsymbol{x})$ produces a gravitational field $-\nabla V(\boldsymbol{x})$ through the Poisson equation

$$\nabla^2 V(\boldsymbol{x}) = 4\pi G\rho(\boldsymbol{x}). \tag{A.58}$$

In turn, matter respond to the field as particles are accelerated by

$$\frac{\mathrm{d}^2\boldsymbol{x}}{\mathrm{d}t^2} = -\nabla V(\boldsymbol{x}). \tag{A.59}$$

Given the initial distribution and velocities of matter, these two coupled differential equations determine its movement forever and thus contain all of Newtonian gravity. Here we will show that general relativity is reducible to Newtonian gravity in the **Newtonian limit** characterized by *slow movement* and a *static* and *weak* gravitational field. In particular, we will demonstrate that the response of matter to the field (A.59) follows from the geodesic equation (A.28), and similarly that the response of the field to matter (A.58) follows from the Einstein field equations (A.57).

Before we set out, however, let us make the Newtonian limit mathematically precise. First, by *slow movement*, we mean that all velocities v are much lower than the speed of light c, so

$$\frac{v}{c} \ll 1. \tag{A.60a}$$

In a potential V measured with respect to $V(\infty) = 0$, freely falling particles are accelerated to kinetic energies on the scale $\frac{1}{2}mv^2 = mV$. Consequently, particles could reach velocities that violate criterion (A.60a) unless the potential is bounded by

$$\frac{V}{c^2} \ll 1. \tag{A.60b}$$

Motion is also generated by internal stresses in the system. For example, in appendix B we study perfect fluids with energy-momentum (B.5). We show that sound waves propagate with the velocity $v = c\sqrt{\mathrm{d}P/\mathrm{d}\epsilon}$ on top of a fluid in equilibrium with $T_\mu{}^\nu = \mathrm{diag}\,(\epsilon, -P, -P, -P)$. It can therefore also be expressed as $v = c\sqrt{-\mathrm{d}T_i{}^i/\mathrm{d}T_0{}^0}$, where $T_i{}^i$ is any *one* diagonal element and there is no sum over i. More generally, we therefore assume slow movement corresponds to $\mathrm{d}T_{ij}/\mathrm{d}T_{00} \ll 1$, and by integration,

$$\frac{T_{ij}}{T_{00}} \ll 1. \tag{A.60c}$$

In other words, we can neglect pressure P in favor of energy density ϵ in the Newtonian limit. This result can be understood physically – pressure is a result of randomized motion and decreases with the velocities of the motion, while energy is equivalent to mass and its presence is unaffected by the velocity of the mass. In summary, slow motion is achieved only if equations (A.60a), (A.60b) and (A.60c) are all satisfied.

The second assumption of a *static* gravitational field means that all time derivatives of the metric vanish like

$$\partial_0 g_{\mu\nu} = 0. \tag{A.61}$$

Third, a *weak* field corresponds to a metric that can be written as a perturbation

$$g_{\mu\nu} = \eta_{\mu\nu} + h_{\mu\nu} \qquad \text{with} \qquad \left|h_{\mu\nu}\right| \ll 1 \tag{A.62a}$$

on top of flat Minkowski space $\eta_{\mu\nu} = \mathrm{diag}(+1, -1, -1, -1)$. The inverse metric $g^{\mu\nu}$ should satisfy $g^{\mu\nu}g_{\nu\sigma} = \delta^\mu_\sigma$, so to first order in h we must have

$$g^{\mu\nu} = \eta^{\mu\nu} - h^{\mu\nu}, \tag{A.62b}$$

where we raise indices of the perturbation $h^{\mu\nu} = \eta^{\mu\rho}\eta^{\nu\sigma}h_{\rho\sigma}$ with the *Minkowski* metric $\eta^{\mu\nu}$.

A.3.1 Matter's response to the field

In general relativity, matter responds to the gravitational field by moving along geodesics $x(\tau)$ that satisfy the geodesic equation

$$\frac{\mathrm{d}^2 x^\mu}{\mathrm{d}\tau^2} + \Gamma^\mu_{\rho\sigma} \frac{\mathrm{d}x^\rho}{\mathrm{d}\tau} \frac{\mathrm{d}x^\sigma}{\mathrm{d}\tau} = 0. \tag{A.63}$$

Let us now show that we recover Newton's second law (A.59) in the Newtonian limit.

The criterion of slow movement equation (A.60a) implies that a particle with four-velocity $\mathrm{d}x^\mu/\mathrm{d}\tau$ has spatial components $\mathrm{d}x^i/\mathrm{d}t \ll c$, so it must be dominated by the temporal component $c\,\mathrm{d}t/\mathrm{d}\tau \approx c$. Then $\mathrm{d}x^i/\mathrm{d}\tau \ll \mathrm{d}x^0/\mathrm{d}\tau$ and the geodesic equation can be approximated by

$$\frac{\mathrm{d}^2 x^\mu}{\mathrm{d}\tau^2} + \Gamma^\mu_{00}\, c^2 \left(\frac{\mathrm{d}t}{\mathrm{d}\tau}\right)^2 = 0. \tag{A.64}$$

In a static field, the vanishing time derivatives (A.61) simplifies the Christoffel symbols (A.24) to $\Gamma^\mu_{00} = -\frac{1}{2} g^{\mu\lambda} \partial_\lambda g_{00}$. Inserting the weak-field metric (A.62a) and its inverse (A.62b) and calculating to first order in h, we then find the Christoffel symbols

$$\Gamma^\mu_{00} = -\frac{1}{2} \eta^{\mu\lambda} \partial_\lambda h_{00}. \tag{A.65}$$

In particular, the static metric (A.61) implies that $\Gamma^0_{00} = 0$, so $\mathrm{d}^2 t/\mathrm{d}\tau^2 = 0$ by the approximated geodesic equation (A.64). As we have neglected $\mathrm{d}x^i/\mathrm{d}\tau \ll c$, we can now regard the geodesic $x(\tau) = x(\tau(t))$ as a function of only t and apply the chain rule and the product rule to get

$$\frac{\mathrm{d}^2 x}{\mathrm{d}\tau^2} = \frac{\mathrm{d}}{\mathrm{d}\tau}\left(\frac{\mathrm{d}x}{\mathrm{d}t}\frac{\mathrm{d}t}{\mathrm{d}\tau}\right) = \left(\frac{\mathrm{d}}{\mathrm{d}\tau}\frac{\mathrm{d}x}{\mathrm{d}t}\right)\left(\frac{\mathrm{d}t}{\mathrm{d}\tau}\right) + \left(\frac{\mathrm{d}x}{\mathrm{d}t}\right)\left(\frac{\mathrm{d}^2 t}{\mathrm{d}\tau^2}\right) = \left(\frac{\mathrm{d}^2 x}{\mathrm{d}t^2}\right)\left(\frac{\mathrm{d}t}{\mathrm{d}\tau}\right)^2. \tag{A.66}$$

Upon insertion into the equation (A.64), we can cancel the common factor $(\mathrm{d}t/\mathrm{d}\tau)^2$ and write the geodesic equation purely in terms of time t as

$$\frac{\mathrm{d}^2 x^\mu}{\mathrm{d}t^2} = \frac{1}{2} c^2 \eta^{\mu\lambda} \partial_\lambda h_{00}. \tag{A.67}$$

The spatial components of this equation is precisely Newton's second law (A.59) *if* $h_{00} = 2V/c^2$. In conclusion, we have showed that a weak relativistic gravitational field with

$$g_{00} = 1 + h_{00} = 1 + \frac{2V}{c^2} \tag{A.68}$$

describes Newtonian motion in the gravitational potential V!

A.3.2 The field's response to matter

In general relativity, the gravitational field is produced by matter that enter the Einstein field equations (A.57) on the right. Let us show that they fall back the Poisson equation (A.58) to first nonzero order in the metric perturbation h of the Newtonian limit.

Suppose we are in the stationary reference frame of a perfect fluid with energy-momentum (B.5) and velocity $u^\mu = (u^0, \mathbf{0})$. To first order in h_{00}, the normalization condition $u^\mu u_\mu = c^2$ then fixes the time component

$$u^0 = \frac{c}{\sqrt{g_{00}}} = \frac{c}{\sqrt{1 + h_{00}}} \simeq c\left(1 - \frac{1}{2} h_{00}\right). \tag{A.69}$$

To lowest order, the energy-momentum (B.5) then simplifies to that of pure dust with

$$T_{00} = \rho u_0 u_0 \simeq \epsilon \qquad \text{and trace} \qquad T = T^\mu{}_\mu = g^{00} T_{00} \simeq \epsilon, \tag{A.70}$$

where we have neglected the pressure components in accordance with criterion (A.60c). Now rewrite the Einstein field equations (A.57) by taking the trace of both sides. Using $g^{\mu}{}_{\mu} = \delta^{\mu}{}_{\mu} = 4$, we find that the Ricci scalar can be expressed as $R = -8\pi GT/c^4$, so the field equations are equivalent to

$$R_{\mu\nu} = \frac{8\pi G}{c^4}\left(T_{\mu\nu} - \frac{1}{2}Tg_{\mu\nu}\right). \tag{A.71}$$

Inserting the energy-momentum (A.70) and setting $\rho = \epsilon/c^2$, we then find the Ricci tensor element

$$R_{00} = \frac{4\pi G\rho}{c^2}. \tag{A.72}$$

Instead of calculating the Ricci tensor from the energy-momentum of matter, we can attack the problem from the geometric point of view and find it from the Riemann curvature tensor

$$R^{\rho}{}_{0\mu 0} = \partial_\mu \Gamma^{\rho}_{00} - \partial_0 \Gamma^{\rho}_{\mu 0} + \Gamma^{\rho}_{\mu\lambda}\Gamma^{\lambda}_{00} - \Gamma^{\rho}_{0\lambda}\Gamma^{\lambda}_{\mu 0}. \tag{A.73}$$

Each Christoffel symbol is of order $\mathcal{O}(h)$, so the two last terms are of order $\mathcal{O}(h^2)$. Additionally, the time derivative vanishes for our stationary metric (A.61), so we are left with only $R^{\rho}{}_{0\mu 0} = \partial_\mu \Gamma^{\rho}_{00}$ to first order. Using the Christoffel symbols (A.65), the Ricci tensor is then

$$R_{00} = R^{\mu}{}_{0\mu 0} = \partial_\mu \Gamma^{\mu}_{00} = -\frac{1}{2}\eta^{\mu\lambda}\partial_\mu\partial_\lambda h_{00} \simeq \frac{1}{2}\delta^{ij}\partial_i\partial_j h_{00} = \frac{1}{2}\nabla^2 h_{00}. \tag{A.74}$$

Inserting $h_{00} = 2V/c^2$ from equation (A.68) and comparing the result to equation (A.72), we see that the Einstein field equations yield the Poisson equation (A.58) in the Newtonian limit!

A.4 CAS derivation of the Tolman-Oppenheimer-Volkoff equation

When we derived the Tolman-Oppenheimer-Volkoff equation (2.16) analytically, we made use of energy-momentum conservation $\nabla_\mu T^{\mu\nu} = 0$ instead of using the last Einstein field equation equation (2.7c). Inspired by [Sag18], we present a small program that derives the Tolman-Oppenheimer-Volkoff equation algebraically from the full system (2.7) *without* using energy-momentum conservation in the computer algebra system SAGE.

tov.sage

```
#!/usr/bin/sage

c = var("c") # speed of light
γ = var("γ", latex_name="\\gamma") # gravitational constant
α(r) = function("α", latex_name="\\alpha")(r)
m(r) = function("m")(r)
#β(r) = function("β", latex_name="\\beta")(r) # uncomment to derive symbolic (α, β) eqs.
β(r) = -1/2 * log(1 - 2*γ*m(r)/(r*c^2)) # uncomment to derive explicit mass equation
P(r) = function("P")(r)
ϵ(r) = function("ϵ", latex_name="\\epsilon")(r)

M = Manifold(4, "M", structure="Lorentzian")
X.<ct,r,θ,ϕ> = M.chart(r"ct r:(0,+oo) θ:(0,pi):\theta ϕ:(0,2*pi):\phi")

g = M.metric(name="g")
g[0,0] = +exp(2*α(r))
g[1,1] = -exp(2*β(r))
g[2,2] = -r^2
g[3,3] = -r^2*sin(θ)^2

G = g.ricci() - 1/2*g.ricci_scalar()*g
G.set_name("G")

u = M.vector_field("u")
u[0] = exp(-α(r)) * c
```

```
u = u.down(g)
u.set_name("u")

T = (ϵ(r)+P(r)) * (u*u) / c^2 - P(r) * g
T.set_name("T")

t = var("t") # substitute ct=c*t later when simplifying equations
eq1 = G[0,0].expr().substitute(ct=c*t) == 8*pi*γ/c^4*T[0,0].expr()
eq2 = G[1,1].expr().substitute(ct=c*t) == 8*pi*γ/c^4*T[1,1].expr()
eq3 = G[2,2].expr().substitute(ct=c*t) == 8*pi*γ/c^4*T[2,2].expr()

eqm = eq1.solve(diff(m,r)(r))[0]
eqα = eq2.solve(diff(α,r)(r))[0]

dαdr(r) = eqα.rhs()

eq3 = eq3.substitute(eqα, diff(α(r),r,r) == diff(dαdr(r),r))
eqP = eq3.solve(diff(P(r),r))[0]
eqP = eqP.substitute(eqm) # eliminate dm/dr term

dPdr(r) = eqP.rhs().factor()
dmdr(r) = eqm.rhs().factor()
print(f"dm/dr = {dmdr(r)}")
print(f"dP/dr) = {dPdr(r)}")
```

The output of the program precisely matches equation (2.11) and (2.16)!

Appendix B

Relativistic Fluid Dynamics

In this appendix, we will derive a number of important results from relativistic fluid mechanics needed for stability analysis of stars. We will look at the flow of fluid elements along streamlines $x(\tau)$ in a **perfect fluid** characterized by its pressure $P = P(x)$ and energy density $\epsilon = \epsilon(x)$.

This appendix is inspired by references [MTW73] and [Wei72].

B.1 Energy-momentum tensor

The definition of a perfect fluid is that the surrounding fluid appears isotropic from the rest frame that follows a given fluid element. In this frame, the energy-momentum tensor must take the standard, diagonal form

$$T^{00} = \epsilon, \qquad T^{0i} = T^{i0} = 0, \qquad T^{ij} = P\delta^{ij}. \tag{B.1}$$

In Minkowski space, the transformation matrix $\partial x^\mu / \partial x^\nu$ in the tensorial transformation law (A.9c) is the Lorentz transformation $\Lambda^\mu{}_\nu$ given in [Kac20], for example. If we are rather viewing the fluid element from the laboratory frame and it is moving with velocity $\boldsymbol{v}$ relative to us, we can therefore find the energy-momentum tensor by making the two Lorentz boosts

$$T^{\mu\nu} \to \Lambda^\mu{}_\alpha(\boldsymbol{v})\Lambda^\nu{}_\beta(\boldsymbol{v})T^{\alpha\beta}. \tag{B.2}$$

Explicitly carrying out the Lorentz transformations, we obtain the nonzero components

$$T^{00} = \frac{\epsilon + P\boldsymbol{v}^2/c^2}{1 - \boldsymbol{v}^2/c^2}, \tag{B.3a}$$

$$T^{0i} = T^{i0} = \frac{(\epsilon + P)v^i/c}{1 - \boldsymbol{v}^2/c^2}, \tag{B.3b}$$

$$T^{ij} = P\delta^{ij} + \frac{(P + \epsilon)v^i v^j/c^2}{1 - \boldsymbol{v}^2/c^2}. \tag{B.3c}$$

With the four-velocity $u^\mu = (u^0, \boldsymbol{v})$ and normalization $u_\mu u^\mu = c^2$, *all* these sixteen elements can be written collectively as the *single* tensor expression

$$T_{\mu\nu} = \frac{1}{c^2}u_\mu u_\nu(\epsilon + P) - \eta_{\mu\nu}P. \tag{B.4}$$

By the equivalence principle, the **energy-momentum tensor** for a perfect fluid in a general metric $g_{\mu\nu}$ is therefore

$$T_{\mu\nu} = \frac{1}{c^2}u_\mu u_\nu(\epsilon + P) - g_{\mu\nu}P. \tag{B.5}$$

B.2 Conservation of baryon number

Due to both the geometry of spacetime and spatial change of velocities, the volume $V(x(\tau))$ of a fluid element changes as it moves along a streamline. Let us derive the rate of change of this volume element in Minkowski space, then generalize the result to curved space using the equivalence principle. In a flat spacetime frame that follows the fluid element, the four-velocity is $u^\mu(x) \simeq (c, \boldsymbol{v}(x))$, where $\boldsymbol{v}(x)$ is a small velocity field in the vicinity of the fluid element. As the fluid element flows from one place to the next in a short time $\mathrm{d}t = \mathrm{d}\tau$, the length L^i of the fluid element along a spatial dimension i changes by

$$\mathrm{d}L^i = \Big[v^i(x + L^i) - v^i(x)\Big]\,\mathrm{d}\tau = \frac{\partial v^i(x)}{\partial x^i} L^i\,\mathrm{d}\tau \qquad \Big(\text{no sum}\Big). \tag{B.6}$$

The volume of the fluid element then changes by

$$\begin{aligned}
\mathrm{d}V &= \mathrm{d}\left(L^1 L^2 L^3\right) \\
&= \left(\mathrm{d}L^1\right) L^2 L^3 + L^1 \left(\mathrm{d}L^2\right) L^3 + L^1 L^2 \left(\mathrm{d}L^3\right) \\
&= V\left(\frac{\mathrm{d}L^1}{L^1} + \frac{\mathrm{d}L^2}{L^2} + \frac{\mathrm{d}L^3}{L^3}\right) \\
&= V\left(\frac{\partial v^1}{\partial x^1} + \frac{\partial v^2}{\partial x^2} + \frac{\partial v^3}{\partial x^3}\right)\mathrm{d}\tau.
\end{aligned} \tag{B.7}$$

Since $u^0 = c$ in our reference frame, we make no mistake by including $\partial u^0/\partial x^0 = 0$ in this sum. The rate of change is then given by the *tensorial* law

$$\frac{\mathrm{d}V}{\mathrm{d}\tau} = V\frac{\partial u^\mu}{\partial x^\mu} = V\nabla_\mu u^\mu, \tag{B.8}$$

where $\nabla_\mu = \partial_\mu$ because the Christoffel symbols vanish in Minkowski space. By the equivalence principle, this law then holds in any spacetime and reference frame.

Like the volume element, the baryon number density $n(x(\tau))$ can change along a streamline. But the total **baryon number** $N = nV$ must be conserved, as expressed by

$$\frac{\mathrm{d}}{\mathrm{d}\tau}(nV) = 0. \tag{B.9}$$

It will be very useful to rewrite this law in multiple different ways. First, let us differentiate it and insert the volume element rate of change (B.8). Then it is equivalent to

$$\begin{aligned}
0 &= \frac{1}{V}\frac{\mathrm{d}}{\mathrm{d}\tau}(nV) && \big(\text{by (B.9)}\big) \\
&= \frac{\mathrm{d}n}{\mathrm{d}\tau} + \frac{n}{V}\frac{\mathrm{d}V}{\mathrm{d}\tau} && \big(\text{by forward product rule}\big) \\
&= u^\mu\nabla_\mu n + n\nabla_\mu u^\mu && \big(\text{by chain rule and (B.8)}\big) \\
&= \nabla_\mu(nu^\mu) && \big(\text{by backwards product rule}\big),
\end{aligned} \tag{B.10}$$

with the elegant interpretation that there is no flux of the baryon number density current nu^μ out of the volume element. From equation (B.10), we can rewrite the conservation law in the alternative form

$$\frac{\mathrm{d}n}{\mathrm{d}\tau} = u^\mu\nabla_\mu n = -n\nabla_\mu u^\mu, \tag{B.11}$$

expressing the rate of change of the density along a streamline.

In the Newtonian limit, $u^\mu = (c, \boldsymbol{v})$ and the vanishing divergence equation (B.10) can be rewritten as a familiar continuity equation for the baryon number density,

$$\frac{\partial n}{\partial t} - \boldsymbol{\nabla}\cdot(n\boldsymbol{v}) = 0. \tag{B.12}$$

B.3 Conservation of energy and the Euler equation

The conservation of energy-momentum $\nabla_\mu T^{\mu\nu} = 0$ implies

$$\begin{aligned} 0 &= \nabla_\mu T^{\mu\nu} \\ &= \nabla_\mu \left[\frac{1}{c^2} u^\mu u^\nu (\epsilon + P) - g_{\mu\nu} P \right] \\ &= \frac{1}{c^2} \left[\Big(\epsilon + P\Big) \Big(u^\nu \nabla_\mu u^\mu + u^\mu \nabla_\mu u^\nu \Big) + u^\mu u^\nu \nabla_\mu \Big(\epsilon + P\Big) \right] - \nabla^\nu P. \end{aligned} \tag{B.13}$$

It is convenient to rewrite this as one scalar equation and another vector equation. To do so, we can *project* out the part of the vector $\nabla_\mu T^{\mu\nu}$ that is parallel and orthogonal to u^μ. If we have two vectors $\boldsymbol{u}$ and $\boldsymbol{v}$, then we define the parallel and orthogonal projection of $\boldsymbol{v}$ on $\boldsymbol{u}$ by

$$\boldsymbol{v}_\parallel = (\hat{\boldsymbol{u}} \cdot \boldsymbol{v})\, \hat{\boldsymbol{u}} = \frac{\boldsymbol{u} \cdot \boldsymbol{v}}{\boldsymbol{u} \cdot \boldsymbol{u}} \boldsymbol{u} \qquad \text{and} \qquad \boldsymbol{v}_\perp = \boldsymbol{v} - \boldsymbol{v}_\parallel. \tag{B.14}$$

With index notation, this can be written

$$v_\parallel^\alpha = \big(P_\parallel\big)^\alpha{}_\beta \, v^\beta \qquad \text{and} \qquad v_\perp^\alpha = (P_\perp)^\alpha{}_\beta \, v^\beta, \tag{B.15}$$

where we define the parallel and orthogonal **projection tensors**

$$\big(P_\parallel\big)^\alpha{}_\beta = \frac{u^\alpha u_\beta}{u^\mu u_\mu} \qquad \text{and} \qquad (P_\perp)^\alpha{}_\beta = \left(\delta^\alpha{}_\beta - \frac{u^\alpha u_\beta}{u^\mu u_\mu} \right). \tag{B.16}$$

These projectors are valid for any normalization $u^\mu u_\mu$, but with our conventions and choice of units we can always replace $u^\mu u_\mu = c^2$. It is straightforward to verify that both projectors have the characteristic property $(P^\alpha{}_\beta)^2 = P^\alpha{}_\gamma P^\gamma{}_\beta = P^\alpha{}_\beta$, expressing the geometrically intuitive fact that a projection does not alter a vector that has already been projected.

B.3.1 Energy conservation

First, let us see what the parallel part of $\nabla_\mu T^{\mu\nu} = 0$ gives us. Multiplying equation (B.13) with the parallel projector (B.16), we obtain

$$\begin{aligned} 0 &= \frac{u^\alpha u_\nu}{c^2} \nabla_\mu T^{\mu\nu} \\ &= \frac{u^\alpha}{c^2} \left\{ \frac{1}{c^2} \left[\Big(\epsilon + P\Big) \Big(u_\nu u^\nu \nabla_\mu u^\mu + u^\mu u_\nu \nabla_\mu u^\nu \Big) + u^\mu u_\nu u^\nu \nabla_\mu \Big(\epsilon + P\Big) \right] - u_\nu \nabla^\nu P \right\}. \end{aligned} \tag{B.17}$$

We can simplify this equation by using the normalization

$$u^\nu u_\nu = c^2 \qquad \text{and its implication} \qquad \nabla_\mu \left(u^\nu u_\nu \right) = 2 u^\nu \nabla_\mu u^\nu = 0. \tag{B.18}$$

The first property multiplies two terms by c^2, while the second kills one term in the square brackets. Since the right side of equation (B.17) must vanish for arbitrary u^α, the whole expression inside the curly parenthesis must vanish. This leaves

$$\begin{aligned} 0 &= \Big(\epsilon + P\Big) \nabla_\mu u^\mu + u^\mu \nabla_\mu \Big(\epsilon + P\Big) - u_\nu \nabla^\nu P \\ &= \nabla_\mu \left[u^\mu \Big(\epsilon + p\Big) \right] - u^\mu \nabla_\mu P && \text{(by backward product rule)} \\ &= \nabla_\mu \Big(\epsilon\, u^\mu \Big) + P\, \nabla_\mu u^\mu && \text{(by forward product rule)} && \text{(B.19a)} \\ &= u^\mu \nabla_\mu \epsilon + (\epsilon + P)\, \nabla_\mu u^\mu && \text{(by forward product rule)} && \text{(B.19b)} \\ &= \frac{\mathrm{d}\epsilon}{\mathrm{d}\tau} + (\epsilon + P)\, \nabla_\mu u^\mu && \text{(by chain rule).} && \text{(B.19c)} \end{aligned}$$

This is the announced scalar equation that follows from conservation of energy-momentum. Either of the equivalent forms is known as the **relativistic equation of energy conservation**. In the Newtonian limit (A.60c), the pressure term in the form (B.19a) is negligible, so it reduces to the familiar continuity equation for mass density $\rho = \epsilon/c^2$ from fluid mechanics, [Bre16, equation 7.1]

$$0 = \nabla_\mu \Big(\rho\, u^\mu \Big) = \frac{\partial \rho}{\partial t} - \boldsymbol{\nabla} \cdot \Big(\rho \boldsymbol{v} \Big). \tag{B.20}$$

B.3.2 The Euler equation

Second, let us inspect the component of $\nabla_\mu T^{\mu\nu}$ orthogonal to u^μ. Multiplying equation (B.13) by the orthogonal projection tensor (B.16), a straightforward calculation using the same properties (B.18) gives

$$\begin{aligned}
0 &= (P_\perp)^\alpha{}_\nu \, \nabla_\mu T^{\mu\nu} \\
&= \left\{ \delta^\alpha{}_\nu - \frac{u^\alpha u_\nu}{c^2} \right\} \\
&\times \left\{ \frac{1}{c^2} \left[\Big(\epsilon + P \Big) \Big(u^\nu \nabla_\mu u^\mu + u^\mu \nabla_\mu u^\nu \Big) + u^\mu u^\nu \nabla_\mu \Big(\epsilon + P \Big) \right] - \nabla^\nu P \right\} \\
&= \frac{1}{c^2} \left[\Big(\epsilon + P \Big) \Big(u^\alpha \nabla_\mu u^\mu + u^\mu \nabla_\mu u^\alpha \Big) + u^\mu u^\alpha \nabla_\mu \Big(\epsilon + P \Big) \right] - \nabla^\alpha P \\
&- \frac{1}{c^2} \left[\Big(\epsilon + P \Big) u^\alpha \nabla_\mu u^\mu + u^\alpha u^\mu \nabla_\mu \Big(\epsilon + P \Big) - u^\alpha u^\nu \nabla_\nu P \right] \\
&= \frac{1}{c^2} \Big(\epsilon + P \Big) u^\mu \nabla_\mu u^\alpha - \nabla^\alpha P + \frac{1}{c^2} u^\alpha u^\mu \nabla_\mu P.
\end{aligned} \tag{B.21}$$

This is the **relativistic Euler equation**. In the Newtonian limit $u^\mu = (c, \boldsymbol{v})$ with small velocity (A.60a) and pressure (A.60c), the rightmost term is negligible because it contains the product of two velocities, and so is the pressure contribution in the leftmost term. Then the three spatial indices $\alpha = a = \{1, 2, 3\}$ reduce to $\rho u^\mu \nabla_\mu u^a - \nabla^a P = 0$, where $\rho = \epsilon/c^2$ by the mass-energy equivalence (2.2). Another way to find this is to substitute $\epsilon = \rho c^2$ into equation (B.21) and send $c \to \infty$, where the Lorentz transformations reduce to the Galilei transformations. In the first term, $u^\mu \nabla_\mu u^a \simeq u^\mu \partial_\mu u^a + u^0 \Gamma^a_{00} u^0$ and $\Gamma^a_{00} = -\eta^{\mu\lambda} \partial_\lambda h_{00}/2 = -\eta^{\mu\lambda} \partial_\lambda V/c^2$, as we found in equations (A.65) and (A.68) in appendix A.3. The second term can be rewritten $\nabla^a P = -\nabla_a P$ in the Minkowski metric. We therefore recover the Euler equation [Bre16, equation 4.3]

$$\frac{\partial \boldsymbol{v}}{\partial t} + (\boldsymbol{v} \cdot \boldsymbol{\nabla})\, \boldsymbol{v} = -\frac{1}{\rho} \nabla P + \boldsymbol{g}, \qquad \text{where } \boldsymbol{g} = -\nabla V, \tag{B.22}$$

from fluid mechanics, expressing the acceleration of fluid elements on the left in terms of the gravitational field $\boldsymbol{g}$ and the pressure gradient ∇P.

B.4 Adiabaticity

The flow of a perfect fluid is adiabatic, meaning there is no transfer of heat between fluid elements. One way to understand this is that the energy-momentum tensor is diagonal, and that any exchange of heat would have to come from off-diagonal energy flux terms. A more verbose way to understand it is to consider the first law of thermodynamics,

$$\mathrm{d}E = \mathrm{d}Q + \mathrm{d}W = T\, \mathrm{d}S - P\, \mathrm{d}V. \tag{B.23}$$

Consider a fluid element with volume V, internal energy $E = V\epsilon$, fixed number of particles $N = nV$ and entropy $s = S/N$ per particle. Then the first law can be rewritten

$$\mathrm{d} \left(\epsilon \frac{N}{n} \right) = NT\, \mathrm{d}s - P\, \mathrm{d} \left(\frac{N}{n} \right). \tag{B.24}$$

Explicitly writing out the differentials and canceling the constant N, we find

$$\mathrm{d}\epsilon = \frac{\epsilon + P}{n}\,\mathrm{d}n + nT\,\mathrm{d}s. \tag{B.25}$$

To relate this to our flow, combine conservation of energy and baryon number into

$$\begin{aligned} 0 &= u^\mu \nabla_\mu \epsilon + \frac{\epsilon + P}{n}\, n \nabla_\mu u^\mu && \text{(by conservation of energy (B.19b))} \\ &= u^\mu \nabla_\mu \epsilon - \frac{\epsilon + P}{n}\, u^\mu \nabla_\mu n && \text{(by baryon number conservation (B.10))} \\ &= \frac{\mathrm{d}\epsilon}{\mathrm{d}\tau} - \frac{\epsilon + P}{n}\frac{\mathrm{d}n}{\mathrm{d}\tau} && \text{(by chain rule).} \end{aligned} \tag{B.26}$$

This is precisely the first law of thermodynamics (B.25) *with* $\mathrm{d}Q = nT\,\mathrm{d}s = 0$, showing that the flow is adiabatic!

A useful consequence of adiabaticity is that it enables us to define the **adiabatic index**

$$\gamma = \left(\frac{\partial \log(P/P_0)}{\partial \log(n/n_0)}\right)_s, \tag{B.27}$$

relative to some arbitrary pressure and number density scales P_0 and n_0. The derivative must be taken at constant specific entropy s, or equivalently *along the flow*. In our case, we can take the derivative and rewrite the adiabatic index by eliminating the baryon number density with equation (B.26). It then takes the practical form

$$\gamma = \frac{n}{P}\left(\frac{\partial P}{\partial n}\right)_s = \frac{n}{P}\frac{\mathrm{d}P/\mathrm{d}\tau}{\mathrm{d}n/\mathrm{d}\tau} = \frac{\epsilon + P}{P}\frac{\mathrm{d}P/\mathrm{d}\tau}{\mathrm{d}\epsilon/\mathrm{d}\tau} = \frac{\epsilon + P}{P}\left(\frac{\partial P}{\partial \epsilon}\right)_s. \tag{B.28}$$

The last expression is possible to calculate from the equation of state $\epsilon = \epsilon(P)$.

B.5 Speed of sound

We can derive a simple expression for the speed of sound in a perfect fluid. Suppose we are in Minkowski space, and consider a background equilibrium fluid with four-velocity $u^\mu = (u^0, \mathbf{0})$, density n_0, pressure P_0 and energy density ϵ_0 that are all *constant* in both time and space. On top of this background, place *small* variations $\delta n(x)$, $\delta P(x)$, $\delta\epsilon(x)$ and $\boldsymbol{v}(x)$ in the total density $n = n_0 + \delta n$, pressure $P = P_0 + \delta P$, energy density $\epsilon = \epsilon_0 + \delta\epsilon$ and four-velocity $u^\mu = (u^0, \boldsymbol{v})$. How do sound waves result from these variations?

To first order in all the small quantities, the Euler equation (B.21) reads

$$\frac{\partial \boldsymbol{v}}{\partial t} = -c^2 \frac{\nabla(\delta P)}{\epsilon_0 + P_0}. \tag{B.29}$$

Likewise, the adiabaticity equation (B.26) gives

$$\frac{\partial(\delta\epsilon)}{\partial t} = \frac{\epsilon_0 + P_0}{n_0}\frac{\partial(\delta n)}{\partial t}, \qquad \text{or} \qquad \delta\epsilon = \frac{\epsilon_0 + P_0}{n_0}\delta n \tag{B.30}$$

after integration, where we forget the integration constant, so $\delta\epsilon = 0$ when we are back in equilibrium with $\delta n = 0$. Using equation (B.30) to eliminate $\epsilon_0 + P_0$ in equation (B.29), we find

$$\frac{\partial \boldsymbol{v}}{\partial t} = -c^2 \frac{\nabla(\delta P)}{\delta\epsilon}\frac{\delta n}{n_0}. \tag{B.31}$$

Intuitively, the pressure and density gradients ∇P and ∇n should be parallel. Mathematically, this can be expressed by the two equal unit vectors

$$\frac{\nabla(\delta P)}{\delta P} = \frac{\nabla(\delta n)}{\delta n}. \tag{B.32a}$$

A more rigorous way to see this is to note that the pressure at a point $\boldsymbol{x}$ depends on the density at that point through an equation of state $P = P(n(t, \boldsymbol{x}))$. For example, the pressure (4.10c) is a function of $x_F = p_F/mc$, which in turn is determined by the density (4.10a). By the chain rule, then,

$$\nabla P = \frac{\mathrm{d}P}{\mathrm{d}n}\nabla n = \frac{\delta P}{\delta n}\nabla n, \tag{B.32b}$$

where we have interpreted the derivative $\mathrm{d}P/\mathrm{d}n$ as the ratio $\delta P/\delta n$ between the two small changes. Using either equation (B.32a) or (B.32b), we can reexpress equation (B.31) as

$$\frac{\partial \boldsymbol{v}}{\partial t} = -c^2\frac{\delta P}{\delta \epsilon}\frac{\nabla(\delta n)}{n_0} = -c^2\frac{\mathrm{d}P_0}{\mathrm{d}\epsilon_0}\frac{\nabla(\delta n)}{n_0}. \tag{B.33}$$

Again, we have interpreted $\delta P/\delta\epsilon$ as the derivative $\mathrm{d}P_0/\mathrm{d}\epsilon_0$, because $\delta P = P - P_0$ and $\delta\epsilon = \epsilon - \epsilon_0$ are both changes from the equilibrium values. Next, to first order in the small quantities, the baryon number equation (B.11) says

$$\frac{\partial(\delta n)}{\partial t} + n_0\nabla\cdot\boldsymbol{v} = 0. \tag{B.34}$$

Finally, differentiate this equation with respect to time and then substitute expression (B.33) for $\partial\boldsymbol{v}/\partial t$ to obtain

$$\left(\frac{\partial^2}{\partial t^2} - c^2\frac{\mathrm{d}P_0}{\mathrm{d}\epsilon_0}\nabla^2\right)\delta n = 0. \tag{B.35}$$

This is a ***wave equation*** *for density waves* $\delta n = \delta n(\boldsymbol{x} \mp \boldsymbol{v}_s t)$ *traveling at the* ***speed of sound***

$$v_s = c\sqrt{\frac{\mathrm{d}P_0}{\mathrm{d}\epsilon_0}}. \tag{B.36}$$

Appendix C

Matsubara Energy Summation

This appendix is inspired by reference [Alt+10].

When doing thermal field theory, one often encounters sums

$$S = \sum_{n=-\infty}^{+\infty} s(E_n) \tag{C.1}$$

of functions $s(E_n)$ over all **Matsubara energies**

$$E_n = \begin{cases} 2\pi n/\beta & \text{for bosons} \\ 2\pi \left(n + \frac{1}{2}\right)/\beta & \text{for fermions.} \end{cases} \tag{C.2}$$

For example, we encountered the sum

$$S = \sum_{n=-\infty}^{+\infty} \frac{1}{E_n^2 + E^2} \tag{C.3}$$

for bosons in equation (3.80), and again for fermions (3.107). In this appendix we will demonstrate an elegant general method for computing such sums by contour integration in the complex plane.

First, we define the complex functions

$$n_\pm(z) = \frac{1}{e^{\beta z} \mp 1} = \begin{cases} \dfrac{1}{e^{\beta z} - 1} & \text{for bosons} \\ \dfrac{1}{e^{\beta z} + 1} & \text{for fermions.} \end{cases} \tag{C.4}$$

Here and below, the upper and lower signs correspond to bosons and fermions, respectively. This is the familiar Bose-Einstein distribution $n_+(z)$ for bosons and the Fermi-Dirac distribution $n_-(z)$ for fermions. Importantly, they have simple poles at all imaginary Matsubara frequencies $z = iE_n$, as indicated by the crosses in figure C.1.

For reasons that will soon be clear, consider the contour integral

$$\oint_{C_N^A} \mathrm{d}z\, s(-iz) n_\pm(z) \tag{C.5}$$

along the contour C_N^A drawn in figure C.1a that encircle the $2N+1$ poles of $n_\pm(z)$ that are closest to the origin. To proceed in a mathematically well-defined way, we consider only a finite number of poles for now, but will include all poles by taking the limit $N \to \infty$ at the very end

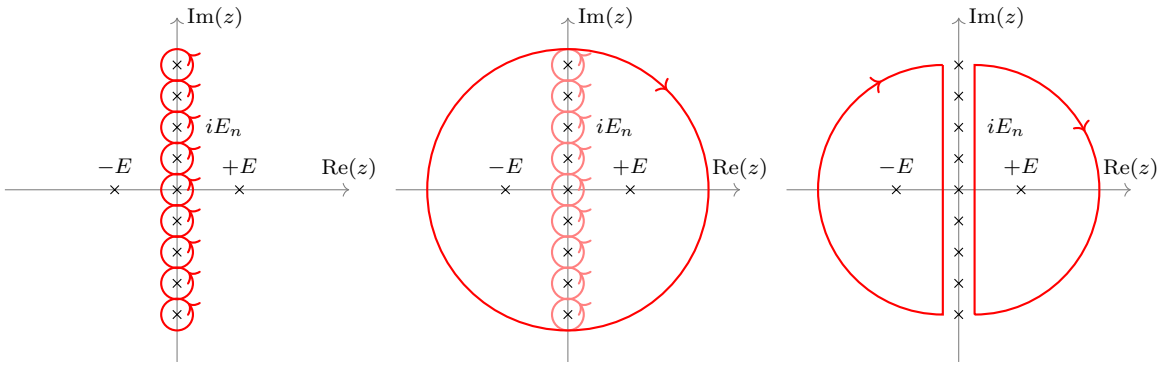

(a) Contour C_N^A. **(b)** Contour C_N^B. **(c)** Contour C_N^C.

Figure C.1: To evaluate a Matsubara energy sum $S_N = \sum_{n=-N}^{N} s(E_n)$ in the limit $N \to \infty$, we can use the residue theorem to transform it into a complex integral $\oint \mathrm{d}z\, s(-iz) n_\pm(z)$ along the contour C_N^A that encloses some of the infinitely many poles of $n_\pm(z)$. Then we add the integral along the circular contour C_N^B, resulting in the equivalent contour C_N^C. If the integrand vanishes on C_N^B as $N \to \infty$, we can trade C_N^A for C_N^C to transform the *infinite* Matsubara sum into a sum over the assumed *finite* number of residues of $s(-iz)$ in the real half planes.

of this derivation. Otherwise, we would have to argue that C_∞^A can be closed at infinity, if it were to include *all* poles of $n_\pm(z)$. Our strategy will circumvent this difficulty.

How does this contour integral relate to the Matsubara sum (C.1)? First recall the residue theorem

$$\oint_C \mathrm{d}z\, f(z) = 2\pi i \sum_n \operatorname*{Res}_{z=z_n} [f(z)], \tag{C.6}$$

where the sum runs over all poles z_n of $f(z)$ inside the region enclosed by the contour C. Second, recall that the residue of a quotient function $f(z)/g(z)$ at a simple pole $z = z_0$ where $g(z_0) = 0$, but $g'(z_0) \neq 0$ is

$$\operatorname*{Res}_{z=z_0} \left[\frac{f(z)}{g(z)}\right] = \frac{f(z_0)}{g'(z_0)}. \tag{C.7}$$

Let us apply this to our integral (C.5) with $f(z) = s(-iz)$ and $g(z) = n_\pm(z)^{-1} = e^{\beta z} \mp 1$. We then find that the residues of the integrand in the contour integral (C.5) are

$$\operatorname*{Res}_{z=iE_n} [s(-iz) n_\pm(z)] = \pm \frac{1}{\beta} s(E_n), \tag{C.8}$$

By the residue theorem (C.6), the contour integral (C.5) is then

$$\oint_{C_N^A} \mathrm{d}z\, s(-iz) n_\pm(z) = 2\pi i \sum_{n=-N}^{N} \operatorname*{Res}_{z=iE_n} [s(-iz) n_\pm(z)] = \pm \frac{2\pi i}{\beta} \sum_{n=-N}^{N} s(E_n). \tag{C.9}$$

In other words, the contour integral gives the finite Matsubara sum

$$S_N = \sum_{n=-N}^{N} s(E_n) = \pm \frac{\beta}{2\pi i} \oint_{C_N^A} \mathrm{d}z\, s(-iz) n_\pm(z), \tag{C.10}$$

and the full sum (C.1) is given by the limit $S = S_\infty = \lim_{N\to\infty} S_N$.

What is the use of transforming a simple sum into a complex (in both senses) contour integral? Consider now the circular contour C_N^B in figure C.1b that touches C_N^A at the uppermost and lowermost intersections with the imaginary axis. Now

$$\oint_{C_N^A} \mathrm{d}z + \oint_{C_N^B} \mathrm{d}z = \oint_{C_N^C} \mathrm{d}z, \tag{C.11}$$

where C_N^C is the contour shown in figure C.1c. The overlapping circular parts of C_N^A run opposite ways and cancel, producing the vertical parts of C_N^C. The clockwise circular contour C_N^B cancels the top and bottom parts of C_N^A, and also closes the contour with semicircles in the real half planes.

Finally, include all poles by taking the limit $N \to \infty$. This sends the radii of the two semicircles to infinity, inflating the contour C_N^C to the full real half planes, except the imaginary axis $\operatorname{Re} z = 0$. Assume now that $s(-iz)$ – as in our motivating example (C.3) – satisfies

$$|s(-iz)n_\pm(z)| < \frac{1}{|z|} \quad \text{as} \quad |z| \to \infty. \tag{C.12}$$

For general $s(-iz)$, this assumption is not as restrictive as it may sound, since there must be some bound on $s(-iz)$ anyway if the sum (C.1) is to converge at all. With this assumption, $\oint_{C_B} \mathrm{d}z\, s(-iz)n_\pm(z) \to 0$ as $N \to \infty$, and by equation (C.11) we can then trade C_N^A for C_N^C in the contour integral (C.10)!

There is a big benefit to this change of contour. After sending $N \to \infty$ and using the new contour C_∞^C, we can apply the residue theorem *again* to the contour integral (C.10) to obtain

$$S = \frac{\pm\beta}{2\pi i} \oint_{C_\infty^C} \mathrm{d}z\, s(-iz)n_\pm(z) = \mp\beta \sum_n \operatorname*{Res}_{z=z_n} [s(-iz)n_\pm(z)]. \tag{C.13}$$

The sum now runs over the poles of $s(-iz)$ in the real half planes, and not the poles of $n_\pm(z)$ like in equation (C.9). Note also that the sign change following the *clockwise* orientation of C_∞^C compared to the *counter-clockwise* orientation of C_∞^A. Like in our example (C.3), most $s(-iz)$ will have a *finite* number of poles, in stark contrast to the *infinite* number of poles of $n_\pm(z)$. We have thus transformed the Matsubara sum over an infinite number of residues of $n_\pm(z)$ to a sum over a finite number of residues of $s(-iz)$ – a much more manageable task! This is our proclaimed elegant and general method of evaluating the Matsubara sum (C.1).

Example: Let us use now use this technique to evaluate the sum (C.3) with

$$S = \sum_{n=-\infty}^{+\infty} \frac{1}{E_n^2 + E^2} = \sum_{n=-\infty}^{+\infty} s(E_n) \qquad \text{and} \qquad s(-iz) = \frac{1}{-z^2 + E^2}. \tag{C.14}$$

It has two poles at $z = +E$ and $z = -E$. Using equation (C.7) with $f(z) = n_\pm(z)$ and $g(z) = s(-iz)^{-1} = -z^2 + E^2$, we obtain the residues

$$\operatorname*{Res}_{z=+E} [s(-iz)n_\pm(z)] = -\frac{n_\pm(+E)}{2E} \qquad \text{and} \qquad \operatorname*{Res}_{z=-E} [s(-iz)n_\pm(z)] = +\frac{n_\pm(-E)}{2E}. \tag{C.15}$$

Using our main result (C.13), the Matsubara sum (C.14) is therefore

$$S = \sum_{n=-\infty}^{+\infty} \frac{1}{E_n^2 + E^2} = \mp\beta \sum_i \operatorname*{Res}_{z=z_n} [s(-iz)n_\pm(z)] = \mp\frac{\beta}{2E} \left[n_\pm(-E) - n_\pm(E)\right]. \tag{C.16}$$

We can now evaluate the sum explicitly by inserting the Bose-Einstein distribution and the Fermi-Dirac distribution (C.4). After some simplification, we obtain

$$S = \sum_{n=-\infty}^{+\infty} \frac{1}{E_n^2 + E^2} = \frac{\beta}{2E} \left[1 \pm \frac{2}{e^{\beta E} \mp 1}\right] = \frac{\beta}{2E} \Big[1 \pm 2n_\pm(E)\Big]. \tag{C.17}$$

Recall that the upper and lower signs hold for bosons and fermions, respectively.

Appendix D

Renormalization of the Dirac Sea

In the calculation of the grand potential (8.16) of the quark-meson model, we encountered (N_c copies of) the ultraviolet-divergent Dirac sea vacuum contribution

$$\Omega_0 = -2\int \frac{\mathrm{d}^3p}{(2\pi)^3} E(\boldsymbol{p}) = -2\int \frac{\mathrm{d}^3p}{(2\pi)^3}\sqrt{p^2+m^2}. \tag{D.1}$$

This can be interpreted as an infinite contribution from all negative energy states. Here we renormalize it with dimensional regularization in the (modified) minimal subtraction scheme. In $d = 3-2\epsilon$ spatial dimensions, it can be regularized as

$$\Omega_0 = -2\Lambda^{3-d}\int \frac{\mathrm{d}^dp}{(2\pi)^d}\sqrt{p^2+m^2} = -2\Lambda^{3-d}\frac{2\pi^{d/2}}{\Gamma(d/2)}\int_0^\infty \frac{\mathrm{d}p\, p^{d-1}}{(2\pi)^d}\sqrt{p^2+m^2}. \tag{D.2}$$

We have multiplied the integral by $\Lambda^{3-d} = \Lambda^{2\epsilon}$ where Λ is a *renormalization scale* with $[\Lambda] = [p] = \mathrm{MeV}$, so that $[\lambda^{3-d}\,\mathrm{d}^dp] = [\mathrm{d}^3p]$ and Ω_0 is well-defined with the correct physical dimension of a potential in all spatial dimensions d. The new integral (D.2) reduces to the old integral (D.1) when we send $\epsilon \to 0$. The d-dimensional momentum integral can be written as an analytical continuation of the *Beta function* [NIST22]

$$B(x,y) = \int_0^\infty \mathrm{d}t\, \frac{t^{x-1}}{(1+t)^{x+y}} = \frac{\Gamma(x)\Gamma(y)}{\Gamma(x+y)} \tag{D.3}$$

if we substitute $t = p^2/m^2$ with $\mathrm{d}t = 2p\,\mathrm{d}p/m^2$. We then find

$$\begin{aligned}\Omega_0 &= -\frac{2\Lambda^{3-d}m^{d+1}}{(4\pi)^{d/2}\,\Gamma\left(\frac{d}{2}\right)}\int_0^\infty \mathrm{d}t\, \frac{t^{d/2-1}}{(1+t)^{-1/2}} \\ &= -\frac{2\Lambda^{3-d}m^{d+1}}{(4\pi)^{d/2}\,\Gamma\left(\frac{d}{2}\right)}\frac{\Gamma\left(\frac{d}{2}\right)\Gamma\left(-\frac{d+1}{2}\right)}{\Gamma\left(-\frac{1}{2}\right)}.\end{aligned} \tag{D.4}$$

We now cancel $\Gamma\left(\frac{d}{2}\right)$ and replace $\Gamma\left(-\frac{1}{2}\right) = -2\sqrt{\pi}$. Then we restore $d = 3-2\epsilon$ and apply the property $\Gamma(z) = \Gamma(z+1)/z$ twice to transport the argument of the gamma function $\Gamma\left(-\frac{d+1}{2}\right) = \Gamma\left(-2+\epsilon\right)$ infinitesimally close to its pole at 0, using its asymptotic expansion $\Gamma(\epsilon) = 1/\epsilon - \gamma + \mathcal{O}(\epsilon)$ upon arrival. Expanding everything to zeroth order in ϵ then leaves

$$\Omega_0 = \frac{m^4}{8\pi^2}\left(4\pi\frac{\Lambda^2}{m^2}\right)^\epsilon \Gamma(-2+\epsilon) \simeq \frac{m^4}{16\pi^2}\left(\frac{1}{\epsilon} + \log\frac{\Lambda^2}{m^2} + \frac{3}{2} - \gamma + \log 4\pi\right) \qquad (\mathrm{MS}). \tag{D.5a}$$

The pole in ϵ exposes the ultraviolet divergence and can be removed by a counterterm in a renormalizable theory. In the *minimal subtraction* (MS) *scheme* only this divergent term is absorbed. In the *modified minimal subtraction* ($\overline{\mathrm{MS}}$) *scheme*, the terms $-\gamma + \log 4\pi$ that *always* arise in dimensional regularization calculations are also absorbed. This is equivalent to rescaling $\Lambda^2 \to \Lambda^2 e^\gamma/4\pi$, so in this scheme one finds

$$\Omega_0 \simeq \frac{m^4}{16\pi^2}\left(\frac{1}{\epsilon} + \log\frac{\Lambda^2}{m^2} + \frac{3}{2}\right) \qquad (\overline{\mathrm{MS}}). \tag{D.5b}$$

Appendix E

Calculation of the Three-Flavor Meson Potential

The following program, written in the SAGE computer algebra system, symbolically calculates a long explicit representation of the meson potential (9.2) in the three-flavor quark-meson model by brute-force calculation of the traces (9.10) from the identity-extended Gell-Mann matrices (9.3). It then evaluates its value (9.12), first derivatives (9.13) and second derivatives (9.15) in the minimum (9.4).

lsm3f_meson_potential.sage

```
#!/usr/bin/sage

λ0 = matrix([[1, 0, 0],[0, 1, 0],[0, 0, 1]])*sqrt(2/3)
λ1 = matrix([[0, 1, 0],[1, 0, 0],[0, 0, 0]])
λ2 = matrix([[0,-I, 0],[I, 0, 0],[0, 0, 0]])
λ3 = matrix([[1, 0, 0],[0,-1, 0],[0, 0, 0]])
λ4 = matrix([[0, 0, 1],[0, 0, 0],[1, 0, 0]])
λ5 = matrix([[0, 0,-I],[0, 0, 0],[I, 0, 0]])
λ6 = matrix([[0, 0, 0],[0, 0, 1],[0, 1, 0]])
λ7 = matrix([[0, 0, 0],[0, 0,-I],[0, I, 0]])
λ8 = matrix([[1, 0, 0],[0, 1, 0],[0, 0,-2]])*sqrt(1/3)
λ  = [λ0, λ1, λ2, λ3, λ4, λ5, λ6, λ7, λ8]
T  = [λ/2 for λ in λ]

m2 = var("m2", latex_name=r"m^2")
g = var("g")
λ1, λ2 = [var(f"λ{i}", latex_name=f"\\lambda_{i}") for i in range(1, 3)] # unpack
σ = [var(f"σ{a}", latex_name=f"\\sigma_{a}") for a in range(0, 9)]
π = [var(f"π{a}", latex_name=f"\\pi_{a}") for a in range(0, 9)]
h = [var(f"h{a}", latex_name=f"h_{a}") for a in range(0, 9)]
ϕ = [σ[a] + I*π[a] for a in range(0, 9)]

σx, σy = var("σx", latex_name=r"\sigma_x"), var("σy", latex_name=r"\sigma_y")
hx, hy = var("hx", latex_name=r"h_x"), var("hy", latex_name=r"h_y")
transf = matrix([[sqrt(2/3), sqrt(1/3)], [sqrt(1/3), -sqrt(2/3)]])
eqsxy = [
    σ[0] == (transf.inverse() * vector([σx, σy]))[0],
    σ[8] == (transf.inverse() * vector([σx, σy]))[1],
    h[0] == (transf.inverse() * vector([hx, hy]))[0],
    h[8] == (transf.inverse() * vector([hx, hy]))[1],
]
eqs08 = [
    σx == (transf * vector([σ[0], σ[8]]))[0],
    σy == (transf * vector([σ[0], σ[8]]))[1],
    hx == (transf * vector([h[0], h[8]]))[0],
    hy == (transf * vector([h[0], h[8]]))[1],
]
avgeqs = [σ[a]==0 for a in range(1, 8)] + [π[a]==0 for a in range(0, 9)]
```

```
# Compute potential symbolically with brute force
trϕϕ, trϕϕϕϕ, trHϕ = 0, 0, 0
for a in range(0, 9):
    for b in range(0, 9):
        trϕϕ += conjugate(ϕ[a])*ϕ[b] * (T[a]*T[b]).trace()
        trHϕ += h[a] * (conjugate(ϕ[b]) + ϕ[b]) * (T[a]*T[b]).trace()
        for c in range(0, 9):
            for d in range(0, 9):
                trϕϕϕϕ += conjugate(ϕ[a]*ϕ[c])*ϕ[b]*ϕ[d] * (T[a]*T[b]*T[c]*T[d]).trace()
V = expand(simplify(m2 * trϕϕ + λ1 * trϕϕ^2 + λ2 * trϕϕϕϕ - trHϕ))
Vtree = V.substitute(avgeqs, eqsxy).expand().simplify().collect(λ1).collect(λ2)
print(f"V = {Vtree}")

dVxtree = diff(V.substitute(eqsxy),σx).substitute(avgeqs).simplify_full().collect(λ1)
dVytree = diff(V.substitute(eqsxy),σy).substitute(avgeqs).simplify_full().collect(λ1)
print(f"dVx = {dVxtree}")
print(f"dVy = {dVytree}")
for a in range(0, 9):
    dVσa = diff(V,σ[a]).substitute(avgeqs)
    print(f"dVσ{a} = {dVσa}")
for a in range(0, 9):
    dVπa = diff(V,π[a]).substitute(avgeqs)
    print(f"dVπ{a} = {dVπa}")

# mass matrices
m2σσ = matrix(9, 9, lambda a, b: diff(V,σ[a],σ[b]).subs(avgeqs).collect(λ1).collect(λ2))
m2σπ = matrix(9, 9, lambda a, b: diff(V,σ[a],π[b]).subs(avgeqs).collect(λ1).collect(λ2))
m2ππ = matrix(9, 9, lambda a, b: diff(V,π[a],π[b]).subs(avgeqs).collect(λ1).collect(λ2))
for a in range(0, 9):
    for b in range(0, 9):
        print(f"m2σσ[{a},{b}] = {m2σσ[a,b]}")
for a in range(0, 9):
    for b in range(0, 9):
        print(f"m2σπ[{a},{b}] = {m2σπ[a,b]}")
for a in range(0, 9):
    for b in range(0, 9):
        print(f"m2ππ[{a},{b}] = {m2ππ[a,b]}")
```

Appendix F

Integrals

First rational integral for incompressible star:

$$\int \frac{x\,\mathrm{d}x}{ax^2+b} = \frac{1}{2a}\log\left(ax^2+b\right) + C. \tag{F.1}$$

Proof: Substitute $y = ax^2 + b$ with $\mathrm{d}y = 2ax\,\mathrm{d}x$ to obtain

$$\int \frac{x\,\mathrm{d}x}{ax^2+b} = \frac{1}{2a}\int \frac{\mathrm{d}y}{y} = \frac{1}{2a}\log y + C = \frac{1}{2a}\log\left(ax^2+b\right) + C.$$

Second rational integral for incompressible star:

$$\int \frac{\mathrm{d}x}{ax^2+bx} = -\frac{1}{b}\log\left(a+\frac{b}{x}\right) + C. \tag{F.2}$$

Proof: Complete the square in the denominator to obtain

$$\begin{aligned}
I &= \int \frac{\mathrm{d}x}{ax^2+bx} \\
&= \frac{1}{\sqrt{a}}\int \frac{\mathrm{d}y}{y^2 - b^2/4a} && \left(\text{complete square with } y = \sqrt{a}x + b/2\sqrt{a}\right) \\
&= \frac{2}{b}\int \frac{\mathrm{d}z}{z^2-1} && \left(\text{substitute } z = 2\sqrt{a}y/b\right) \\
&= \frac{1}{b}\left(\int \frac{\mathrm{d}z}{z-1} - \int \frac{\mathrm{d}z}{z+1}\right) && \left(\text{partial fraction decomposition}\right) \\
&= \frac{1}{b}\log\left(\frac{z-1}{z+1}\right) + C \\
&= -\frac{1}{b}\log\left(a+\frac{b}{x}\right) + C + \frac{\log a}{b} && \left(\text{reexpress } z \text{ in terms of } x\right).
\end{aligned}$$

Gaussian integral over one real number:

$$\int_{-\infty}^{+\infty} \mathrm{d}x\, e^{-ax^2} = \sqrt{\frac{\pi}{a}}. \tag{F.3}$$

Proof: It is easier to calculate the *square* of the integral using polar coordinates:

$$\begin{aligned}
\left[\int_{-\infty}^{+\infty} \mathrm{d}x\, e^{-ax^2}\right]^2 &= \frac{1}{a}\left[\int_{-\infty}^{+\infty} \mathrm{d}x\, e^{-x^2}\right]^2 && \Big(\text{rescale } x \to \sqrt{a}x\Big) \\
&= \frac{1}{a}\int_{-\infty}^{+\infty} \mathrm{d}x \int_{-\infty}^{+\infty} \mathrm{d}y\, e^{-(x^2+y^2)} \\
&= \frac{1}{a}\int_0^{2\pi} \mathrm{d}\theta \int_0^{\infty} \mathrm{d}r\, r e^{-r^2} && \Big(\text{convert to polar coordinates } (r,\theta)\Big) \\
&= \frac{2\pi}{a}\left[-\frac{1}{2}e^{-r^2}\right]_{r=0}^{r=\infty} = \frac{\pi}{a}.
\end{aligned}$$

Gaussian integral over one pair of Grassmann numbers:

$$\int \mathrm{d}\psi^* \int \mathrm{d}\psi\, e^{-\psi^* a \psi} = a \qquad \text{for real } a \text{ and Grassmann numbers } (\psi, \psi^*). \tag{F.4}$$

Proof: Using the Taylor expansion (3.34), and the Grassmann number integral definitions (3.35a) and (3.35b) and the anti-commutator (3.32),

$$\int \mathrm{d}\psi^* \int \mathrm{d}\psi\, e^{-\psi^* a \psi} = \int \mathrm{d}\psi^* \int \mathrm{d}\psi\, (1 - \psi^* a \psi) = a \int \mathrm{d}\psi^* \int \mathrm{d}\psi\, \psi\psi^* = a.$$

Gaussian integral over multiple pairs of Grassmann numbers:

$$\int \mathrm{d}\psi^\dagger \int \mathrm{d}\psi\, e^{-\psi^\dagger A \psi} = \det A \qquad \text{for Hermitian } A \text{ and Grassmann numbers } (\psi, \psi^\dagger). \tag{F.5}$$

Proof: The Hermitian matrix A can be diagonalized by a unitary transformation U as $A = U^\dagger D U$, where D is a diagonal matrix with the eigenvalues of A on its diagonal. Thus,

$$\psi^\dagger A \psi = \psi^\dagger U^\dagger D U \psi = (U\psi)^\dagger D (U\psi) = \tilde{\psi}^\dagger D \tilde{\psi}, \quad \text{where } \tilde{\psi} = U\psi.$$

The unitary transformation has $|\det U| = 1$, so the integration measure $\mathrm{d}\psi = \mathrm{d}\tilde{\psi}$ is unchanged upon changing variables from ψ to $\tilde{\psi}$. A Hermitian matrix has real eigenvalues, so we can use integral (F.4) to show that

$$\begin{aligned}
\int \mathrm{d}\psi^\dagger \int \mathrm{d}\psi\, e^{-\psi^\dagger A \psi} &= \int \mathrm{d}\tilde{\psi}^\dagger \int \mathrm{d}\tilde{\psi}\, e^{-\tilde{\psi}^\dagger D \tilde{\psi}} \\
&= \prod_i \int \mathrm{d}\tilde{\psi}_i^* \int \mathrm{d}\tilde{\psi}_i\, e^{-\tilde{\psi}_i^* \lambda_i \tilde{\psi}_i} \\
&= \prod_i \lambda_i = \det A.
\end{aligned}$$

Degenerate Fermi gas energy density integral:

$$\int_0^{x_F} \mathrm{d}x\, x^2\sqrt{x^2+1} = \frac{1}{8}\left[\left(2x_F^3+x_F\right)\sqrt{x_F^2+1} - \log\left(x_F+\sqrt{x_F^2+1}\right)\right]. \tag{F.6}$$

Proof: The appearance of $\sqrt{x^2+1}$ makes it handy to change variables to $x=\sinh\theta$. Using a number of hyperbolic identities, we then find

$$\begin{aligned}
I &= \int_0^{x_F} \mathrm{d}x\, x^2\sqrt{x^2+1} \\
&= \int_0^{\theta_F} \mathrm{d}\theta\, \cosh^2\theta\sinh^2\theta && \left(\text{use } \cosh^2\theta-\sinh^2\theta=1\right) \\
&= \frac{1}{4}\int_0^{\theta_F} \mathrm{d}\theta\, \sinh^2(2\theta) && \left(\text{use } \sinh(2\theta)=2\sinh\theta\cosh\theta\right) \\
&= \frac{1}{8}\int_0^{\theta_F} \mathrm{d}\theta\, \left[\cosh(4\theta)-1\right] && \left(\text{use } \sinh^2\theta=\frac{1}{2}\left[\cosh(2\theta)-1\right]\right) \\
&= \frac{1}{8}\left[\frac{1}{4}\sinh(4\theta_F)-\theta_F\right].
\end{aligned}$$

Inserting $\theta_F=\operatorname{asinh} x_F$, using the definitions $\sinh\theta=\left(e^{\theta}-e^{-\theta}\right)/2$ and $\operatorname{asinh} x=\log\left(x+\sqrt{x^2+1}\right)$ and simplifying then eventually yields

$$I = \frac{1}{8}\left[\left(2x_F^3+x_F\right)\sqrt{x_F^2+1} - \log\left(x_F+\sqrt{x_F^2+1}\right)\right].$$

Degenerate Fermi gas pressure integral:

$$\int_0^{x_F} \frac{\mathrm{d}x\, x^4}{\sqrt{x^2+1}} = \frac{1}{8}\left[\left(2x_F^3-3x_F\right)\sqrt{x_F^2+1} + 3\log\left(x_F+\sqrt{x_F^2+1}\right)\right]. \tag{F.7}$$

Proof: The appearance of $\sqrt{x^2+1}$ makes it handy to change variables to $x=\sinh\theta$. Using a number of hyperbolic identities, we then find

$$\begin{aligned}
I &= \int_0^{x_F} \frac{\mathrm{d}x\, x^4}{\sqrt{x^2+1}} \\
&= \int_0^{\theta_F} \mathrm{d}\theta\, \sinh^4\theta && \left(\text{use } \cosh^2\theta-\sinh^2\theta=1\right) \\
&= \frac{1}{4}\int_0^{\theta_F} \mathrm{d}\theta\, \left[\cosh^2(2\theta)-2\cosh(2\theta)+1\right] && \left(\text{use } \sinh^2\theta=\frac{1}{2}\left[\cosh(2\theta)-1\right]\right) \\
&= \frac{1}{8}\int_0^{\theta_F} \mathrm{d}\theta\, \left[\cosh(4\theta)-4\cosh(2\theta)+3\right] && \left(\text{use } \cosh^2\theta=\frac{1}{2}\left[\cosh(2\theta)+1\right]\right) \\
&= \frac{1}{8}\left[\frac{1}{4}\sinh(4\theta_F)-2\sinh(2\theta_F)+3\theta_F\right].
\end{aligned}$$

Inserting $\theta_F=\operatorname{asinh} x_F$, using the definitions $\sinh\theta=\left(e^{\theta}-e^{-\theta}\right)/2$ and $\operatorname{asinh} x=\log\left(x+\sqrt{x^2+1}\right)$ and simplifying then eventually yields

$$I = \frac{1}{8}\left[\left(2x_F^3-3x_F\right)\sqrt{x_F^2+1} + 3\log\left(x_F+\sqrt{x_F^2+1}\right)\right].$$

Appendix G

Numerical Implementations

In this appendix, we explain and lay out all Python code used to produce the results of this thesis. The code is also available online at https://github.com/hersle/master-thesis for convenience, but could be taken down from there at any time.

G.1 Natural dimensionless quantities for compact stars

In order to avoid numerical instability when integrating the Tolman-Oppenheimer-Volkoff equation (2.38), it is wise to eliminate physical scales from the problem, so floating-point numbers can be kept as close to 1 as possible. To this end, we define the dimensionless

$$\text{radius} \qquad \hat{r} = \frac{r}{r_0}, \qquad \text{where} \qquad r_0 = 10\,\text{km}, \tag{G.1a}$$

$$\text{mass} \qquad \hat{m} = \frac{m}{m_0}, \qquad \text{where} \qquad m_0 = M_\odot = 1.99 \cdot 10^{30}\,\text{kg}, \tag{G.1b}$$

$$\text{energy density} \qquad \hat{\epsilon} = \frac{\epsilon}{\epsilon_0}, \qquad \text{where} \qquad \epsilon_0 = \frac{m_0 c^2}{4\pi r_0^3/3}, \tag{G.1c}$$

$$\text{pressure} \qquad \hat{P} = \frac{P}{\epsilon_0}, \tag{G.1d}$$

$$\text{gravitational constant} \qquad \hat{G} = \frac{G}{G_0}, \qquad \text{where} \qquad G_0 = \frac{r_0 c^2}{m_0}. \tag{G.1e}$$

The precise values of r_0 and m_0 are chosen to be natural scales for radii and masses of compact stars, and the values of the remaining quantities follow from these and fundamental physical constants. In short, any variable in this appendix that wears a hat $\hat{}$ is the dimensionless version of its hatless dimensionful sibling, obtained by dividing the latter by whichever constant in equation (G.1) that has the same dimension. We define the constants in a separate file:

constants.py

```
import scipy.constants
π = scipy.constants.pi
ħ = scipy.constants.hbar
c = scipy.constants.c
mn = scipy.constants.neutron_mass

r0 = 1e3 # m
m0 = 1.98847e30 # kg, solar mass
b = 3
ϵ0 = m0*c**2 / (4*π*r0**3/b)
G = scipy.constants.G / (r0*c**2/m0) # dimensionless gravitational constant

fm = 1e-15
MeV = 1e6 * 1.6e-19
GeV = 1e9 * 1.6e-19
```

G.2 Integration of the Tolman-Oppenheimer-Volkoff equation

In chapter 2, we derived the Tolman-Oppenheimer-Volkoff system (2.38) for the unknown pressure and mass profiles $P(r)$ and $m(r)$, subject to the boundary conditions $P(0) = P_c$ and $m(0) = 0$. After solving the system, one can calculate the metric function $\beta(r)$ from definition (2.10), and $\alpha(r)$ by integrating equation (2.15) subject to matching the Schwarzschild metric (2.8) at $r = R$. From a numerical perspective, it is more practical to integrate $\alpha(r)$ simultaneously with the Tolman-Oppenheimer-Volkoff system. We therefore extend it with the additional equation (2.15). Since it is only the derivative of α that enters it, we start with any convenient value such as $\alpha(0) = 0$ at the center, then simply shift all values of $\alpha(r)$ after the integration to match the Schwarzschild metric at the surface. With this additional equation, the system reads

$$\frac{\mathrm{d}P}{\mathrm{d}r} = -\frac{Gm\epsilon(P)}{r^2c^2}\left[1+\frac{P}{\epsilon(P)}\right]\left[1+\frac{4\pi r^3P}{mc^2}\right]\left[1-\frac{2Gm}{rc^2}\right]^{-1}, \tag{G.2a}$$

$$\frac{\mathrm{d}m}{\mathrm{d}r} = \frac{4\pi r^2\epsilon}{c^2}, \tag{G.2b}$$

$$\frac{\mathrm{d}\alpha}{\mathrm{d}r} = -\frac{1}{\epsilon(P)+P}\frac{\mathrm{d}P}{\mathrm{d}r}. \tag{G.2c}$$

This is a system of three differential equations in the form $\mathrm{d}\boldsymbol{y}/\mathrm{d}t = f(t, \boldsymbol{y})$ with $t = r$ and $\boldsymbol{y} = [P, m, \alpha]$ that is suitable for Runge-Kutta integration algorithms. With the dimensionless variables (G.1), the Tolman-Oppenheimer-Volkoff system (G.2) is equivalent to

$$\frac{\mathrm{d}\hat{P}}{\mathrm{d}\hat{r}} = -\frac{\hat{G}\hat{m}\hat{\epsilon}(\hat{P})}{\hat{r}^2}\left[1+\frac{\hat{P}}{\hat{\epsilon}(\hat{P})}\right]\left[1+\frac{3\hat{r}^3\hat{P}}{\hat{m}}\right]\left[1-\frac{2\hat{G}\hat{m}}{\hat{r}}\right]^{-1}, \tag{G.3a}$$

$$\frac{\mathrm{d}\hat{m}}{\mathrm{d}\hat{r}} = 3\hat{r}^2\hat{\epsilon}(\hat{P}), \tag{G.3b}$$

$$\frac{\mathrm{d}\hat{\alpha}}{\mathrm{d}\hat{r}} = -\frac{1}{\hat{\epsilon}(\hat{P})+\hat{P}}\frac{\mathrm{d}\hat{P}}{\mathrm{d}\hat{r}}, \tag{G.3c}$$

which we wish to solve subject to the boundary conditions $\hat{P}(0) = \hat{P}_c$ and $\hat{m}(0) = 0$ for some dimensionless central pressure $\hat{P}_c$, and $\alpha(R) = \log(1 - 2\hat{G}\hat{M}/\hat{R})/2$ to match the Schwarzschild metric (2.8) at the surface. As explained at the start of this chapter, we implement the latter boundary condition by integrating from $\alpha(0) = 0$, then finally shift all values of $\alpha(r)$ by

$$\alpha(r) \to \alpha(r) - \alpha(\hat{R}) + \frac{1}{2}\log\left(1-\frac{2\hat{G}\hat{M}}{\hat{R}}\right). \tag{G.4}$$

To find the mass and radius of some star with central pressure $\hat{P}_c$, we integrate the system (G.3) until $\hat{P} \leq 0$. We then terminate the integration algorithm and call the final radius $\hat{r} = \hat{R}$ the radius of the star, and the corresponding mass $\hat{m}(\hat{R}) = \hat{M}$ the mass of the star. By parametrizing multiple stars with a range of central pressures $\hat{P}_c$ and performing this task for each of them, we obtain a mass-radius curve for the stars.

Below is a small Python program that accomplishes all of this for an arbitrary equation of state $\hat{\epsilon} = \hat{\epsilon}(\hat{P})$. The function `massradiusplot` can be run with the optional parameter `visual=True` to show the mass-radius relation in real-time, updating it every time the mass and radius of a new star is found. Typically, stars distributed uniformly between two central pressures may be located very non-uniformly in the mass-radius space. To circumvent this difficulty and make the mass-radius curve as smooth as possible, we take an adaptive approach by recursively splitting an initial central pressure interval $(\hat{P}_1, \hat{P}_2)$ until the Euclidean distance $[\,(\hat{R}_2 - \hat{R}_1)^2 + (\hat{M}_2 - \hat{M}_1)^2\,]^{1/2}$ between all points in the mass-radius diagram is below some given tolerance. Optionally, the program checks the stability of stars using the numerical method described in the next section.

tov.py

```
#!/usr/bin/python3

import numpy as np
import scipy.integrate
import matplotlib.pyplot as plt
import matplotlib.colors
import utils
from stability import eigenmode

from constants import *

def soltov(ϵ, P0, maxdr=1e-3, Psurf=0, progress=True, newtonian=False):
    def printprogress(r, m, P, E, message="", end=""):
        print(f"\r", end="") # reset line
        print(f"Solving TOV: ", end="")
        print(f"ϵ = {ϵ.__name__}, ", end="")
        print(f"Newtonian={newtonian}, ", end="")
        print(f"P0 = {P0:9.2e}, maxdr = {maxdr:9.2e}, ", end="")
        print(f"r = {r:8.5f}, m = {m:8.5f}, P/P0 = {P/P0:.4f}", end="")
        if message != "":
            print(f", {message}", end="")
        print("", end=end, flush=True) # flush without newline

    def rhs(r, y):
        m, P, α = y[0], y[1], y[2]
        E = ϵ(P) # computation can be expensive, only do it once
        if progress:
            printprogress(r, m, P, E)
        dmdr = b*r**2*E
        if r == 0:
            dPdr = 0 # avoid division by r = 0 (m = 0 implies dPdr = 0)
            dαdr = 0
        else:
            if newtonian:
                dPdr = -G*E*m/r**2
            else:
                dPdr = -G/r**2 * (E + P) * (m + b*r**3*P) / (1 - 2*G*m/r)
            #dαdr = (m + 4*π*r**3*P) / (r*(r-2*m))
            if newtonian:
                dαdr = 0
            else:
                dαdr = -dPdr / (E + P)
        return np.array([dmdr, dPdr, dαdr])

    def terminator(r, y):
        m, P, α = y[0], y[1], y[2]
        return P - Psurf
    terminator.terminal = True # stop integration when P == 0, use as last point

    r1, r2 = 0, np.inf
    res = scipy.integrate.solve_ivp(
        rhs, (0, np.inf), (0, P0, 0), events=terminator, max_step=maxdr
    )
    assert res.success, "ERROR: " + res.message
    rs, ms, Ps, αs = res.t, res.y[0,:], res.y[1,:], res.y[2,:]

    # match α to the Schwarzschild metric at the surface Glendenning (2.226)
    αs = αs - αs[-1] + 1/2 * np.log(1-2*G*ms[-1]/rs[-1])

    ϵs = np.array([ϵ(P) for P in Ps]) # (can compute more efficiently than this)

    if progress: # finish progress printer with newline
        printprogress(rs[-1], ms[-1], Ps[-1], ϵs[-1], res.message, end="\n")

    return rs, ms, Ps, αs, ϵs

# Bisect [P1, P2] to make points evenly
def massradiusplot(
    ϵ, P1P2, tolD=1e-5, tolP=1e-6, maxdr=1e-3, Psurf=0, nmodes=0, newtonian=False,
    outfile="", visual=False
):
    def solvestar(P0):
        rs, ms, Ps, αs, ϵs = soltov(ϵ, P0, maxdr=maxdr, Psurf=Psurf, newtonian=newtonian)
```

```
        R, M = rs[-1], ms[-1]

        nunstable, ω2s = 0, []
        for mode in range(0, nmodes):
            ω2, _ = eigenmode(rs, ms, Ps, αs, ϵs, mode)
            ω2s.append(ω2)
            if ω2 < 0:
                nunstable += 1 # count number of unstable modes with ω2 < 0
        return R, M, ω2s, nunstable

    P1, P2 = P1P2[0], P1P2[1]
    R1, M1, ω2s1, nu1 = solvestar(P1)
    R2, M2, ω2s2, nu2 = solvestar(P2)
    Ps, Ms, Rs, ω2s, nus = [P1, P2], [M1, M2], [R1, R2], [ω2s1, ω2s2], [nu1, nu2]

    if visual:
        plt.ion() # automatically update open figure
        if nmodes > 0: # check stability
            graph, = plt.plot([], [], "k-", zorder=0) # modify graph data later
            scatt = plt.scatter([], [], zorder=1) # modify graph data later
            cbar = plt.colorbar()
        else:
            graph, = plt.plot([], [], "k-o") # modify graph data later

    i = 0
    while i < len(Ps) - 1:
        P1, M1, R1, nu1 = Ps[i],   Ms[i],   Rs[i],   nus[i]
        P2, M2, R2, nu2 = Ps[i+1], Ms[i+1], Rs[i+1], nus[i+1]

        # Split intervals based on Euclidean distance between (R, M)-points in plot
        # But make sure P1, P2 do not get too close, otherwise algorithm gets stuck
        D = np.sqrt((R1 - R2)**2 + (M1 - M2)**2)
        if D > tolD and P2 - P1 > tolP:
            # split [P1, P2] into [P1, (P1+P2)/2] and [(P1+P2)/2, P2]
            P3 = (P1 + P2) / 2
            R3, M3, ω2s3, nu3 = solvestar(P3)
            Ps.insert(i+1, P3)
            Ms.insert(i+1, M3)
            Rs.insert(i+1, R3)
            ω2s.insert(i+1, ω2s3)
            nus.insert(i+1, nu3)

            if visual:
                # Animate plot in real-time for immediate feedback
                # inspired by https://stackoverflow.com/a/10944967
                graph.set_data(Rs, Ms)
                if nmodes > 0: # check stability
                    scatt.set_offsets(np.transpose([Rs, Ms]))
                    scatt.set_array(np.array(nus))
                    scatt.set_cmap("jet")
                    scatt.set_clim(0, np.max(nus))
                plt.gca().relim() # autoscale only works in animation after this
                plt.autoscale()
                plt.draw()
                plt.pause(0.001)
        else:
            i += 1

    if visual:
        plt.ioff() # leave original state
        plt.show() # leave final plot open

    if outfile != "":
        heads = ["P", "M", "R"] + [f"omega2{mode}" for mode in range(0, nmodes)] + ["nu"]
        cols  = [Ps, Ms, Rs]
        for m in range(0, nmodes): # for all modes
            cols.append([]) # append one column for this mode
            for n in range(0, len(Ps)): # for all stars
                cols[-1].append(ω2s[n][m]) # add frequencies for all stars
        cols += [nus]
        utils.writecols(cols, heads, outfile)

    return Ps, Ms, Rs
```

G.3 Stellar stability analysis with the shooting method

In section 4.3.2, we showed that the stability of a star could be determined by checking the sign of the lowest squared eigenvalue of a Sturm-Liouville problem. Here, we describe how we use the shooting method to determine the eigenvalues ω_n^2 and corresponding eigenfunctions $U_n(r)$ of the Sturm-Liouville problem that we encountered in equation (4.65) in section 4.3.2,

$$\frac{\mathrm{d}}{\mathrm{d}r}\left[\Pi(r)\frac{\mathrm{d}U_n(r)}{\mathrm{d}r}\right] + Q(r)\,U_n(r) = -\omega_n^2 W(r) U_n(r) \qquad \text{for } 0 \le r \le R, \tag{G.5a}$$

$$\text{subject to} \quad U_n(r) \propto r^3 \qquad \text{near } r = 0, \tag{G.5b}$$

$$\text{and} \quad \frac{\mathrm{d}U_n(r)}{\mathrm{d}r} < \infty \qquad \text{at } r = R, \tag{G.5c}$$

with the coefficient functions (4.55). We recommend reading this explanation in parallel with figure 4.7, which illustrates how this method finds the mode $n = 0$ for such a Sturm-Liouville problem.

Description

The shooting method finds any *one* eigenvalue ω_n^2 and its corresponding eigenfunction $U_n(r)$ with the following strategy:

1. **Guess** *any* value ω^2 for the eigenvalue ω_n^2.
2. **Impose** the boundary condition (G.5b) by setting $U(r) \propto r^3$ near $r = 0$.
3. **Shoot** the corresponding guess $U(r)$ for the eigenfunction $U_n(r)$ by numerically integrating the Sturm-Liouville equation (G.5a) to $r = R$.
4. **Count** the number of nodes $n(\omega^2)$ of $U(r)$ corresponding to the guess ω^2.
   (a) If $n(\omega^2) > n$, then Sturm-Liouville property 2 on page 56 implies that $\omega^2 > \omega_n^2$, so **decrease** the guess for ω^2 and repeat this process.
   (b) If $n(\omega^2) \le n$, then Sturm-Liouville property 2 on page 56 implies that $\omega^2 < \omega_n^2$, so **increase** the guess for ω^2 and repeat this process.

By repeating this process with increasingly better guesses ω^2, we get ever closer to the true eigenvalue ω_n^2.

Figure 4.7 shows that every $U(r)$ seems to diverge as $r \to R$, breaking boundary condition (G.5c). In theory, $U(r)$ does not diverge and hence satisfies the boundary condition *only* if one guesses the *exact* correct eigenvalue ω_n^2. In practice, inaccuracy of the numerical integration will prevent one from guessing the exact eigenvalue – it will only be possible to guess a value very close to it. As our guess gets very close to the true eigenvalue, the function $U(r)$ will diverge towards $+\infty$ or $-\infty$ with n nodes for guesses $\omega^2 < \omega_n^2$ slightly below the true eigenvalue. For guesses $\omega^2 > \omega_n^2$ slightly above the true eigenvalue, the function will have $n + 1$ nodes and diverge towards the oppositely signed infinity. Essentially, we are looking for the precise value of ω^2 that causes the blowup of $U(r)$ close to $r = R$ to "tip over" from one infinity $\pm\infty$ to other infinity $\mp\infty$, as shown with the red and blue guesses in figure 4.7.

Rule 4b, that we should increase our guess not only if $n(\omega^2) < n$, but also if $n(\omega^2) = n$, is a little technical and deserves an explanation. Suppose we are looking for the lowest mode $n = 0$ and have guessed a value of ω^2 with $n(\omega^2) = 0$ zeros. Is the true eigenvalue ω_n^2 less than or greater than the guess ω^2? If the true eigenvalue ω_n^2 had been *less* than ω^2, then any lower guess of ω^2 would also give $n(\omega^2) = 0$ zeros, for a function cannot have less than zero zeros! But then we could repeat the same reasoning indefinitely and ultimately reach the conclusion that the eigenvalue is $\omega_0^2 = -\infty$, which is neither physically sound nor consistent with the mathematical Sturm-Liouville property 1 on page 56. By contradiction, then, the eigenvalue must be *greater*

than the initial guess, explaining why we should increase our guess also if $n(\omega^2) = n$ with $n = 0$. If instead $n = 1$ and we guess ω^2 with $n(\omega^2) = n = 1$ zeros, then decreasing our guess would eventually yield the incorrect eigenvalue ω_0^2, and not the desired eigenvalue ω_1^2. Thus, we have to increase our guess if $n = 1$ too, and the rule now follows for all n by induction.

The efficiency of the shooting method hinges on the precise way in which it refines the guesses for the eigenvalues in step 4 above. To make it fast, our actual implementation carries out the search in the following way:

1. Establish a lower bound ω_-^2 and an upper bound ω_+^2 for ω_n^2 that have $n(\omega_-^2) \leq n$ and $n(\omega_+^2) > n$ zeros. To do so, guess *any* eigenvalue, for example $\omega^2 = 0$, shoot $U(r)$ and count its number of nodes $n(\omega^2)$.

   - If $n(\omega^2) \leq n$, set the lower bound to $\omega_-^2 = \omega^2$. Find an upper bound by increasing ω^2 *exponentially* up from ω_-^2 and shooting $U(r)$ with step 2 and 3 above until it has $n(\omega^2) > n$ nodes, then set the upper bound $\omega_+^2 = \omega^2$.

   - If $n(\omega^2) > n$, set the upper bound to $\omega_+^2 = \omega^2$. Find a lower bound by decreasing ω^2 *exponentially* down from ω_+^2 and shooting $U(r)$ with step 2 and 3 above until it has $n(\omega^2) \leq n$ nodes, then set the lower bound $\omega_-^2 = \omega^2$.

2. Calculate the new guess $\omega^2 = (\omega_-^2 + \omega_+^2)/2$, shoot $U(r)$ with step 2 and 3 above and count its number of nodes $n(\omega^2)$.

   - If $n(\omega^2) \leq n$, then ω^2 is a tighter lower bound than ω_-^2, so set $\omega_-^2 = \omega^2$.

   - If $n(\omega^2) > n$, then ω^2 is a tighter upper bound than ω_-^2, so set $\omega_+^2 = \omega^2$.

3. Repeat step 2 until the bounds ω_-^2 and ω_+^2 are so close that any value in the interval $[\omega_-^2, \omega_+^2]$ is a satisfactory approximation to the true eigenvalue ω_n^2.

4. Output $\omega^2 = (\omega_-^2 + \omega_+^2)/2 \approx \omega_n^2$ as the final approximation of the true eigenvalue.

This algorithm runs *logarithmically fast*, because the interval $[\omega_-^2, \omega_+^2]$ is enlarged *exponentially* in step 1 and *halved* at every iteration of step 2.

Implementation

The coefficient functions (4.55) of the Sturm-Liouville problem (G.5) are to be calculated from the output of the program in appendix G.2. We therefore recast the problem to dimensionless form by making use of the dimensionless quantities (G.1). It then takes the unchanged "hatted form"

$$\frac{\mathrm{d}}{\mathrm{d}\hat{r}}\left[\hat{\Pi}(\hat{r})\frac{\mathrm{d}\hat{U}_n(\hat{r})}{\mathrm{d}\hat{r}}\right] + \hat{Q}(\hat{r})\,\hat{U}_n(\hat{r}) = -\hat{\omega}_n^2\hat{W}(\hat{r})\hat{U}_n(\hat{r}) \qquad \text{for } 0 \leq \hat{r} \leq \hat{R}, \tag{G.6a}$$

$$\text{subject to} \quad \hat{U}_n(\hat{r}) \propto \hat{r}^3 \qquad \text{near } \hat{r} = 0, \tag{G.6b}$$

$$\text{and} \quad \frac{\mathrm{d}\hat{U}_n(\hat{r})}{\mathrm{d}\hat{r}} < \infty \qquad \text{at } \hat{r} = \hat{R}, \tag{G.6c}$$

where we have defined the dimensionless quantities

$$\hat{U}_n = \frac{U_n}{r_0^3}, \tag{G.7a}$$

$$\hat{\omega} = \frac{\omega_n}{c/r_0}, \tag{G.7b}$$

$$\hat{\Pi} = \frac{\Pi}{\epsilon_0/r_0^2} = e^{\beta_0+3\alpha_0}\frac{1}{\hat{r}^2}\gamma_0\hat{P}_0, \tag{G.7c}$$

$$\hat{Q} = \frac{Q}{\epsilon_0/r_0^4} = e^{\beta_0+3\alpha_0}\left[-4\frac{1}{\hat{r}^3}\frac{\mathrm{d}\hat{P}_0}{\mathrm{d}\hat{r}} - \frac{8\pi\hat{G}}{4\pi/3}\hat{P}_0\left(\hat{P}_0+\hat{\epsilon}_0\right)\frac{e^{2\beta_0}}{\hat{r}^2} + \frac{1}{\hat{r}^2}\frac{\left(\mathrm{d}\hat{P}_0\middle/\mathrm{d}\hat{r}\right)^2}{\hat{P}_0+\hat{\epsilon}_0}\right], \tag{G.7d}$$

$$\hat{W} = \frac{W}{\epsilon_0/r_0^2c^2} = e^{3\beta_0+\alpha_0}\frac{1}{\hat{r}^2}\left(\hat{P}_0+\hat{\epsilon}_0\right). \tag{G.7e}$$

Note that there is a difference between the numerical prefactors in the second terms of $\hat{Q}$ above and its dimensionful counterpart (4.55b).

On top of this, we implement the shooting method as described in this appendix. Some further remarks about our implementation are in order.

- To impose boundary condition (G.6b) in step 2 on page 165, we set $\hat{U}(\hat{r}) = \hat{r}^3$ for all discrete points with $\hat{r} < 0.01\hat{R}$.
- To numerically integrate the Sturm-Liouville differential equation (G.6a) for $\hat{r} \geq 0.01\hat{R}$ in step 3 on page 165, we first use the product rule to rewrite it as

  $$0 = \hat{\Pi}\hat{U}'' + \hat{\Pi}'\hat{U}' + \left(\hat{Q}+\hat{\omega}^2\hat{W}\right)\hat{U}. \tag{G.8}$$

  Denoting the discrete points by $\hat{r}_i$ and values of functions there by $\hat{f}_i = \hat{f}(\hat{r}_i)$, we approximate all derivatives with the central finite differences

  $$\hat{f}_i'' \approx \frac{\hat{f}'_{i+1/2} - \hat{f}'_{i-1/2}}{\hat{r}_{i+1/2} - \hat{r}_{i-1/2}} \qquad \text{and} \qquad \hat{f}_i' \approx \frac{\hat{f}_{i+1} - \hat{f}_{i-1}}{\hat{r}_{i+1} - \hat{r}_{i-1}}. \tag{G.9}$$

  This lets us compute the next, unknown value

  $$\hat{U}_{i+1} = \frac{1}{C_i^+}\left(C_i\cdot\hat{U}_i + C_i^-\cdot\hat{U}_{i-1}\right) \tag{G.10}$$

  from the two previous known values $\hat{U}_i$ and $\hat{U}_{i-1}$ and the known coefficients

  $$C_i^- = -\frac{2\hat{\Pi}_i}{\hat{r}_i - \hat{r}_{i-1}} + \hat{\Pi}_i', \tag{G.11a}$$

  $$C_i = +\frac{2\hat{\Pi}_i}{\hat{r}_{i+1} - \hat{r}_i} + \frac{2\hat{\Pi}_i}{\hat{r}_i - \hat{r}_{i-1}} - \left(\hat{r}_{i+1} - \hat{r}_{i-1}\right)\left(\hat{Q}_i + \hat{\omega}^2\hat{W}_i\right), \tag{G.11b}$$

  $$C_i^+ = +\frac{2\hat{\Pi}_i}{\hat{r}_{i+1} - \hat{r}_i} + \hat{\Pi}_i'. \tag{G.11c}$$

- To prevent numerical integration from breaking down, we stop the numerical integration at $\hat{r} = 0.99\hat{R}$ and linearly interpolate

  $$\hat{U}_{i+1} = \hat{U}_i + \frac{\hat{U}_i - \hat{U}_{i-1}}{\hat{r}_i - \hat{r}_{i-1}}\left(\hat{r}_{i+1} - \hat{r}_i\right) \tag{G.12}$$

  for the remaining points $\hat{r} > 0.99\hat{R}$. The point $r = R$ is a singular point because $Q(R) = W(R) = 0$, causing $\hat{U}(\hat{r})$ to blow up there and making it very difficult for

numerical integration to follow it. Our assumption is that at $\hat{r} = 0.99\hat{R}$, the blowup has already started, and the purpose of the linear interpolation is merely to capture the blowup all the way out to $\hat{r} = \hat{R}$ without care of the exact functional form of $\hat{U}(\hat{r})$ there, so we can check boundary condition (G.6c).

- It should also be noted that numerical errors may occur due to division by zero in the coefficient functions in the regions $\hat{r} < 0.01\hat{R}$ and $\hat{r} > 0.99\hat{R}$, but not in the intermediate region $0.01\hat{R} < \hat{r} < 0.99\hat{R}$. This is not an issue, because we enforce the form of $\hat{U}(\hat{r})$ in these two regions independently of the coefficient functions.

Here is our implementation of the shooting method in Python based on this description:

stability.py

```
from constants import *
import matplotlib.pyplot as plt
import numpy as np
from utils import *

def cut_divergence(u, r):
    # find index where derivative becomes zero, and cut away divergence after it
    du = np.gradient(u, r)
    i = len(u) - 1
    while i >= 0 and du[i] * du[i-1] >= 0:
        i -= 1
    return u[:i+1]

def shoot(r, Π, Q, W, ω2, p1, p2):
    dΠdr = np.gradient(Π, r)
    R = r[-1]

    u = np.empty(np.shape(r))

    # Start: set boundary condition u ∝ r^3
    i = 0
    while r[i] / R < p1:
        u[i] = 1 * r[i]**3
        i += 1

    # Middle: integrate Sturm-Liouville equation
    i -= 1 # i in next loop is shifted by -1
    while r[i] / R < p2:
        hp = r[i+1] - r[i]
        hm = r[i] - r[i-1]
        H = hp + hm
        factorp = 2 * Π[i] / hp + dΠdr[i]
        factor0 = 2 * Π[i] * (1/hp + 1/hm) - H * (Q[i] + ω2 * W[i])
        factorm = dΠdr[i] - 2*Π[i]/hm
        u[i+1] = 1/factorp * (u[i] * factor0 + u[i-1] * factorm)
        i += 1

    # End: linearly interpolate to capture divergence without numerical error
    while i < len(r) - 1:
        u[i+1] = u[i] + (u[i]-u[i-1]) * (r[i+1]-r[i]) / (r[i]-r[i-1])
        i += 1

    nodes = sum(u[1:] * u[:-1] < 0) # nodes where u[i] * u[i-1] < 0
    return u, nodes

def search(r, Π, Q, W, N, p1, p2, plot=False, progress=False, outfile=""):
    def increaseuntil(ω20, cond, sign=+1):
        ω2 = ω20
        u, n = shoot(r, Π, Q, W, ω2, p1, p2)
        while not cond(u, n):
            ω2 += sign*1 if ω2 == ω20 else (ω2 - ω20) # exponential increase
            u, n = shoot(r, Π, Q, W, ω2, p1, p2)
        return ω2

    def decreaseuntil(ω20, cond):
        return increaseuntil(ω20, cond, sign=-1)

    def bisectuntil(ω21, ω22, tol=1e-8):
```

```
        u1, n1 = shoot(r, Π, Q, W, ω21, p1, p2)
        u2, n2 = shoot(r, Π, Q, W, ω22, p1, p2)
        i = 0
        ω2s, us = [ω21, ω22], [u1, u2]
        while ω22 - ω21 > tol:
            ω23 = (ω21 + ω22) / 2
            u3, n3 = shoot(r, Π, Q, W, ω23, p1, p2)
            if progress:
                print(f"\rShooting with ω2 = {ω23:.15f} -> {n3:3d} nodes", end="")
            ω2s.append(ω23)
            us.append(u3)
            if n3 > N:
                ω22, u2, n2 = ω23, u3, n3
            else:
                ω21, u1, n1 = ω23, u3, n3
            i += 1
        # always choose the one that inflects at the end,
        # so its derivative looks like zero right before it diverges
        ω2 = ω21 if N % 2 == 0 else ω22
        u, n = shoot(r, Π, Q, W, ω2, p1, p2)

        if progress:
            print() # newline
        if plot:
            for i in range(0, len(us)):
                plt.plot(r, us[i], color=(i/len(us), 0, 0))
            ymax = np.max(np.abs(cut_divergence(u, r)))
            plt.ylim(-2*ymax, +2*ymax)
            plt.show()
        if outfile:
            cols = [ω2s, r] + us
            headers = ["omega2", "r"] + [f"U{i}" for i in range(0, len(us))]
            writecols(cols, headers, outfile)
            print(f"Wrote shooting method to {outfile}")

        return ω2, u, n

    ω20 = 0
    u, n = shoot(r, Π, Q, W, ω20, p1, p2)
    if n > N:
        # ω20 is an upper bound, search for a lower bound
        ω22 = ω20
        ω21 = decreaseuntil(ω20, lambda u, n: n <= N)
    else:
        # ω20 is a lower bound, search for an upper bound
        ω21 = ω20
        ω22 = increaseuntil(ω20, lambda u, n: n > N)
    ω2, u, n = bisectuntil(ω21, ω22)
    return ω2, u, n

def coeffs(r, m, P, α, ϵ):
    dPdr = np.gradient(P, r)
    dPdϵ = np.gradient(P, ϵ)
    β = -1/2*np.log(1-2*G*m/r) # β(0) = 0, avoid division by 0, already dimensionless
    Γ = (P + ϵ) / P * dPdϵ # already dimensionless
    Π = np.exp(β+3*α)/r**2 * Γ * P
    Q  = -4*np.exp(β+3*α)/r**3*dPdr
    Q -= (8*π*G/(4*π/3))*np.exp(3*β+3*α)/r**2*P*(ϵ+P)
    Q += np.exp(β+3*α)*dPdr**2 / (r**2*(ϵ+P))
    W = np.exp(3*β+α)*(ϵ+P)/r**2
    return Π, Q, W

def eigenmode(
    r, m, P, α, ϵ, Ns, p1=0.01, p2=0.99, plot=False, progress=True,
    cut=False, normalize=False, outfile="", outfileshoot=""
):
    if type(Ns) == type(0):
        ω2s, us = eigenmode(
            r, m, P, α, ϵ, [Ns], p1=p1, p2=p2, plot=plot, progress=progress,
            cut=cut, normalize=normalize, outfile=outfile
        )
        ω2, u = ω2s[0], us[0]
        return ω2, u

    Π, Q, W = coeffs(r, m, P, α, ϵ)
```

```
    ω2s, us = [], []
    for N in Ns:
        ω2, u, n = search(
            r, Π, Q, W, N, p1, p2, plot=plot, progress=progress, outfile=outfileshoot
        )
        if cut:
            uc = cut_divergence(u, r)
            u[:len(uc)] = uc
            u[len(uc):] = np.nan
        if normalize:
            u = u / np.nanmax(np.abs(u))
        ω2s.append(ω2)
        us.append(u)

    if outfile != "":
        cols = [ω2s, r]
        heads = ["omega2", "r"]
        for u, N in zip(us, Ns):
            cols.append(u)
            heads.append(f"U{N}")
        writecols(cols, heads, outfile)
        print(f"Wrote (ω2, r, U) to {outfile}")

    return ω2s, us
```

G.4 Equations of state for ideal neutron stars

Below, we use the general framework above to find the mass-radius relation for ideal neutron stars. We make a total of four sweeps for the mass-radius diagram in figure 4.3, using both the non-relativistic equation of state (4.16) and the general equation of state (4.17), and solving both the relativistic Tolman-Oppenheimer-Volkoff equation (2.38) and its Newtonian limit with the pressure gradient (2.33).

neutron_stars.py

```
#!/usr/bin/python3

from constants import *
from tov import *
from stability import *
from utils import *
import numpy as np
import scipy.optimize

def ϵUR(P): # ultra-relativistic equation of state
    return 3 * P

def ϵNR(P): # non-relativistic equation of state
    if P <= 0: return 0
    prefactor = (5**3*4**2 / (3**2*π**2*b**2) * mn**8*c**6*r0**6 / (m0**2*ħ**6))**(1/5)
    return prefactor * P**(3/5)

def ϵGR(P): # general equation of state
    if P <= 0: return 0
    prefactor = mn**4*c**3*r0**3 / (6*π*b*m0*ħ**3)
    def f(x):
        Px = prefactor * ((2*x**3 - 3*x) * np.sqrt(x**2 + 1) + 3*np.arcsinh(x))
        return Px - P
    sol = scipy.optimize.root_scalar(f, method="bisect", bracket=(0, 1e5))
    assert sol.converged, "ERROR: equation of state root finder did not converge"
    x = sol.root
    ϵx = 3*prefactor * ((2*x**3+x) * np.sqrt(x**2 + 1) - np.arcsinh(x))
    return ϵx

P = np.linspace(0, 20, 500)
ϵs = [[ϵ(P) for P in P] for ϵ in (ϵUR, ϵNR, ϵGR)]
writecols([P, *ϵs], ["P", "epsUR", "epsNR", "epsGR"], "data/eos.dat")

opts = { "tolD": 0.05, "tolP": 1e-5, "maxdr": 1e-3, "visual": True }
```

```
massradiusplot(
    ϵNR, (1e-6, 1e0), **opts, nmodes=0, newtonian=True, outfile="data/nrnewt.dat"
)
massradiusplot(
    ϵGR, (1e-6, 1e0), **opts, nmodes=0, newtonian=True, outfile="data/grnewt.dat"
)
massradiusplot(
    ϵNR, (1e-6, 1e7), **opts, nmodes=0,  newtonian=False, outfile="data/nr.dat"
)
massradiusplot(
    ϵGR, (1e-6, 1e7), **opts, nmodes=6,  newtonian=False, outfile="data/gr.dat"
)

P0s = list(np.geomspace(1e-6, 1e7, 14))
xs, ps = [], []
for P0 in P0s:
    r, m, P, α, ϵ = soltov(ϵGR, P0)
    xs.append(list(r / r[-1]))
    ps.append(list(P / P0))
P0head = ["P0"]
xheads = [f"x{i}" for i in range(0, len(P0s))]
pheads = [f"p{i}" for i in range(0, len(P0s))]
writecols([P0s] + xs + ps, P0head + xheads + pheads, "data/pressures.dat")

r, m, P, α, ϵ = soltov(ϵGR, 1e3)
ω2s, us = eigenmode(r, m, P, α, ϵ, [0], plot=True, outfileshoot="data/shoot.dat")

r, m, P, α, ϵ = soltov(ϵGR, 3e2)
ns = range(0, 12)
ω2s, us = eigenmode(
    r, m, P, α, ϵ, ns, cut=True, normalize=False, outfile="data/nmodes.dat"
)
ω2s, us = eigenmode(
    r, m, P, α, ϵ, ns, cut=True, normalize=True, outfile="data/nmodes_norm.dat"
)
```

G.5 Equations of state for quark stars and hybrid stars

These programs find all equations of state and stellar solutions in chapters 7, 8, 9 and 10. The models are organized as classes according to the following diagram:

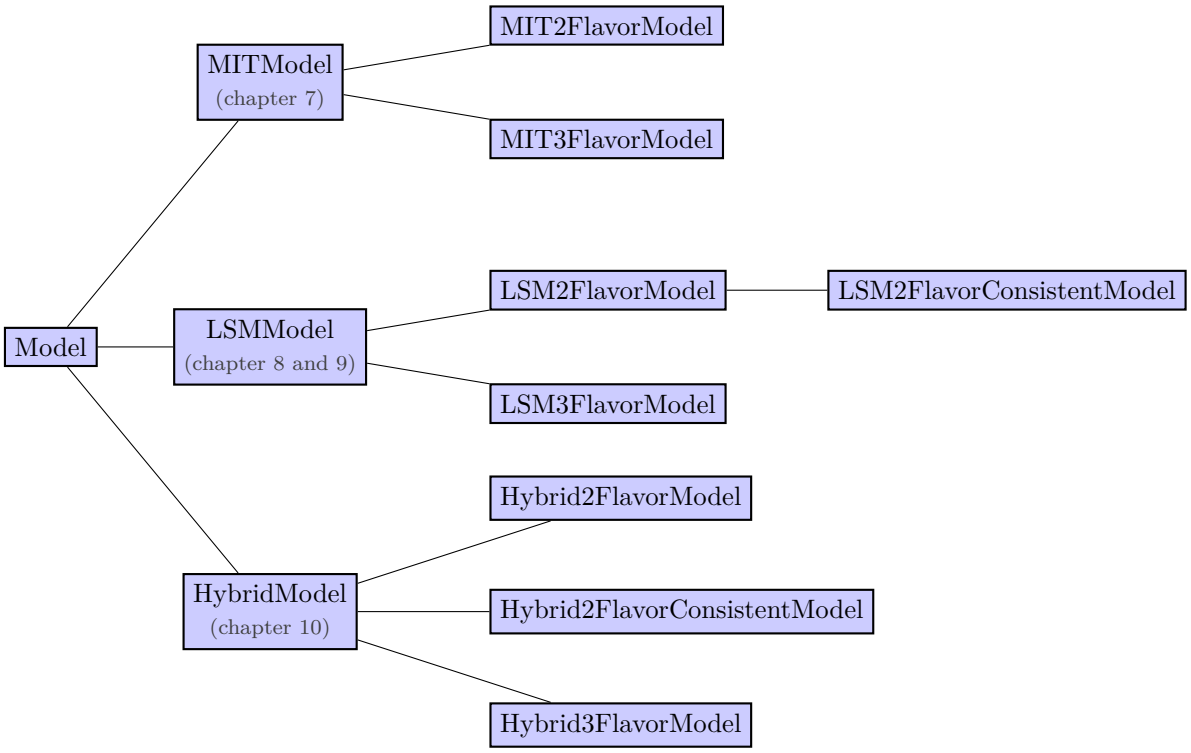

For all the models, the program performs the following tasks:

- It numerically fits parameters to the grand potential (7.3), (8.19), (8.28) or (9.24) and evaluates it and its derivatives with respect to any mean fields that are present.
- It finds the equation of state $\epsilon(P)$. First, from the grand potential (6.3), it parametrizes pressures (6.4a), densities (6.4b) and energy densities (6.4d) at zero temperature with one independent mean field or chemical potential. Simultaneously, the other mean fields and chemical potentials are determined by solving the system of equations (7.5), (8.23) or (9.27). Finally, the independent variable is eliminated numerically to yield the equation of state $\epsilon(P)$. Numerically, the function $\epsilon(P)$ is implemented as a linearly interpolating spline between the parametrized points. For the hybrid model, the equation of state is constructed as described in section 10.1.
- If the equation of state exhibits a phase transition, it is corrected with the Maxwell construction by establishing one vapor pressure at which the transition takes place, as explained in [Pog17, equation (4.69)].
- It establishes upper or lower bounds for the bag constant B by making shifts (7.10) with different bag constants and solving the side of inequality (7.12) that matches the number of flavors in the model.
- It integrates the Tolman-Oppenheimer-Volkoff equation (6.1) using the program in appendix G.2, producing mass-radius relations for stellar sequences and radial profiles for various quantities in individual stars.

Common code for all quark and hybrid star models (chapters 7 to 10)

quark_hybrid_stars_common.py

```
#!/usr/bin/python3

from constants import π, ħ, c, ϵ0, MeV, GeV, fm
from tov import massradiusplot, soltov
import utils

import numpy as np
import sympy as sp
import scipy.optimize
import scipy.interpolate
import matplotlib.pyplot as plt

Nc = 3
me = 0.5

tovopts = {"tolD": 0.01, "maxdr": 1e-2, "nmodes": 0}

def charge(mu, md, ms, μu, μd, μs, μe):
    nu = Nc/(3*π**2) * np.real((μu**2-mu**2+0j)**(3/2))
    nd = Nc/(3*π**2) * np.real((μd**2-md**2+0j)**(3/2))
    ns = Nc/(3*π**2) * np.real((μs**2-ms**2+0j)**(3/2))
    ne =  1/(3*π**2) * np.real((μe**2-me**2+0j)**(3/2))
    return +2/3*nu - 1/3*nd - 1/3*ns - 1*ne

# solve μQ=(μu+μd)/2, μd=μu+μe, μs=μd for (μu,μd,μs)
def μelim(μQ, μe):
    μu = μQ - μe/2
    μd = μu + μe
    μs = μd
    return μu, μd, μs

class Model:
    def __init__(self, name, mσ=0, mπ=0, mK=0):
        self.name = name
        self.mu, self.md, self.ms = self.vacuum_masses()
        print(f"Meson masses: mσ = {mσ:.1f} MeV, mπ = {mπ:.1f}, mK = {mK:.1f}")
        print(f"Quark masses: mu = md = {self.mu:.1f} MeV, ms = {self.ms:.1f} MeV")
```

```
        self.mσ = mσ
        self.mπ = mπ
        self.mK = mK

    def eos(self, B=0, N=1000, plot=False, write=False, debugmaxwell=False):
        mu, md, ms, μu, μd, μs, μe = self.eossolve(N=N) # model-dependent function

        # extend solutions to μ = 0 to show Silver-Blaze property
        μu = np.insert(μu, 0, 0)
        μd = np.insert(μd, 0, 0)
        μs = np.insert(μs, 0, 0)
        μe = np.insert(μe, 0, 0)
        mu = np.insert(mu, 0, mu[0])
        md = np.insert(md, 0, md[0])
        ms = np.insert(ms, 0, ms[0])

        μQ = (μu + μd) / 2

        Ω = self.Ω(mu, md, ms, μu+0j, μd+0j, μs+0j, μe+0j) # model-dependent
        P, P0 = -Ω, -Ω[0]
        P = P - P0

        nu = Nc/(3*π**2) * np.real((μu**2-mu**2+0j)**(3/2))
        nd = Nc/(3*π**2) * np.real((μd**2-md**2+0j)**(3/2))
        ns = Nc/(3*π**2) * np.real((μs**2-ms**2+0j)**(3/2))
        ne =  1/(3*π**2) * np.real((μe**2-me**2+0j)**(3/2))
        ϵ  = -P + μu*nu + μd*nd + μs*ns + μe*ne

        # print bag constant bound (upper or lower, depending on circumstances)
        nB = 1/3*(nu+nd+ns)
        def EperB(B):
            PB = P - B
            ϵB = ϵ + B
            return np.interp(0, PB, ϵB/nB) # at P=0
        f = lambda B: EperB(B) - 930
        Bs = np.linspace(0, 300, 10000)**4
        if plot:
            plt.plot(Bs**(1/4), [f(Bs) for Bs in Bs])
            plt.ylim(-500, +500)
            plt.show()
        try:
            # note: bracket lower bound is sensitive
            sol = scipy.optimize.root_scalar(f, method="brentq", bracket=(1e5, 300**4))
            assert sol.converged
            Bbound = sol.root
        except ValueError:
            print("alternative bag bound method")
            Bs = np.linspace(0, 300, 10000)**4
            Bbound = Bs[np.argmin([f(B) for B in Bs])]
        print(f"Bag constant bound: B^(1/4) = {Bbound**(1/4)} MeV", end=" ")
        print(f"({(P0+Bbound)**(1/4)} MeV)")

        P -= B
        ϵ += B

        if plot:
            plt.plot(P, ϵ/nB, ".-k")
            plt.axhline(930, color="red")
            plt.show()

        # plot bag pressure
        if plot:
            μvac = np.full_like(mu, 0+0j)
            PB = -self.Ω(mu, md, ms, μvac, μvac, μvac, μvac) - P0 - B
            PQ = P - PB
            plt.plot((μu+μd)/2, np.sign(PB)*np.abs(PB)**(1/4), label="bag")
            plt.plot((μu+μd)/2, np.sign(PQ)*np.abs(PQ)**(1/4), label="quark")
            plt.plot((μu+μd)/2, np.sign(P)*np.abs(P)**(1/4), label="total")
            plt.xlabel(r"$\mu$")
            plt.ylabel(r"$P$")
            plt.legend()
            plt.show()

        P1 = P[0]
        i2 = np.argmax(np.gradient(P) < 0) # last index of increasing pressure
```

```
    P2 = P[i2]
    have_phase_transition = (i2 != 0) and (P2 > 0)
    print("Phase transition?", have_phase_transition)
    Porg, ϵorg = np.copy(P), np.copy(ϵ) # save pre-Maxwell-construction P, ϵ
    if have_phase_transition:
        i3 = i2 + np.argmax(np.gradient(P[i2:]) > 0) - 1
        P3 = P[i3]

        # debug Maxwell construction
        if debugmaxwell:
            plt.plot(P[:i2+1], ϵ[:i2+1], marker=".", color="red")
            plt.plot(P[i2:i3+1], ϵ[i2:i3+1], marker=".", color="green")
            plt.plot(P[i3:], ϵ[i3:], marker=".", color="blue")
            plt.show()

        def gibbs_area(Pt):
            j1 = np.argmax(P[:i2+1] >= Pt) # first pt on 1-curve with greater P
            j2 = i3 + np.argmax(P[i3:] >= Pt) # first pt on 2-curve with greater P
            ϵ1 = np.interp(Pt, P[:i2+1], ϵ[:i2+1])
            ϵ2 = np.interp(Pt, P[i3:], ϵ[i3:])
            P12 = np.concatenate([[Pt], P[j1:j2], [Pt]])
            ϵ12 = np.concatenate([[ϵ1], ϵ[j1:j2], [ϵ2]])
            ret = np.trapz(1/ϵ12, P12)
            print(f"gibbs_area({Pt}) = {ret}")
            return ret

        # find P that gives zero Gibbs area
        # (pray that P[0]+1e-3 works, since P[0] = 0 gives 0-div error
        sol = scipy.optimize.root_scalar(gibbs_area, bracket=(P[0]+1e-3, P[i2]), \
                                         method="brentq")
        assert sol.converged
        Pt = sol.root
        print(f"Phase transition pressure: {Pt} MeV^4")

        if debugmaxwell:
            plt.plot(1/ϵ, P, color="gray")
            plt.ylim(1.1*np.min(P), -1.1*np.min(P))

        j1 = np.argmax(P[:i2+1] >= Pt) # first pt on 1-curve with greater P
        j2 = i3 + np.argmax(P[i3:] >= Pt) # first pt on 2-curve with greater P
        ϵ1 = np.interp(Pt, P[:i2+1], ϵ[:i2+1])
        ϵ2 = np.interp(Pt, P[i3:], ϵ[i3:])

        # fix array by only modifying EOS,
        # but fill out with points in phase transition
        ϵ1 = np.interp(Pt, P[:i2+1], ϵ[:i2+1])
        ϵ2 = np.interp(Pt, P[i3:], ϵ[i3:])
        Ntarget = len(mu)
        Nnow = len(ϵ[:j1]) + len(ϵ[j2:])
        Nadd = Ntarget - Nnow
        ϵ = np.concatenate((ϵ[:j1], np.linspace(ϵ1, ϵ2, Nadd), ϵ[j2:]))
        P = np.concatenate((P[:j1], np.linspace(Pt, Pt, Nadd), P[j2:]))

        if debugmaxwell:
            plt.plot(1/ϵ, P, color="black")
            plt.show()

    # convert interesting quantities to SI units
    nu *= MeV**3 / (ħ*c)**3 * fm**3 # now in units 1/fm^3
    nd *= MeV**3 / (ħ*c)**3 * fm**3 # now in units 1/fm^3
    ns *= MeV**3 / (ħ*c)**3 * fm**3 # now in units 1/fm^3
    ne *= MeV**3 / (ħ*c)**3 * fm**3 # now in units 1/fm^3
    P0 *= MeV**4 / (ħ*c)**3 # now in units kg*m^2/s^2/m^3
    P  *= MeV**4 / (ħ*c)**3 # now in units kg*m^2/s^2/m^3
    ϵ  *= MeV**4 / (ħ*c)**3 # now in units kg*m^2/s^2/m^3
    Porg *= MeV**4 / (ħ*c)**3 # now in units kg*m^2/s^2/m^3
    ϵorg *= MeV**4 / (ħ*c)**3 # now in units kg*m^2/s^2/m^3

    # convert interesting quantities to appropriate units
    P0 *= fm**3 / GeV # now in units GeV/fm^3
    P  *= fm**3 / GeV # now in units GeV/fm^3
    ϵ  *= fm**3 / GeV # now in units GeV/fm^3
    Porg *= fm**3 / GeV # now in units GeV/fm^3
    ϵorg *= fm**3 / GeV # now in units GeV/fm^3
```

```
        print(f"P0 = {P0}")

        if write:
            cols  = [mu, md, ms, μu, μd, μs, μe, nu, nd, ns, ne, ϵ, P, ϵorg, Porg]
            heads = ["mu", "md", "ms", "muu", "mud", "mus", "mue", \
                     "nu", "nd", "ns", "ne", "epsilon", "P", "epsilonorg", "Porg"]
            outfile = f"data/{self.name}/eos_sigma_{self.mσ}.dat"
            utils.writecols(cols, heads, outfile)

        if plot:
            fig, (ax1, ax2, ax3, ax4) = plt.subplots(1, 4, figsize=(25, 5))

            ax1.set_xlabel(r"$\mu_Q$")
            ax1.plot(μQ, mu, ".-", color="orange", label=r"$m_u$")
            ax1.plot(μQ, md, ".-", color="orange", label=r"$m_d$")
            ax1.plot(μQ, ms, ".-", color="yellow", label=r"$m_s$")
            ax1.plot(μQ, μu, ".-", color="red", label=r"$\mu_u$")
            ax1.plot(μQ, μd, ".-", color="green", label=r"$\mu_d$")
            ax1.plot(μQ, μs, ".-", color="purple", label=r"$\mu_s$")
            ax1.plot(μQ, μe, ".-", color="blue", label=r"$\mu_e$")
            ax1.legend()

            ax2.set_xlabel(r"$\mu_Q$")
            ax2.set_ylabel(r"$n$")
            ax2.plot(μQ, nu, ".-", color="red", label=r"$n_u$")
            ax2.plot(μQ, nd, ".-", color="green", label=r"$n_d$")
            ax2.plot(μQ, ns, ".-", color="purple", label=r"$n_s$")
            ax2.plot(μQ, ne, ".-", color="blue", label=r"$n_e$")
            ax2.legend()

            ax3.set_xlabel(r"$P$")
            ax3.set_ylabel(r"$\epsilon$")
            ax3.plot(Porg, ϵorg, ".-", color="gray") # compare
            ax3.plot(P, ϵ, ".-", color="black")

            ax4.plot(μQ, (P/(MeV**4 / (ħ*c)**3)/(fm**3 / GeV))**0.25)
            #P0 *= (MeV**4 / (ħ*c)**3) # now in units kg*m^2/s^2/m^3
            #P0 *= (fm**3 / GeV) # now in units GeV/fm^3
            ax4.set_xlabel(r"$\mu / MeV$")
            ax4.set_ylabel(r"$P^{\frac{1}{4}} / MeV$")
            ax4.set_xlim(0, 1000)
            ax4.set_ylim(0, 500)

            plt.show()

        # interpolate dimensionless EOS
        P /= (fm**3/GeV) * ϵ0 # now in TOV-dimensionless units
        ϵ /= (fm**3/GeV) * ϵ0 # now in TOV-dimensionless units
        ϵ = np.concatenate(([0, np.interp(0, P, ϵ)], ϵ[P>0]))
        nu = np.concatenate(([0, np.interp(0, P, nu)], nu[P>0]))
        nd = np.concatenate(([0, np.interp(0, P, nd)], nd[P>0]))
        ns = np.concatenate(([0, np.interp(0, P, ns)], ns[P>0]))
        ne = np.concatenate(([0, np.interp(0, P, ne)], ne[P>0]))
        μQ = np.concatenate(([0, np.interp(0, P, μQ)], μQ[P>0]))
        P = np.concatenate(([P[0] - 10, 0], P[P>0])) # avoid interp errors w/ ϵ(P<Pmin)=0
        print(f"interpolation range: {P[0]} < P < {P[-1]}")
        ϵint = scipy.interpolate.interp1d(P, ϵ); ϵint.__name__ = self.name
        nuint = scipy.interpolate.interp1d(P, nu)
        ndint = scipy.interpolate.interp1d(P, nd)
        nsint = scipy.interpolate.interp1d(P, ns)
        neint = scipy.interpolate.interp1d(P, ne)
        μQint = scipy.interpolate.interp1d(P, μQ)
        return ϵint, nuint, ndint, nsint, neint, μQint

    def star(self, Pc, B14, plot=False, write=False):
        ϵ, nu, nd, ns, ne, μQ = self.eos(B=B14**4)
        rs, ms, Ps, αs, ϵs = soltov(ϵ, Pc, maxdr=tovopts["maxdr"])
        nus, nds, nss, nes, μQs = nu(Ps), nd(Ps), ns(Ps), ne(Ps), μQ(Ps)
        xs = rs / rs[-1] # dimensionless radius [0, 1]

        Ps *= (fm**3/GeV) * ϵ0 # now in GeV/fm^3
        ϵs *= (fm**3/GeV) * ϵ0 # now in GeV/fm^3
        nus /= 0.165 # now in units of n_sat
        nds /= 0.165 # now in units of n_sat
        nss /= 0.165 # now in units of n_sat
```

```
        nes /= 0.165 # now in units of n_sat

        if plot:
            fig, (ax1, ax2, ax3, ax4) = plt.subplots(1, 4)
            ax1.set_xlabel(r"$r$")
            ax2.set_xlabel(r"$r$")
            ax3.set_xlabel(r"$r$")
            ax4.set_xlabel(r"$r$")
            ax1.plot(rs, Ps, label=r"$P$")
            ax1.plot(rs, ϵs, label=r"$\epsilon$")
            ax2.plot(rs, ms, label=r"$m$")
            ax3.plot(rs, μQs, label=r"$\mu_Q$")
            ax4.plot(rs, nus, label=r"$n_u$")
            ax4.plot(rs, nds, label=r"$n_d$")
            ax4.plot(rs, nss, label=r"$n_s$")
            ax4.plot(rs, nes, label=r"$n_e$")
            ax1.legend()
            ax2.legend()
            ax3.legend()
            ax4.legend()
            plt.show()

        if write:
            heads = ["r", "x", "m", "P", "epsilon", "nu", "nd", "ns", "ne", "muQ"]
            cols = [rs, xs, ms, Ps, ϵs, nus, nds, nss, nes, μQs]
            outfile = f"data/{self.name}/star_sigma_{self.mσ}_B14_{B14}_Pc_{Pc:.7f}.dat"
            utils.writecols(cols, heads, outfile)

    def stars(self, B14, P1P2, N=1000, plot=False, write=False):
        if write:
            outfile = f"data/{self.name}/stars_sigma_{self.mσ}_B14_{B14}.dat"
        else:
            outfile = ""
        print(f"B = ({B14} MeV)^4, outfile = {outfile}")
        ϵ, _, _, _, _, _ = self.eos(N=N, B=B14**4, plot=False)
        massradiusplot(ϵ, P1P2, **tovopts, visual=plot, outfile=outfile)
```

MIT bag model (chapter 7)

quark_stars_mit.py

```
#!/usr/bin/python3

from quark_hybrid_stars_common import *

muf = 5 # current/lone/free masses (i.e. without gluons)
mdf = 7
msf = 150

class MITModel(Model):
    pass # will only inherit

class MIT2FlavorModel(MITModel):
    def __init__(self):
        Model.__init__(self, "MIT2F")
        self.Ω = lambda mu, md, ms, μu, μd, μs, μe: np.real(
            -Nc/(24*π**2)*((2*μu**2-5*mu**2)*μu*np.sqrt(μu**2-mu**2+0j)+\
            3*mu**4*np.arcsinh(np.sqrt(μu**2/mu**2-1+0j))) + \
            -Nc/(24*π**2)*((2*μd**2-5*md**2)*μd*np.sqrt(μd**2-md**2+0j)+\
            3*md**4*np.arcsinh(np.sqrt(μd**2/md**2-1+0j))) + \
            -1/(24*π**2)*((2*μe**2-5*me**2)*μe*np.sqrt(μe**2-me**2+0j)+\
            3*me**4*np.arcsinh(np.sqrt(μe**2/me**2-1+0j)))
        )

    def vacuum_masses(self):
        return muf, mdf, 0

    def solve(self, μQ):
        def q(μe):
            μu, μd, _ = μelim(μQ, μe)
            return charge(muf, mdf, 0, μu, μd, 0, μe)
        sol = scipy.optimize.root_scalar(q, method="bisect", bracket=(0, 1e5))
```

```
        assert sol.converged, f"{sol.flag} (μQ = {μQ})"
        μe = sol.root
        μu, μd, _ = μelim(μQ, μe)
        return μu, μd, μe

    def eossolve(self, N):
        μQ = np.linspace(muf, 2000, N)
        μu = np.empty_like(μQ)
        μd = np.empty_like(μQ)
        μe = np.empty_like(μQ)

        for i in range(0, len(μQ)):
            μu[i], μd[i], μe[i] = self.solve(μQ[i])
            print(f"μQ = {μQ[i]:.2f}, μu = {μu[i]:.2f}, ", end="")
            print(f"μd = {μd[i]:.2f}, μe = {μe[i]:.2f}")

        mu = np.full_like(μQ, muf)
        md = np.full_like(μQ, mdf)
        ms = np.full_like(μQ, 0)
        μs = np.full_like(μQ, 0)
        return mu, md, ms, μu, μd, μs, μe

class MIT3FlavorModel(MITModel):
    def __init__(self):
        Model.__init__(self, "MIT3F")
        self.Ω = lambda mu, md, ms, μu, μd, μs, μe: np.real(
            -Nc/(24*π**2)*((2*μu**2-5*mu**2)*μu*np.sqrt(μu**2-mu**2)+\
            3*mu**4*np.arcsinh(np.sqrt(μu**2/mu**2-1))) + \
            -Nc/(24*π**2)*((2*μd**2-5*md**2)*μd*np.sqrt(μd**2-md**2)+\
            3*md**4*np.arcsinh(np.sqrt(μd**2/md**2-1))) + \
            -Nc/(24*π**2)*((2*μs**2-5*ms**2)*μs*np.sqrt(μs**2-ms**2)+\
            3*ms**4*np.arcsinh(np.sqrt(μs**2/ms**2-1))) + \
            -1/(24*π**2)*((2*μe**2-5*me**2)*μe*np.sqrt(μe**2-me**2)+\
            3*me**4*np.arcsinh(np.sqrt(μe**2/me**2-1)))
        )

    def vacuum_masses(self):
        return muf, mdf, msf

    def solve(self, μQ):
        def q(μe):
            μu, μd, μs = μelim(μQ, μe)
            return charge(muf, mdf, msf, μu, μd, μs, μe)
        sol = scipy.optimize.root_scalar(q, method="bisect", bracket=(0, 1e5))
        assert sol.converged, f"{sol.flag} (μQ = {μQ})"
        μe = sol.root
        μu, μd, μs = μelim(μQ, μe)
        return μu, μd, μs, μe

    def eossolve(self, N):
        μQ = np.linspace(muf, 2000, N)
        μu = np.empty_like(μQ)
        μd = np.empty_like(μQ)
        μs = np.empty_like(μQ)
        μe = np.empty_like(μQ)

        for i in range(0, len(μQ)):
            μu[i], μd[i], μs[i], μe[i] = self.solve(μQ[i])
            print(f"μQ = {μQ[i]:.2f}, μu = {μu[i]:.2f}, μd = {μd[i]:.2f}, ", end="")
            print(f"μs = {μs[i]:.2f}, μe = {μe[i]:.2f}")

        mu = np.full_like(μQ, muf)
        md = np.full_like(μQ, mdf)
        ms = np.full_like(μQ, msf)
        return mu, md, ms, μu, μd, μs, μe

if __name__ == "__main__": # uncomment lines/blocks to run
    """
    models = [MIT2FlavorModel, MIT3FlavorModel]
    for model in models:
        model = model()
        model.eos(plot=False, write=True)
        for B14 in (145, 150, 155):
            model.stars(B14, (1e-7, 1e-2), write=True)
    """
```

Quark-meson model (chapters 8 and 9)

quark_stars_lsm.py

```
#!/usr/bin/python3

from quark_hybrid_stars_common import *
import os; os.environ["XDG_SESSION_TYPE"] = "x11" # for mayavi to work
import mayavi.mlab as mlab

mu0 = 300 # constituent masses (i.e. with gluons)
md0 = mu0
ms0 = 429 # only used for root equation guess

fπ = 93
fK = 113
σx0 = fπ
σy0 = np.sqrt(2)*fK-fπ/np.sqrt(2)

mσ = 800
mπ = 138
mK = 496

class LSMModel(Model):
    def eossolve(self, N):
        Δx = np.linspace(self.mu, 0, N)[:-1] # shave off erronous 0
        Δy = np.empty_like(Δx)
        μQ, μu, μd, μs, μe = Δy, Δy, Δy, Δy, Δy # copy

        for i in range(0, len(Δx)):
            mu, md ,ms = self.vacuum_masses()
            guess = (μQ[i-1], Δy[i-1], μe[i-1]) if i > 0 else (mu, ms, 0) # use prev sol
            μQ[i], Δy[i], μu[i], μd[i], μs[i], μe[i] = self.solve(Δx[i], guess)
            print(f"Δx = {Δx[i]:.2f}, Δy = {Δy[i]:.2f}, ", end="")
            print(f"μu = {μu[i]:.2f}, μd = {μd[i]:.2f}, ", end="")
            print(f"μs = {μs[i]:.2f}, μe = {μe[i]:.2f}")

        return Δx, Δx, Δy, μu, μd, μs, μe

    def vacuum_masses(self):
        min = scipy.optimize.minimize(
            lambda ΔxΔy: self.Ω(ΔxΔy[0], ΔxΔy[0], ΔxΔy[1], 0, 0, 0, 0),
            x0=(mu0, ms0), method="Nelder-Mead"
        )
        if min.success:
            Δx0, Δy0 = min.x
        else:
            Δx0, Δy0 = np.nan, np.nan
        return Δx0, Δx0, Δy0

    def vacuum_potential(self, Δx, Δy, write=False):
        fig, axl = plt.subplots()
        axr = axl.twinx()
        ΔxΔx, ΔyΔy = np.meshgrid(Δx, Δy)

        Ωf = lambda Δx, Δy: self.Ω(Δx, Δx, Δy, 0, 0, 0, 0) / fπ**4 # in vacuum

        Ω = Ωf(ΔxΔx, ΔyΔy)
        Ω0 = np.max(np.abs(Ω))
        mlab.mesh(ΔxΔx / Δx[-1], ΔyΔy / Δy[-1], Ω / Ω0)
        mlab.mesh(ΔxΔx / Δx[-1], ΔyΔy / Δy[-1], Ω / Ω0, representation="wireframe")
        mlab.axes()

        Δx0, _, Δy0 = self.vacuum_masses()
        if not np.isnan(Δx0) and not np.isnan(Δy0):
            print(f"mσ = {self.mσ} MeV: found minimum (Δx, Δy, Ω/fπ^4) = ", end="")
            print(f"({Δx0:.0f} MeV, {Δy0:.0f} MeV, {Ωf(Δx0, Δy0)})")
            Ωx0 = Ωf(Δx, Δy0)
            Ωy0 = Ωf(Δx0, Δy)
            mlab.plot3d(np.full(Δy.shape, Δx0) / Δx[-1], Δy / Δy[-1], Ωy0 / Ω0)
            mlab.plot3d(Δx / Δx[-1], np.full(Δx.shape, Δy0) / Δy[-1], Ωx0 / Ω0)
        else:
            print(f"mσ = {self.mσ} MeV: no minimum!")

        if write:
```

```
            cols  = [ΔxΔx.flatten(), ΔyΔy.flatten(), Ω.flatten()]
            heads = ["Deltax", "Deltay", "Omega"]
            utils.writecols(
                cols, heads, f"data/{self.name}/potential_vacuum_sigma{mσ}.dat",
                skipevery=len(Δx)
            )

        mlab.show()

class LSM2FlavorModel(LSMModel):
    def __init__(self, mσ=mσ, mπ=mπ, renormalize=True):
        Nf = 2
        m2 = 1/2*(3*mπ**2-mσ**2)
        λ  = 3/fπ**2 * (mσ**2-mπ**2)
        h  = fπ * mπ**2
        g  = mu0 / fπ
        Λ2 = mu0**2 / np.e
        print(f"m2  = {np.sign(m2)}*({np.sqrt(np.abs(m2))} MeV)^2 ")
        print(f"λ   = {λ}")
        print(f"g   = {g}")
        print(f"h   = {np.sign(h)}*({np.abs(h)**(1/3)} MeV)^3 ")
        print(f"Λ   = {np.sqrt(Λ2)} MeV")

        Δ, μu, μd, μe = sp.symbols("Δ μ_u μ_d μ_e", complex=True)
        σ = Δ / g
        Ω0 = 1/2*m2*σ**2 + λ/24*σ**4 - h*σ
        Ωr = Nc*Nf*Δ**4/(16*π**2)*(3/2+sp.log(Λ2/Δ**2)) if renormalize else 0
        Ωu = -Nc/(24*π**2)*((2*μu**2-5*Δ**2)*μu*sp.sqrt(μu**2-Δ**2)+\
             3*Δ**4*sp.asinh(sp.sqrt(μu**2/Δ**2-1)))
        Ωd = -Nc/(24*π**2)*((2*μd**2-5*Δ**2)*μd*sp.sqrt(μd**2-Δ**2)+\
             3*Δ**4*sp.asinh(sp.sqrt(μd**2/Δ**2-1)))
        Ωe = -1/(24*π**2)*((2*μe**2-5*me**2)*μe*sp.sqrt(μe**2-me**2)+\
             3*me**4*sp.asinh(sp.sqrt(μe**2/me**2-1)))
        Ω  = Ω0 + Ωr + Ωu + Ωd + Ωe
        dΩ = sp.diff(Ω, Δ)

        Ω  = sp.lambdify((Δ, μu, μd, μe),  Ω, "numpy")
        dΩ = sp.lambdify((Δ, μu, μd, μe), dΩ, "numpy")
        self.Ω  = lambda mu,md,ms,μu,μd,μs,μe: np.real( Ω(mu+0j,μu+0j,μd+0j,μe+0j))
        self.dΩ = lambda mu,md,ms,μu,μd,μs,μe: np.real(dΩ(mu+0j,μu+0j,μd+0j,μe+0j))

        Model.__init__(self, "LSM2F", mσ=mσ, mπ=mπ)

    def solve(self, Δx, guess):
        def system(μQ_Δy_μe):
            μQ, Δy, μe = μQ_Δy_μe # unpack variables
            μu, μd, _ = μelim(μQ, μe)
            μs = 0
            return (self.dΩ(Δx, Δx, 0, μu, μd, 0, μe), Δy, # hack to give Δy = 0
                    charge(Δx, Δx, 0, μu, μd, 0, μe))
        sol = scipy.optimize.root(system, guess, method="lm") # lm and krylov works
        assert sol.success, f"{sol.message} (Δx = {Δx})"
        μQ, Δy, μe = sol.x
        μu, μd, _ = μelim(μQ, μe)
        Δy, μs = 0, 0
        return μQ, Δy, μu, μd, μs, μe

class LSM2FlavorConsistentModel(LSM2FlavorModel):
    def __init__(self, mσ=mσ, mπ=mπ):
        Δ, μu, μd, μe = sp.symbols("Δ μ_u μ_d μ_e", complex=True)
        def r(p2): return sp.sqrt(4*mu0**2/p2-1)
        def F(p2): return 2 - 2*r(p2)*sp.atan(1/r(p2))
        def dF(p2): return 4*mu0**2*r(p2)/(p2*(4*mu0**2-p2))*sp.atan(1/r(p2))-1/p2
        Ω  = 3/4*mπ**2*fπ**2*(1-4*mu0**2*Nc/(4*π*fπ)**2*mπ**2*dF(mπ**2)) * (Δ/mu0)**2
        Ω -= mσ**2*fπ**2/4*(1+4*mu0**2*Nc/(4*π*fπ)**2*((1-4*mu0**2/mσ**2)*F(mσ**2)+\
             4*mu0**2/mσ**2-F(mπ**2)-mπ**2*dF(mπ**2))) * (Δ/mu0)**2
        Ω += mσ**2*fπ**2/8*(1-4*mu0**2*Nc/(4*π*fπ)**2*(4*(mu0/mσ)**2*sp.log((Δ/mu0)**2)-\
             (1-4*mu0**2/mσ**2)*F(mσ**2)+F(mπ**2)+mπ**2*dF(mπ**2))) * (Δ/mu0)**4
        Ω -= mπ**2*fπ**2/8*(1-4*mu0**2*Nc/(4*π*fπ)**2*mπ**2*dF(mπ**2)) * (Δ/mu0)**4
        Ω -= mπ**2*fπ**2*(1-4*mu0**2*Nc/(4*π*fπ)**2*mπ**2*dF(mπ**2)) * Δ/mu0
        Ω += 3*Nc/(16*π**2) * Δ**4
        Ω -= Nc/(24*π**2)*((2*μu**2-5*Δ**2)*μu*sp.sqrt(μu**2-Δ**2)+\
             3*Δ**4*sp.asinh(sp.sqrt(μu**2/Δ**2-1)))
        Ω -= Nc/(24*π**2)*((2*μd**2-5*Δ**2)*μd*sp.sqrt(μd**2-Δ**2)+\
             3*Δ**4*sp.asinh(sp.sqrt(μd**2/Δ**2-1)))
```

```
        Ω -= 1/(24*π**2)*((2*μe**2-5*me**2)*μe*sp.sqrt(μe**2-me**2)+\
             3*me**4*sp.asinh(sp.sqrt(μe**2/me**2-1)))

        dΩ = sp.diff(Ω, Δ) # (numerical differentiation also works)
        dΩ = sp.lambdify((Δ, μu, μd, μe), dΩ, "numpy")
        self.dΩ = lambda mu, md, ms, μu, μd, μs, μe: np.real(dΩ(mu+0j,μu+0j,μd+0j,μe+0j))

        Ω  = sp.lambdify((Δ, μu, μd, μe),  Ω, "numpy")
        self.Ω  = lambda mu, md, ms, μu, μd, μs, μe: np.real( Ω(mu+0j,μu+0j,μd+0j,μe+0j))

        Model.__init__(self, "LSM2FC", mσ=mσ, mπ=mπ)

class LSM3FlavorModel(LSMModel):
    def __init__(self, mσ=mσ, mπ=mπ, mK=mK):
        def mesonmasses(m2, λ1, λ2):
            rt2 = np.sqrt(2)

            m2σσ00 = m2+λ1/3*(4*rt2*σx0*σy0+7*σx0**2+5*σy0**2)+λ2*(σx0**2+σy0**2)
            m2σσ11 = m2+λ1*(σx0**2+σy0**2)+3/2*λ2*σx0**2
            m2σσ44 = m2+λ1*(σx0**2+σy0**2)+λ2/2*(rt2*σx0*σy0+σx0**2+2*σy0**2)
            m2σσ88 = m2-λ1/3*(4*rt2*σx0*σy0-5*σx0**2-7*σy0**2)+λ2/2*(σx0**2+4*σy0**2)
            m2σσ08 = 2/3*λ1*(rt2*σx0**2-rt2*σy0**2-σx0*σy0)+λ2/rt2*(σx0**2-2*σy0**2)

            m2ππ00 = m2+λ1*(σx0**2+σy0**2)+λ2/3*(σx0**2+σy0**2)
            m2ππ11 = m2+λ1*(σx0**2+σy0**2)+λ2/2*σx0**2
            m2ππ44 = m2+λ1*(σx0**2+σy0**2)-λ2/2*(rt2*σx0*σy0-σx0**2-2*σy0**2)
            m2ππ88 = m2+λ1*(σx0**2+σy0**2)+λ2/6*(σx0**2+4*σy0**2)
            m2ππ08 = λ2/6*(rt2*σx0**2-2*rt2*σy0**2)

            θσ = np.arctan(2*m2σσ08 / (m2σσ88-m2σσ00)) / 2
            θπ = np.arctan(2*m2ππ08 / (m2ππ88-m2ππ00)) / 2

            m2f0 = m2σσ00*np.sin(θσ)**2 + m2σσ88*np.cos(θσ)**2 + m2σσ08*np.sin(2*θσ)
            m2σ  = m2σσ00*np.cos(θσ)**2 + m2σσ88*np.sin(θσ)**2 - m2σσ08*np.sin(2*θσ)
            m2a0 = m2σσ11
            m2κ  = m2σσ44
            m2η  = m2ππ00*np.sin(θπ)**2 + m2ππ88*np.cos(θπ)**2 + m2ππ08*np.sin(2*θπ)
            m2ηp = m2ππ00*np.cos(θπ)**2 + m2ππ88*np.sin(θπ)**2 - m2ππ08*np.sin(2*θπ)
            m2π  = m2ππ11
            m2K  = m2ππ44
            return m2f0, m2σ, m2a0, m2κ, m2η, m2ηp, m2π, m2K

        def system(m2_λ1_λ2):
            m2, λ1, λ2 = m2_λ1_λ2
            _, m2σ, _, _, _, _, m2π, m2K = mesonmasses(m2, λ1, λ2)
            return (m2σ - mσ**2, m2π - mπ**2, m2K - mK**2)

        sol = scipy.optimize.root(system, (-100, -10, +100), method="hybr")
        m2, λ1, λ2 = sol.x
        g = 2*mu0/σx0
        hx = σx0 * (m2 + λ1*(σx0**2+σy0**2) + λ2/2*σx0**2)
        hy = σy0 * (m2 + λ1*(σx0**2+σy0**2) + λ2*σy0**2)
        Λx = g*σx0/(2*np.sqrt(np.e))
        Λy = g*σy0/(np.sqrt(2*np.e))
        common_renormalization_scale = False
        if common_renormalization_scale:
            Λ = (2*Λx+Λy)/3
            Λx, Λy = Λ, Λ # set common, averaged renormalization scale
        print(f"m2 = {np.sign(m2)}*({np.sqrt(np.abs(m2))} MeV)^2 ")
        print(f"λ1 = {λ1}")
        print(f"λ2 = {λ2}")
        print(f"g  = {g}")
        print(f"hx = ({hx**(1/3)} MeV)^3")
        print(f"hy = ({hy**(1/3)} MeV)^3")
        print(f"Λx = {Λx} MeV")
        print(f"Λy = {Λy} MeV")
        print(f"mx = {g*σx0/2} MeV")
        print(f"my = {g*σy0/np.sqrt(2)} MeV")

        # predict (remaining) meson masses
        m2f0, m2σ, m2a0, m2κ, m2η, m2ηp, m2π, m2K = mesonmasses(m2, λ1, λ2)
        print(f"mf0 = {np.sqrt(m2f0):.0f} MeV")
        print(f"mσ  = {np.sqrt(m2σ):.0f} MeV")
        print(f"ma0 = {np.sqrt(m2a0):.0f} MeV")
        print(f"mκ  = {np.sqrt(m2κ):.0f} MeV")
```

```
        print(f"mη  = {np.sqrt(m2η):.0f} MeV")
        print(f"mηp = {np.sqrt(m2ηp):.0f} MeV")
        print(f"mπ  = {np.sqrt(m2π):.0f} MeV")
        print(f"mK  = {np.sqrt(m2K):.0f} MeV")

        Δx, Δy, μu, μd, μs, μe = sp.symbols("Δ_x Δ_y μ_u μ_d μ_s μ_e", complex=True)
        σx = 2*Δx/g
        σy = np.sqrt(2)*Δy/g
        Ωb = m2/2*(σx**2+σy**2) + λ1/4*(σx**2+σy**2)**2 + λ2/8*(σx**4+2*σy**4) -\
             hx*σx - hy*σy
        Ωr = Nc/(16*π**2)*(Δx**4*(3/2+sp.log(Λx**2/Δx**2))+\
             Δx**4*(3/2+sp.log(Λx**2/Δx**2))+Δy**4*(3/2+sp.log(Λy**2/Δy**2)))
        Ωu = -Nc/(24*π**2)*((2*μu**2-5*Δx**2)*μu*sp.sqrt(μu**2-Δx**2)+\
             3*Δx**4*sp.asinh(sp.sqrt(μu**2/Δx**2-1)))
        Ωd = -Nc/(24*π**2)*((2*μd**2-5*Δx**2)*μd*sp.sqrt(μd**2-Δx**2)+\
             3*Δx**4*sp.asinh(sp.sqrt(μd**2/Δx**2-1)))
        Ωs = -Nc/(24*π**2)*((2*μs**2-5*Δy**2)*μs*sp.sqrt(μs**2-Δy**2)+\
             3*Δy**4*sp.asinh(sp.sqrt(μs**2/Δy**2-1)))
        Ωe =  -1/(24*π**2)*((2*μe**2-5*me**2)*μe*sp.sqrt(μe**2-me**2)+\
             3*me**4*sp.asinh(sp.sqrt(μe**2/me**2-1)))

        Ω  = Ωb + Ωr + Ωu + Ωd + Ωs + Ωe
        dΩx = sp.diff(Ω, Δx)
        dΩy = sp.diff(Ω, Δy)

        Ω   = sp.lambdify((Δx, Δy, μu, μd, μs, μe), Ω,   "numpy")
        dΩx = sp.lambdify((Δx, Δy, μu, μd, μs, μe), dΩx, "numpy")
        dΩy = sp.lambdify((Δx, Δy, μu, μd, μs, μe), dΩy, "numpy")
        self.Ω   = lambda mu, md, ms, μu, μd, μs, μe: \
                   np.real(  Ω(mu+0j, ms+0j, μu+0j, μd+0j, μs+0j, μe+0j))
        self.dΩx = lambda mu, md, ms, μu, μd, μs, μe: \
                   np.real(dΩx(mu+0j, ms+0j, μu+0j, μd+0j, μs+0j, μe+0j))
        self.dΩy = lambda mu, md, ms, μu, μd, μs, μe: \
                   np.real(dΩy(mu+0j, ms+0j, μu+0j, μd+0j, μs+0j, μe+0j))

        Model.__init__(self, f"LSM3F", mσ=mσ, mπ=mπ, mK=mK)

    def solve(self, Δx, guess):
        def system(μQ_Δy_μe):
            μQ, Δy, μe = μQ_Δy_μe # unpack variables
            μu, μd, μs = μelim(μQ, μe)
            return (self.dΩx(Δx, Δx, Δy, μu, μd, μs, μe),
                    self.dΩy(Δx, Δx, Δy, μu, μd, μs, μe),
                    charge(Δx, Δx, Δy, μu, μd, μs, μe))
        sol = scipy.optimize.root(system, guess, method="lm")
        assert sol.success, f"{sol.message} (Δx = {Δx})"
        μQ, Δy, μe = sol.x
        μu, μd, μs = μelim(μQ, μe)
        return μQ, Δy, μu, μd, μs, μe

if __name__ == "__main__": # uncomment lines/blocks to run
    # plot 3D potential for 2-flavor model with μu=μd
    """
    mσ = 700
    model = LSM2FlavorModel(mσ=mσ)
    Δ = np.linspace(-1000, +1000, 100)
    μQ = np.linspace(0, 500, 50)
    Ω = np.array([model.Ω(Δ, Δ, 0, μQ, μQ, 0, 0) for μQ in μQ])
    Δ0 = np.empty_like(μQ)
    Ω0 = np.empty_like(μQ)
    for i in range(0, len(μQ)):
        μQ0 = μQ[i]
        def Ω2(Δ): return model.Ω(Δ, Δ, 0, μQ0, μQ0, 0, 0)
        sol = scipy.optimize.minimize_scalar(Ω2, bounds=(0, 350), method="bounded")
        assert sol.success, f"{sol.message} (μ = {μQ0})"
        Δ0[i] = sol.x
        Ω0[i] = Ω2(Δ0[i])
    plt.xlabel(r"$\Delta$")
    plt.ylabel(r"$\Omega$")
    plt.plot(Δ, Ω.T / 100**4, "-k")
    plt.plot(Δ0, Ω0 / 100**4, "-r.")
    plt.show()
    Δc, μQc, Ωc = [], [], []
    for i in range(0, len(Δ)):
        for j in range(0, len(μQ)):
```

```
            μQc.append(μQ[j])
            Δc.append(Δ[i])
            Ωc.append(Ω[j,i])
    cols = [μQc, Δc, list(np.array(Ωc)/100**4), μQc, list(Δ0), list(Ω0/100**4)]
    heads = ["mu", "Delta", "Omega", "mu0", "Delta0", "Omega0"]
    utils.writecols(
        cols, heads, f"data/{model.name}/potential_noisospin_sigma_{mσ}.dat",
        skipevery=len(μQ)
    )
    """

    # vacuum potentials
    """
    Δ = np.linspace(-600, +600, 300)
    for mσ in [500, 600, 700, 800]:
        LSM2FlavorModel(mσ=mσ).vacuum_potential(Δ, np.array([ms0]), write=True)
    for mσ in [400, 500, 600, 700, 800]:
        LSM2FlavorConsistentModel(mσ=mσ).vacuum_potential(Δ, np.array([ms0]), write=True)
    Δ = np.linspace(-1000, +1000, 50)
    for mσ in [500, 600, 700, 800]:
        LSM3FlavorModel(mσ=mσ).vacuum_potential(Δ, Δ, write=True)
    """

    #LSM2FlavorModel(mσ=600).eos(write=True)
    #LSM2FlavorModel(mσ=700).eos(write=True)
    #LSM2FlavorModel(mσ=800).eos(write=True)
    #LSM2FlavorModel(mσ=600).stars(111, (1e-7, 1e-2), write=True)
    #LSM2FlavorModel(mσ=600).stars(131, (1e-7, 1e-2), write=True)
    #LSM2FlavorModel(mσ=600).stars(151, (1e-7, 1e-2), write=True)
    #LSM2FlavorModel(mσ=700).stars(68,  (1e-7, 1e-2), write=True)
    #LSM2FlavorModel(mσ=700).stars(88,  (1e-7, 1e-2), write=True)
    #LSM2FlavorModel(mσ=700).stars(108, (1e-7, 1e-2), write=True)
    #LSM2FlavorModel(mσ=800).stars(27,  (1e-7, 1e-2), write=True)
    #LSM2FlavorModel(mσ=800).stars(47,  (1e-7, 1e-2), write=True)
    #LSM2FlavorModel(mσ=800).stars(67,  (1e-7, 1e-2), write=True)
    #LSM2FlavorModel(mσ=800).star(0.0012500875, 27, write=True)

    #LSM2FlavorConsistentModel(mσ=400).eos(plot=False, write=True)
    #LSM2FlavorConsistentModel(mσ=500).eos(plot=False, write=True)
    #LSM2FlavorConsistentModel(mσ=600).eos(plot=False, write=True)
    #LSM2FlavorConsistentModel(mσ=400).stars(107, (1e-7, 1e-2), write=True)
    #LSM2FlavorConsistentModel(mσ=400).stars(127, (1e-7, 1e-2), write=True)
    #LSM2FlavorConsistentModel(mσ=400).stars(147, (1e-7, 1e-2), write=True)
    #LSM2FlavorConsistentModel(mσ=500).stars(84,  (1e-7, 1e-2), write=True)
    #LSM2FlavorConsistentModel(mσ=500).stars(104, (1e-7, 1e-2), write=True)
    #LSM2FlavorConsistentModel(mσ=500).stars(124, (1e-7, 1e-2), write=True)
    #LSM2FlavorConsistentModel(mσ=600).stars(27,  (1e-7, 1e-2), write=True)
    #LSM2FlavorConsistentModel(mσ=600).stars(47,  (1e-7, 1e-2), write=True)
    #LSM2FlavorConsistentModel(mσ=600).stars(67,  (1e-7, 1e-2), write=True)

    #LSM3FlavorModel(mσ=600).eos(plot=False, write=True)
    #LSM3FlavorModel(mσ=700).eos(plot=False, write=True)
    #LSM3FlavorModel(mσ=800).eos(plot=False, write=True)
    #LSM3FlavorModel(mσ=600).stars(111, (1e-7, 1e-2), write=True)
    #LSM3FlavorModel(mσ=600).stars(131, (1e-7, 1e-2), write=True)
    #LSM3FlavorModel(mσ=600).stars(151, (1e-7, 1e-2), write=True)
    #LSM3FlavorModel(mσ=700).stars(68,  (1e-7, 1e-2), write=True)
    #LSM3FlavorModel(mσ=700).stars(88,  (1e-7, 1e-2), write=True)
    #LSM3FlavorModel(mσ=700).stars(108, (1e-7, 1e-2), write=True)
    #LSM3FlavorModel(mσ=800).stars(27,  (1e-7, 1e-2), write=True)
    #LSM3FlavorModel(mσ=800).stars(47,  (1e-7, 1e-2), write=True)
    #LSM3FlavorModel(mσ=800).stars(67,  (1e-7, 1e-2), write=True)
    #LSM3FlavorModel(mσ=800).star(0.000937590625, 27, write=True)
```

Hybrid quark-hadron model (chapter 10)

hybrid_stars_apr_lsm.py

```
#!/usr/bin/python3

from quark_hybrid_stars_common import *
import quark_stars_lsm

class HybridModel(Model):
    def eos(self, N=1000, B=111**4, hybrid=True, plot=False, write=False):
        arr = np.loadtxt("data/APR/eos.dat")
        mn = 900 # MeV
        nB = arr[:,0]
        P_over_nB = arr[:,1]
        μB_over_mn_minus_one = arr[:,3]
        ϵ_over_nBmn_minus_one = arr[:,6]
        P = P_over_nB * nB
        ϵ = (ϵ_over_nBmn_minus_one + 1) * (nB*mn)

        nB1 = nB
        μB1 = (μB_over_mn_minus_one + 1) * mn
        P1  = P * 1e-3 * (GeV/fm**3) / ϵ0 # MeV/fm^3 -> GeV/fm^3 -> SI -> TOV-dimless
        ϵ1  = ϵ * 1e-3 * (GeV/fm**3) / ϵ0 # MeV/fm^3 -> GeV/fm^3 -> SI -> TOV-dimless

        ϵ2int, nu2int, nd2int, ns2int, _, μQ2int = self.quarkmodel(
            mσ=self.mσ).eos(N=N-len(P1), B=B
        )
        nB2 = (nu2int(P1)+nd2int(P1)+ns2int(P1)) / 3
        μB2 = μQ2int(P1) * 3

        if plot:
            fig, (ax1, ax2) = plt.subplots(1, 2)
            ax1.plot(μB1, P1, "-b.")
            ax1.plot(μB2, P1, "-r.")
            ax2.plot(μB1, nB1/0.165, "-b.")
            ax2.plot(μB1, nB2/0.165, "-r.")
            plt.show()

        # find intersecting nB (from top)
        P1i = scipy.interpolate.interp1d(μB1, P1)
        P2i = scipy.interpolate.interp1d(μB2, P1)
        sol = scipy.optimize.root_scalar(
            lambda μB: P2i(μB)-P1i(μB), method="brentq", bracket=(1200, 2000)
        )
        assert sol.converged
        μB0 = sol.root
        if not hybrid:
            μB0 = 2700 # will use only hadronic EOS
        P0 = P1i(μB0)
        print(f"μB0 = {μB0}")
        print(f"P0  = {P0} = 10^({np.log10(P0*ϵ0)}) Pa")
        print(f"Δϵ  = {ϵ2int(P0)-np.interp(P0, P1, ϵ1) * ϵ0 / (GeV/fm**3)}")

        # should it be stable? see ref:hybrid_star_stability_criterion, equation 15
        lhs = ϵ2int(P0)-np.interp(P0, P1, ϵ1)
        rhs = np.interp(P0,P1,ϵ1)/2+3/2*P0
        print(f"Should be stable? {lhs} < {rhs} ? {lhs < rhs}")

        # compute pressure for larger values to increase interpolation range
        P2 = np.linspace(P0, 1e-1, N-len(P1))
        ϵ2 = ϵ2int(P2)
        P  = np.concatenate((P1[P1<P0], [P0], P2))
        ϵ  = np.concatenate((ϵ1[P1<P0], [np.interp(P0, P1, ϵ1)], ϵ2))

        if plot:
            plt.plot(P, ϵ, "-k.", linewidth=4)
            plt.plot(P1, ϵ1, "-b.")
            plt.plot(P, ϵ2int(P), "-r.")
            plt.show()

        # hack: exploit nu=nd=ns=nB for density interpolation
        nB2 = (nu2int(P2)+nd2int(P2)+ns2int(P2)) / 3 # compute with P2 instead of P1
        nB = np.concatenate((nB1[P1<P0], [np.interp(P0, P1, nB1)], nB2))
```

```
        nu = np.concatenate((nB1[P1<P0], [np.interp(P0, P1, nB1)], nu2int(P2)))
        nd = np.concatenate((nB1[P1<P0], [np.interp(P0, P1, nB1)], nd2int(P2)))
        ns = np.concatenate((nB1[P1<P0], [np.interp(P0, P1, nB1)], ns2int(P2)))

        μB1 = μB1 # already have from data set
        μB2 = μQ2int(P2) * 3
        μB = np.concatenate((μB1[P1<P0], [np.interp(P0, P1, μB1)], μB2))

        ϵ = np.concatenate(([0], ϵ))
        P = np.concatenate(([-10], P)) # force ϵ(P<Pmin)=0 (avoid interpolation errors)
        nB = np.concatenate(([0], nB))
        nu = np.concatenate(([0], nu))
        nd = np.concatenate(([0], nd))
        ns = np.concatenate(([0], ns))
        μB = np.concatenate(([0], μB))
        ϵint = scipy.interpolate.interp1d(P, ϵ); ϵint.__name__ = self.name
        nBint = scipy.interpolate.interp1d(P, nB)
        nuint = scipy.interpolate.interp1d(P, nu)
        ndint = scipy.interpolate.interp1d(P, nd)
        nsint = scipy.interpolate.interp1d(P, ns)
        μBint = scipy.interpolate.interp1d(P, μB)

        if write:
            nB2 = (nu2int(P)+nd2int(P)+ns2int(P)) / 3 # compute with P instead
            μB2 = μQ2int(P) * 3 # compute with P instead
            ϵ1 = ϵ1 * ϵ0 / (GeV/fm**3)
            ϵ2 = np.concatenate(([0], ϵ2int(P[1:]))) * ϵ0 / (GeV/fm**3) # skip -10
            ϵ  = ϵ * ϵ0 / (GeV/fm**3)
            P  = P * ϵ0 / (GeV/fm**3)
            P1 = P1* ϵ0 / (GeV/fm**3)
            cols  = [nB, nB1, nB2, μB, μB1, μB2, P, P1, ϵ, ϵ1, ϵ2]
            heads = ["nB", "nB1", "nB2", "muB", "muB1", "muB2", "P", "P1",
                     "epsilon", "epsilon1", "epsilon2"]
            outfile = f"data/{self.name}/eos_sigma_{self.mσ}.dat"
            utils.writecols(cols, heads, outfile)

        μQint = lambda P: μBint(P) / 3
        return ϵint, nuint, ndint, nsint, lambda x: 0*x, μQint # ignore electrons

class Hybrid2FlavorModel(HybridModel):
    def __init__(self, mσ=600):
        self.name = "LSM2F_APR"
        self.mσ = mσ
        self.quarkmodel = quark_stars_lsm.LSM2FlavorModel

class Hybrid3FlavorModel(HybridModel):
    def __init__(self, mσ=600):
        self.name = "LSM3F_APR"
        self.mσ = mσ
        self.quarkmodel = quark_stars_lsm.LSM3FlavorModel

class Hybrid2FlavorConsistentModel(HybridModel):
    def __init__(self, mσ=600):
        self.name = "LSM2FC_APR"
        self.mσ = mσ
        self.quarkmodel = quark_stars_lsm.LSM2FlavorConsistentModel

if __name__ == "__main__": # uncomment lines/blocks to run
    #Hybrid2FlavorModel(mσ=600).eos(B=111**4, plot=True, write=True)
    #Hybrid2FlavorModel(mσ=700).eos(B=68**4, plot=True, write=True)
    #Hybrid2FlavorModel(mσ=800).eos(B=27**4, plot=True, write=True)
    #Hybrid2FlavorModel(mσ=600).stars(111, (1e-5, 1e-2), write=True)
    #Hybrid2FlavorModel(mσ=700).stars(68,  (1e-5, 1e-2), write=True)
    #Hybrid2FlavorModel(mσ=800).stars(27,  (1e-5, 1e-2), write=True)
    #Hybrid2FlavorModel(mσ=600).star(0.001180703125, 111, write=True)

    #Hybrid3FlavorModel(mσ=600).eos(B=111**4, plot=True, write=True)
    #Hybrid3FlavorModel(mσ=700).eos(B=68**4, plot=True, write=True)
    #Hybrid3FlavorModel(mσ=800).eos(B=27**4, plot=True, write=True)
    #Hybrid3FlavorModel(mσ=600).stars(111, (1e-5, 1e-2), write=True)
    #Hybrid3FlavorModel(mσ=700).stars(68,  (1e-5, 1e-2), write=True)
    #Hybrid3FlavorModel(mσ=800).stars(27,  (1e-5, 1e-2), write=True)
    #Hybrid3FlavorModel(mσ=600).star(0.0008160778808593749, 111, write=True)

    #Hybrid2FlavorConsistentModel(mσ=400).eos(B=107**4, plot=True, write=True)
```

```
    #Hybrid2FlavorConsistentModel(mσ=500).eos(B=84**4, plot=True, write=True)
    #Hybrid2FlavorConsistentModel(mσ=600).eos(B=27**4, plot=True, write=True)
    #Hybrid2FlavorConsistentModel(mσ=400).stars(107, (1e-5, 1e-2), write=True)
    #Hybrid2FlavorConsistentModel(mσ=500).stars(84,  (1e-5, 1e-2), write=True)
    #Hybrid2FlavorConsistentModel(mσ=600).stars(27,  (1e-5, 1e-2), write=True)
    #Hybrid2FlavorConsistentModel(mσ=400).star(0.001180703125, 107, write=True)
```

G.6 Utilities

We also write a utility function for data management:

utils.py

```
import numpy as np

def writecols(cols, headers, filename, skipevery=-1):
    cols = [list(col) for col in cols]
    maxlen = max(len(col) for col in cols)
    for col in cols:
        while len(col) < maxlen:
            col.append(np.nan)

    file = open(filename, "w")
    file.write(" ".join(headers) + "\n")
    for r in range(0, maxlen):
        for col in cols:
            if len(str(col[r])) > 0:
                file.write(str(col[r]) + " ")
        file.write("\n")
        if skipevery > 0 and r % skipevery == skipevery - 1:
            file.write("\n")
    file.close()
    print(f"Wrote {headers} to {filename}")
```

References

[Adh+17a] P. Adhikari, J. O. Andersen and P. Kneschke: *On-Shell Parameter Fixing in the Quark-Meson Model*. In: *Physical Review D* 95.3, page 036017, **2017**. DOI: 10.1103/PhysRevD.95.036017.

[Adh+17b] P. Adhikari, J. O. Andersen and P. Kneschke: *Inhomogeneous Chiral Condensate in the Quark-Meson Model*. In: *Physical Review D* 96.1, page 016013, **2017**. DOI: 10.1103/PhysRevD.96.016013.

[Alt+10] A. Altland and B. Simons: *Condensed Matter Field Theory* (2nd edition). Cambridge: Cambridge University Press, **2010**. ISBN: 978-0-521-76975-4.

[And+18] J. O. Andersen and P. Kneschke: *Chiral Density Wave versus Pion Condensation at Finite Density and Zero Temperature*. In: *Physical Review D* 97.7, page 076005, **2018**. DOI: 10.1103/PhysRevD.97.076005.

[And+19] J. O. Andersen, P. Adhikari and P. Kneschke: *Pion Condensation and the QCD Phase Diagram at Finite Isospin Density*. In: *Proceedings of XIII Quark Confinement and the Hadron Spectrum — Confinement2018*, page 197, **2019**. DOI: 10.22323/1.336.0197.

[And12] J. O. Andersen: *Introduction to Statistical Mechanics* (1st edition). Trondheim: Akademika forlag, **2012**. ISBN: 978-82-321-0105-4.

[Ant+13] J. Antoniadis, P. C. C. Freire, N. Wex and others: *A Massive Pulsar in a Compact Relativistic Binary*. In: *Science* 340.6131, page 1233232, **2013**. DOI: 10.1126/science.1233232.

[APR15] CompStar Online Supernovae Equations of State: *APR*. **2015**. URL: https://compose.obspm.fr/eos/68 (downloaded 2022-05-12).

[APR98] A. Akmal, V. R. Pandharipande and D. G. Ravenhall: *Equation of State of Nucleon Matter and Neutron Star Structure*. In: *Physical Review C* 58.3, pages 1804–1828, **1998**. DOI: 10.1103/PhysRevC.58.1804.

[Arz+18] Z. Arzoumanian, A. Brazier, S. Burke-Spolaor and others: *The NANOGrav 11-Year Data Set: High-precision Timing of 45 Millisecond Pulsars*. In: *The Astrophysical Journal Supplement Series* 235.2, page 37, **2018**. DOI: 10.3847/1538-4365/aab5b0.

[Baa+34] W. Baade and F. Zwicky: *Cosmic Rays from Super-Novae*. In: *Proceedings of the National Academy of Sciences* 20.5, pages 259–263, **1934**. DOI: 10.1073/pnas.20.5.259.

[Bar+66] J. M. Bardeen, K. S. Thorne and D. W. Meltzer: *A Catalogue of Methods for Studying the Normal Modes of Radial Pulsation of General-Relativistic Stellar Models*. In: *The Astrophysical Journal* 145, pages 505–513, **1966**. DOI: 10.1086/148791.

[Bay+18] G. Baym, T. Hatsuda, T. Kojo and others: *From Hadrons to Quarks in Neutron Stars: A Review*. In: *Reports on Progress in Physics* 81.5, page 056902, **2018**. DOI: 10.1088/1361-6633/aaae14.

[Ber13] E. S. Berge: *The Structure of Quark Stars*. Master's thesis. Norwegian University of Science and Technology, **2013**. URL: http://hdl.handle.net/11250/246997.

[Bla09] M. Blau: *A Useful Identity Involving the Determinant of the Metric*. **2009**. URL: http://www.blau.itp.unibe.ch/GREX/0904sup.pdf (downloaded 2021-03-09).

[Bod71] A. R. Bodmer: *Collapsed Nuclei*. In: *Physical Review D* 4.6, pages 1601–1606, **1971**. DOI: 10.1103/PhysRevD.4.1601.

[Bra17] C. Brandt Kjelsen Strømberg: *Nuclear Equation of State and Neutron Stars*. Master's thesis. Norwegian University of Science and Technology, **2017**. URL: http://hdl.handle.net/11250/2433719.

[Bre16] I. H. Brevik: *Elementær Utledning Av Fluidmekanikkens Grunnligninger*. **2016**. URL: http://www.ivt.ntnu.no/ept/fag/tep4105/pensum/pensum/kompendium_i_fluidmekanikk.pdf (downloaded 2021-11-29).

[Buc59] H. A. Buchdahl: *General Relativistic Fluid Spheres*. In: *Physical Review* 116.4, pages 1027–1034, **1959**. DOI: 10.1103/PhysRev.116.1027.

[Car19] S. M. Carroll: *Spacetime and Geometry: An Introduction to General Relativity*. New York: Cambridge University Press, **2019**. ISBN: 978-1-108-48839-6.

[Cha+09] T. C. Chan, K. S. Cheng, T. Harko and others: *Could the Compact Remnant of SN 1987A Be a Quark Star?* In: *The Astrophysical Journal* 695.1, pages 732–746, **2009**. DOI: 10.1088/0004-637X/695/1/732.

[Cha32] J. Chadwick: *The Existence of a Neutron*. In: *Proceedings of the Royal Society of London. Series A, Containing Papers of a Mathematical and Physical Character* 136.830, pages 692–708, **1932**. DOI: 10.1098/rspa.1932.0112.

[Cha35] S. Chandrasekhar: *The Highly Collapsed Configurations of a Stellar Mass. (Second Paper.)* In: *Monthly Notices of the Royal Astronomical Society* 95.3, pages 207–225, **1935**. DOI: 10.1093/mnras/95.3.207.

[Cha64] S. Chandrasekhar: *The Dynamical Instability of Gaseous Masses Approaching the Schwarzschild Limit in General Relativity*. In: *The Astrophysical Journal* 140, pages 417–433, **1964**. DOI: 10.1086/147938.

[Cho+74] A. Chodos, R. L. Jaffe, K. Johnson and others: *New Extended Model of Hadrons*. In: *Physical Review D* 9.12, pages 3471–3495, **1974**. DOI: 10.1103/PhysRevD.9.3471.

[Com+69] J. M. Comella, H. D. Craft, R. V. E. Lovelace and others: *Crab Nebula Pulsar NP 0532*. In: *Nature* 221.5179, pages 453–454, **1969**. DOI: 10.1038/221453a0.

[Con+17] G. A. Contrera, M. Orsaria, I. F. Ranea-Sandoval and others: *Hybrid Stars in the Framework of NJL Models*. In: *International Journal of Modern Physics: Conference Series* 45, page 1760026, **2017**. DOI: 10.1142/S2010194517600266.

[Dai+16] Z. G. Dai, S. Q. Wang, J. S. Wang and others: *The Most Luminous Supernova ASASSN-15lh: Signature of a Newborn Rapidly Rotating Strange Quark Star*. In: *The Astrophysical Journal* 817.2, page 132, **2016**. DOI: 10.3847/0004-637X/817/2/132.

[dCar+14] S. M. de Carvalho, R. Negreiros, J. A. Rueda and others: *Thermal Evolution of Neutron Stars with Global and Local Neutrality*. In: *Physical Review C* 90.5, page 055804, **2014**. DOI: 10.1103/PhysRevC.90.055804.

[Eic20] G. Eichmann: *Lecture Notes for QCD and Hadron Physics*. **2020**. URL: http://cftp.ist.utl.pt/~gernot.eichmann/lecture-notes (downloaded 2022-05-20).

[Ein05] A. Einstein: *Zur Elektrodynamik bewegter Körper*. In: *Annalen der Physik* 322.10, pages 891–921, **1905**. DOI: 10.1002/andp.19053221004.

[Ein16] A. Einstein: *Die Grundlage der allgemeinen Relativitätstheorie*. In: *Annalen der Physik* 354.7, pages 769–822, **1916**. DOI: 10.1002/andp.19163540702.

[Fol18] Å. S. Folkestad: *Effective Polyakov Loop Modeling of QCD*. Master's thesis. Norwegian University of Science and Technology, **2018**. URL: http://hdl.handle.net/11250/2568085.

[Fon+21] E. Fonseca, H. T. Cromartie, T. T. Pennucci and others: *Refined Mass and Geometric Measurements of the High-mass PSR J0740+6620*. In: *The Astrophysical Journal Letters* 915.1, page L12, **2021**. DOI: 10.3847/2041-8213/ac03b8.

[Fu+08] W.-j. Fu, Z. Zhang and Y.-x. Liu: $2+1$ *Flavor Polyakov–Nambu–Jona-Lasinio Model at Finite Temperature and Nonzero Chemical Potential*. In: *Physical Review D* 77.1, page 014006, **2008**. DOI: 10.1103/PhysRevD.77.014006.

[Fuk+11] K. Fukushima and T. Hatsuda: *The Phase Diagram of Dense QCD*. In: *Reports on Progress in Physics* 74.1, page 014001, **2011**. DOI: 10.1088/0034-4885/74/1/014001.

[Fuk04] K. Fukushima: *Chiral Effective Model with the Polyakov Loop*. In: *Physics Letters B* 591.3-4, pages 277–284, **2004**. DOI: 10.1016/j.physletb.2004.04.027.

[Gam70] G. Gamow: *My World Line: An Informal Autobiography*. New York: Viking Press, **1970**. ISBN: 978-0-670-50376-6.

[Gel+60] M. Gell-Mann and M. Lévy: *The Axial Vector Current in Beta Decay*. In: *Il Nuovo Cimento* 16.4, pages 705–726, **1960**. DOI: 10.1007/BF02859738.

[Gle00] N. K. Glendenning: *Compact Stars: Nuclear Physics, Particle Physics, and General Relativity* (2nd edition). New York: Springer, **2000**. ISBN: 978-0-387-98977-8.

[Gol68] T. Gold: *Rotating Neutron Stars as the Origin of the Pulsating Radio Sources*. In: *Nature* 218.5143, pages 731–732, **1968**. DOI: 10.1038/218731a0.

[Gro+73] D. J. Gross and F. Wilczek: *Ultraviolet Behavior of Non-Abelian Gauge Theories*. In: *Physical Review Letters* 30.26, pages 1343–1346, **1973**. DOI: 10.1103/PhysRevLett.30.1343.

[Has+78] P. Hasenfratz and J. Kuti: *The Quark Bag Model*. In: *Physics Reports* 40.2, pages 75–179, **1978**. DOI: 10.1016/0370-1573(78)90076-5.

[Heh+76] F. W. Hehl, P. von der Heyde, G. D. Kerlick and others: *General Relativity with Spin and Torsion: Foundations and Prospects*. In: *Reviews of Modern Physics* 48.3, pages 393–416, **1976**. DOI: 10.1103/RevModPhys.48.393.

[Hew+68] A. Hewish, S. J. Bell, J. D. H. Pilkington and others: *Observation of a Rapidly Pulsating Radio Source*. In: *Nature* 217.5130, pages 709–713, **1968**. DOI: 10.1038/217709a0.

[Hil24] D. Hilbert: *Die Grundlagen der Physik*. In: *Mathematische Annalen* 92.1-2, pages 1–32, **1924**. DOI: 10.1007/BF01448427.

[Hon+08] Z. Hong-Hao, Y. Wen-Bin and L. Xue-Song: *Trace Formulae of Characteristic Polynomial and Cayley–Hamilton's Theorem, and Applications to Chiral Perturbation Theory and General Relativity*. In: *Communications in Theoretical Physics* 49.4, pages 801–808, **2008**. DOI: 10.1088/0253-6102/49/4/01.

[Iva+67] D. D. Ivanenko and D. F. Kurdgelaidze: *Hypothesis Concerning Quark Stars*. In: *Astrophysics* 1.4, pages 251–252, **1967**. DOI: 10.1007/BF01042830.

[Iva+69] D. Ivanenko and D. F. Kurdgelaidze: *Remarks on Quark Stars*. In: *Lettere al Nuovo Cimento* 2.1, pages 13–16, **1969**. DOI: 10.1007/BF02753988.

[Jia+02] H.-y. Jia, B.-x. Sun, J. Meng and others: *Describing Neutron Stars by the Relativistic Mean Field Theory*. In: *Chinese Astronomy and Astrophysics* 26.4, pages 404–413, **2002**. DOI: 10.1016/S0275-1062(02)00091-7.

[Kac18] M. Kachelriess: *Quantum Fields: From the Hubble to the Planck Scale* (1st edition). Oxford: Oxford University Press, **2018**. ISBN: 978-0-19-880287-7.

[Kac20] M. Kachelriess: *Lecture Notes for FY3452 Gravitation and Cosmology*. **2020**. URL: http://web.phys.ntnu.no/~mika/skript_grav.pdf (downloaded 2020-08-26).

[Kap+06] J. I. Kapusta and C. Gale: *Finite-Temperature Field Theory: Principles and Applications* (2nd edition). Cambridge: Cambridge University Press, **2006**. ISBN: 978-0-521-82082-0.

[Kar07] M. Kardar: *Statistical Physics of Particles*. Cambridge : New York: Cambridge University Press, **2007**. ISBN: 978-0-521-87342-0.

[Kep09] J. Kepler: *Astronomia Nova*. Prague: G. Voegelinus, **1609**. URL: https://archive.org/details/Astronomianovaa00Kepl.

[Kep19] J. Kepler: *Harmonices Mundi*. Linz: G. Tampachii, **1619**. URL: https://archive.org/details/ioanniskepplerih00kepl.

[KKK12] KKK: *Taylor Expansion of Metric | Mathematics@CUHK*. **2012**. URL: https://cuhkmath.wordpress.com/2012/03/16/taylor-expansion-of-metric/ (downloaded 2021-09-17).

[Lai16] M. Laine: *Basics of Thermal Field Theory: A Tutorial on Perturbative Computations*. New York: Springer, **2016**. ISBN: 978-3-319-31932-2.

[Le 59] U. Le Verrier: *Lettre de M. Le Verrier à M. Faye Sur La Théorie de Mercure et Sur Le Mouvement Du Périhélie de Cette Planète*. In: *Comptes Rendus Hebdomadaires Des Séances de l'Académie Des Sciences* 49, pages 379–383, **1859**. URL: https://archive.org/details/comptesrendusheb49acad/page/378.

[Len+00] J. T. Lenaghan, D. H. Rischke and J. Schaffner-Bielich: *Chiral Symmetry Restoration at Nonzero Temperature in the $SU(3)_r \times SU(3)_l$ Linear Sigma Model*. In: *Physical Review D* 62.8, page 085008, **2000**. DOI: 10.1103/PhysRevD.62.085008.

[Li+20] C.-M. Li, S.-Y. Zuo, Y. Yan and others: *Strange Quark Stars within Proper Time Regularized $(2+1)$-Flavor NJL Model*. In: *Physical Review D* 101.6, page 063023, **2020**. DOI: 10.1103/PhysRevD.101.063023.

[Liu+12] X. W. Liu, J. D. Liang, R. X. Xu and others: *The Missing Compact Star of SN1987A: A Solid Quark Star?: The Missing Compact Star of SN1987A*. In: *Monthly Notices of the Royal Astronomical Society* 424.4, pages 2994–2998, **2012**. DOI: 10.1111/j.1365-2966.2012.21447.x.

[Lov+21] R. V. E. Lovelace and G. L. Tyler: *On the Discovery of the Period of the Crab Nebular Pulsar*. In: *The Observatory* 132, pages 186–188, **2021**. URL: https://ui.adsabs.harvard.edu/link_gateway/2012Obs...132..186L/ADS_PDF.

[Luc+13] B. Lucini and M. Panero: *Gauge Theories at Large*. In: *Physics Reports* 526.2, pages 93–163, **2013**. DOI: 10.1016/j.physrep.2013.01.001.

[Lug16] G. Lugones: *From Quark Drops to Quark Stars: Some Aspects of the Role of Quark Matter in Compact Stars*. In: *The European Physical Journal A* 52.3, page 53, **2016**. DOI: 10.1140/epja/i2016-16053-x.

[Mat+21] O. A. Mattos, T. Frederico, C. H. Lenzi and others: *PNJL Model at Zero Temperature: The Three-Flavor Case*. In: *Physical Review D* 104.11, page 116001, **2021**. DOI: 10.1103/PhysRevD.104.116001.

[Mor+99] P. M. Morse and H. Feshbach: *Methods of Theoretical Physics*. Boston: McGraw-Hill, **1999**. ISBN: 978-0-07-043316-8.

[MTW73] C. W. Misner, K. S. Thorne and J. A. Wheeler: *Gravitation*. San Francisco: W. H. Freeman and Company, **1973**. ISBN: 978-0-7167-0334-1.

[New87] I. Newton: *Philosophiæ Naturalis Principia Mathematica*. London: E. Halley, **1687**. URL: http://cudl.lib.cam.ac.uk/view/PR-ADV-B-00039-00001.

[NICER17] NASA/HEASARC: *The Neutron Star Interior Composition Explorer Mission*. **2017**. URL: https://heasarc.gsfc.nasa.gov/docs/nicer/.

[NIST22] National Institute of Standards and Technology: *Digital Library of Mathematical Functions: 5.12 Beta Function*. **2022**. URL: https://dlmf.nist.gov/5.12 (downloaded 2022-02-25).

[Opp+39] J. R. Oppenheimer and G. M. Volkoff: *On Massive Neutron Cores*. In: *Physical Review* 55.4, pages 374–381, **1939**. DOI: 10.1103/PhysRev.55.374.

[Ott+20] K. Otto, M. Oertel and B.-J. Schaefer: *Hybrid and Quark Star Matter Based on a Nonperturbative Equation of State*. In: *Physical Review D* 101.10, page 103021, **2020**. DOI: 10.1103/PhysRevD.101.103021.

[Öze+16] F. Özel and P. Freire: *Masses, Radii, and the Equation of State of Neutron Stars*. In: *Annual Review of Astronomy and Astrophysics* 54.1, pages 401–440, **2016**. DOI: 10.1146/annurev-astro-081915-023322.

[PDG20] Particle Data Group: *Review of Particle Physics*. In: *Progress of Theoretical and Experimental Physics* 2020.8, page 083C01, **2020**. DOI: 10.1093/ptep/ptaa104.

[Pel14] J. Peláez: *Present Status of the $f_o(500)$ or σ Meson*. In: *EPJ Web of Conferences* 73. Ed. by M. Battaglieri, A. D'Angelo, R. De Vita and others, page 03003, **2014**. DOI: 10.1051/epjconf/20147303003.

[Pog17] F. Pogliano: *Neutron Stars — Study of the Mass-Radius Relation and Mean-Field Approaches to the Equation of State*. Master's thesis. Norwegian University of Science and Technology, **2017**. URL: http://hdl.handle.net/11250/2445966.

[Pol73] H. D. Politzer: *Reliable Perturbative Results for Strong Interactions?* In: *Physical Review Letters* 30.26, pages 1346–1349, **1973**. DOI: 10.1103/PhysRevLett.30.1346.

[Pot10] A. Y. Potekhin: *The Physics of Neutron Stars*. In: *Physics-Uspekhi* 53.12, pages 1235–1256, **2010**. DOI: 10.3367/UFNe.0180.201012c.1279.

[Pra+03] M. Prakash, J. Lattimer, A. Steiner and others: *Observability of Neutron Stars with Quarks*. In: *Nuclear Physics A* 715, pages 835c–838c, **2003**. DOI: 10.1016/S0375-9474(02)01514-2.

[Ran+16] I. F. Ranea-Sandoval, S. Han, M. G. Orsaria and others: *Constant-Sound-Speed Parametrization for Nambu–Jona-Lasinio Models of Quark Matter in Hybrid Stars*. In: *Physical Review C* 93.4, page 045812, **2016**. DOI: 10.1103/PhysRevC.93.045812.

[Res16] S. Resch: *Mass Sensitivity of the QCD Phase Structure*. Master's thesis. Justus Liebig University Giessen, **2016**. URL: https://www.uni-giessen.de/fbz/fb07/fachgebiete/physik/institute/theorie/inst/theses/master/master_folder/MA.pdf.

[Sag18] SageManifolds: *Tolman-Oppenheimer-Volkoff Equations*. **2018**. URL: https://nbviewer.jupyter.org/github/sagemanifolds/SageManifolds/blob/master/Worksheets/v1.3/SM_TOV.ipynb (downloaded 2021-08-26).

[Sak+21] J. J. Sakurai and J. Napolitano: *Modern Quantum Mechanics* (3rd edition). Cambridge: Cambridge University Press, **2021**. ISBN: 978-1-108-47322-4.

[Sch+07a] B.-J. Schaefer, J. M. Pawlowski and J. Wambach: *Phase Structure of the Polyakov-Quark-Meson Model*. In: *Physical Review D* 76.7, page 074023, **2007**. DOI: 10.1103/PhysRevD.76.074023.

[Sch+07b] B.-J. Schaefer and J. Wambach: *Susceptibilities near the QCD (Tri)Critical Point*. In: *Physical Review D* 75.8, page 085015, **2007**. DOI: 10.1103/PhysRevD.75.085015.

[Sch+09] B.-J. Schaefer and M. Wagner: *Three-Flavor Chiral Phase Structure in Hot and Dense QCD Matter*. In: *Physical Review D* 79.1, page 014018, **2009**. DOI: 10.1103/PhysRevD.79.014018.

[Sch+10] B.-J. Schaefer, M. Wagner and J. Wambach: *Thermodynamics of $(2+1)$-Flavor QCD: Confronting Models with Lattice Studies*. In: *Physical Review D* 81.7, page 074013, **2010**. DOI: 10.1103/PhysRevD.81.074013.

[Sch13] A. Schmitt: *Lecture Notes for Thermal Field Theory*. **2013/2014**. URL: http://hep.itp.tuwien.ac.at/~aschmitt/thermal13.pdf (downloaded 2021-07-10).

[Sch14] M. D. Schwartz: *Quantum Field Theory and the Standard Model*. New York: Cambridge University Press, **2014**. ISBN: 978-1-107-03473-0.

[Shi+19] M. Shibata, E. Zhou, K. Kiuchi and others: *Constraint on the Maximum Mass of Neutron Stars Using GW170817 Event*. In: *Physical Review D* 100.2, page 023015, **2019**. DOI: 10.1103/PhysRevD.100.023015.

[Sil00] J. R. Silvester: *Determinants of Block Matrices*. In: *The Mathematical Gazette* 84.501, pages 460–467, **2000**. DOI: 10.2307/3620776.

[Tho66] K. S. Thorne: *The General-Relativistic Theory of Stellar Structure and Dynamics*. In: *Proceedings of the International School of Physics "Enrico Fermi"* 35, pages 165–280, **1966**. URL: https://www.its.caltech.edu/~kip/index.html/PubScans/II-12.pdf.

[Tol34] R. C. Tolman: *Relativity, Thermodynamics and Cosmology*. Oxford: Oxford Clarendon Press, **1934**. URL: https://lccn.loc.gov/34032023.

[Ton12] D. Tong: *Lecture Notes for Statistical Physics*. **2012**. URL: https://archive.org/download/David_Tong___Statistical_Physics/sp.pdf (downloaded 2021-12-04).

[Trü+04] J. Trümper, V. Burwitz, F. Haberl and others: *The Puzzles of RX J1856.5-3754: Neutron Star or Quark Star?* In: *Nuclear Physics B - Proceedings Supplements* 132, pages 560–565, **2004**. DOI: 10.1016/j.nuclphysbps.2004.04.094.

[Wei21] S. Weinberg: *On the Development of Effective Field Theory*. In: *The European Physical Journal H* 46.1, page 6, **2021**. DOI: 10.1140/epjh/s13129-021-00004-x.

[Wei72] S. Weinberg: *Gravitation and Cosmology: Principles and Applications of the General Theory of Relativity*. New York: Wiley, **1972**. ISBN: 978-0-471-92567-5.

[Wiki21a] Wikipedia: *Cosmological Constant Problem*. **2021**. URL: https://en.wikipedia.org/w/index.php?title=Cosmological_constant_problem&oldid=1054628851.

[Wiki21b] Wikipedia: *Einstein Field Equations*. **2021**. URL: https://en.wikipedia.org/w/index.php?title=Einstein_field_equations&oldid=1039437590.

[Wiki21c] Wikipedia: *Neutron Star*. **2021**. URL: https://en.wikipedia.org/w/index.php?title=Neutron_star&oldid=1058140577.

[Wiki21d] Wikipedia: *Tolman–Oppenheimer–Volkoff Limit*. **2021**. URL: https://en.wikipedia.org/w/index.php?title=Tolman%E2%80%93Oppenheimer%E2%80%93Volkoff_limit&oldid=1056349917.

[Wit84] E. Witten: *Cosmic Separation of Phases*. In: *Physical Review D* 30.2, pages 272–285, **1984**. DOI: 10.1103/PhysRevD.30.272.

[Yue+06] Y. L. Yue, X. H. Cui and R. X. Xu: *Is PSR B0943+10 a Low-Mass Quark Star?* In: *The Astrophysical Journal* 649.2, pages L95–L98, **2006**. DOI: 10.1086/508421.

[Zac+15] A. Zacchi, R. Stiele and J. Schaffner-Bielich: *Compact Stars in a $SU(3)$ Quark-Meson Model*. In: *Physical Review D* 92.4, page 045022, **2015**. DOI: 10.1103/PhysRevD.92.045022.

[Zac+16] A. Zacchi, M. Hanauske and J. Schaffner-Bielich: *Stable Hybrid Stars within a $SU(3)$ Quark-Meson-Model*. In: *Physical Review D* 93.6, page 065011, **2016**. DOI: 10.1103/PhysRevD.93.065011.

[Zsc+07] D. Zschiesche, L. Tolos, J. Schaffner-Bielich and others: *Cold, Dense Nuclear Matter in a $SU(2)$ Parity Doublet Model*. In: *Physical Review C* 75.5, page 055202, **2007**. DOI: 10.1103/PhysRevC.75.055202.

Herman Sletmoen

Quark and Hybrid Stars with the Quark-Meson Model

NTNU
Norwegian University of
Science and Technology